Insights into the Geological History of Mars through Impact Craters

A thesis submitted in partial fulfilment of

the requirements for the degree of

Doctor of Philosophy

by

Harish

(Roll No. 16330006)

Under the guidance of

Dr. Vijayan S

Assistant Professor

Planetary Sciences Division

Physical Research Laboratory, Ahmedabad

Discipline of Earth Sciences

Indian Institute of Technology Gandhinagar, India

To,

My Family

Declaration

I declare here that this thesis report represents my own ideas in my own words and I have included others ideas with appropriate citations from original sources. I also declare that I have followed all principles of academic honesty and integrity and have not misrepresented or fabricated or falsified any idea/fact/source/data in my submission. I understand that any violation of the above can cause disciplinary action by the Institute and can also evoke penal action from the sources which have thus not been properly cited or from whom proper permission has not been taken when needed.

Harish

Date: June 25, 2021 (Roll No.: 16330006)

Department of Earth Sciences

Indian Institute of Technology, Gandhinagar

Gandhinagar, Gujarat-382355

CERTIFICATE

It is certified that the work contained in the thesis titled **“Insights into the Geological History of Mars through Impact Craters”** by **Mr. Harish** (Roll no: 16330006), has been carried out under my supervision and that this work has not been submitted elsewhere for a degree.

Dr. Vijayan S

(Thesis Supervisor)

Assistant Professor,

Planetary Sciences Division,

Physical Research Laboratory,

Ahmedabad, India

Date: June 25, 2021

Acknowledgments

My years of Ph.D. at Physical Research Laboratory (PRL) were one of the best years in my life during which I learnt the most and at the same time enjoyed the most. It started in 2016 and during these years of my Ph.D. many people supported and encouraged me through this journey. This section provides me the opportunity to express my gratitude to all those people.

First and foremost, I wish to express my deepest gratitude to my supervisor, Dr. Vijayan S, for providing me continuous support during my Ph.D. I thank him for giving me freedom to work on my own ideas and always encouraging me to learn new things. His positive attitude towards solving scientific problems encourages me to probe deeper into the subject. His valuable suggestions and critical comments have helped me to improve scientific outcomes. Discussing the scientific ideas for long hours was the best opportunity for me to avail with my supervisor and I feels lucky for those long hours' discussions. He was always very patient to hear from me during the discussions especially during the tea time and that helps me a lot to gain the confidence and put forward my ideas on any stage. His constant guidance, inspiration, encouragement and motivation during this entire period really helped me to develop as a researcher.

Further, I take this opportunity to express my sincere gratitude towards my Doctoral Scientific Committee (DSC) members, Dr. Dwijesh Ray, Dr. A.D. Shukla and Dr. B. Sivaraman, and my collaborators Dr. Nicolas Mangold, Dr. David Kring, who have always guided me during my research work by providing constructive remarks. I am thankful to them for their welcoming behaviour and motivation towards my thesis work. I am also thankful to the Academic Committee members for their insightful comments and encouragement during my research period. I would also like to thank Mr. Rishitosh K. Sinha for being a guide cum friend and considering me like a family member during my initial months of Ph.D. and encouraging me every time whenever I felt low. I express my sincere thanks to Prof. Varun Sheel, Chairman, Planetary Sciences Division and all the faculty and staff members of the division for their assistance in the form of academic and administrative guidance. I am grateful to the Director, Prof. Anil Bhardwaj; Dean, Prof. D. Pallamraju; and Head of Academic Services, Dr. Bhushit Vaishnav for their continuous support during my Ph.D. tenure. Also, I thank the people from accounts, purchase, library, administration, canteen, CMD, dispensary, transport, and housekeeping sections. I am also thankful to the Computer Center staff, specifically Jigar, Tejas, and Vaibhav for their help. I would like to extend my special regards to all my teachers who taught me at different stages of my professional career.

Life is always joyful with friends. To start with, I thank to the people in my group; Kimi and Tuhi, with whom I discussed on scientific problem and always enjoyed the discussions. I would also like to thank my batch-mates; Priyank, Naveen, Somdutta, Sushree, Nisha, Prabir, Surender, Abdur, Sandeep, Sajan, Deepika, and Ayan for the memories we shared together including stress-relieving chit-chats, games and cooking together. I would like to express my heartfelt gratitude to my friends; Shivani, Sachin, Chanpreet, Ankit and Lalit, whose presence always inspired me and make me to trust on myself. Last but not least, I am thankful to my mates at PRL hostel; Rukmani, Archita, Kuldeep, Kumar, Rahul, Subir, Richa, Shefali, Anshika, Madhu, Ritu, Rushi, Himanshu, Aravind, Meghna, Anju, Akansha, Deepak, Yash, Monika, and Vikas for all the wonderful time I spent with them during my PhD. It was a pleasure to meet people like them, who are always there whenever you are in need.

Words would fail in expressing the love, strength, and encouragement of my family members towards me. I am lifelong grateful to my beloved parents, Smt. Parkashi Devi and Shri Ramesh Kumar, who always believed in me and encouraged me to pursue my dreams. A special thanks to my elder sister Mrs. Asha Rana, elder brother Virender, sister-in-law Mrs. Monika Nandal and Jiju Mr. Deepak Rana for being the best support anyone can get. Their continuous encouragement and care helped me to go through any tough situation easily. My thesis will be incomplete if I don't express my love and thanks to all my family members; Mrs. Bhago devi, Bde papa Mr. Rajendar Nandal, Bdi Maa Mrs. Rajo Nandal, Mausi Ji, elder sisters Kavita and Sarika, my nephews Yash, Deven and Karthik, and my niece Bhumi. At last, I thank to God for this opportunity and for everything I have.

Harish

Abstract

The geological history of Mars is complex as the planet has gone through various widespread processes such as volcanic, fluvial, glacial, tectonic, magmatic, and impact-cratering. These processes left shreds of evidence on the surface of Mars in the form of surface features, depositional and erosional landforms. The study of these processes is of paramount importance to understand the history of the planet. Impact-cratering is one of the fundamental processes in the Solar System, and impact craters are pervasive on the surface of the planet Mars. Thus, in this thesis work, impact craters are used to study various geological processes (glacial, fluvial, volcanic, tectonic, and magmatic), which prevailed on Mars from the Amazonian (younger) period to the Noachian (older) period. Impact craters located in different latitudes are used to study 1) Water-ice exposing scarps within the northern midlatitude craters on Mars 2) Fluvial and glacial processes within the southern low-latitude impact craters that excavated into a Noachian volcanic dome, and 3) Graben and collapse-pit formation processes associated with impact craters in the vicinity of Valles Marineris region of Mars.

Near-surface exposed water-ice was recently discovered on Mars, though the discovery is majorly limited to southern mid to high-latitudes. In this regard, this thesis work revealed near-surface water ice deposits exposed by erosional scarps within two impact craters located in the northern midlatitude of Mars. These two craters are ~5000 km spatially apart and provide ample evidence that the water-ice is widespread just a few meters below the Martian surface. This study also substantiated that snow/ice may have deposited and accumulated within the last 100 to 10 million years, and water-ice got exposed within the last 1 million years. In the northern lowlands, this thesis work

mainly focused on the recent (Amazonian) depositional (snow) and erosional (scarp) history of Mars.

In the southern highlands, this thesis work focused on Degana crater, a ~50 km diameter impact crater, which formed on top of a ~4 billion-year-old volcanic dome. After the Degana formation, the climatic condition favored snow/ice precipitation and which formed multiple depositional fans within this crater. In a later stage, these fan deposits are superposed by glacial remains (moraine ridges). This study found that the volcanic dome contains Mg-rich olivine and low-calcium pyroxene, excavated by Degana and superposed crater Degana-A. This study provided evidence for volcanic material, fluvial-related depositional fan, and glacial moraines within the same crater on Mars.

In the equatorial region, ~4000 km long canyon system is located, which is called Valles Marineris (VM). Such an extensive canyon system has been modified over time by tectonic and magmatic processes. Thus, studying the spatial and temporal modification of this vast canyon system is essential to understand the tectonic and magmatic processes on Mars. The VM region is modified and developed through graben and collapse pits, which are surface expressions of tectonic and magmatic processes. To study these processes, this thesis work used those craters, which are: 1) located within the ~100 km distance from the boundary of Valles Marineris and 2) associated with graben and collapse pits. 1516 craters (diameter >1 km) are studied, and out of these, 48 craters have an association with graben and collapse pits. The detailed chronological analysis revealed that the modification of VM varies spatially as well as temporally (~3.7 to 1.2 Ga). The result from this study substantiates that the modification of VM occurred until the Middle Amazonian epoch, which is much younger than previously thought.

Overall, this thesis work provided new insights into the geological history of Mars by exploring the impact craters, which recorded and preserved the evidence for diverse geological processes that occurred at different epochs.

Keywords: Mars; Impact Craters; Martian geological History; Surface Processes; Water Ice; Volcanic; Fluvial; Glacial; Tectonic; Graben; Pit

Contents

List of Figures

List of Tables

Abbreviations

AU	Astronomical Unit
CTX	Context Camera
HiRISE	High Resolution Imaging Experiment
HRSC	High Resolution Stereo Camera
ISRO	Indian Space Research Organisation
Ls	Solar Longitude
MCC	Mars Color Camera
MEX	Mars Express
MGS	Mars Global Surveyor
MOLA	Mars Orbiter Laser Altimeter
MOM	Mars Orbiter Mission
MRO	Mars Reconnaissance Orbiter
MY	Martian Year
THEMIS	Thermal Emission Imaging System

Chapter 1 Introduction

The planet Mars, known for its geologically active history [1–4], is one of the enigmatic planets in the Solar System. The history of Mars is preserved in the markers left behind by various geological processes (e.g., fluvial, glacial, volcanic, and tectonics) that underwent on Mars [1, 2]. These activities can cause modifications of the crust of Mars and leave geological markers in the form of depositional, erosional features, and associated minerals [2, 5]. Thus, these geological features, along with the associated minerals, worked as traces to identify 1) the geological processes that occurred on Mars and 2) the climatic conditions prevailed in the past.

1.1 Introduction to Mars

In relation to the distance from Sun, Mars is the fourth planet in our solar system, located ~1.5 Astronomical units (AU) away. In terms of diameter, Mars is (~6779 km) approximately half that of the Earth (~12,742 km). Mass of the planet Mars is nearly one-tenth to the Earth, whereas the volume is almost one-fifteenth to the Earth. The surface gravity of Mars is ~3.7 m/s^2, which is ~38% that of the Earth (9.8 m/s^2) [6]. In present conditions, the maximum temperature of Mars rises to ~300 K during the summer noon on the equator, whereas the lowest temperature can go up to ~130 K during the winter night. The average temperature on the surface of Mars is ~215 K [6].

Martian northern and southern regions are separated by the dichotomy boundary (Figure 1.1). The northern region is relatively smooth and topographically low-lying surface and known as northern lowlands. The southern region is a hummocky and undulated surface, known as southern highlands. Notably, the crater density is more in the southern highlands relative to the northern lowlands. Therefore, based on the crater density, it is understood that the northern lowlands are relatively younger surface on Mars as compared to southern highlands [2]. The southern highlands of Mars host the largest basin in the solar system, the Hellas basin (~2300 km diameter), and the equatorial region host a ~4000 km long canyon feature, which is ~300 km wide and ~10 km deep [7, 8]. Mars is also home of many large volcanoes on its surface in the low to mid-latitude regions [2]. In polar regions, Mars is home of large scale ice deposits layers [2].

1.2 The geological time scale of Mars

The geological time scale of Mars is broadly divided into three major periods: Noachian, Hesperian, and the Amazonian period from older to younger time [2, 9, 10]. The surface features on Mars are divided into these periods based on 1) the intersection relationships and 2) the frequency and diameter of impact craters present on the surface of Mars [2, 9]. As per Neukum system (Table 1.1), the period older than ~3.7 Ga is known as Noachian period. Hesperian period ranges from ~3.7 Ga to ~3.0 Ga. A period younger than ~3.0 Ga is known as the Amazonian period [9, 11]. These periods further sub-divided into epochs from early to late based on older to younger time as shown in Table 1.1 [9, 11].

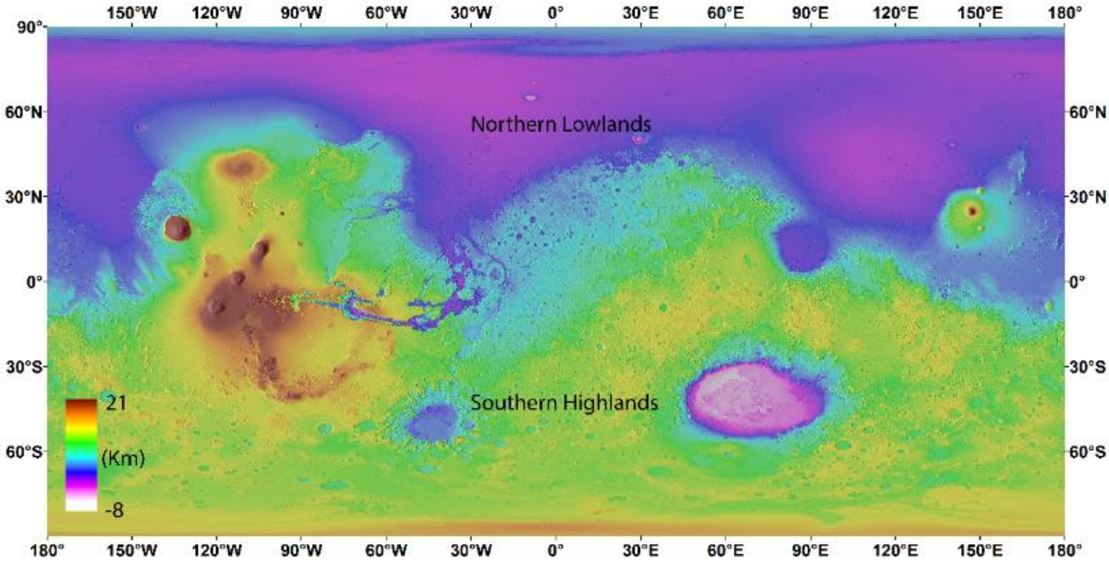

Figure 1.1: Global topographic map of Mars. MOLA DEM overlaid MOLA hillshade.

Table 1.1: Martian epoch boundaries (adapted from Michael, 2013)

Epoch	Reference crater diameter (km)	Crater density (per Mkm^2)	Start of epoch (Ga)	
			Hartmann 2004 iteration	Neukum system
Late Amazonian	1	160	0.274	0.328
Middle Amazonian	1	600	1.03	1.23
Early Amazonian	1	2100	3.24	3.37
Late Hesperian	5	125	3.39	3.61
Early Hesperian	5	200	3.56	3.71
Late Noachian	16	100	3.85	3.83
Middle Noachian	16	200	3.96	3.94
Early Noachian	–	–	–	–

1.3 The Martian climate

The presence of well-integrated and wide-spread valley networks and hydrated and hydrous minerals on the Noachian terrains of Mars indicate that the conditions during the Early Mars was hot and wet. This favors warm and wet climatic conditions during the Noachian period on Mars, however, it is still debatable whether the planet supported cold and dry conditions in its early history [12]. Also, the climatic conditions during the Hesperian and Amazonian periods are not constrained fully. Many studies [13, 14] modeled that the temperature on Mars does not rise above the freezing point of water even if the pressure rise in multiples of bars. In addition, migration of ice and formation of large ice sheets in the highlands is postulated [14]. These ice deposits can be melted by the volcanism and impacts [15–18], which further result in liquid water considering favorable climatic conditions. Thus, targeting diverse geological activities can help to understand the climate conditions that prevailed locally on Mars.

1.4 Impact craters

Impact cratering is one of the fundamental and dominant processes in the solar system [19]. Impact craters are the main surficial landform on the surface of Mars, many other planetary bodies, and their satellites. However, crater mechanics, i.e., initiation of multiple events when a projectile moving with hypervelocity hits the surface of a body, is a complex phenomenon [19]. The sequence of impact events classified into three main stages: 1) Contact and compression stage, 2) excavation stage, and 3) modification stage [19, 20]. Though the formation of an impact crater is a continuous process, however, dividing it into distinct stages is a convenient and standard way of defining crater mechanics. Therefore, it should not be forgotten that there is no exact separation between the three stages. Here, each stage is discussed in detail.

1.4.1 Contact and compression stage

This is the first stage that initiates once the projectile comes in contact with the target surface. This stage lasts equivalent to the time taken by the projectile to transverse its diameter. Mathematically, if L is the projectile diameter and v is the projectile velocity, then the duration of contact and compression τ will be equal to the ratio of projectile diameter to the projectile velocity. As the projectile will come in contact with the target, it will transfer its energy and momentum to the target material. As a result of this interaction, shock waves will propagate both into the projectile and the target. They will compress and slow down the projectile velocity, and accelerate the target material in the downward direction. The material in the projectile and the target move with the same speed at the interface between the two. In the projectile, the shock waves move up and reach the top. Therefore, the surface of the compressed projectile expands upward, and the pressure is released. The released pressure caused relief waves that propagate towards the interface. Once the pressure-relief waves reach the interface, the contact and compression stage is considered to terminate. Note that, at this time, the projectile pressure can reach hundreds of gigapascal (Gpa), which generated high heat. Therefore, the projectile can reach the liquid or gaseous state after the decompression. [19–21]. The target material may also melt, which depends on the projectile size and velocity.

1.4.2 Excavation stage

This stage starts once the contact and compression stage terminates. The shock waves formed during the contact and compression stage convert into elastic waves due to expansion and cause an outward motion of the particles. At the same time, the pressure-relief waves caused an upward motion of the particles. The motion of particles in outward and upward directions causes the excavation of materials. The crater formed at this stage is known as a transient crater. The duration of excavation lasts few seconds to minutes depends on the diameter of the crater and the gravity of the planetary body. [19–21]

1.4.3 Modification stage

After the excavation stage, the transient crater starts to modify. This stage is known as the modification stage. The modification of the transient crater is caused by a key change in the motion of material within and beneath the transient crater. The material/debris begins to collapse downward and towards the center that is inverse to the motion of material during the excavation stage. The collapse is mainly gravity-driven; however, the elastic rebound of the underlying rock may have caused significant modification to the crater. Modification processes are not only limited to debris sliding but also affect the floor rise, central peak appearance, multi-ring formation, central pit, and formation of stepped terraces over the wall of a crater. These modification processes initiate immediately after the formation of a transient crater and last similar to the excavation stage. Again a clean line of separation between the transient crater formation and initiation of modification is difficult to determine. The modified crater after the modification stage is subject to other geological processes of erosion, deposition, and post-modification over time. These processes may leave evidence preserved within the crater, and eventually, the crater can be used as a proxy to understand various geological processes underwent and render the information about the geological past of the planet. [19–21].

Overall, impact craters can be used as fingerprints, which exposed the surface material and preserved the post impact geological processes.

1.5 Major geological processes on Mars

Major geological processes that occurred on Mars are volcanic, fluvial, glacial and tectonics. This thesis work focused on the below-listed processes with an aim to understand the history of Mars. 1) Erosional processes that caused the formation of scarps, gullies, fluvial channels, glacial valleys, and lava channels. 2) Depositional processes that caused deposition of lava due to volcanic activities, fans and delta due to fluvial activities, and lobate debris apron and moraines features due to glacial activities. 3) Tectonics processes that caused the formation of graben, ridges, and thrust faults. 4) Collapse processes that caused the formation of collapsed pits with depression. 5) Impact cratering that caused the excavation and alteration of the crustal material and they are associated with the above-listed processes.

1.5.1 Formation of scarps

Scarps on Mars are interpreted to have formed due to erosion caused by the sublimation of ice over time [22]. The steep slope wall of scalloped depressions is considerably termed as scarp, where scalloped depressions generally show oval shape [23]. In general, they are thought to be considered as periglacial landforms and thus dominant within mid to high latitudes of Mars. In line with this, many previous studies [22, 24–26] reported the presence of near-surface large water-ice sheets from mid to high-latitudes on Mars. Generally, scarps form over the inner wall of the craters and follow the pole-facing scenario; however, they are not limited to within the crater's rim. The scarps generally have a steep wall (greater >45°). The scarps are the important target as they expose evidence of preserved water-ice located few meters below the surface [22].

1.5.2 Glacial processes

A huge and dense mass of constantly and slowly moving ice over the surface is known as a glacier. On Mars, glacial activities are majorly reported in mid to high latitudes [27, 28], though a very few reports are there, which suggest their possible occurrence in the lower latitudes also [29]. Glacial activities on Mars are also intriguing as multiple pieces of evidence suggest their occurrence during recent history. These evidences include viscous flow features (VFF), lobate debris aprons (LDAs), lineated valley fill (LVF), eskers, moraines, and gullies [27, 30]. Among these, moraines are one of the least discussed features, though they are important to understand glacial retreat phenomena on Mars. Multiple terminal moraines are reported in the Arsia Mons region, which suggests glacial retreating over a large period of time [31].

1.5.3 Fluvial processes

Fluvial valley and channel networks on Mars bear a resemblance with the river networks on Earth. These channels are majorly present in the southern highland of Mars and formed alluvial fans and delta deposits [2, 32]. Most of the fluvial activities are reported to occur during Noachian, and Hesperian periods [2, 3], though a very few have been emphasized on Amazonian-period outflow channels on Mars [33]. Fluvial-related activities on Mars can be indicated mainly by surface morphology and mineralogy. Fluvial activities commonly cause 1) change in the surface morphology and 2) deposition and alteration of aqueous minerals. Changes in the surface morphology include 1) erosion in the form of valleys and channels and 2) deposition in the form of fan or delta deposits. There are many locations on Mars where the channel(s) breach through the crater's rim and deposit the sediments to form alluvial fan(s) and/or delta(s), for example, Gale and Jezero craters [34, 35]. Based on the flow direction, the channels are subcategories as 1) inflow and 2) outflow channels and the hosted craters named as close and open basin lakes, respectively [36–38].

1.5.4 Volcanic processes

Magma rupture through the crust of a body is known as a volcano. Mars is home to the largest volcanoes in the solar system, including Alba and Olympus mons. Volcanic activities on Mars cover a large span of time from the Noachian to Amazonian period. Though, the rate of volcanism on Mars was high during the first few billion years after its formation, however, mostly geomorphic evidence has been destroyed for the oldest volcanism on Mars [2]. During later epochs the rate of volcanism declined rapidly, however, most of the reports for volcanic activities on Mars have focused on the Hesperian and Amazonian period activities [2]. Thus, there is a scarcity of evidence of volcanism occurred during the early times. Volcanic activities are important to study as they contain evidence for the thermal history of the planet and the crustal evolution as well.

1.5.5 Pit collapse processes

In general, pits are elliptical to circular depressions that are formed by collapse into a subsurface cavity. The cavity can be caused mainly due to: 1) lava tube, 2) migration of magma, 3) fissuring, 4) dilational normal faulting and 5) dissolution of the substrate [39]. On Mars, pits are one of the enigmatic feature whose source and origin are debatable. In comparison to impact craters, pits lacks elevated rims and generally show more depth to diameter ratio [39]. Pits are mainly reported in the regions of regional extension and/or in the vicinity of local fissures. In addition, a strong association between pits and graben has been observed over many regions on Mars [39, 40].

1.5.6 Tectonic processes

Mars is dominated by tectonic processes especially in the western hemisphere of Mars [41]. These tectonics activities include compressional features such as wrinkle ridges and extensional features such as graben [41, 42]. In general, graben is a linear depression formed by two opposite dipping normal faults. However, narrow graben on Mars are reported as collapse features and are suggested to have a volcanic origin [42]. Overall, graben forming activities are more prominent during the Hesperian period [43].

1.6 Objective of the thesis: Craters as a probe to understand the Martian geological history

Mars host ~0.38 million craters on its surface which are greater than or equal to 1 km diameter [44]. These large number of craters are formed over the different time period on Mars, which ranges from Noachian to Amazonian period. Additionally, various geological processes (e.g. volcanic, fluvial etc.) on Mars occurred over this time. Therefore, the impact craters can be used as a probe to understand the diverse geological processes occurred in different epochs. Figure 1.2 shows a schematic that display association of impact craters with diverse geological activities on Mars from Amazonian to Noachian period. These processes occurred over the different latitudes on Mars and they can be studied using the features associated/causedby these processes. These features either superposed to the impact craters (such as formation of alluvial fans) or vice versa (such as crooscut of a graben by an impact crater), however, in both the cases they modified the impact craters. Overall, this thesis work focussed on these modified impact craters and thus impact craters, which formed in different epochs and are located in different latitudes, are used as a probe to understand the geological history of Mars.

1.6.1 Craters in Northern lowlands: Motivation and scientific questions

On Mars, one of the most important question is the spatial distribution of exposed water ice. Exposed water-ice is recently reported on Mars, however, these locations are mainly concentrated in the southern highland of Mars and only one location has been discovered in the Northern lowland [22]. Thus, the existence of a widespread distribution of near-surface exposed ice remains an open question. Identifying more craters with water-ice deposits indeed improve to understand their spatial distribution on Mars.

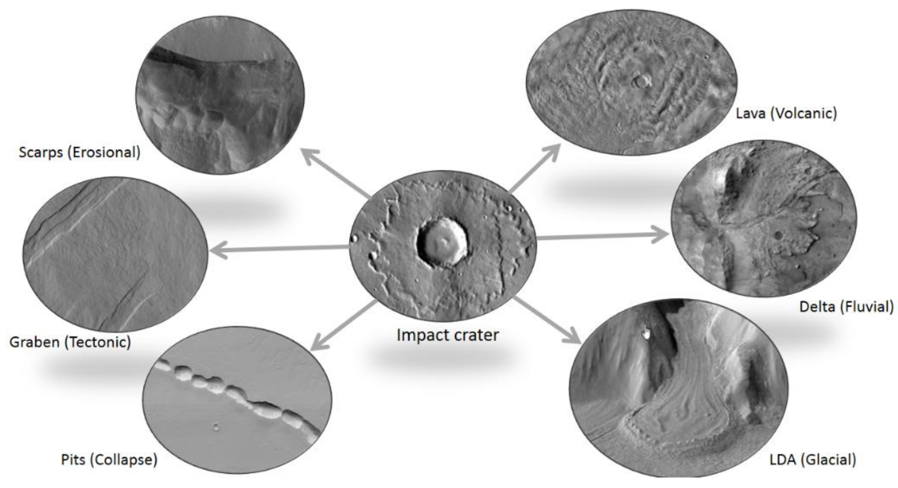

Figure 1.2: Schematic showing impact crater and its association with diverse geological processes.

1.6.2 Craters in Southern highlands: Motivation and scientific questions

The planet Mars is a host for widespread past volcanic, fluvial and glacial activities on its surface. However, to date no clear spectral evidence of early to mid Noachian volcanic material is known on Mars due to high dust cover in the volcanic regions of Mars [45]. In addition, snow/ice precipitation in the lower latitudes of Mars during the Hesperian/Amazonian period and its melting due to impact ejecta remains an open question. Also there will be few locations on Mars where volcanic, fluvial and glacial evidence all co-existing within impact craters. Such craters retains the potential environmental records of Mars.

1.6.3 Craters around Valles Marineris: Motivation and scientific questions

Valles Marineris (VM) is ~4000 km long, ~300 km wide and ~10 km deep feature located in the equatorial region of Mars [7, 8]. This feature has majorly formed during the Hesperian period and modified over the time [2]. However, not much is known about the modification and its variation over time and space. Thus, the spatial modification and extension of Valles Marineris over the time remains an open question, which is addressed through craters surrounding the VM region.

Based on motivation presented above, this thesis will present three research works regarding the understanding of geological processes on Mars and climatic evolution using impact craters. The thesis is composed of three parts. In the first part, I will discuss the results of the analysis of spectral and imagery data in the northern lowlands, aiming to understand the distribution of the near-surface water-ice in the northern lowlands of Mars and the period of ice accumulation, compaction and exposure by the scarps. In the second part, I will discuss the results obtained through spectral and image analysis in the southern highlands of Mars, aiming to understand the geological context of volcanic, fluvial and glacial activities, and climatic evolution over the region of interest. In the third part, I will discuss the results of morphological and chronological analysis in the near equatorial region of Mars, aiming to understand the modification of Valles Marineris region over the time.

Chapter 2 Data and Methods

This chapter outlines the datasets and method used throughout the thesis work. The datasets are described as follows: first the imagery datasets range from low resolution to high resolution are described, which are used for the geomorphological studies. Secondly, the topography datasets from low resolution to high resolution are described, which are used for the elevation variations. Third, hyperspectral dataset which was used for the mineralogical study was described. And in the end of this chapter, the software and methods are described.

2.1 Martian datasets used in this thesis

2.1.1 Imagery data

In this thesis work, orbital images mainly from different Mars missions were used: The Thermal Emission Imaging System (THEMIS) onboard 2001 Mars Odyssey (MO) Instrument [46], Mars Color Camera (MCC) onboard 2014 Mars Orbiter Mission (MOM) Instrument [47] and Context Camera (CTX) and High Resolution Imaging Science Experiment (HiRISE) onboard 2006 Mars Reconnaissance Orbiter (MRO) instrument [48, 49]. Here, these datasets are described one by one as following:

2.1.1.1 Thermal Emission Imaging System (THEMIS) day/night time infrared images

THEMIS started imaging the Mars from 2001. THEMIS consist of two instruments: 1) Visible and near-infrared camera (VNIR) of wavelength range from 0.42-0.86 µm, and 2) multispectral thermal infrared spectrometer of wavelength range from 6.8-14.9 µm. VNIR camera has mapped the Martian surface at visible wavelengths with a resolution of ~18 meters/pixel and at infrared wavelengths with a resolution of 100 meters/pixel. However, this thesis work mainly used infrared THEMIS camera data for the regional context. THEMIS has mapped global Mars in both day and night infrared at a resolution of 100 meters/pixel. Global mosaics from 60°N-60°S for THEMIS day-time version 12[1] and night–time infrared version 12[2] are downloaded through the United States Geological Survey (USGS) [50]. The primary objective of THEMIS instrument was to determine the thermal and spectral properties of the Martian surface [46].

2.1.1.2 Mars Color Camera (MCC) images

MCC started imaging the surface of Mars from 2014. MCC was designed to provide RGB images at a resolution of 20-166 meters/pixel [47]. It operates in the wavelength range of 0.4 to 0.7 µm. Field of view of MCC varies from tens of meters to

[1]https://astrogeology.usgs.gov/search/map/Mars/Odyssey/THEMIS-IR-Mosaic-ASU/Mars_MO_THEMIS-IR-Day_mosaic_global_100m_v12

[2]https://astrogeology.usgs.gov/search/map/Mars/Odyssey/THEMIS-IR-Mosaic-ASU/Mars_MO_THEMIS-IR-Night_mosaic_60N60S_100m_v14

kilometers and it used 16 varies modes of exposures [47]. The major scientific objective of MCC was to image the surface of Mars and features present on it at different scales and resolution. MCC images were downloaded in tiff format from Science Data Archive of Indian Space Research Organistaion (ISRO)[3].

2.1.1.3 ConTeXt Camera (CTX) images

CTX started imaging the surface of Mars from 2006. CTX was designed to provide context images at a resolution of 6 meters/pixel for data acquired by other instruments of MRO. Another objective of CTX was to observe regions and features of interest for upcoming Mars missions and future Mars exploration. CTX images covered the entire surface of Mars. Each images are ~30 kilometers wide swath and they are captured from an altitude of ~290 kilometers with almost circular and polar mapping orbit. CTX images were downloaded in Pyramidized GeoTIFF format from Mars Orbital Data Explorer (ODE) of PDS Geosciences Node[4]. [48]

2.1.1.4 High Resolution Imaging Science Experiment (HiRISE) images

HiRISE started imaging the Mars since 2006. HiRISE images provide the best resolution images (25 centimeters/pixel) of the surface of Mars. HiRISE images are taken by a pushbroom camera which covers ~6 kilometers swath width at a spatial resolution of 25 centimeters/pixel to 1.3 meters/pixel. This camera has a primary mirror

[3] https://mrbrowse.issdc.gov.in/MOMLTA/

[4] https://ode.rsl.wustl.edu/mars/

of diameter 0.5 meters, and effective focal length of 12 meters. Detectors of 14 charge coupled devices (CCD) with 2 output channels for each detector and varying pixel binning acquires HiRISE images. HiRISE covers two sets of images: grayscale images and false colored images. Color images are acquired with most grayscale images and they covers around one-fifth of the field of view of grayscale images. HiRISE images downloaded from Mars ODE[5] have some projection issue which was fixed using a simple script called “fix_jp2”. To fix the projection issue, the script has to be copied in the folder where the HiRISE images were downloaded. Then, using the Geospatial Data Abstraction Library (GDAL) tool associated with QGIS open source software run the command “fix_jp2 HiRISE_image_id.jp2”[6] to fix the issue. [49]

2.1.2 Topography data

2.1.2.1 Mars Orbiter Laser Altimeter (MOLA)

MOLA started acquiring elevation of Mars from 1996. The major objective of the MOLA was to map the topography of the Mars globally. The altimeter used incident laser pulses, which were fired on the surface of mars 10 times in a second, and using the time delay the topography of the surface is obtained. Locations of these pulses reconstructed to get a global topographic map of Mars at a spatial resolution of ~400 meters and vertical uncertainty of ~3 meters. [51]

[5] https://ode.rsl.wustl.edu/mars/

[6] http://planetarygis.blogspot.com/2016/07/more-hirise-conversion-tips-until.html

2.1.2.2 MOLA-HRSC blended DEM

This DEM has been generated using digital elevation models from the MOLA and the High-Resolution Stereo Camera (HRSC) onboard Mars Express (MEX) spacecraft, which was launched in 2003 by the European Space Agency (ESA). HRSC is the dedicated stereo camera orbiting to Mars, which comprises parallel mounted 9 charge coupled devices (CCD) line sensors for simultaneous stereo imaging of Mars. Digital elevation models derived using HRSC stereo images can have a spatial resolution of ~50 meters and vertical accuracy of ~10 meters. However, HRSC stereo generated DEM does not have a full coverage of the Mars. Therefore, HRSC stereo generated DEM are blended with MOLA DEM to get a global coverage of Mars, which has higher spatial resolution than MOLA and global coverage in comparison of limited coverage of HRSC stereo DEM. MGS MOLA and MEX HRSC blended DEM covers globally on Mars at a resolution of ~200 meters per pixel and is downloaded from USGS[7] [52].

2.1.2.3 CTX and HiRISE DEM

Though, the MOLA and MGS MOLA- MEX HRSC blended global DEM datasets have revolutionised understanding of the Martian topography, however, their low spatial resolution limits to detect topographic features less than hundreds of meters across. Therefore, for areas of interest where CTX and HiRISE stereo images are

---

[7]https://astrogeology.usgs.gov/search/map/Mars/Topography/HRSC_MOLA_Blend/Mars_HRSC_MOLA_BlendDEM_Global_200mp_v2

available, CTX and HiRISE derived digital elevation models are used. To generate CTX and HiRISE DEM using their stereo images, Martian Surface Data Processing Service (MarsSI) pipeline is used[8]. MarsSI is using NASA AMES Stereo pipeline[9] [53] to generate CTX and HiRISE DTM images. Using MarsSI, the desired CTX and HiRISE raw images in a standard format termed as Experiment Data Record (EDR) are downloaded and they are converted into reflectance termed as Radiometric Data Record (RDR). These RDR are projected to form map projected RDRs (MRDR) and from them CTX DTM files are computed which are not aligned to MOLA data and termed as Experiment Digital Terrain Model (EDTM) images. These EDTM files are used for producing the CTX DTMs that are aligned to MOLA data and termed as Aligned Experiment Digital Terrain Model (ALEDTM) images. ALEDTMs are the final product of CTX and HiRISE stereo image processing through the pipeline of MarsSI and are used for high-resolution topographical analysis.

2.1.3 Spectral dataset

Compact Reconnaissance Imaging Spectrometer on Mars (CRISM)

CRISM is a visible-infrared imaging spectrometer on-board Mars Reconnaissance Orbiter (MRO) spacecraft to map the surface mineralogy of Mars. It has two detectors named S-band and L-band detectors, which overall cover

[8] (https://marssi.univ-lyon1.fr/MarsSI/

[9] https://ti.arc.nasa.gov/tech/asr/groups/intelligent-robotics/ngt/stereo/

wavelengths from 0.36 to 3.92 µm. The S-band detector covers the wavelengths from 0.36 to 1.015 µm, whereas, L-band detector covers 1.0 to 3.92 µm wavelengths. Both the detectors overlap around 1 µm, therefore, care has to be taken while merging the spectrum from the two detectors. CRISM works in two operating modes: 1) Multispectral survey and 2) Hyper-spectral survey. In multispectral survey, ~72 channels are used to cover the Mars globally with a resolution of 100-200 meters/pixel. Whereas in hyperspectral survey, ~544 channels are used in full spatial resolution of 15-19 meters/pixel which target the high priority candidate sites with a spectral resolution of 6.55 nm/channel. The candidate sites mainly include sedimentary deposits, aqueous minerals, exposed crustal sections in escarpments, and volcanic regions. Also, during the hyperspectral survey CRISM uses nadir pointed gimbal to cover 10 km X 10 km field of view via along-track motion. Whereas in multispectral survey CRISM uses nadir pointed gimbal to cover large field of view via cross-track motion. Surface spectra recorded by CRISM includes atmospheric effects, therefore to remove atmospheric effects from the surface spectra an emission phase function (EPF) is determined by taking ten additional images before and after the main image. In the later observations, CRISM was targeted to record seasonal variations in: water content of the surface material, ice aerosols in the atmosphere and atmospheric dust. To implement these investigations, global hyperspectral EPFs grids after every 10° degrees of solar longitude are measured repeatedly throughout the Martian year. The raw CRISM dataset need pre-processing before extracting the spectral signature. The pre-processing steps are described in section 2.2.2. [54]

2.2 Software and methods

2.2.1 ArcGIS

All the imagery datasets used in this thesis work were accomplished and incorporated into Geographical Information System (GIS) tasks using the ESRI software package ArcGIS 10.5. ArcMap programme was used for the data analysis and for the geomorphological mapping. In ArcMap, images were compiled as layer files and be used for analysis and geomorphological mapping. As the lighting conditions vary from image to image, therefore display settings in ArcMap were used to change the contrast and brightness to normalize the lightning conditions. In addition, 3D analyst toolkit inbuilt in ArcMap was used to get the elevation profiles across the surfaces using digial elevation models. Also, ArcGIS is used to produce 3D representations of digital elevation models using inbuilt ArcScene programme.

2.2.2 Quantum Geographic Information System (QGIS)

Along with ArcGIS, QGIS is also used for the imagery and elevation datasets. QGIS is a open source Geographic Information System (GIS) and is licensed under the GNU general public license (GPL). In QGIS, data were compiled as layer files and used for topographical and photogeological analysis. Profile tool extension was added to QGIS to get the elevation profile on the surface of Mars.

2.2.3 Exelis Visual Information Solutions (ENVI)

ENVI software is used for spectral analysis from CRISM. To do so, CAT tool was added to ENVI, which is the standard toolkit used for the processing of CRISM. Once the CAT tool is added in ENVI, the following steps are carried out to get the reflectance spectra from CRISM. CRISM trr3 images were converted from PDS to CAT. Then, CRISM data was corrected for atmospheric noise using the atmospheric correction inbuilt within the CAT tool. This correction used the default volcano scan method to correct for atmospheric disturbances. After the atmospheric correction, CRISM data is corrected for additional spikes in the spectra and unwanted strips in the data. This is done using destrip and despiking corrections included in CAT toolkit. Once all the corrections were applied, the CRISM data is georeferenced to project it well over the other MRO datasets (CTX and HiRISE).

2.2.4 Craters tools and crater stats

For a planetary body, the best technique available to determine the age of a surface, that too without a sample, is crater size-frequency distribution (CSFD) [55]. Generally, the area which hosts more number of craters of larger diameter is relative older to the area which hosts less and/or smaller size craters. For the determination of CSFD, cratertools extension is added added in ArcGIS. Using this tool, two shape files are prepared which includes: 1) area shape file that contains single geological unit (example: ejecta or floor of a crater) and 2) crater shape files that contains number of craters with their diameter superposed over the geological unit. Once the area and CSFD of craters in that area is known, then the modelled absolute age of that area using the Cratestats tool is determined[10], which works on IDL platform. Craterstats 2.0 is used for plotting the crater counts. Craterstats has inbuilt isochrons and it can plot CSFD in cumulative, differential, Hartmann and R-plot. The isochrons can be fit to both cumulative and differential data [10]. In this thesis work, isochrons are generally fitted to cumulative data.

Origin pro version 7.5 was used for the plots which are prepared during this thesis work. Also, Adobe Photoshop is used for 1) preparing the final set of figures and 2) stacking multiple images in a single figure.

[10]https://www.geo.fu-berlin.de/en/geol/fachrichtungen/planet/software/_content/software/craterstats.html

Chapter 3 Water-ice exposing scarps within the northern mid-latitude craters

3.1 Introduction

Water-ice on Mars is a vital source for ascertaining the aqueous history of the planet. The occurrence of near subsurface shallow water-ice can be used to infer the snow accumulation processes and related climatic conditions that prevailed on Mars. Also, these shallow water-ice rich locations can be prime target sites for future missions to Mars [22, 24–26], specifically the northern mid-latitude regions because of their low elevation and smooth terrain [26]. Precipitation, accumulation, and compaction of snow would have caused formation of massive (few meters to hundreds of meters thick) water-ice layers during the high obliquity (>30°) periods of Mars [22, 24, 25, 56]. These compacted shallow water-ice layers are located few meters to 10's of meters below the surface and suggested to cover one-third of the planet Mars [22, 24, 56].

On Mars, shallow ground water-ice can be found in the form of pore-filling or nearly pure water-ice [22, 24, 56–58]. To date, exposures of pure water-ice deposits in cliff scarps at eight locations on Mars has been reported [22], which are mostly located in the south-eastern side of the Hellas basin. Only one such location in the northern lowlands within the Milankovič crater has been reported on Mars [22]. Additionally, widespread shallow water-ice in the high and mid-latitude up to 35°N/45°S of Mars has been reported on the basis of seasonal surface temperature trends [26]. However, direct spectral observations of spatially distributed shallow ground water-ice in the northern mid-latitude are limited. Many studies [24, 59–63] suggested instability of water-ice on the surface in the mid-latitude, however, stable ground water-ice favoured below a dust cover [22, 25, 56]. Water-ice was suggested to be relatively more preserved over the pole-facing walls of the craters on Mars on the basis of slope orientation [22, 64]. Independent to the pole-facing scenario, shallow ground water-ice in the mid-latitude region of Mars was suggested to survive throughout the whole year [65]. However, the period of accumulation of water-ice in the mid-latitude regions and its preservation on equator-facing crater walls is not known in detail.

The craters located in the mid-latitude regions record the history of snow transport and these craters could be the potential reservoirs to improve the understanding of the recent climatic conditions on Mars. In this study, two unnamed craters (UC1 and UC2) have identified in the northern mid latitude region of Mars (Figure 3.1) with a clear signature of water-ice exposures. The identification of new craters (Figure 3.2) with exposure of water-ice deposits at different locations, spatially far from each other, is certainly important to: 1) support the widespread global interpretation of shallow water-ice, 2) use as a resource in future manned exploration, 3) landing site determination for upcoming Mars robotic/human missions, and 4) in-situ resource utilization.

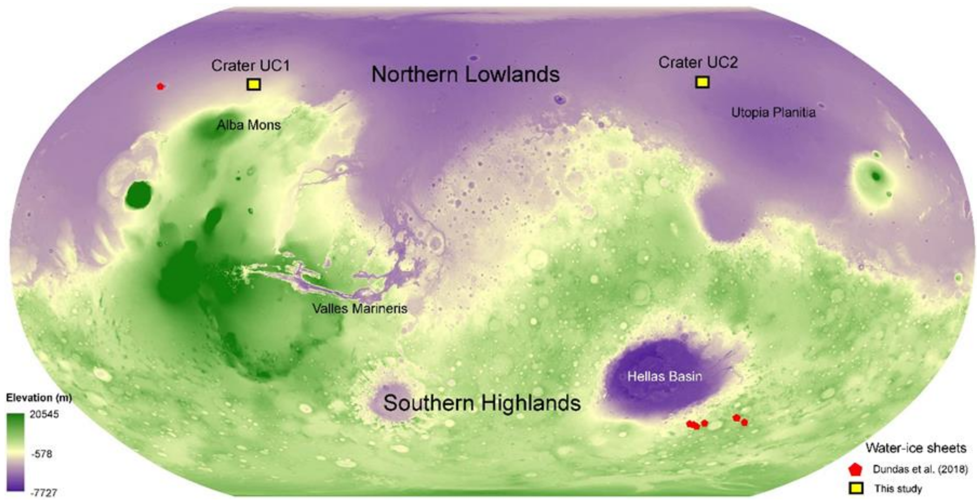

Figure 3.1: Location map of regions where water-ice were detected previously by Dundas et al. (2018) (marked by red pentagon) and unnamed craters (UC1 and UC2) used in the study (yellow boxes). The background is the topographic map of Mars.

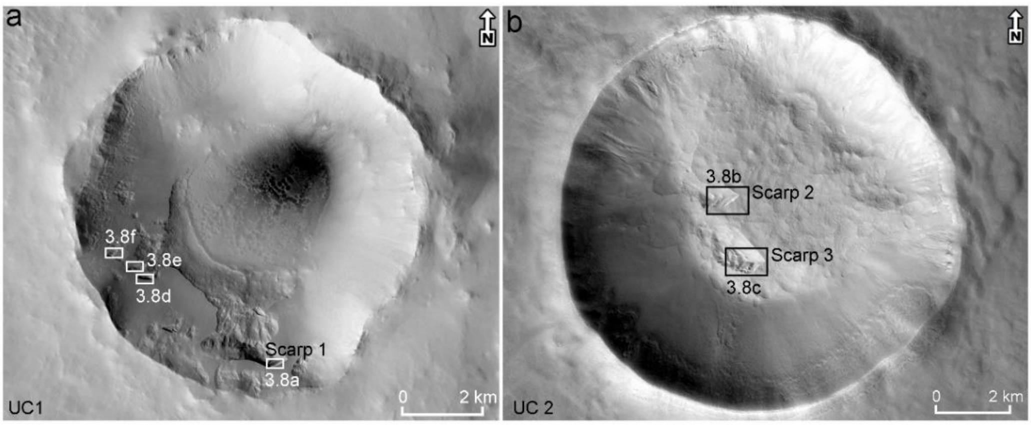

Figure 3.2: a) UC1 crater with scarps on pole-facing wall. b) UC2 crater with scarps on its floor.

3.2 Data used

Image data: MRO - CTX and HiRISE images of resolution ~6 m/px and ~25 cm/px respectively [48, 49] were used for the photogeological analysis. Table 3.1

provides the details of HiRISE images used in this study. CTX image IDs are mentioned in the figure captions wherever used in the figures.

Table 3.1: Details of HiRISE images used in this study.

Product ID	**Date**	**Time**	**Solar longitude (Ls)**	**Seasons**
Crater UC1				
ESP_035517_2355	2014-02-23	00:27:6	93.5°	Northern Summer
ESP_035174_2355	2014-01-27	07:59:43	81.7°	Northern Spring
ESP_026880_2355	2012-04-21	00:06:10	99.7°	Northern Summer
ESP_026959_2355	2012-04-27	04:50:05	102.5°	Northern Summer
ESP_033974_2355	2013-10-26	19:45:11	40.6°	Northern Spring
ESP_033684_2355	2013-10-03	04:25:34	30.4°	Northern Spring
ESP_062853_2355	2019-12-24	15:11:00	125.0°	Northern Summer
Crater UC2				
ESP_017563_2375	2010-4-26	0:18:17	82.5°	Northern Spring
ESP_018420_2375	2010-7-2	19:0:46	112.3°	Northern Summer
PSP_008425_2375	2008-5-14	23:59:23	71.5°	Northern Spring

Topographical data: MGS – MOLA, MEX- HRSC blended DEM [52], and high-resolution CTX DEM generated using the open-source pipeline of MarsSI [66] are used for the topographical analysis.

Spectral data: L-detector (IR) datasets of MRO - CRISM for Mars, a hyper-spectral imaging spectrometer on Mars [54], are used for the spectral analysis. Table 3.1 and 3.2 provides the details of HiRISE and CRISM images used in this study.

Table 3.2: Details of CRISM images used in this study.

Product ID	Martian year	Solar Longitude	Seasons
Crater UC1			
FRT000247B6_07_IF169L	MY 31	99.7°	Northern Summer
FRT0002498F_07_IF167L	MY 31	102.5°	Northern Summer
Crater UC2			
HRL00018499_07_IF184L	MY 30	82.6°	Northern spring

Spectral datasets of CRISM were processed using the CAT toolkit added in the Exelis Visual Information Solutions (ENVI). Photometric, atmospheric, destrip and despike corrections (included in the CAT tool) were applied to the CRISM full resolution (FRT) and half resolution long (HRL) targeted datasets. For atmospheric correction, volcano scan algorithm, which is inbuilt in CAT was used. After applying these corrections, the CRISM image were projected and spectrums were taken from the ROIs (Table 3.3). These spectra were ratioed with the featureless spectra extracted from the same columns. Browse product BD_1500 is used from the derived summary products [67] using "Spectral Analysis Utilities" tool in CAT.

Table 3.3: Details of center pixel and the number of pixels used for the spectrum shown in figure 3.7.

Labels	**Center Pixel/Pixels**	**Number of Pixels**
FRT000247B6_07_IF169L		
Scarp 1		
Red **(**numerator); **(**denominator)	X:417, Y:718 ; X:417, Y:689	2*2
Blue **(**numerator); **(**denominator)	X:420, Y:717 ; X:420, Y:688	3*2
Green **(**numerator); **(**denominator)	X:423, Y:716 ; X:423, Y:686	3*2
Cyan **(**numerator); **(**denominator)	X:428, Y:714 ; X:428, Y:691	2*2
FRT0002498F_07_IF167L		
Red **(**numerator); **(**denominator)	X:418, Y:697 ; X:418, Y:605	3*3
Blue **(**numerator); **(**denominator)	X:426, Y:697 ; X:426, Y:660	3*3
Purple **(**numerator); **(**denominator)	X:436, Y:690; X:436, Y:652	2*2
Green **(**numerator); **(**denominator)	X:430, Y:697 ; X:430, Y:611	2*2
HRL00018499_07_IF184L		
Scarp 2		

Red (numerator); (denominator)	X:193, Y:231 ; X:193, Y:200	2*3
Blue (numerator); (denominator)	X:201, Y:231 ; X:201, Y:202	3*3
Scarp 3		
Red (numerator); (denominator)	X:189, Y:184 ; X:189, Y:194	3*3
Blue (numerator); (denominator)	X:178, Y:181 ; X:178, Y:191	2*2

Thermal data: THEMIS [46] brightness temperature (BTR) observations at scarps 1-3 (Table 3.4) are used to compare the surface temperatures with the likely atmospheric frost point on Mars that is 209 K [68]. The inspection of minimum BTR values at the scarps 1-3, which are much higher than the atmospheric frost point on Mars, evident that ice deposits reported at scarps 1-3 are not seasonal frost.

Table 3.4: Details of THEMIS BTR observations at scarps 1-3.

Site	Observation ID	Date	Local time	T_{min}
Scarp 1	I43945003	MY 31, L_s 27	15.5	228 K
Scarp 2 and Scarp 3	I38422006	MY 30, L_s 132	16.5	244 K
	I37249012	MY 30, L_s 87	16.3	240 K
	I36937013	MY 30, L_s 76	16.3	221 K

3.3 Observations and interpretation

The two unnamed craters documented in this study are shown in figure 3.2. Figure 3.1 shows the locations of these two craters along with the other locations of shallow ground water-ice deposits reported by Dundas et al. (2018). The two craters are of nearly same diameter ~11 km, however, UC1 is ~1.1 km deep and UC2 is ~800 m deep. Also, both the craters have preserved layered ejecta. The crater UC1 is located to the north of Alba mons (Figure 3.1, Figure 3.2a), while the crater UC2 is located to the west of Utopia Planitia (Figure 3.1, Figure 3.2b). These craters are ~5100 km spatially apart, but they are located more or less in the same latitude and with exposed scarps (Figure 3.1, Figure 3.2). Scarps on Mars are recognised as erosional features which are interpreted to retreating actively due to the ice sublimation [22]. They commonly have steep highly vertical walls (slope >40°) and exposes the vertical structure of the shallow ground [22]. In crater UC1, there are four major scarps, few small scarps, and one large scarp on the southern wall (Figure 3.2a). In crater UC2, there are two scarps, both are located on the floor of the crater (Figure 3.2b).

3.3.1 Spectral analysis

The color composite maps of CRISM are produced by using the summary product BD_1500 derived in the same way to Viviano-Beck *et al.* (2014). These derived false-color composite maps for UC1crater (Figure 3.3) and UC2 crater (Figure 3.4) are used to identify the regions containing water-ice. From the water-ice highlighted regions in BD_1500 map (Figure 3.3b, Figure 3.4b), the water-ice spectra were extracted from 12 regions of interest (Table 3.1, 3.2). These highlighted regions fall within the scarps (colored boxes in figure 3.5, 3.6). Figure 3.7a,b displays ratioed CRISM spectra from scarp1, which is located on the pole-facing wall of UC1 crater, using temporal images (Table 3.1). The spectra extracted from the scarp1 have absorptions close to 1.5 μm and 2 μm wavelengths which indicates water-ice [22, 69]. Other than the scarp1, no significant signature of water-ice spectra is seen in other scarps located within the crater UC1 (Figure 3.3). The possible explanations for the absence of ice signatures could be: poor signal to noise ratio, location of their exposure, high dust cover and/or sublimation of ice partially or completely which is causing masking of the water-ice and longstanding scarps of longer exposure time [22, 58].

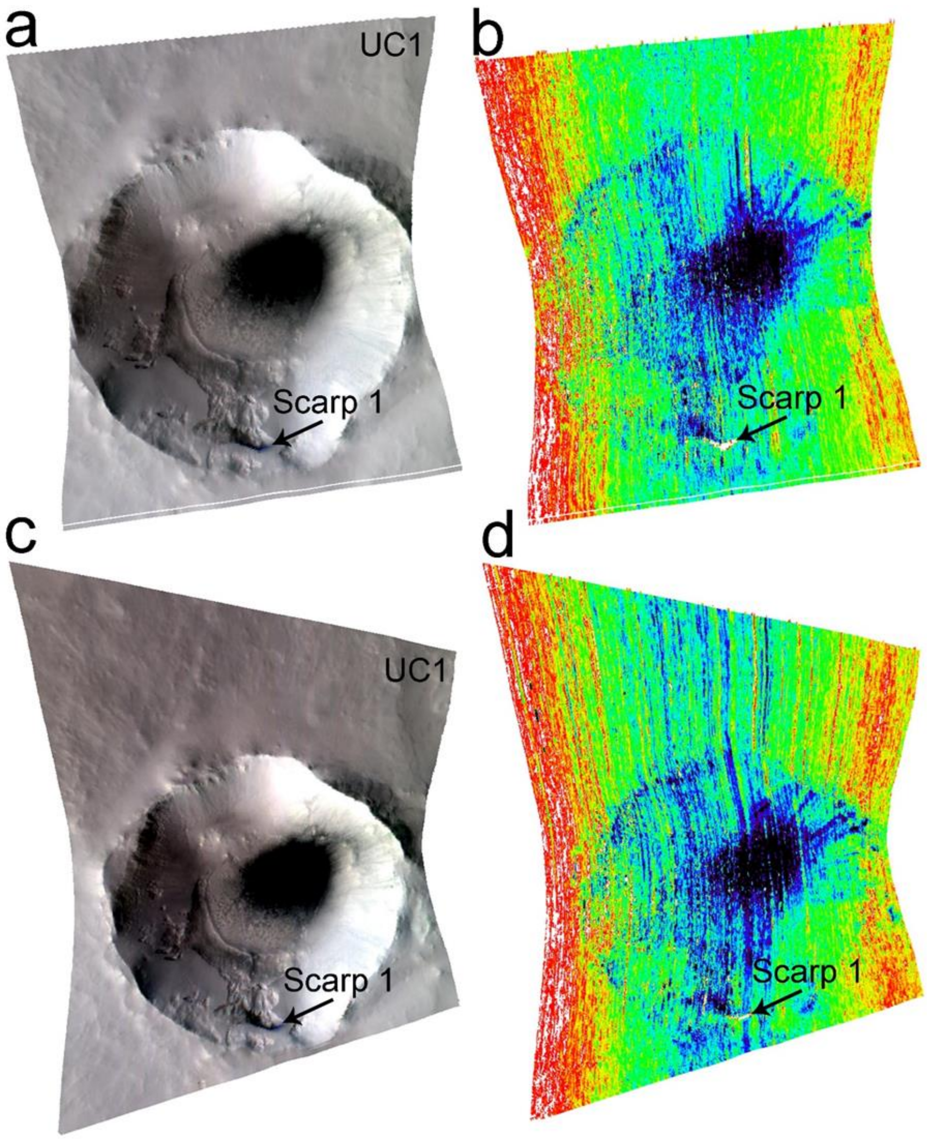

Figure 3.3: Unnamed crater UC1 (CRISM images –left) with false-color generated image for summary parameter BD_1500 (right) in two CRISM images (FRT0002498F_07_IF167L – Top FRT000247B6_07_IF169L - bottom). The white patch at the scarp 1 (in b and d) potentially represent water- ice rich regions within the crater. North is up in all the images. For scale reference, the crater dimeter is 11 Km.

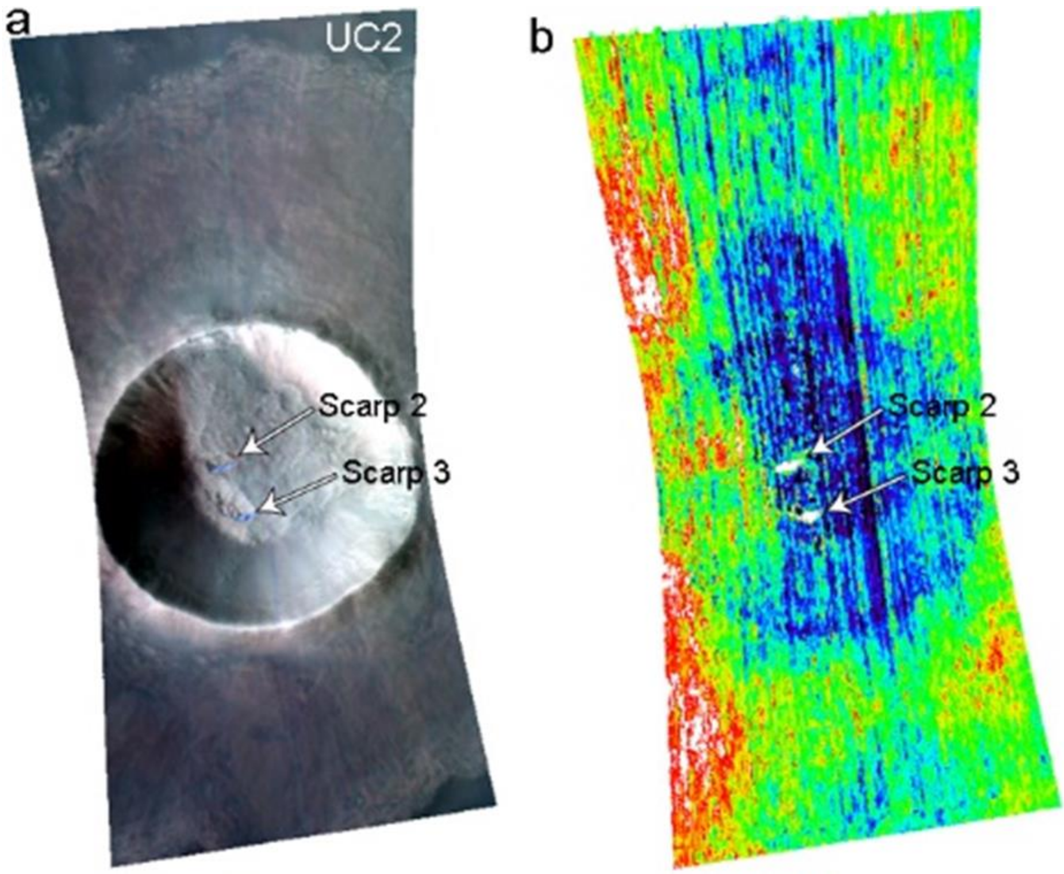

Figure 3.4: Unnamed crater UC2 (CRISM image HRL00018499_07_IF184L– left) with false-color generated for summary parameter BD_1500 (right). The white patch at the scarp 2 and scarp 3 in figure (b) potentially represent water-ice rich regions within the crater. North is up in all the images. For scale reference, the crater diameter is ~11 Km.

Figure 3.7c,d displays CRISM spectra for scarp2 and scarp3, which are located on the floor of the crater UC2. These spectra are characterized by absorptions at 1.5 µm and 2 µm wavelengths and that confirms the water-ice deposits within crater UC2. In scarp2, the detected water-ice spectral signatures spatially cover few tens of meters along the wall (Figure 3.6) suggesting their wide coverage within the scarp. In scarp3, the spectral signature of water-ice are observed to cover a few tens of meters vertically or across the scarp wall.

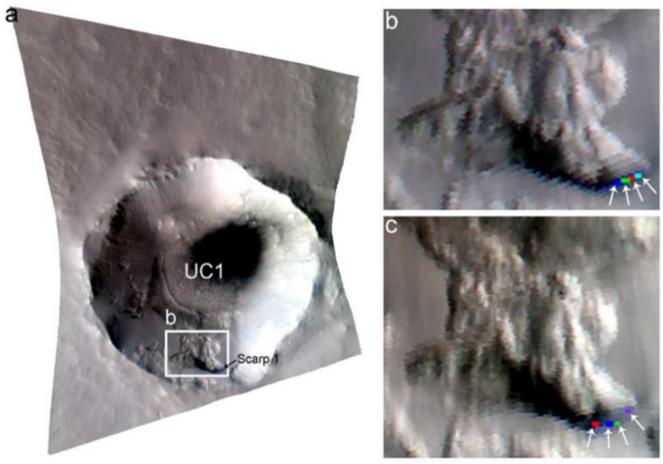

Figure 3.5: a) Crater UC1 in CRISM projected image (FRT000247B6_07_IF169L). b) Location of the region of interest (ROIs) marked by white arrows from where spectra were extracted in figure 3.7a. c) Location of the region of interest (ROIs) marked by white arrows from where spectra were extracted in figure 3.7b. North is up in all the images. For scale reference, the crater diameter is ~11 Km.

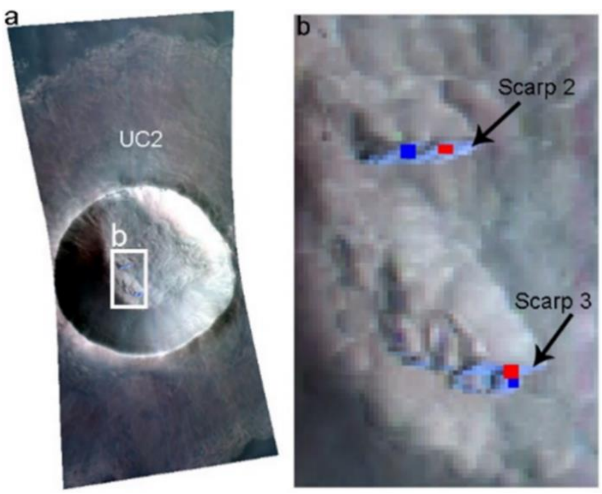

Figure 3.6: a) Crater UC2 in CRISM projected image (HRL00018499_07_IF184L). b) Location of the region of interest (ROIs) marked by red and blue boxes from where spectra were extracted in figure 3.7c and 3.7d. North is up in all the images. For scale reference, the crater diameter is ~11 Km.

Though the scarp2 and scarp3 are formed over the floor deposits (Figure 3.2b), however, these floor deposits originated from the equator-facing wall of UC2 crater (see section 3.3.2). This study reports the unique exposure of water-ice from the crater floor deposits, thus providing the evidence for preserved ice-deposits at the UC2 crater floor.

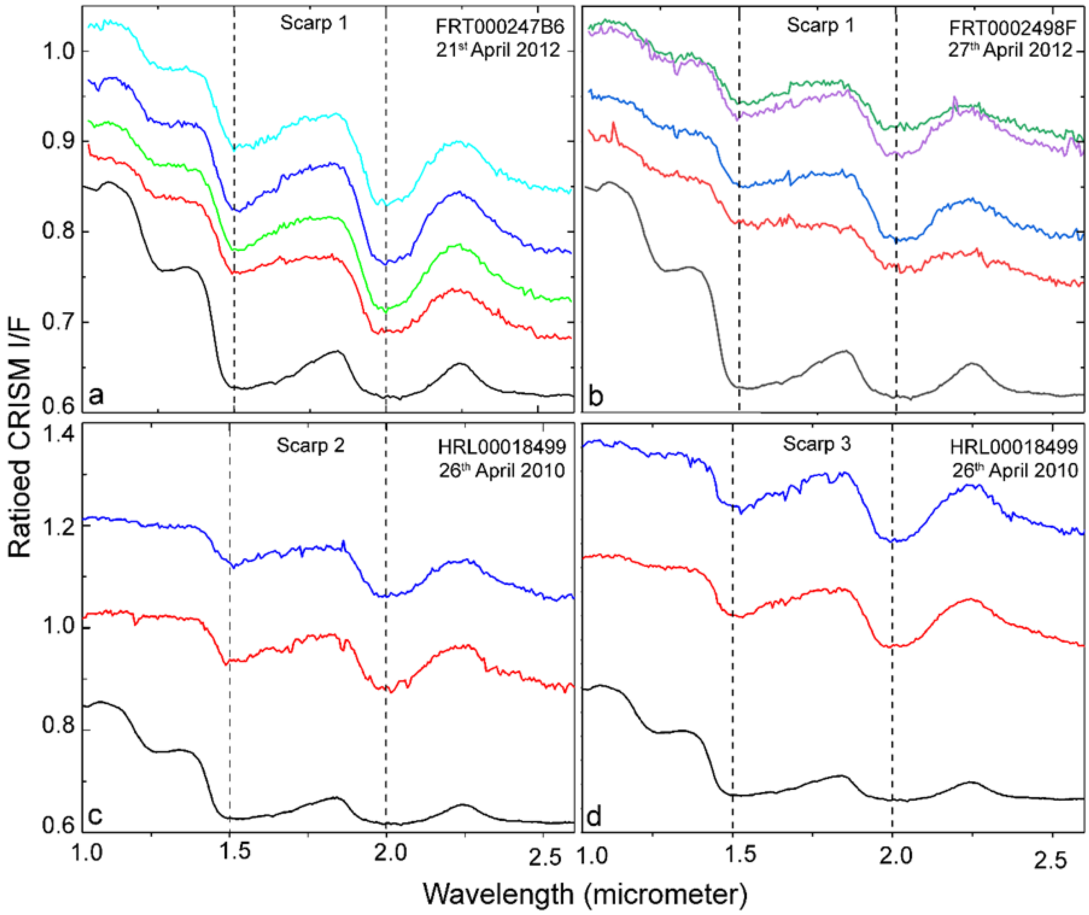

Figure 3.7: CRISM Spectrum for water-ice from the: a) Scarp1, b) Scarp1 but CRISM observation was taken after a week, c) Scarp2, and d) Scarp3 (for spectrum locations refer Figure 3.5,3.6).

In temporal CRISM spectral signatures (Figure 3.7a,b), few variations can be observed in terms of absorptions depth. A comparatively shallower absorption is observed in the spectrum after a week (Figure 3.7b). These images were acquired during the last phase of northern spring in MY 31 similar to Dundas et al. (2018). It could be noted that though the spectra shown in figure 3.7a,b are taken from the scarp1, they are not exactly from the same pixels. The factors like dust mixing into ice, difference in pixel, one-week temporal difference, and the viewing geometry may be the potential reasons that cause variations in the reflectance spectra. Overall, the small temporal variations of water-ice spectrums offer vital evidence that the exposed water-ice last for a certain duration on Mars.

3.3.2 HiRISE observations

Figure 3.8 displays the false-color RGB HiRISE images (Table 3.3) of water-ice scarps present within both the craters. There are three major scarps, one in UC1 crater and two in UC2 crater (Figure 3.8a-c)**,** in which clear spectral evidence for water-ice was obtained (Figure 3.7)**.** In crater UC1, the scarps are formed over the pole-facing wall (Figure 3.2a) and scarp1 is formed nearly 1 km downward from the southern rim crest. Figure 3.9 displays the vertical structure of the pole-facing crater wall over which the scarp1 is located. The steep-sided wall of the scarp1 with exposed ice has a slope of ~45°. Topographic profile across the UC1 crater and through scarp1 reveals its steep slope (~45°) at the location where the ice is exposed. Clearly, slope of scarp1 wall is much higher than the average slope of the crater wall (~15°) (Figure 3.10a). Within the scarp1 (Figure 3.8a), three layers were observed: an uppermost bluish-white layer similar to Dundas et al. (2018), a middle dark-toned layer appears as dust-covered with non-ice deposits, and a lowermost layer with bluish-white color again.

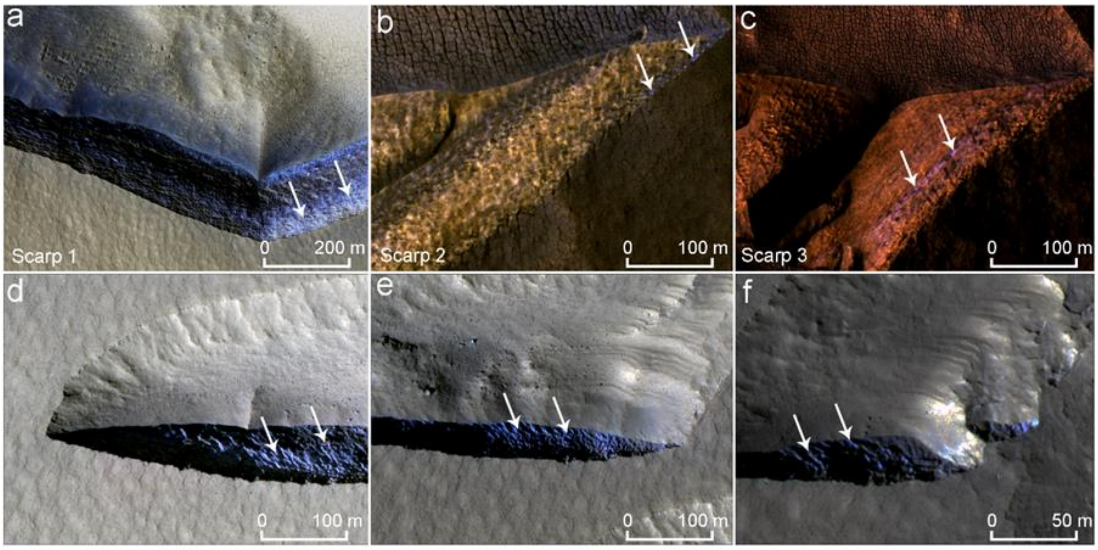

Figure 3.8: False colored HiRISE images with bluish-white contrast represent the water-ice rich regions (a-c) and spectrum shown in figure 3.7 were extracted from these scarps. (d-f) also shows bluish-white color, but no prominent water–ice spectra. North is up and sun-light is from the left in all figures. (HiRISE images a:ESP_026959_2355, b-c:ESP_018420_2375, d-f:ESP_062853_2355)

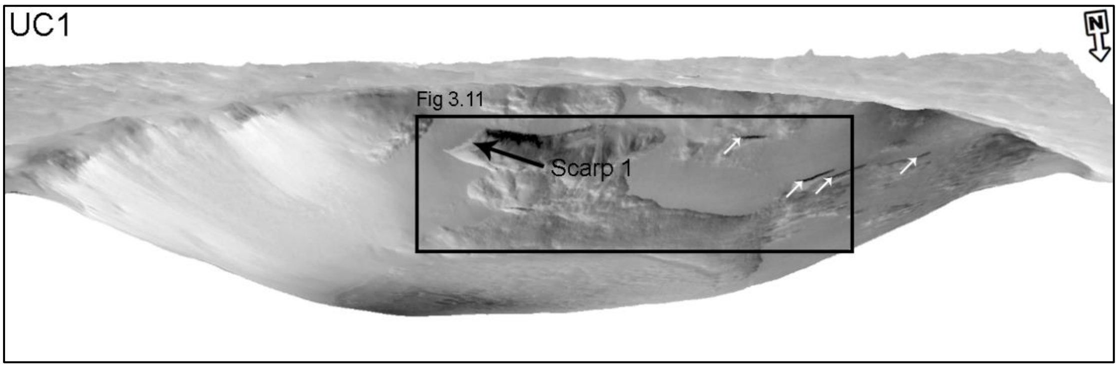

Figure 3.9: 3D view of the scarp 1 within the crater UC1 generated by overlying CTX image (CTX_033974_2356) over the CTX DEM prepared by CTX stereo images (CTX_033974_2356_035174_2356). The inset shows the location of Figure 3.11.

From the uppermost layer, water-ice spectral signature are obtained (Figure 3.7a, b).The scarp1 is located ~2 km below the Martian geoid. The thickness of the uppermost exposed water-ice deposit is estimated as ~20 m, whereas the total vertical thickness of the exposed scarp is ~150 m after correcting for the regional slope. The lowermost bluish layer of scarp1 is not showing water-ice spectrum in CRISM analysis, therefore, it is difficult to identify the lowermost bluish layer in HiRISE false color image as a water-ice deposit (Figure 3.8a). Additionally, the viewing geometry and high slope make it difficult to get any suitable spectrum from this bottom-most layer. Hence, in such cases photo-geological interpretation were made only with HiRISE images. However, care was taken for the dust deposits, which may also result in the blue color in the HiRISE imagery [70]. The western part of scarp1 and the adjoining floors also show blue color which is due to dust mantling [70]. However, the third bottom-most layer is more towards bluish-white tone, whereas the immediate floor lacks such bluish-white color. This observation helps in hypothesizing that this layer could be one ice layer. Thus, the scarp1 over the pole-facing wall exposed the possible layered ice-deposits as anticipated in earlier studies [22, 26]. This suggests that the current to past climatic conditions could have favor to form internal layering [63, 71] and the same may be exposed on the scarp1 walls.

Figure 3.8b shows the enhanced HiRISE false color image of scarp2 within the crater UC2 with little bluish-white contrast in the upper part of the scarp. The strong CRISM spectral signature from this location (Figure 3.7c) coincides with the HiRISE observations and reveals this bluish-white layer as potential water-ice. Other scarp in the UC2 crater, scarp3 (Figure 3.8c), also displays a little bluish-white color and has a strong spectral signature of water-ice in CRISM analysis (Figure 3.7d). The HiRISE photogeological interpretations of scarp2 and scarp3 are much supported by CRISM spectral signatures (Figure 3.7c,d) and reveals that CRISM is capable of detecting small quantity of ice exposures, if not covered by dust.

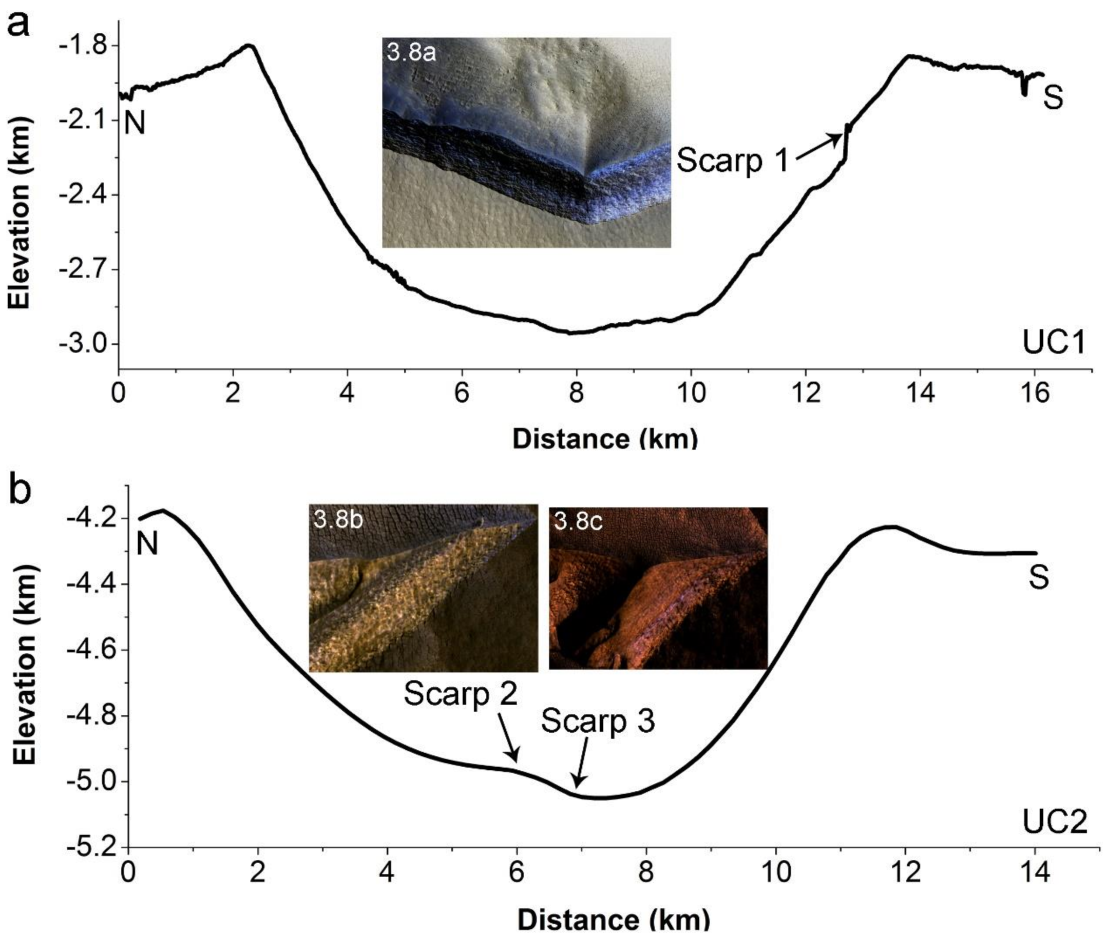

Figure 3.10: North-south trending topographic profiles a) across the crater UC1 and through scarp 1 (using CTX-DEM) b) across the crater UC2 and through scarp 2 and 3 (drawn using MOLA-HRSC blended DEM).

Apart from the spectrally distinct water-ice signature within scarp1 in UC1 crater, few other scarps are observed with bluish-white tone in UC1 from HiRISE images (Figure 3.8d-f). However, these scarps (Figure 3.8d-f) do not have any distinct spectral signatures from CRISM. Although, the bluish-white tone at these scarps is notably different from the blue color appeared due to the dust cover in HiRISE false color images [70]. Such scarps also (Figure 3.8d-f) possibly host water-ice exposures postulated on the basis of their close proximity to water-ice rich scarp1. Moreover, all the scarps including scarp1 in UC1 crater are located over the bumpy textured latitude dependent mantled (LDM) unit [25, 72, 73]. Figure 3.11 displays the preserved latitude dependent mantled unit over the southern wall, whereas the rest of the southern wall is eroded by scarps. Moreover, all the exposed scarps in UC1 share boundaries with the LDM unit (Figure 3.11). It is likely inferred that all the scarps shown in figure 3.8d-f may contain water-ice signatures. However, the role of sublimed ice over a long period [74] is not contested, and these exposures may partially be covered by dust and can hinder the information below the dust.

In crater UC2, both the scarps (scarp2 and scarp3) are located within the floor deposits (Figure 3.2b), The two scarps within UC2 crater are located ~2 km apart from each other and have hundreds of meter elevation difference. Scarp2 is sited in the mid of the floor deposits, whereas scarp3 is sited at the toe of the deposits **(**Figure 3.10b). Topographic profile across the UC2 crater and through the scarp2 and scarp3 (Figure 3.10b) displays a higher slope over the pole-facing wall (~13°) as compare to the equator-facing wall (~9°). It is inferred that the material deposited over the floor came from the equator-facing wall of the UC2 crater [75]. The water-ice deposits which currently found on the crater floor are possibly originated from the equator-facing wall and moved down to the floor due to erosion of wall material. Based on this observation from this work it is revealed that not only the pole-facing wall (Figure 3.10a) host the ice-deposits, but the equator-facing wall origin floor deposits (Figure 3.10b) also host water-ice. This study provides evidence that both the pole- and equator-facing walls of the craters are likely for snow accumulation and preservation of water-ice.

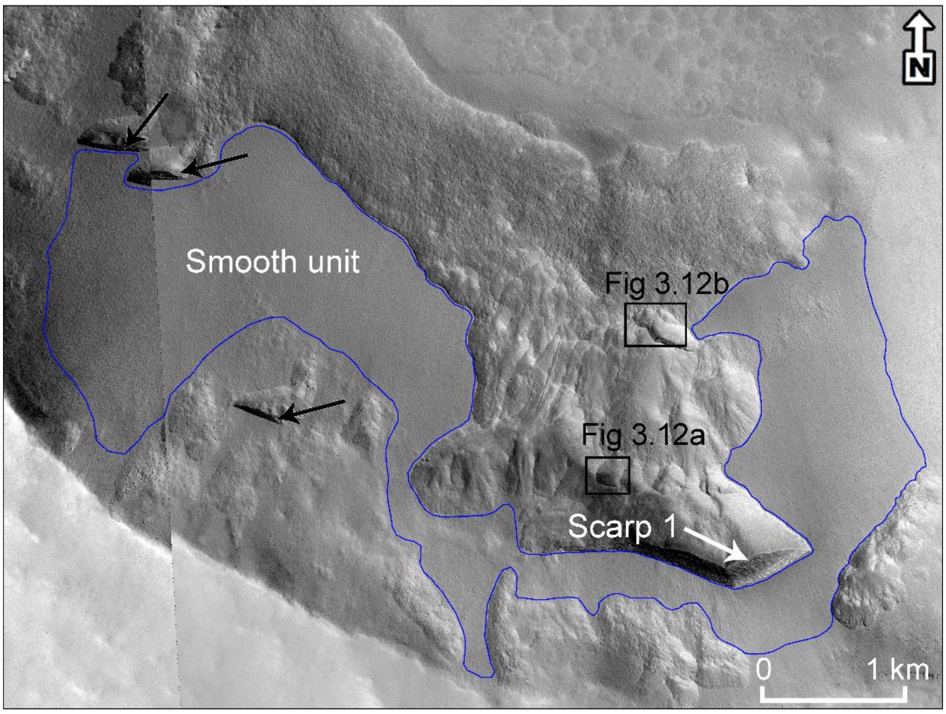

Figure 3.11: Mapped smooth unit around the Scarp 1 within the crater UC1. Inset shows the locations of scarps mentioned in figure 3.12.

Other scarps within the UC1 crater (Figure 3.12) lack HiRISE bluish-white tone and water-ice spectral signature in CRISM analysis. The possible reason could be that these scarps may be the older exposures and the ice could have sublimed over the time [65, 74] and therefore currently appear as dry scarps. Dry scarps with complete lack of water-ice (Figure 3.12) could be used to infer that whether the ice reported within the scarp1 is exposed or seasonal deposits [76] as they are located in the close proximity of the sacrp1.

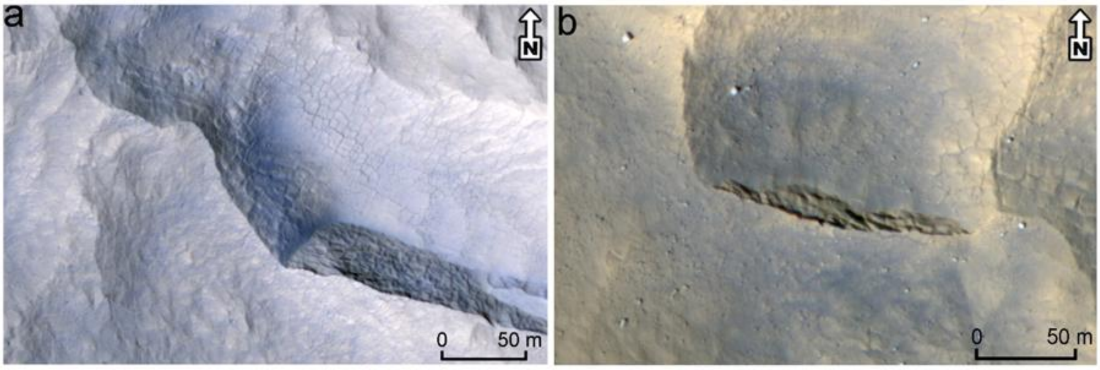

Figure 3.12: Other scarps (a,b) within the crater UC1 that don't show any prominent spectra for water-ice and also lack prominent white-bluish color in the HiRISE image (ESP_026959_2355).

3.3.3 Chronological relationship

For age determination, the ejecta boundary of craters UC1 and UC2 (Figure 3.13) are demarcated and did a robust counting of craters which superposed over the ejecta to determine the ages. For this study, the production and chronology function of Hartmann, 2005 was used. Poisson timing analysis [11] was used to determine the modelled age of craters UC1 and UC2 using cumulative crater size frequency distribution. To determine the age of smooth unit within UC1 (Figure 3.11) where no craters were observed, the upper limit of a crater that can be present and is adequate to be observed is determined first. This limit is determined as 20 m based on the texture of the unit. Then using the area of the smooth unit which is determined as 7.8 km^2, calculations were made for the number of craters per km^2. This value (0.12 craters/km^2) is plotted in figure 3.14 similar to [77].

Crater ejecta is used to determine the upper bound for the period of ice exposures. Crater size-frequency distribution for UC1 crater (Figure 3.15, 3.14) shows total superposed crater count as n=101, whose diameter ranges from ~60 m to ~300 m. The resultant best fit model age for the formation of UC1 crater is ~25 Myr by fitting 81 craters with diameter >85 m (Figure 3.15).

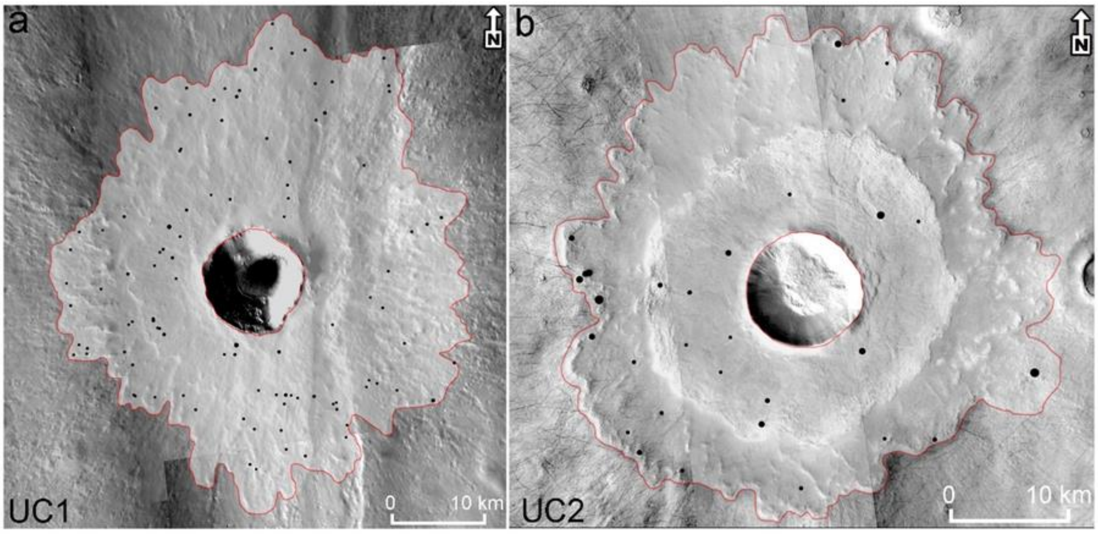

Figure 3.13: Red outlines represent crater counting areas (ejecta boundary) and black filled circles represent superposed crater over the ejecta of the craters UC1 (a) and UC2 (b). The count was conducted using CTX images.

This age represents the crater formation age, whereas all the scarps which formed over the wall must be younger than the smooth latitude dependent mantled unit. The tentative age of the smooth unit is assessed to infer the possible time frame after which the scarps have formed in UC1 crater. The smooth unit surrounding the scarp1 (Figure 3.11) lacks superposed craters even at HiRISE resolution (~25 cm/pixel). In this regard, tens of meter-scale bumpy texture [25, 73] of the smooth unit is considered

(Figure 3.11) that formed due to the ice mantling. Such texture could hide or have deformed the small craters <20 m in diameter. Thus, considering this limit, the crater density is determined by the presence of one crater of typical size > 20 m and same was plotted in the differential plot [77]. The plot demonstrate (Figure 3.14) that it is statistically likely that the tentative age of the smooth unit is ~1 Myr or younger [78], and the scarp1 could have exposed the water-ice in last 1 Myr.

For crater UC2, crater size frequency distribution over the ejecta shows total superposed crater count as n=31 and the diameter of the craters ranges from ~30 m to ~515 m. The best fit model age is determined as ~95 Myr by fitting 11 craters whose diameter is >~200 m (Figure 3.15). The crater floor is hummocky and lacks superposed

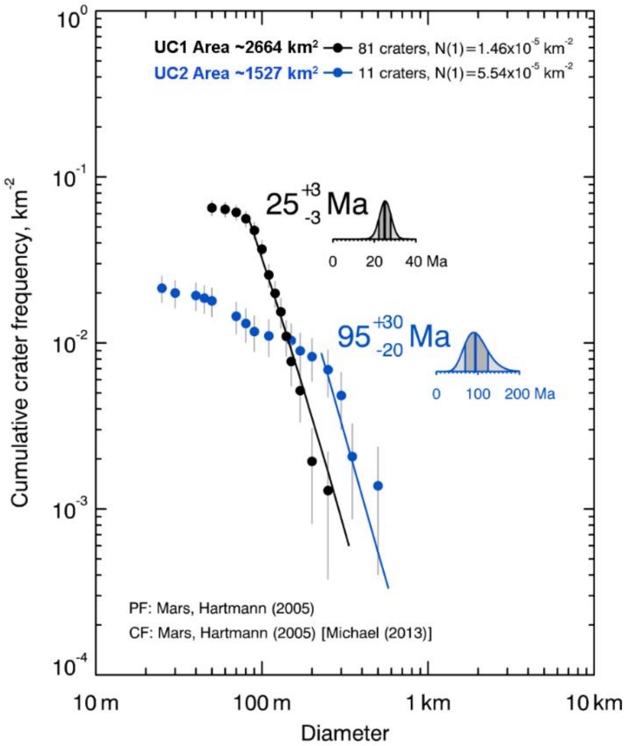

Figure 3.14: Crater size-frequency distribution ages for the UC1 and UC2 craters using Poisson analysis tend to ~25 Ma and ~95 Ma

craters. Thus, the chronological interpretation in this study is limited to the ejecta of the crater. It is inferred that the UC2 crater either represents an older ice-deposit (post crater formation) contained within the wall deposits that are exposed more recently, or it represents a younger material accumulated more recently during the high obliquity of Mars [79, 80].

Regardless of any scenario, UC2 crater reveals that the obliquity and climatic conditions favored equator-facing wall deposits within the last 95 Myr in the mid-latitude craters on Mars [81].

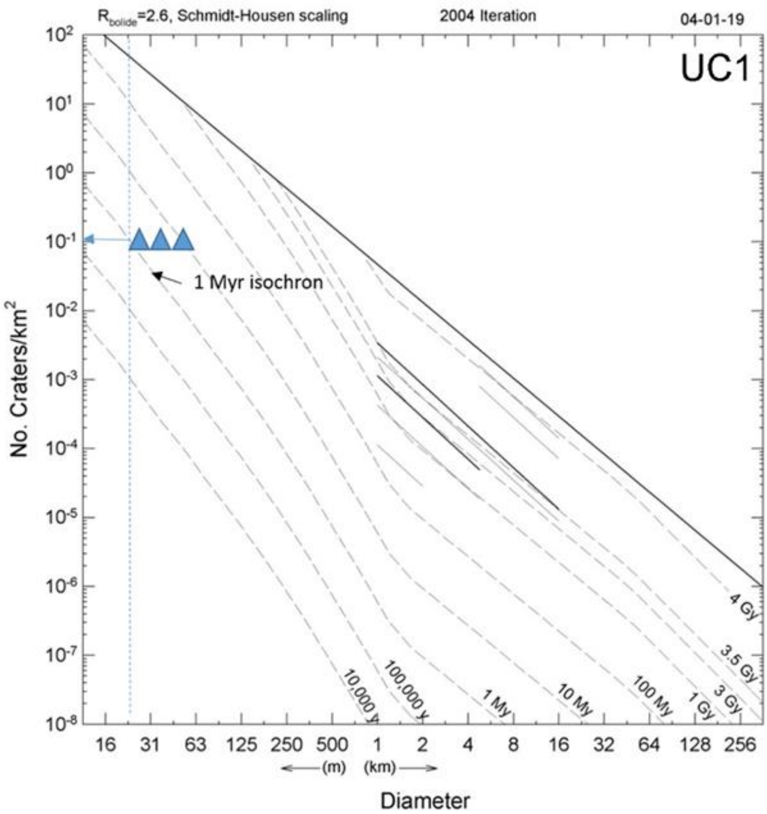

Figure 3.15: Model age of the smooth unit surrounding the scarp 1 within crater UC1 was determined similar to Hartmann (2005) that suggests an age less than 1 Myr.

Whereas, UC1 crater provides evidence for the ice precipitation and accumulation over the pole-facing wall occurred within the last 25 Myr [80]. Irrespective of the formation ages of craters, the ice-deposits exposed in these two craters reveal that these scarps are formed much recently compared to the formation age of impact craters UC1 and UC2, which makes them capable to retain the exposed water-ice till the CRISM observation in present time.

3.4 Discussion

Water-ice deposits have been recognised in the northern plains of Mars using Neutron spectroscopy [56, 82] and variations in seasonal surface temperature [24, 26] suggesting they will be shallow (<1-2 m depth). Figure 3.16 reveals the correlation between the locations of water-ice in the mid-to-high latitudes [56] and reported craters in this study match unprecedentedly. Hence, results from this study are consistent with orbital detection of hydrogen at shallow depth [22, 24, 56, 82], and the results are added to this observation that both pole- and equator-facing [64, 83] deposits within the craters could preserve significant water-ice. The water-ice/glacial origin deposits are predominantly observed only on the pole-facing walls within craters [22, 64, 83]. In contrast, deposits over the equator-facing walls remains an enigma. The equator-facing walls are more prevalent for the formation of gully and glacial origin landforms with preserved ice-deposits between ~45° and 60° [75, 81] during the Amazonian period. In UC2, the ice possibly accumulated all over the crater wall and this is apparent from the LDM mantling (Figure 3.2b). The net accumulation of ice occurs on all surfaces within craters located poleward of ~45°[81]. The UC2 crater floor hosts a thick deposit (>100 m) with a continuous association with the N-NE equator facing wall. Using the topographic profile (Figure 3.10b), it is interpreted that this deposit has been eroded from the equator-facing wall, moved towards the floor and settled there. Therefore, a substantial contribution of floor material is attained from the equator-facing wall deposits (Figure 3.10b), where it remains preserved until younger epochs. Such a setup can be explained by the obliquity trends on Mars that changes over time [79, 80].

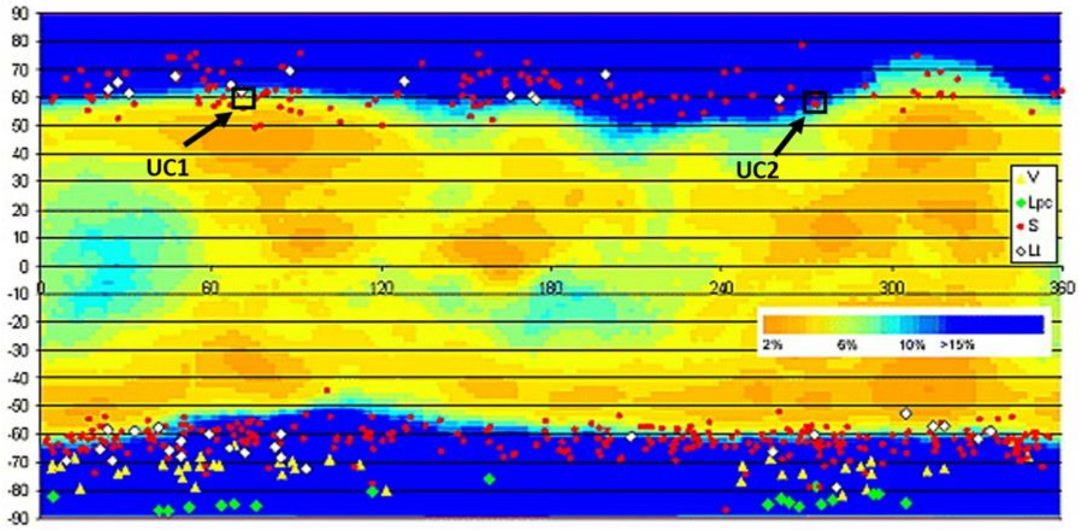

Figure 3.16: The location map of unnamed craters UC1 and UC2. Background is the color map by Mangold et al. (2004) that corresponds to ground ice proportion in mass with a spatial relationship to polygons (V- large heterogeneous polygons, Lpc - straight crack networks close to south polar cap, S - homogeneous polygons of size smaller than 40 m, Lt - large homogeneous polygons formed by cracks associated with topography).

In this scenario, the next question that arises is whether all the wall deposits will host water-ice? It is anticipated that these two craters are spatially apart by 5100 km and similar water-ice deposits are reported in previous studies and suggested a global mid- to high- latitude distribution of ice on Mars [22, 24, 56]. To infer whether the water-ice deposits within craters are subsurface exposures or they are related to seasonal frost, following observations deduced that: 1) The water-ice-rich scarp1 (Figure 3.2a) and the dry scarps (Figure 3.12) are located only ~1km apart and located within the same elevation range. If seasonally driven topographically controlled ice mantled on the scarp1, then such deposits are anticipated in the nearby scarps (Figure 3.12). However, no spectral or geomorphic evidence for the presence of preserved water-ice is found in these dry scarps. 2) The average temperature value at the scarp1 (minimum 228 K, Table 3.4) is above the likely frost point of water [22]. Therefore, in line to the previous report [22], it is proposed that the ice exposed by the scarps is subsurface ice rather than persistent seasonal frost. Following mechanisms can be possible for this subsurface ice: 1) snow accumulation and compaction [22], 2) water-vapor diffusion [84], 3) growth of ice-lenses [85]. The last two mechanisms are slow and usually occur only at shallow depth [22]. The interpretation of LDM units mantled on the wall of the craters UC1 and UC2 suggest that the snow accumulation and compaction with dust is the most likely process responsible for the ice-deposits [25, 86]. It is equally likely that initially ice/snow would have accumulated by the atmospheric precipitation and later by the process of vapor diffusion [84]

Scarps within the crater floor and on the walls reveal the preserved vertical structure of young ice-deposits in the northern mid-latitudes on Mars. The spectral signatures acquired over one-week difference provide evidence that the current temperature and pressure conditions on Mars are not subliming the ice or that the sublimation rate is slow for the ice preserved in the steep walls of the scarps [62, 63, 87]. Though the temporal difference is of short duration (one-week), however, it provides unique spectral evidence that the ice on Mars can be exposed on the surface for fairly a long time [65, 88]. The possible layered ice-deposits over the pole-facing wall within the scarp1 in UC1 crater (Figure 3.8a), and over the equator-facing wall origin floor deposits in scarp2 and scarp3 of UC2 crater likely indicate multiple cycles of deposition of ice-rich mantles and/or linked to obliquity conditions prevailed on Mars [75, 81].

3.5 Conclusions

This study demonstrated the sustainability of shallow ground water-ice deposits on Mars using spectral analysis of CRISM and photogeological observations of HiRISE. Strong evidence have been shown that the pole-facing wall deposits and equator-facing wall-associated floor deposits within the craters at mid-latitudes comprise shallow water-ice. This study provides evidence for the water-ice deposits preserved and exposed on the crater floor which originated from the equator-facing wall of the crater. The exposure of water-ice deposits on the floor specifically implies that the mid-latitude craters with pole/equator facing deposits can be potential reservoirs for water-ice. Chronological analysis reveals evidence for snow precipitation, accumulation and compaction within the last 25 Myr which exposed by scarps within the last 1 Myr. The pole-facing walls and equator-facing wall origin deposits within northern mid-latitude craters are more likely to preserve shallow ground water-ice, which can be of prime interest for future robotic/human missions to Mars, and vital for understanding the climatic conditions that prevailed on Mars in different epochs.

Chapter 4 Evidence for fluvial and glacial activities within impact craters exposing a Noachian volcanic dome

4.1 Introduction

Sedimentary deposits on Mars retain the record of ancient environments and prevailing climatic conditions [32, 89–93]. Sedimentary deposits are more developed in the Late Noachian and Early Hesperian epochs, where they are frequently associated with widespread mineralogical assemblages as observed in-situ at Gale crater [94] and from orbit [95]. However, among the various sedimentary deposits observed on Mars, mid-latitude alluvial fans date predominantly from the Late Hesperian-Early Amazonian epochs, so they are of great interest as they represent fluvial activity that occurred after a potential climatic optimum of the Noachian [32, 89, 91, 92, 96–98]. Although many studies have described alluvial fans, their origin remains debated among several hypotheses: snowmelt versus rainfall [14, 99–103], transient or stable climatic conditions [32, 91, 98, 104, 105], the role of impact or volcanic activity in melting water ice [15–18]. Thus, finding key locations to better understand these processes is an important challenge to provide answers on Martian climate change.

In this context, new observations of fluvial and glacial landforms in Degana crater **(**23.72°S, 314.50°E), an impact crater that formed on a Noachian volcanic dome [45], are presented in this study (Figure 4.1). Xiao et al. (2012) mapped almost all the ancient volcanoes on Mars, excluding the Tharsis region. Their study identified the region over which Degana crater is located as a huge Noachian-age volcanic dome. They suggested these domes are mostly conical in shape and lack calderas. However, no direct observation has yet been made to show that they host fluvial deposits and glacial landforms. Likewise, no mineralogical analysis has been carried out over this volcanic dome to decipher the Noachian mineralogy. Thus, this region offers a unique chance to observe volcanic, impact, glacial and fluvial landforms in the same location, assessing whether the processes that formed them occurred in concert or not. In addition, the composition of such Noachian volcanoes is critical to understand the evolution of ancient volcanic crust on Mars [45]. In this study, new information about the geological context and bedrock composition and then to detail the morphology of fluvial and glacial landforms have been provided. In addition, the relative stratigraphic relationships between the volcanic dome, impact craters, fluvial deposits, and glacial landforms within both impact craters has been established. Then, quantitative analysis on fluvial deposit and glacial landforms are performed, based on which the extent of fluvial and glacial activities constrained. Also, using crater-size frequency analysis, the apparent ages of these processes are determined. At last, a formation hypothesis for the fluvial and glacial deposits and the climatic evolution of Mars are discussed in this study.

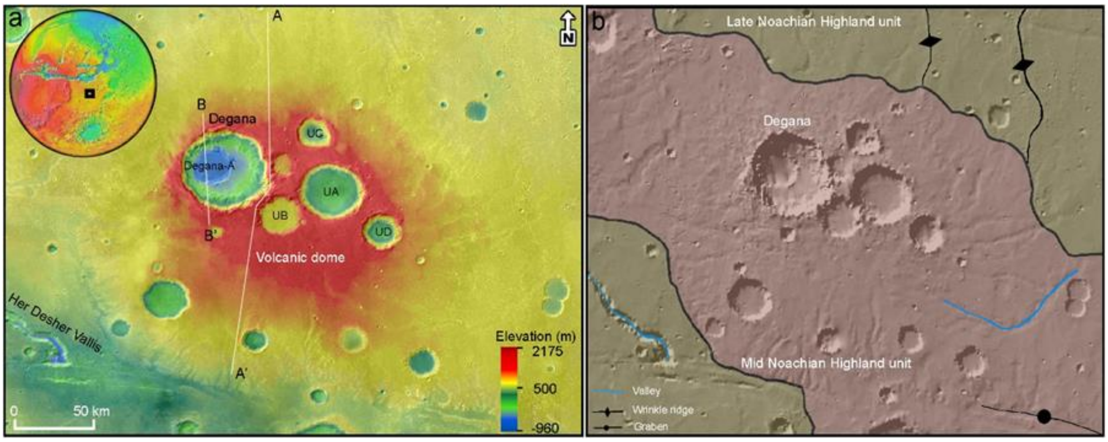

Figure 4.1: Location map of Degana crater, Mars. a) Topographic map of Degana crater and its surrounding region. b) Geologic map from Tanaka et al. (2014) indicates the terrain is Noachian in age.

4.2 Data used

For the geomorphological analysis, ~6 m/px MRO-CTX, and ~25 cm/px MRO-HiRISE images [48, 49] were used. For the topographic analyses, ~463 m/px MGS-MOLA DEM [51], and the ~200 m/px MEX-HRSC – MGS MOLA blended DEM [52] were used. High-resolution CTX DEM and HiRISE DEMs (wherever available) were generated using the open-source pipeline of MarsSI [66].

For the mineralogical analysis, MRO-CRISM for Mars , a hyper-spectral camera [54], was used. CRISM used two detectors with 544 channels in the visible to the near-infrared spectral region (0.4 to 4.0 µm) [54] was used. In this study, CRISM data analysis was performed using both S-detector (VNIR) and L-detector (IR) datasets [54]. The short wavelength (VNIR) data ranges from 0.36 to 1.05 µm, while the long-wavelength (IR) data ranges from 1.0 to 3.92 µm. The analysis was performed using the CRISM Analysis Toolkit (CAT) plug-in added to ENVI 4.5. CRISM observations were converted into I/F reflectances by applying corrections for instrumental artifacts [54]. Degana crater includes only one full resolution targeted (FRT00023F32), which was processed to correct for photometric, and atmospheric noise in the spectral data using the method suggested by Murchie et al. (2007) and Flahaut et al. (2011).

For identifying the composition, the spectral parameters OLINDEX2, LCPINDEX, and HCPINDEX mentioned in Viviano-Beck et al. (2014) was generated. OLINDEX2 is the modified olivine parameter that measures olivine’s 1.0 µm band depth in the presence of spectral slopes [107]. LCPINDEX and HCPINDEX are the low Calcium-pyroxene and high Calcium-pyroxene parameters, respectively, that measure the pyroxene’s 1.0 µm and 2.0 µm band depth [108]. The regions highlighted in spectral parameters were examined in more detail to get a diagnostic spectral signature. Areas with strong spectral absorption signatures were used to determine the region of interest **(**ROI) and spectra were taken from ROIs of several pixels. In this study, a minimum of 3*3 pixels ROI for each average spectrum is considered in this study (Table 4.1). In this study, the spectral data in the wavelength range from 0.5 to 2.6 µm was used by integrating the VNIR and IR data to confirm the mineral absorptions of the Fe-bearing phases, which generally turned up around 1 µm [109]. The selected ROI spectra were ratioed with the neutral spectra, mostly a dust-rich area obtained from the same column [5] to enhance the spectral features. Ratioed spectra for each detector **(**VNIR and IR) is generated separately and then integrated. The overlapping spectral data from 1.0 to 1.05 µm in the S-detector and L-detector datasets was removed as suggested by Murchie et al. (2007).

Table 4.1: Details of center pixel and the number of pixels used for the spectra shown in figure 4.4b,c.

Labels	Center Pixel/Pixels	Number of Pixels
Figure 4.4b		
P1 **(**numerator); **(**denominator)	X:551, Y:344; X:551, Y:301	5*5
P2 **(**numerator); **(**denominator)	X:370, Y:358; X:370, Y:149	3*3
P3 **(**numerator); **(**denominator)	X:575, Y:338; X:575, Y:282	5*5
P4 **(**numerator); **(**denominator)	X:323, Y:283; X:323, Y:96	3*2
P5 **(**numerator); **(**denominator)	X:581, Y:101; X:581, Y:83	3*3
P6 **(**numerator); **(**denominator)	X:524, Y:410; X:524, Y:100	5*5
Figure 4.4c		
O1 **(**numerator); **(**denominator)	X:615, Y:117; X:615, Y:10	6*3
O2 **(**numerator); **(**denominator)	X:547, Y:99; X:547, Y:8	5*5
O3 **(**numerator); **(**denominator)	X:581, Y:42; X:581, Y:12	9*7

4.3 Observations and interpretations

4.3.1 Geologic context and volcanic dome

The study area (Figure 4.1a) is located at the easternmost side of the Coprates quadrangle in the southern highlands of Mars [110]. Figure 4.1a shows the geologic context of the area of study with an elevated area similar to a dome. This dome extends more than 200 km in diameter (Figure 4.2a). Many impact craters of varying diameters superimpose the dome (Figure 4.1). The largest crater on the western flank of the volcanic dome is Degana crater whose diameter and depth is ~50 km and ~2 km, respectively**.** Another impact within the Degana crater leads to form a ~20 km diameter crater, and depth of ~0.7 km, which is named in this study as 'Degana-A' (Figure 4.2b). Degana crater and its surrounding region are mapped as Mid-Noachian highland unit (Figure 4.1b), which hosts undifferentiated materials formed by volcanic and impact activity [4, 111]. Also, this unit is identified as moderately to heavily degraded, heavily cratered, hosts dense valleys, grabens, and wrinkle ridges [4, 111]. Xiao et al. (2012) categorized this dome structure as a shield volcano.

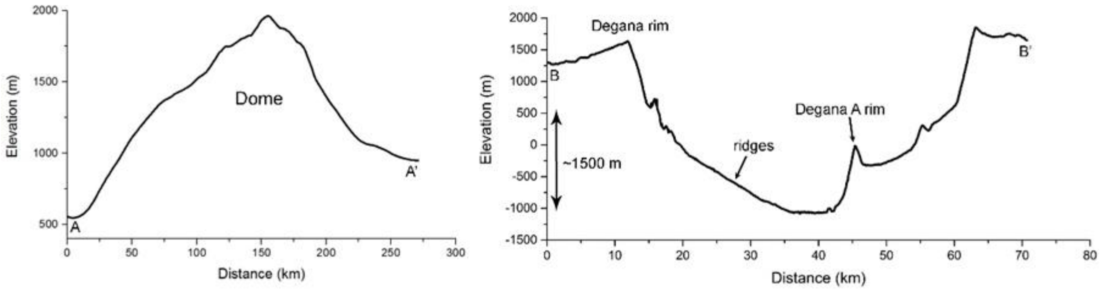

Figure 4.2: MOLA DEM-derived topographic profiles across the dome (a) and across Degana and Degana-A craters (b). The two impacts have excavated ~1.5 km deep material from the base of the dome. (For profile line refer to Figure 4.1a).

The dome is embayed on its edge by Late Noachian volcanic plains, which contain wrinkle ridges as typically observed in Late Noachian and Hesperian plains of Coprates Planum [4]. Tanaka et al. (2014) have mapped two valley networks in the region. The valley network in the south-west is Her Desher Vallis, whereas the other valley network has been mapped on the eastern flank of the dome (Figure 4.1b).

An elevation profile AA' (north to south) taken along this volcano shows typical domical topography (Figure 4.2a). The elevated dome stands ~1.2 km above the adjoining plain surface (Figure 4.2a), whereas, the craters Degana (Figure 4.3a) and Degana-A (Figure 4.3b) have excavated ~1.5 km below the regional baseline defined by the reference elevation of plain surface adjacent to the dome. Overall, the two craters in combination penetrated ~2.7 km deep into the dome (Figure 4.2b). Considering the surrounding plains, the surface elevation at the time of dome formation might be ~500 m. It means Degana-A reached a terrain deeper than the surface exist before dome formation, i.e. an outcrop could be exhumed from the primitive crust below the volcanic dome or from a crystallized magma chamber beneath the dome. If the surrounding plains are thicker than 1.5 km, the outcrop would be exhumed from the deep part of the volcanic dome. In both cases, this observation provides an opportunity to analyze the pristine bedrock of Mars, which is preserved from the middle-Noachian epoch [45]**.** Apart from Degana and Degana-A craters, the other circular features atop the dome (Figure 4.1) are unnamed craters marked in Robbins and Hynek (2012)'s impact crater database. These four large craters are superposed over the volcanic dome, as shown in (Figure 4.3).

The diameter of these craters ranges from ~20 km to 40 km. In this study, the four craters are named as UA, UB, UC and UD (Figure 4.1a). Figure 4.3c-f shows the four individual craters with their raised rims and relatively distinguishable ejecta from two of them (Figure 4.3e,f). Based on their raised rims and ejecta, they are interpreted as impact craters (Figures 4.1a,4.3) and not as volcanic features.

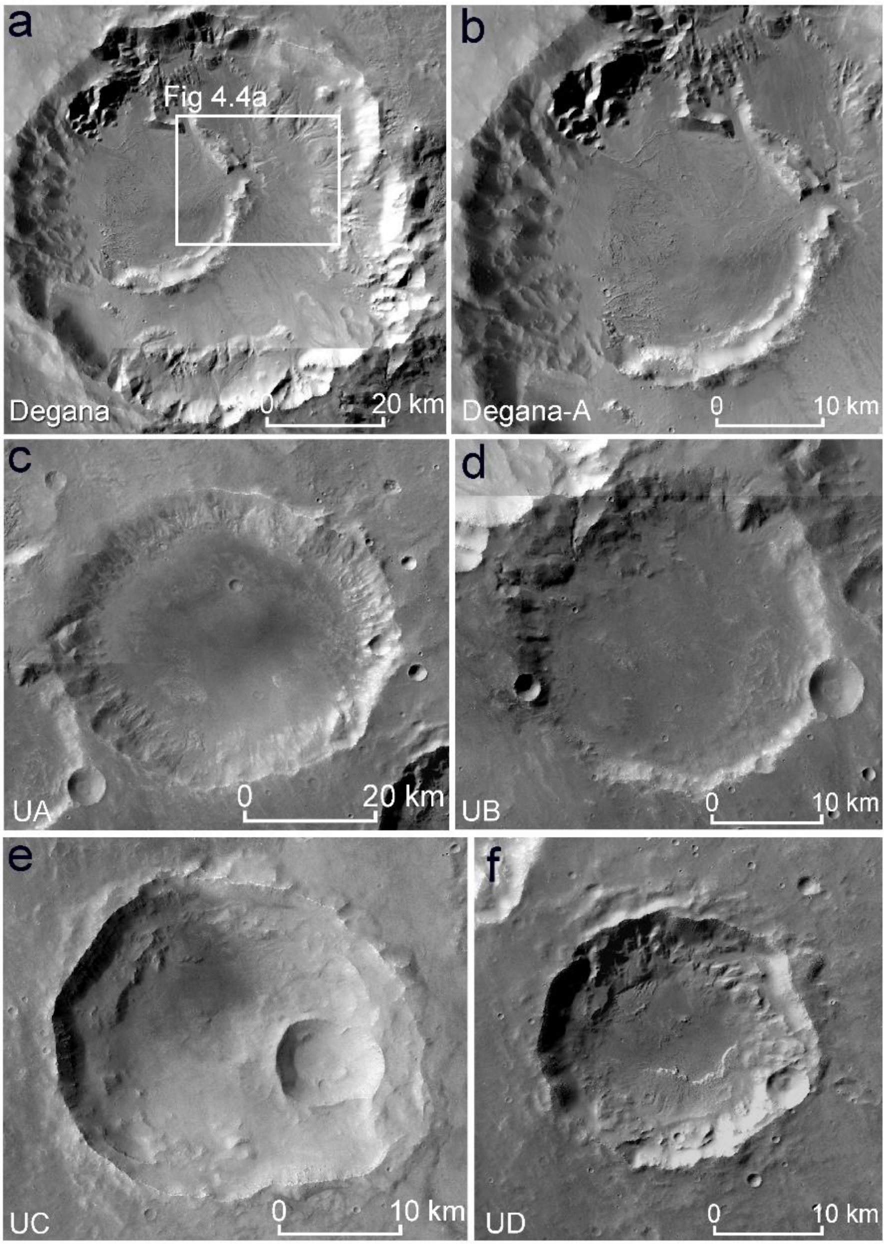

Figure 4.3: Impact craters located on top of the volcanic dome. a) Degana crater, b) Degana-A crater, c) Unnamed crater UA, d) Unnamed crater UB, e) Unnamed crater UC, f) Unnamed crater UD. The location of all the impact craters are marked in figure 4.1a. North is up in all the images.

4.3.2 Bedrock composition

The exposed bedrock material from the two superposed craters was analyzed using CRISM data along with the CRISM color composite map or spectral parameter map according to Viviano-Beck et al. (2014) by using the OLINDEX2, LCPINDEX, and HCPINDEX. This derived color composite image is overlaid over the CTX-DEM (Figure 4.4a) to assess the compositional variation observed within the crater. This RGB combination of spectral parameters **(**OLINDEX2, LCPINDEX, and HCPINDEX) shown in figure 4.4a highlights potential olivine-rich regions in red color, low-calcium pyroxene **(**LCP) regions as green/cyan and high-calcium pyroxene **(**HCP) regions as blue color as suggested by Viviano-Beck et al. (2014).

From these highlighted regions, spectra have been chosen from 9 ROIs (Figure 4.4a), which are mostly located on the northeastern and southeastern wall/rim of Degana-A. The locations of all the numerator spectra, denominator spectra, and the ROI sizes are given in tabel 4.1. These are the locations where the diagnostic absorption features in the spectra are distinguishable. Spectra signature from the northeastern rim of Degana-A shows (Figure 4.4b) a broad absorption near 1 µm and 2 µm wavelength. Absorptions around 1 and 2 µm are spectrally identified as pyroxene, where the band centers strongly dependent on the Ca content [112–115]. All the colored spectra from the green/cyan region (Figure 4.4a,b) exhibit a strong absorption feature between 0.8-1.0 µm, indicating that the ferrous phase is plausibly low-calcium pyroxene (LCP) [116]. An additional broad absorption before 2 µm (Figure 4.4b) implies the presence of low-calcium pyroxene as distinguished elsewhere on Mars [117–119]**.** LCP is observed to be widespread over this part of the north-eastern rim (Figure 4.4a,b). Among the six identified locations of LCP detections, spectra P1, P2, and P6 are located on the northeastern rim. LCP identified in locations P3 and P4 is exposed along the eroded walls of the valleys, which are connected to the east rim of Degana-A. The LCP spectra obtained from P5 are located on the south-eastern wall of Degana-A crater (Figure 4.4a). The LCP ratioed CRISM I/F reflectance spectra obtained from the six ROIs matches with RELAB [69] representative spectra of low-calcium pyroxene (Figure 4.4b).

The other diagnostic spectra are obtained from the south-eastern wall of Degana-A crater. Figure 4.4c shows a broad absorption around 1 μm and no other diagnostic absorption at other wavelengths. A broad absorption around 1 μm in the near-infrared region and a lack of absorption around 2 μm is indicative of olivine where the band center is dependent on the relative content of Fe and Mg [120–122]. The spectra shown in figure 4.4c indicate absorption around shorter wavelengths (<1 μm), which is due to an increase in Mg content [123]. In addition, the absence of strong absorption between 1.2-1.4 μm (Figure 4.4b) also indicates that the olivine is richer in Mg [116]. This suggests that this potential olivine outcrop is consistent with Mg-rich olivine (Figure 4.4c).

Spectra O1 and O2 in figure 4.4c exhibit olivine signatures within Degana crater, whereas, the spectra shown in black is the lab spectrum of Mg-rich olivine

(Forsterite) from RELAB [69]. Similar absorptions at location O3 is also observed (Figure 4.4a).

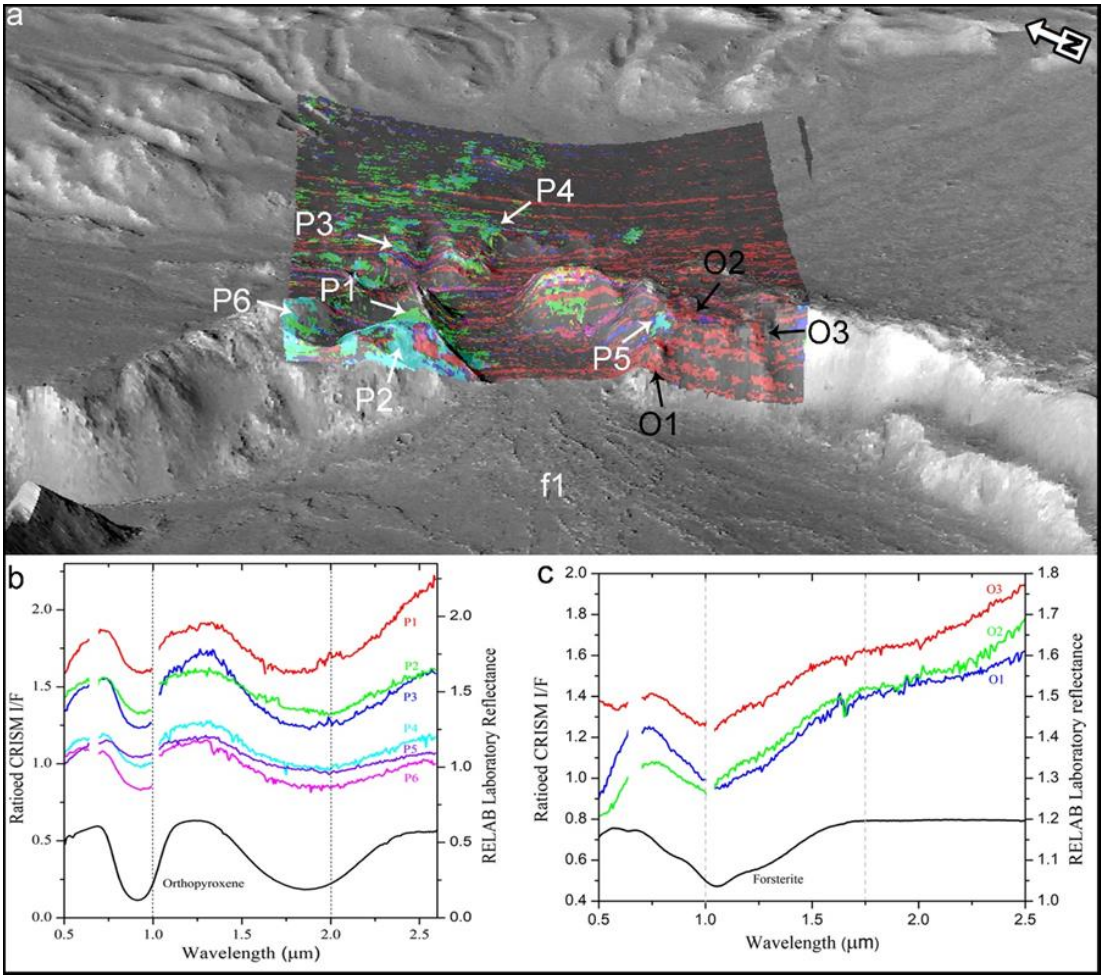

Figure 4.4: a) MRO-CRISM image (ID-FRT00023F32) derived summary parameters overlaid on CTX mosaic around the eastern wall of Degana-A crater.. The summary parameter colors indicate: Red - Olivine, Cyan/green – LCP, Blue – HCP. b) CRISM ratioed spectra for low- Calcium pyroxene identified with diagnostic 1 µm and 2 µm spectral features. Spectra in black color is taken from the RELAB library and is shown here for comparison. Locations P1 to P6 indicate from where the spectras are extracted. c) CRISM ratioed spectra for olivine, identified with diagnostic 1 µm spectral features. RELAB laboratory derived spectrum (black) for forsterite is given here for comparison. Locations O1 to O3 indicates from where the spectras are extracted.

Although the olivine mineral exposures are spatially prevalent on the south-eastern wall of Degana-A, isolated patches have also been observed on the north-eastern wall in the color composite image (Figure 4.4a). CRISM CAT tool associated Modified Gaussian Model **(**MGM) was used to estimate the cation compositions of the pyroxene mineral [124]. Using MGM the normalized LCP/**(**LCP+HCP) ratio was determined, which remains high **(**>70%) in most of the locations, as shown in figure 4.5.

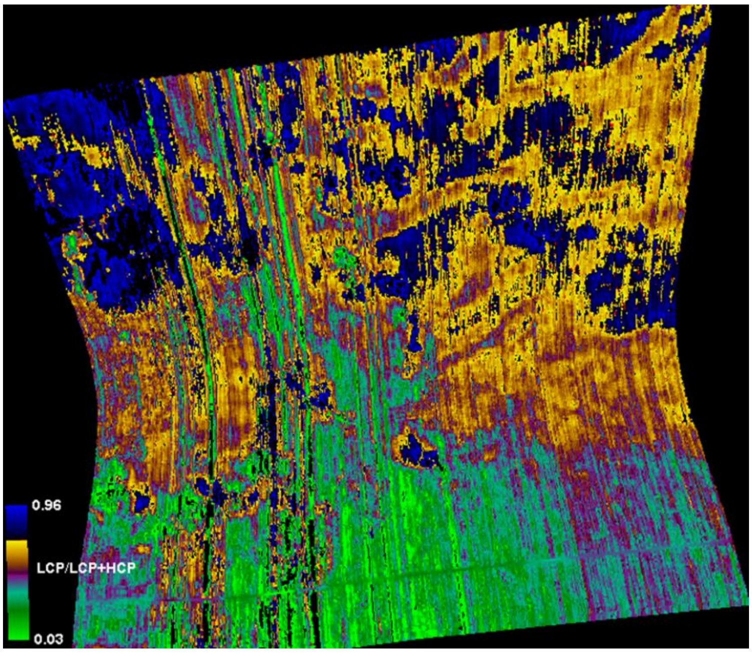

Figure 4.5: MGM map prepared using CRISM image FRT00023F32. The scale has been adjusted to convey the differences. The MGM map shows that the region is enriched in LCP.

This analysis suggests that the proportion of LCP is high within Degana crater in comparison to other mafic minerals. Overall, the minerals identified using CRISM are dominated by primary mafic minerals [69]. However, no hydrated minerals was observed within the fan deposits or along the eroded walls of valleys. The complete lack of hydrated minerals is possibly caused by dust mantling on the floor, or by the limited area covered by the single CRISM cube, so the presence of hydrated minerals cannot be ruled out. .

Figure 4.6 shows the HiRISE RGB and greyscale images locations where CRISM mineral spectra were obtained. Figure 4.6a,b shows the locations of LCP exposures in false-color images by HiRISE, as indicated by cyan coloring [109]. A distinct spectral absorptions over the light-toned outcrop is observed (Figure 4.6c), which is identified as a possible olivine exposure (Figure 4.4c) on the inner crater wall. In addition, olivine exposures were identified along the inner crater wall of Degana-A (Figure 4.6d) in the greyscale HiRISE images. Interestingly, all the LCP and olivine detected within the craters are linked to either the inner crater wall or proximal part of the valley. Overall, the notable mafic signatures are observed along the rim of Degana-A crater, where the slope is high enough (>30°) to expose these signatures. This suggests that the elevated region of the inner crater wall and the adjoining valley wall exposed the mafic minerals due to their steep slope and possible erosion. It also suggests that a significant portion of the mafic minerals is blanketed by alluvial deposits in other areas. The presence of LCP on the northeastern and southeastern wall of Degana-A crater indicates a continuous layer along the rim that was exposed by the impact. This small exposure, although dust-covered, allows us to infer the mineral composition exposed within this dome. Thus, it reveals that these exposed mineral units to be pristine Noachian crust uplifted by volcanic dome formation.

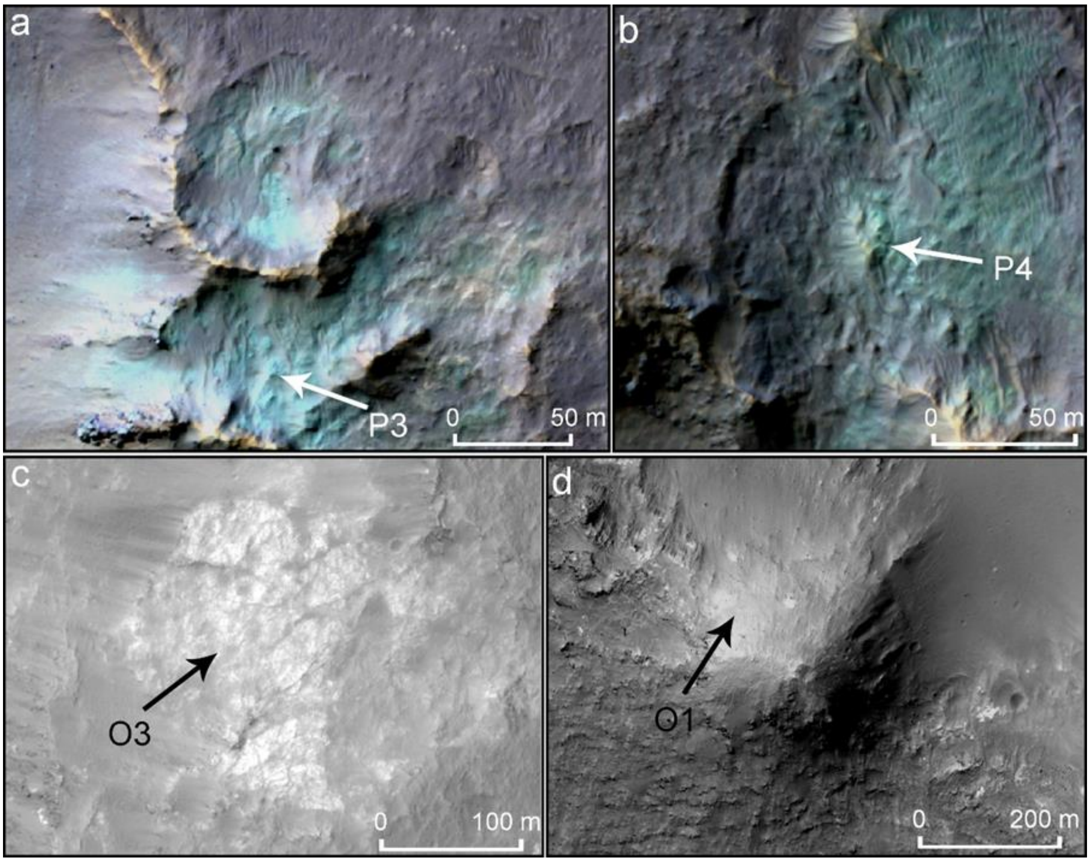

Figure 4.6: Examples locations of pyroxene in HiRISE false colour image a) on the elevated rim and b) along top most part of the eroded valley (HiRISE ESP_026522_1560). Example locations of olivine c) along the eastern wall with light toned exposure and d) on the flank of eastern wall (HiRISE ESP_16540_1560).

4.3.3 Morphology of fan deposits

The geological units, such as fan deposits, the valleys, and the ridges within the crater are demarcated (Figure 4.7). The four fan deposits within Degana-A crater cover the entire floor area (Figure 4.7a,b). The fan deposits are also observed on the floor of Degana crater, especially in the southwestern quadrant of the crater (Figure 4.7b). Figure 4.7b shows the geomorphic map of the impact craters and their diverse features.

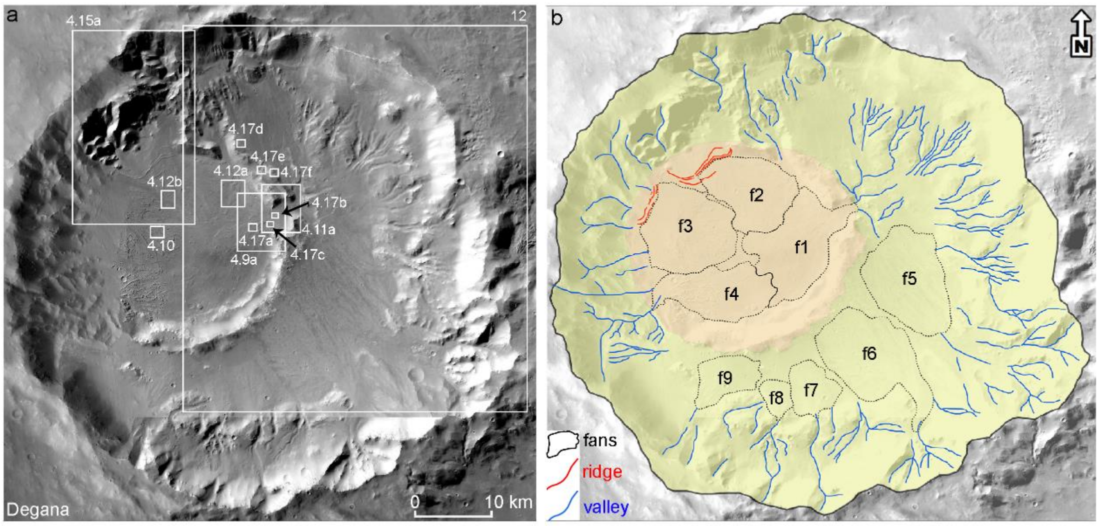

Figure 4.7: a) CTX mosaic of Degana and superposed Degana-A crater. b) Geomorphological map of Degana and Degana-A craters. The predominant mapped units are fan deposits, valleys on Degana crater's inner wall, and moraine-like ridges.

Figure 4.8 shows six prominent fan deposits formed within Degana-A and Degana craters, and their corresponding area, fan length, and slope gradient are given in table 4.2. These fans (Figure 4.8) host several distributaries. Some of these distributaries present on the fans' surface are marked by white arrows (Figure 4.8). These distributaries are mostly radiating away from the fan apex (Figure 4.8). The toe regions of the fans located within Degana-A fused with each other (Figures 4.7,4.8). Within fans (f1-f4), multiple distributaries are observed and they vary in their extent and width. These distributaries are few kilometers long and a couple of meters wide (Figure 4.8). The fans within the Degana-A are of low gradients in the range of 2° to 4° (Table 4.2), and the four fans have almost equal areas (Table 4.2).

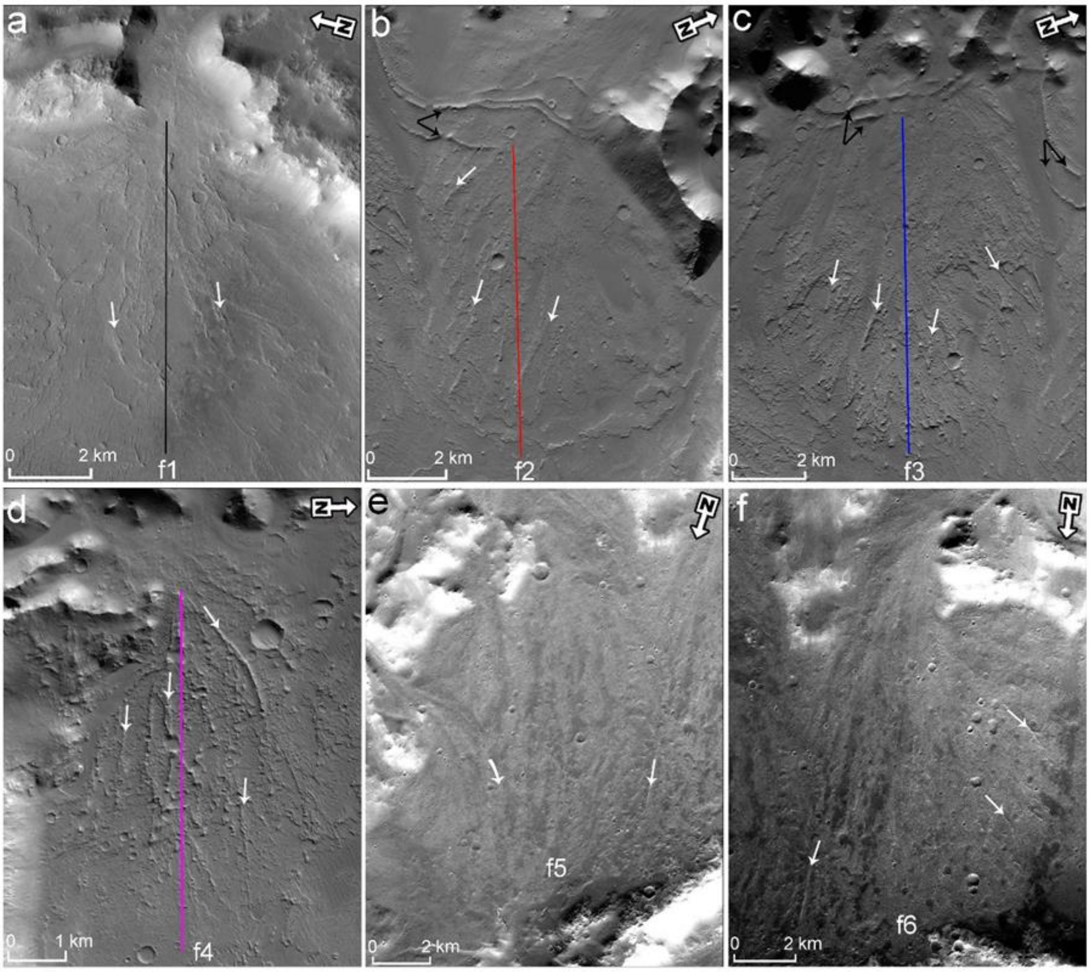

Figure 4.8: Distribution of fan deposits within Degana-A crater (a-d). a) Fan f1, located on the eastern wall. b) Fan f2 from the northern wall. c) Fan f3 from the northwestern side. d) Fan f4 from the southwest side. Distribution of fan deposits within Degana crater (e,f). e) Fan f5, the largest fan within both craters. f) Fan f6 from the southeastern wall. Colored lines over the fans indicate the traverses of topographic profiles shown in figure 4.13, White arrows - distinguishable distributaries over the fans. (CTX IDs a-d: G02_018874_1561_XN_23S045W, and e-f: D19_034592_1579_XN_22S045W)

Figure 4.8a shows the fan deposit f1 from the eastern wall of Degana-A. In almost every fan deposits (Figure 4.8a-d), near to the apex region, the distributaries appear in a cluster, whereas away from the apex region towards the downstream, they are apart from each other and observed to follow the typical topographic driven flow. The distributaries are oriented downslope, and they are aligned along the fan orientation (Figure 4.8d). The fans located on the floor of Degana crater (Figure 4.8e,f) did not show as much sharp distributaries as observed on the fans located within Degana-A. The distributaries are observed only at the termini of fans f5 and f6 (Figure 4.8e, f), and they are mantled by dust cover. Interestingly, figure 4.8e shows the possible coalescing of two fans in the toe region. Dust cover and transverse aeolian ridges **(**TAR) [125, 126] were observed to fill the intermediate troughs within the fan deposits.

Table 4.2: Details of all the fans mapped within Degana crater with length, area, and slope.

Fan Name	Approx. Fan length (along major axis) (in km)	Approx. Area (in km^2)	Slope (degrees)
f1	13.39	70.06	2.62
f2	9.09	60.36	2.47
f3	10.21	76.00	2.71
f4	10.10	52.11	3.81
f5	11.10	79.22	2.32
f6	11.98	85.05	2.50
f7	5.67	25.65	2.98
f8	4.22	10.11	2.75
f9	7.63	27.44	2.59

Figure 4.9a shows the HiRISE DEM of surface features of fan f1, where the prominent distributaries are radiating from the fan apex. The elevation gradient along the distributaries can be seen in the HiRISE DEM. Though all the distributaries are sourced from the apex points, some of them are discontinuous. Figure 4.9b shows a topographic profile with varying elevations along a distributary within fan f1, which has a relief of ~10 m. Figure 4.9c shows distributaries on fan f1, which are often stacked, exhibiting crosscutting and superposition relationships. The width of these distributaries decreases farther from the apex (Figure 4.9c). These distributaries over the Degana fans are up to 10's of meters thick. The observed crosscutting of the distributaries is the most prominent intersection at an acute angle occurred within fan f1 (Figure 4.9c). The distal portion of this distributary is discontinuous (Figure 4.9b) and terminates abruptly.

Apart from distributaries, the fans in Degana-A, particularly fans f1 and f3 (Figure 4.9c,d) exhibit surface textures with noticeable bedding/layered sediments. Fan f1 hosts many distinguishable stratigraphies (Figure 4.9c,d) observed at the distributary termini and along the intermediate region between the distributaries. Figure 4.9d also shows that the layering is evident along the flanks of the distributaries located on the fan f1. These layers are 100s of meters long, and the entire sequence is 10s of meters thick. Also, the source area of fan f3 on the western crater wall (Figure 4.10) shows well exposed layers along the flanks of the distributary. The distributary flank hosts notable small boulders resolvable in HiRISE color images (Figure 4.10).

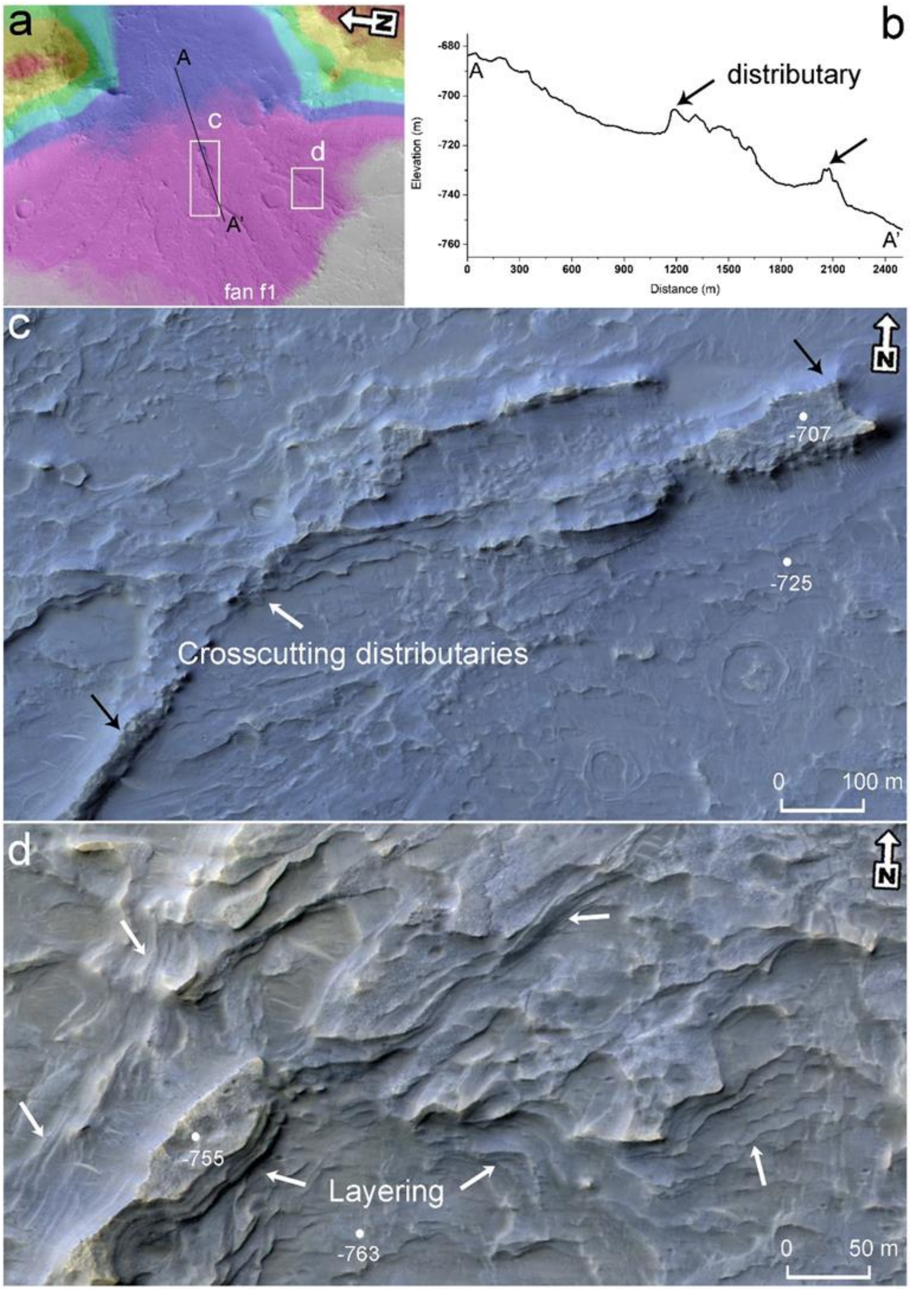

Figure 4.9: HiRISE stereo pair (ESP_016540_1560 and ESP_016039_1560) derived DEM image for fan f1. b) Elevation profile (AA') taken along a discontinuous distributary ridge. c) HiRISE false color image shows some parts of the discontinuous ridge. At the downslope side, crosscutting ridges are observed with exposed stratigraphic deposits (HiRISE ID: ESP_016540_1560). The black arrows display the locations marked on the elevation profile in figure 4.9b. d) HiRISE false color image (ESP_016540_1560) covers the toe region of fan f1. Multiple stratigraphic layers located at different elevations are marked by white arrow. (White filled circle shows elevation value at that particular location.)

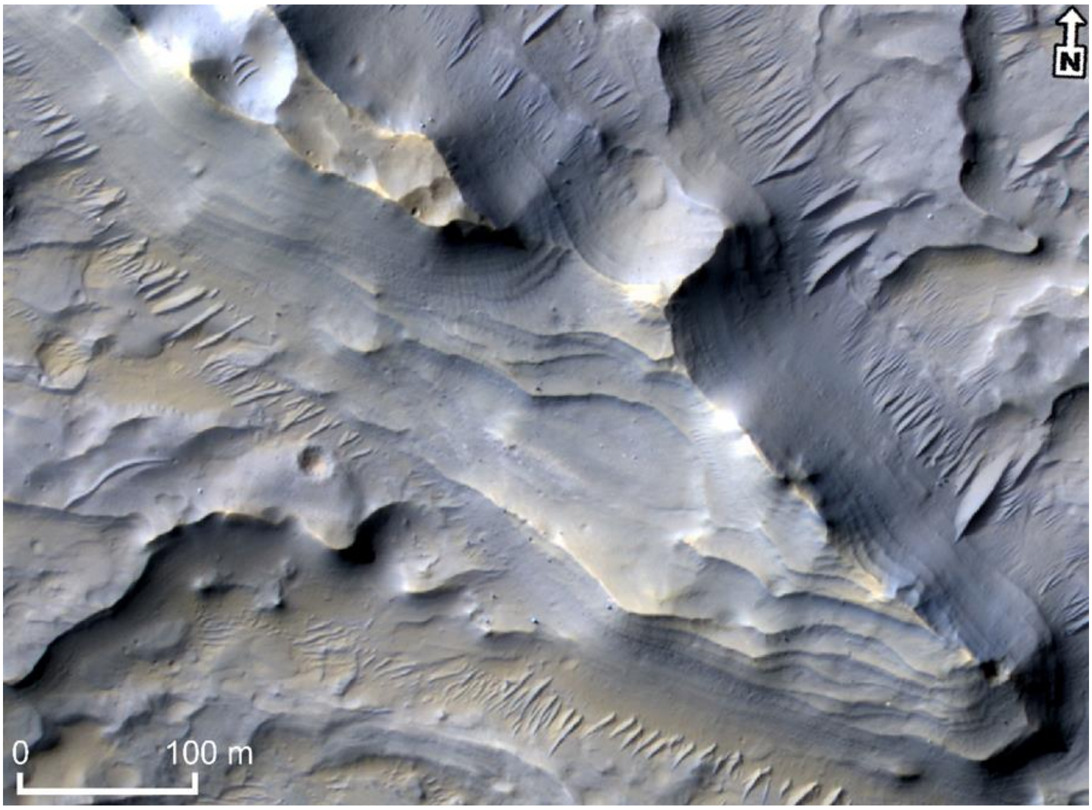

Figure 4.10: HiRISE color image ESP_018874_1560 reveals details of ridges with interbedded fine sediments and exposed stratigraphy. The layers are exposed all around the ridge and they are individually distinguishable. The ridge is surrounded by aeolian deposits, TARs and mantled by dust showcasing the role of wind in eroding the ridge and exposing layers.

Observing the f1 fan apex, a significant part of the crater rim was breached and this breach is associated with five valleys, which originated from Degana's crater wall (Figure 4.11a). Over this part of the Degana-A crater rim, it was observed that the rim height is ~800 m towards the northern side, whereas it is ~920 m towards the southern side. Approximately 800 m of wall has been eroded and made as an inlet for the fan f1 deposits. Nearly all five valleys converge outside the eastern wall of Degana-A crater

(Figure 4.11a) and breach this part to form the f1 fan deposits. Figure 4.11b shows one of the valleys from the Degana eastern wall with exposed layering in the HiRISE color image. This was observed as the earlier deposited sediments over the eastern floor of Degana were incised, possibly during the Degana-A rim breaching.

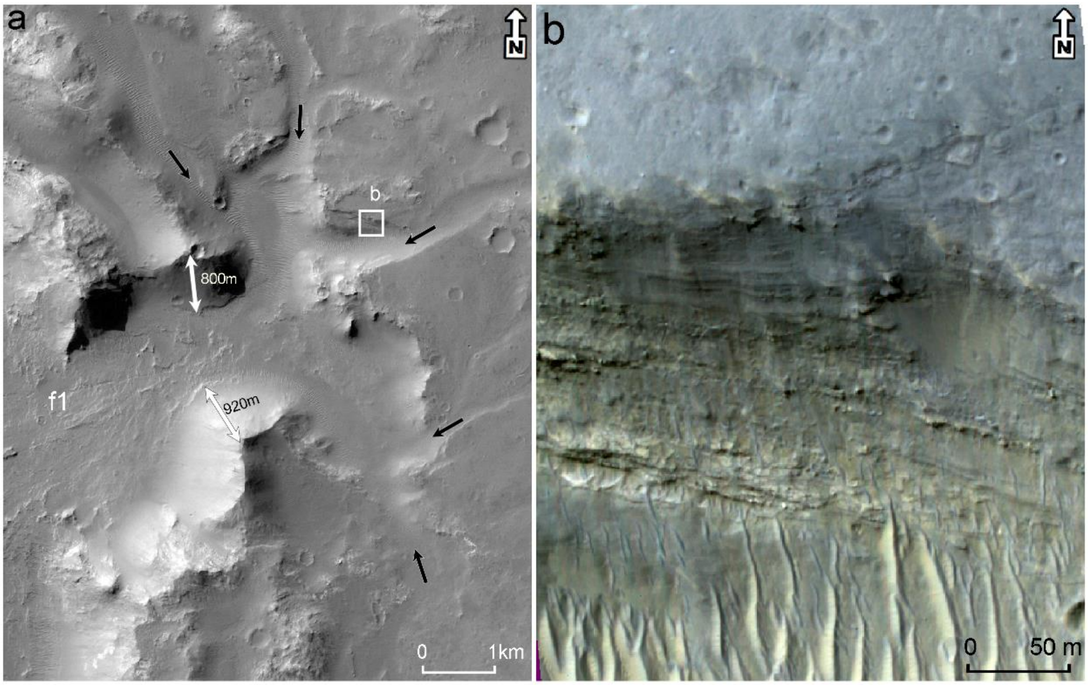

Figure 4.11: a) The apex region of fan f1. Nearly five valleys (marked by black arrows) fed to this fan from from the Degana crater wall. b) HiRISE color image ESP_026522_1560 of one of the eroded walls of the valley displays distinguishable layers.

On observing the fan f2 toe part, it is observed to coalesce with the toe part of fan f1 (Figure 4.12a). Layers are observed at the toe region of both the fans f1 and f2, whereas at their coalescing part, hummocky materials are observed (Figure 4.12a). The region of coalescing can be identified by a rough-textured surface with an absence of distributaries (Figure 4.12a). Figure 4.12b shows distributaries (marked by black arrow) and layering (marked by white arrow) on fan f2. Fan f3 also shows evidence of distributaries (Figure 4.12b) and layering that are distinguishable (Figure 4.10). All the four fans within Degana-A have coalesced at their toe region or by their sides.

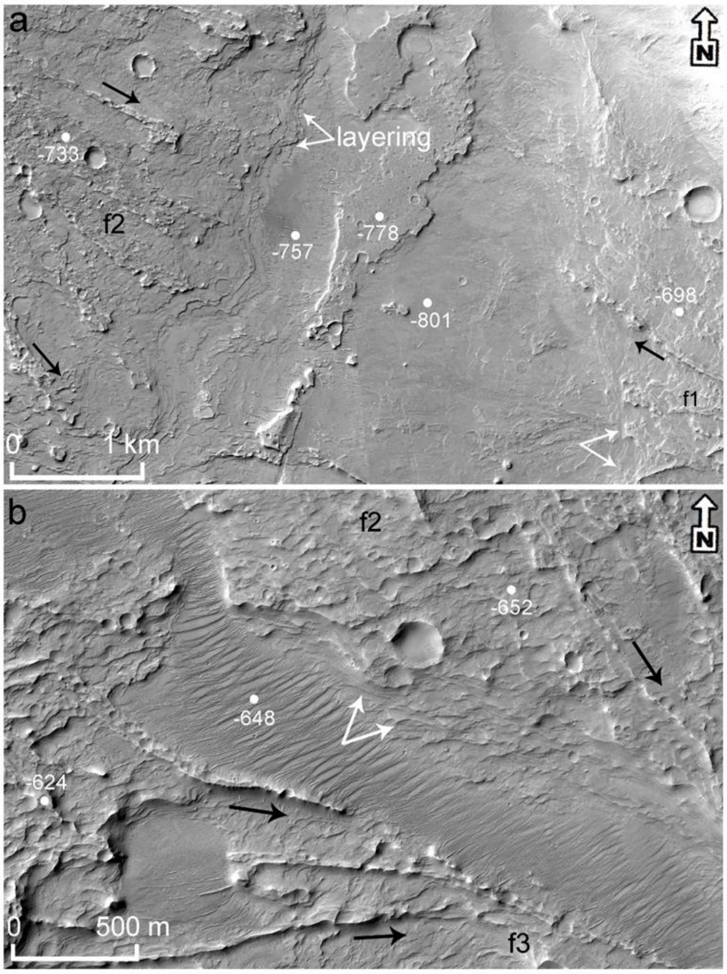

Figure 4.12: Example locations of intersecting fan deposits within Degana-A crater. a) Region of convergence of fan f1 and f2, with marked distributaries (black arrow, aligned in the direction of the fan). Layers were identified at the front scarp of both the fans. (HiRISE ID ESP_016039_1560 and ESP_035159_1560). b) Region of convergence between fan f2 and f3, with marked distributaries (black arrows, aligned in the direction of the fan). Layers were identified at the termini region of fan f2. The dust mantled the trough in between the fan deposits. (HiRISE ID ESP_018874_1560).

Fan deposits are also observed over the walls of Degana crater (f5 to f9), which mostly terminate at the rim of the Degana-A crater (Figure 4.7b). The slopes of these fans are in the range of 2° to 3°. Apparently, they have formed in the south and southeast of Degana-A and connected with the valleys presented on the wall of Degana (Figure 4.7b). Out of fans f5-f9, the smallest fan (f8) is ~4 km long and covers an area of ~10 km^2, while the largest fan (f6) is ~12 km long and covers an area of ~85 km^2. Fan f5 is the second largest fan within Degana crater though it is formed by deposits from multiple valleys (Table 4.2). Based on Blair and McPherson (1994; 2009) definition, alluvial fans are semi-conical depositional landforms that develop through a channel, and branching spreads the sediments across the surface. In general, alluvial fans are hundreds of meters to few kilometers long along their major axis and fed by constrained catchments. This definition applies well to the observed fan deposits (Figure 4.8**)** inside Degana and Degana-A craters.

4.3.4 Hydraulic measurements of alluvial fan

In this section, fan f1 was analysed to estimate the flow velocity and discharge quantitatively (method adapted from Morgan et al., 2014). Fan f1 is used for these measurements due to its complete coverage of HiRISE images. These measurements required the following parameters: fan slope, distributary width, and the grain sizes of the bed or deposited sediments [93]. These estimates employed to assess the flow of water and discharge, which are further used to calculate the supply rate of water for the formation of fan f1. Morgan et al. (2014) suggested that information about these measurements along with the estimated ages of fans formation allows to discriminate between the various plausible environments adequate for the formation of fans on Mars. In addition, Kleinhans (2005) approach was also followed, where channel bed roughness was modeled and used by Morgan et al. (2014). Additionally, using the approach followed in this study values of flow velocity and discharge are calculated for a variable: 1) percentage of sediments mixed with water (i.e., from clear water to 40% mixed sediments in water), 2) sorting of sediments (i.e., partially sorted or well sorted), and 3) grain size (depends on the smallest resolvable size) (Table 4.3). Consideration of clear water flow determined the lower limit for sediment concentration (i.e., almost negligible sediments), but higher sediment loads deemed to be more realistic. The upper limit is determined as a 40% sediment concentration in water [129], which is potentially the maximum sediment concentration carried by a flow. Morgan et al. (2014) suggested that the value of sorting parameter ‘a’ is poorly constrained on Mars and used the same value as used for coarse-grained alluvial fans on Earth (0.5). Hence, used the value of 0.5, assuming that the Degana fans contain coarse-grained sediments. Along with the sorting parameter, the size of the grains (D) is a crucial parameter to constrain the flow velocity and discharge. Morgan et al. (2014) suggested that for Martian fans the most likely parameter for grain size (D) is D_{84} (proportion of grains that are 84% smaller than D) and the values for this are 25cm (Figure 4.9d) and 12.5 cm (smallest grain size). These values show a dependency on data resolution in the case of planetary bodies.

Following Kleinhans (2005) and Morgan et al. (2014) the Darcy-Weisbach equation is used to determine the flow velocity (u) in streams, which is dependent on the channel hydraulic radius (h), slope (S) and gravitational acceleration (g) as given below:

$$u = \sqrt{\frac{8ghS}{f}} \tag{1}$$

where f is the Darcy-Weisbach friction factor. The value of the Darcy-Weisbach friction factor is determined using Ferguson (2007) equation:

$$\sqrt{\frac{8}{f}} = 17.7 \left(\frac{h}{D}\right)(56.25 + 5.5696 \left(\frac{h}{D}\right)^{\frac{5}{3}})^{-0.5} \tag{2}$$

In equation (2), the unknown parameter is the relative depth of the channels (h/D), which is dependent on critical shield stress (ζ). The following equation, which shows the dependency between the critical shield stress (ζ), slope (S), and relative submerged specific gravity (r) to determine the relative depth of the channels [93]:

$$\zeta c = \frac{S}{r}\left(\frac{h}{aD}\right) \tag{3}$$

The estimated slope values for fan f1 by taking four profiles (using CTX-DEM) over fan f1 (Figure 4.13). The average slope for fan f1 is determined as ~0.045. Equation (1) has been calibrated for a slope range of 0.0007-0.21, and found that the slope value for fan f1 lies within the range. Thus, equation (1) can be used for Degana fan f1.

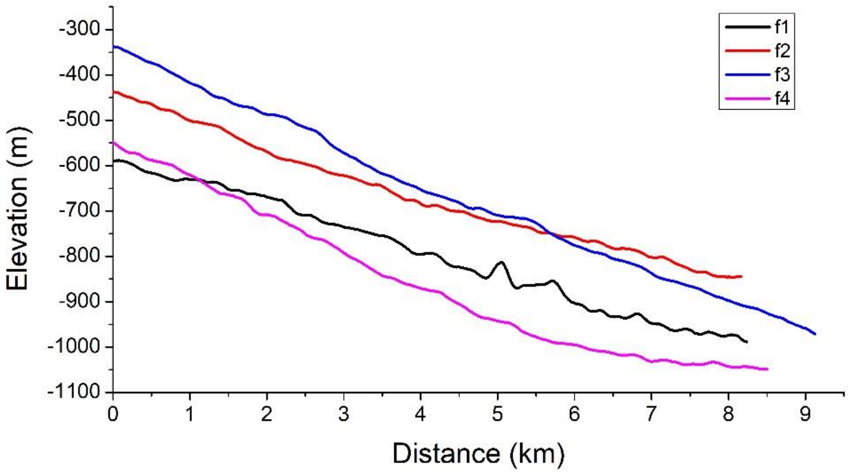

Figure 4.13: Elevation profiles derived along the major axis of four fans (f1-f4, Figure 4.8a-d) located within Degana-A crater.

Further, Lamb, Dietrich, and Sklar (2008) equation was adopted to determine the value of shield stress, which depends on the slope according to the following equation:

$$\zeta c = 0.15\ S^{0.25} \quad (4)$$

For a realistic flow, there must be some concentration of sediments mixed with the water. Therefore, relative submerged specific gravity (r) of the sediment clasts shows dependency on the density of the clasts (ρ_s) and the transporting fluid (ρ_f) as shown below:

$$r = \frac{\rho s - \rho f}{\rho f} \quad (5)$$

For the calculation of ‘r’ in equation (5), the density of clasts is assumed to be 3000 kg/m^3 and the fluid density to be 1000 kg/m^3 [93]. Using the values of ‘r’ from equation (5) and ζc from equation (4), the relative depth of channels (h/D) is determined using equation (3). Then the value of (h/D) was used into equation (2) to determine the values of “f”. All these estimated values of the unknown parameters were used in equation (1) to determine the flow velocity ‘u’ (Table 4.3).

Table 4.3: Flow velocity and discharge rate values for different parameters.

X (% of the flow by volume is sediments)	r (relative submerged specific gravity of the sediment clasts)	a (parameter represents the sorting of the sediment)	D m	h/D (depth relative to the bed grain size)	u (flow velocity) m/s	Q (flow rate) m^3/s
0	2	0.5	0.125	1.53	0.59	6.15
		0.5	0.25	1.53	0.84	17.41
		1	0.125	3.07	1.44	29.79
		1	0.25	3.07	2.03	84.25
10	1.5	0.5	0.125	1.15	0.40	3.10
		0.5	0.25	1.15	0.56	8.76
		1	0.125	2.30	1.01	15.73
		1	0.25	2.30	1.43	44.49
20	1.14	0.5	0.125	0.87	0.27	1.60
		0.5	0.25	0.87	0.38	4.53
		1	0.125	1.75	0.71	8.42
		1	0.25	1.75	1.00	23.81
30	0.87	0.5	0.125	0.67	0.18	0.83
		0.5	0.25	0.67	0.26	2.36
		1	0.125	1.34	0.49	4.48
		1	0.25	1.34	0.70	12.68
40	0.667	0.5	0.125	0.51	0.12	0.43
		0.5	0.25	0.51	0.17	1.21
		1	0.125	1.02	0.34	2.33
		1	0.25	1.02	0.48	6.59

After determining the flow velocity, the discharge (Q) was calculated using the following equation, which is dependent on u, h, and channel width w:

$$Q = u\,h\,w \tag{6}$$

To solve this, the average width of distributaries over the fan f1 was estimated as ~54 m and constrained the area of the source catchment of the fan f1 to ~670 km^2 (Figure 4.14). Using equation (6) the discharge for varying percentages of flow volume, sorting of sediments, and grain sizes were determined (Table 4.3). The value of maximum discharge is estimated as ~84 m^3/s.

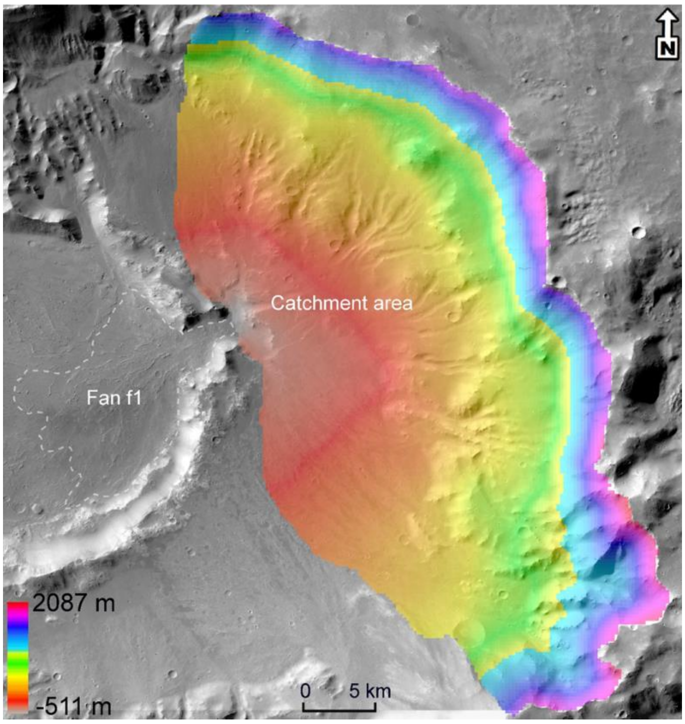

Figure 4.14: Part of MGS MOLA and MEX HRSC blended DEM overlaid on the CTX image showing the eastern side of Degana crater. This part is the possible catchment area for the five valleys, which played a role in breaching the Degana-A eastern rim. The boundary of fan f1 is marked with a dotted gray line.

Further, the supply rate of water was estimated using the relation between maximum discharge and the catchment area. The supply rate of water will be the maximum discharge per total area of source catchment and is estimated to be ~2.25 mm/hr. This value shows that the source catchment would have supplied the water at a rate of ~2.25 mm/hr. As mentioned by Ferguson (2007) and Morgan et al. (2014), all these estimated values have an error of factor two.

4.3.5 Ridges

In Degana-A crater, arcuate or wide U-shaped ridges were observed that are located over fans f2 and f3 (Figure 4.15). Photo-geological observations and profiles across these ridges indicate positive relief features with knobs (Figures 4.15,4.16). They were observed to drape over the eroded wall and fan of the Degana-A crater (Figure 4.15). These ridges are 10s of kilometers long and 100s of meters wide. Two ridges in the center over fan f2 have merge and form a thick ridge towards the west (Figure 4.15). Further to the west, a discontinuity along this merged ridge is observed (Figure 4.15). The ridges in Degana-A appears more degraded towards the eastern side (Figure 4.15). This ridge is relatively thicker in its center and the thickness decreases towards both of its frontal lobes (Figure 4.15). Also, the fan f2 is oriented from northwest to southeast, whereas these ridges are oriented in a northeast-southwest direction (Figure 4.15). Similar, but only 5 km long, ridges are also observed on the alluvial fan f3 (Figure 4.15). Interestingly, the ridges superposed the fan deposits and are observed on the pole-facing wall of Degana crater. The ridges in Degana and their characteristics such as convex geometry, an arcuate shape, and knobs are consistent with other moraines observed on Mars [29, 132, 133].

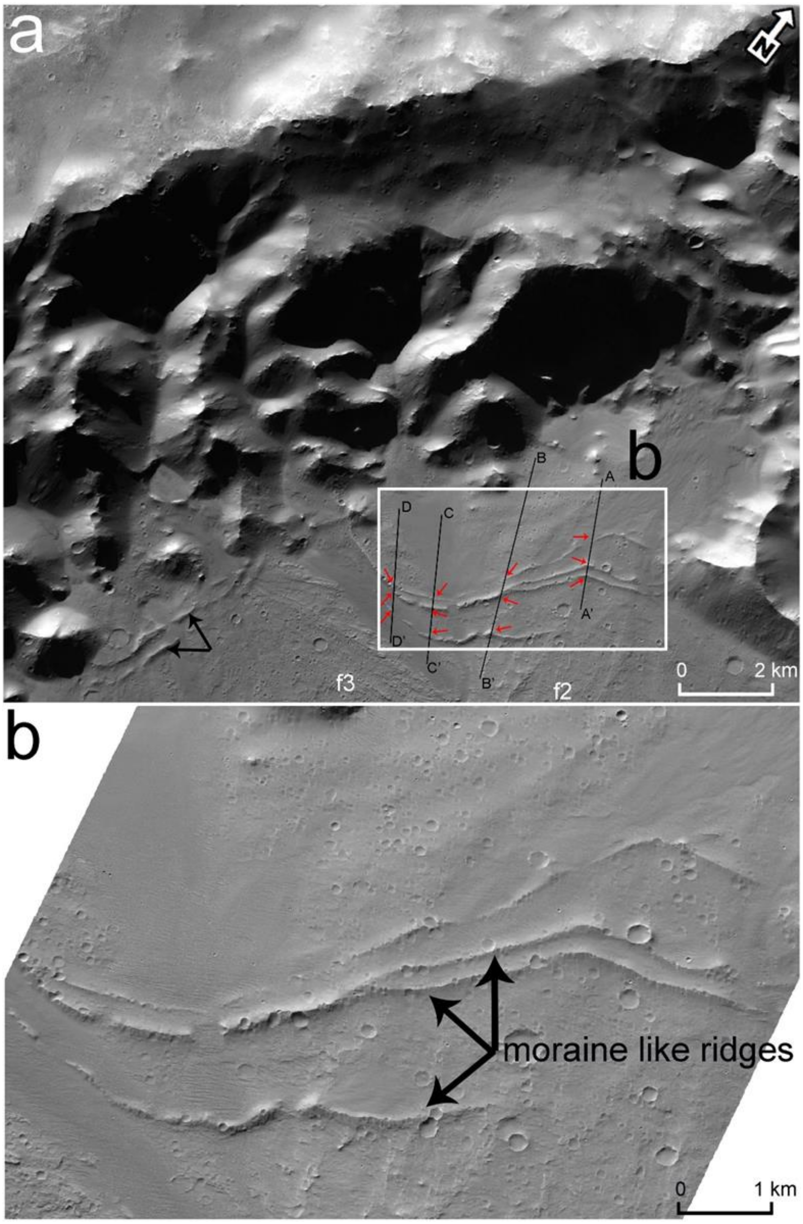

Figure 4.15: a) CTX image (G02_018874_1561_XN_23S045W) of the northern wall of Degana crater showing moraine-like ridges on the pole-facing wall. These ridges superposed over two fan deposits (f2 and f3). b) four distinguishable moraine-like ridges formed on fan f2.

The elevation profiles along north-south directions using the CTX DEM across the ridges located on fan f2 were analyzed (no HiRISE DEM is available for this location). Four profiles were examined for which the average thicknesses were determined. The limited resolution of the CTX DEM does not allow extracting precise thicknesses for some of the ridges (Figure 4.16). These measured thicknesses vary from 8 m (BB') to 51 m (CC') (Figure 4.16, Table 4.4), and considered these values as a range for the possible ridge thickness. Further, the approach by Hartmann et al. (2014) was followed to estimate the ratio of basal stress (ζ) to density (ρ), which provides information about the nature of a glacier. To calculate this ratio, Paterson (1994) relation was used, which suggests a relationship between basal stress and the density given as:

$$\zeta = \rho\ g\ h\ \tan\alpha \tag{7}$$

where g is the gravity (3.72 m/s^2), h is the height/thickness, and α is the slope in degrees [134, 135]. The average and maximum thickness (h) measured for moraine-like ridges over fan f2 is estimated as ~22 m and 51 m, respectively. The average and the maximum values are used because this region could have undergone erosion after their formation. Slope (α) values were also determined, along with all the profiles that are considered for thickness measurements (Table 4.4). The average ratio of basal stress to density for Degana glacier(s) is determined as ~4 m^2/s^2 (Table 4.4).

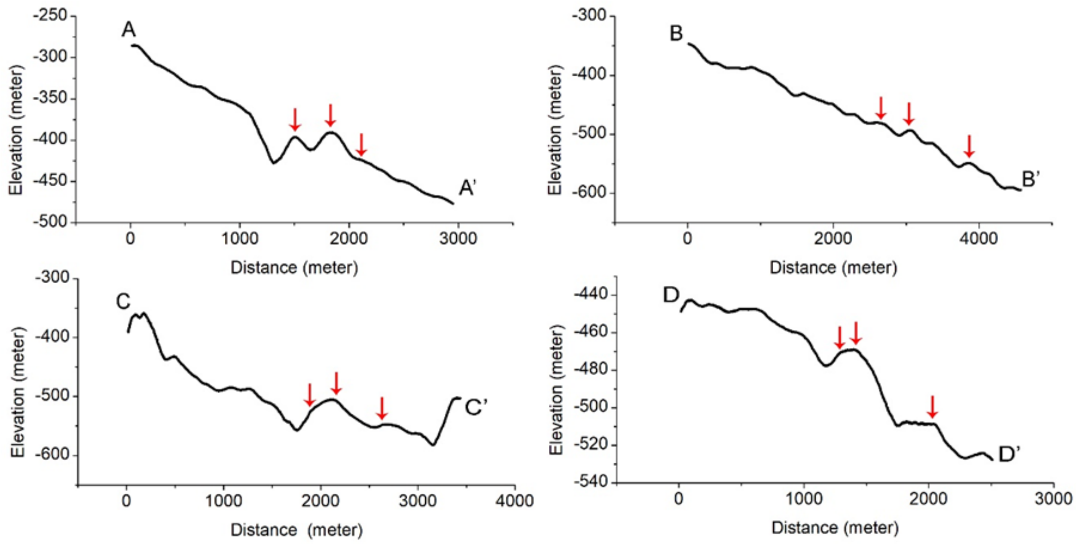

Figure 4.16: Elevation profiles used to determine the thickness of moraine-like ridges extracted from CTX DEM (stereo-pair CTX_016540_1579_034592_1579). Red is the location of ridges. The height of some of the ridges is unresolvable in the CTX DEM.

Table 4.4: Geometric characteristics of moraine-like ridges located on the northern wall of Degana-A.

Profile ID	Maximum height of moraine-like ridges (m)	Slope (in degrees) α	Basal stress/density (m^2/s^2)
AA’	20	3.49	4.5
BB’	8	3.0	1.6
CC’	51	2.74	9.1
DD’	8	2.24	1.2
Average	22		4.1

4.3.6 Small polygonal patterns

Within the Degana crater and on the fan deposits, several polygonal-shaped features are observed (Figure 4.17). Polygonal patterns are observed, especially on the fans in Degana-A, and also on the inner and outer eastern wall of Degana-A crater

(Figure 4.17). The majority of polygons' boundaries or fractures observed on the fans appear irregular (Figure 4.17a-c), whereas polygons over the Degana-A walls visually appear regular or organized to each other (Figure 4.17d-f). These polygons are 10s of meters wide and the fractures length varies accordingly.

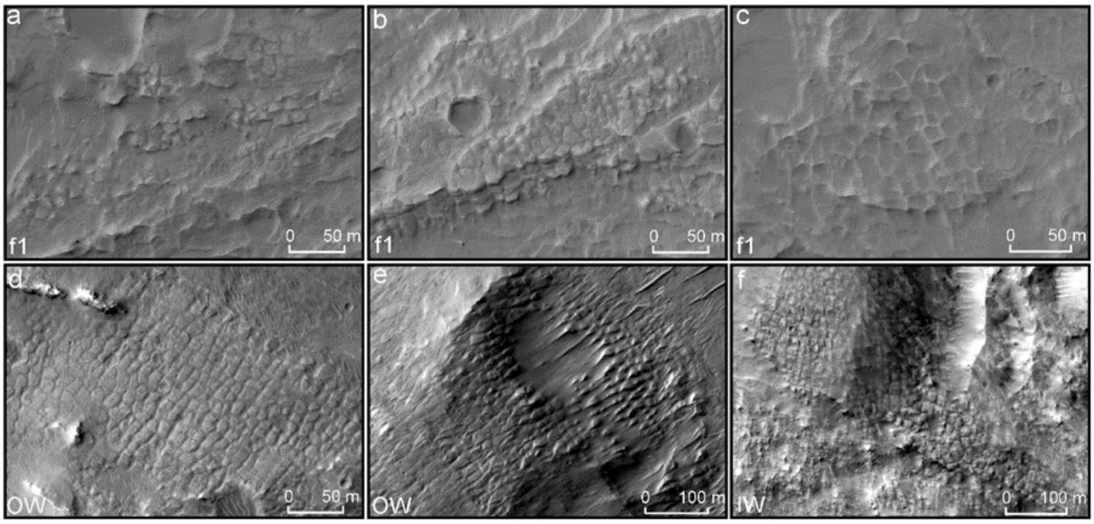

Figure 4.17: Examples of polygons within the Degana-A fan deposits (a-c) and on the walls of Degana crater (d-f). Trough boundary type polygons on fan f1 (a,b). Ridge boundary type polygon with hollows at center and raised ridges at the boundaries (c). Polygons over the outer wall (OW) of Degana-A (d,e). Polygons on the inner walls (IW) of Degana crater (f). (HiRISE ID ESP_016540_1560).

Figure 4.17b shows polygons over the fan f1, with fractures cutting through several layers. The polygonal fractures are well distinguishable over the fan f1 and within the vertically exposed stratigraphy (Figure 4.17b). Over the fans (Figure 4.17 a,b**)** and the wall (Figure 4.17 d-e), most of the polygons are negative reief features. In contrast, Figure 4.17c shows a distinct style of polygons with filled ridges and positive reliefs in some areas on fan f1. Polygons in the wall of Degana-A (Figure 4.17d) are distinct from the polygons observed on the fans (Figure 4.17a-c) in terms of the slope at which they formed. Polygons shown in figure 4.17a-c have formed on the relatively level floor **(**<10°), whereas polygons shown in figure 4.17d have formed on the more inclined wall **(**>30°). Overall, polygons on the fans suggest a potential involvement of volatiles potentially ice or adsorbed water in clay minerals, in their formation and, which would imply a periglacial environment postdating the deposition of the pile of sediments.

4.3.7 Crater size-frequency distributions

Xiao et al. (2012) estimated the age of the volcanic dome as ~4 Ga. In this study, Poisson timing analysis [136] was used to estimate the absolute model ages. The best visible ejecta boundary of Degana crater was mapped and counted the superposed craters over the ejecta (Figure 4.18a). The crater count statistics over the ejecta (area ~6546 km^2) resulted in a total of 362 craters from ~100 m to 20 km. The best fit model age is obtained by fitting 17 craters, whose diameter is greater than 1.3 km (Figure 4.18b). From this, the age of Degana crater is ~3.7 Ga **(**early Hesperian) [11]. Further, the ejecta of Degana-A was analyzed; however, it is difficult to distinguish the ejecta, which is degraded by mass movement processes within the host crater Degana. The floor of Degana-A is almost entirely covered by sediment deposits (Figure 4.7) from all around the wall, occupying an area of ~313 km^2. Hence, all the possible superposed and embedded craters (Figure 4.19) over these alluvial fans (f1-f4) were counted and determined cumulative (Figure 4.18c) and differential (Figure 4.18d) crater size-frequency distributions. The cumulative and differential fan-derived crater size-frequency distribution for Degana-A is early Amazonian [11].

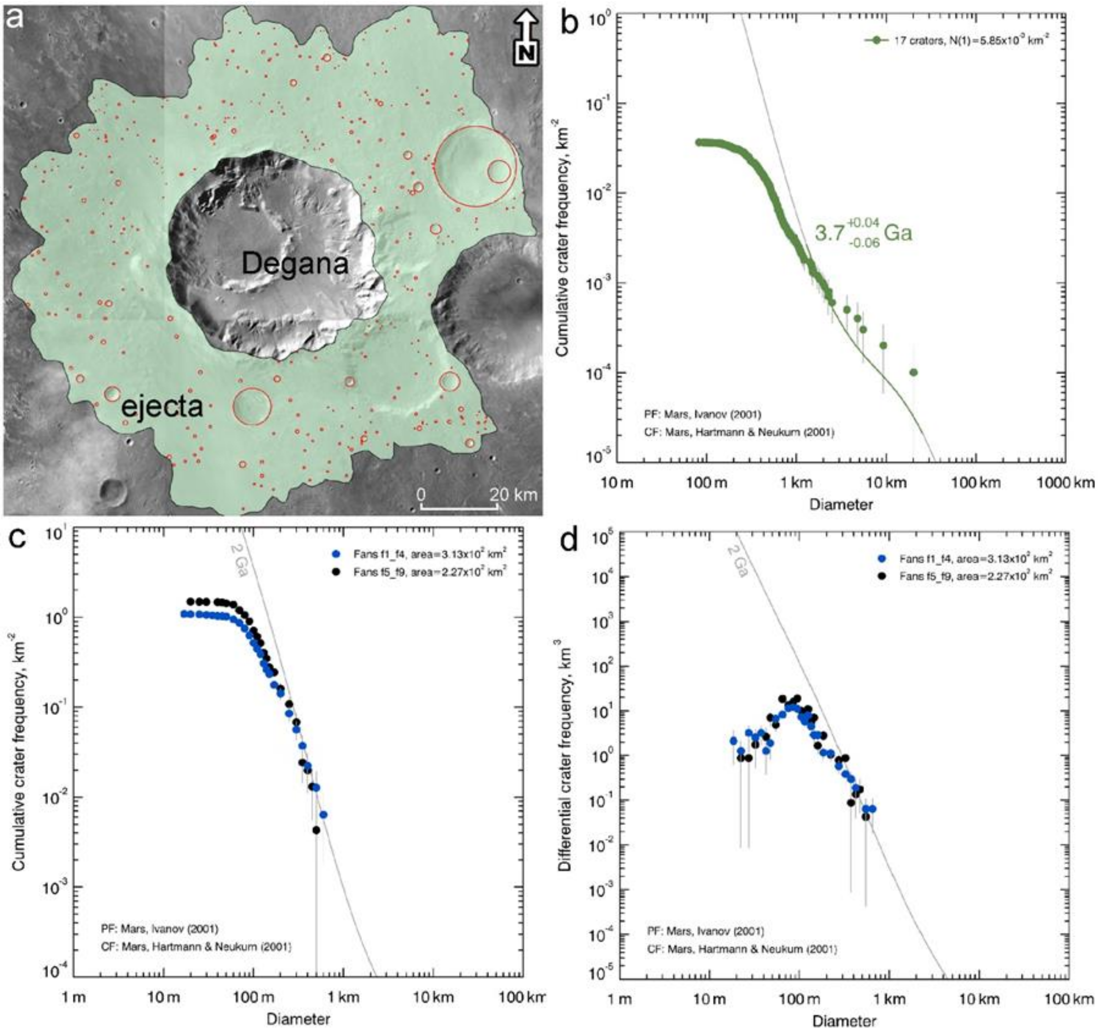

Figure 4.18: a) Degana crater and its ejecta boundary with superposed craters considered for crater chronology. Counts (red circles) were conducted using CTX images. b) Relative ages were determined using the production function of Ivanov (2001) and chronology function of Hartmann and Neukum (2001). The apparent model age of Degana crater is ~3.7 Gyr. c) Cumulative crater size frequency distribution for all the fans located within both craters. d) Differential crater size frequency distribution for all the fans located within both craters.

This age is not the formation age of the fan deposits within Degana-A; rather, it is estimated from the craters retained after their formation. Also, the diverse erosion of fan ridges observed (Figure 4.12) shows the difficulty in determining the model fan age. Note that here this age is the crater retention age for all the alluvial fans and can only suggest a possible lower bound to the deposits within Degana-A. In addition, cumulative (Figure 4.18c) and differential (Figure 4.18d) fan derived crater size-frequency distributions were estimated for the four fans (f5 to f9) located over the walls of Degana crater. The obtained age is also early Amazonian. This suggests that the fan deposits observed within both craters (Degana and Degana-A) are likely Amazonian.

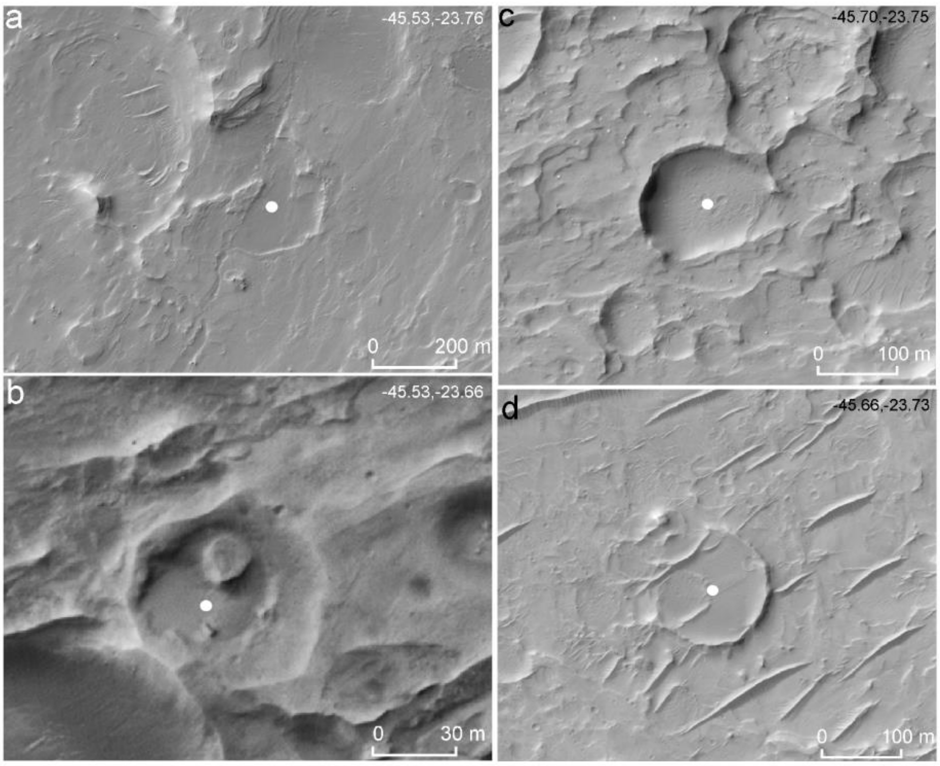

Figure 4.19: Examples of embedded craters identified on fan deposits within Degana-A crater (HiRISE ID: ESP_035159_1560 (a), ESP_018874_1560 (b,d), ESP_016540_1560 (c)).

4.4 Discussion

4.4.1 Evidence for exposure of pristine Noachian crust

The presence of mafic minerals in well-exposed outcrops within Degana crater indicate igneous lithology or basaltic/volcanic subsurface layers [118] exposed by the Degana and Degana-A impact. The following mechanisms have been proposed for the origin of olivine and LCP bearing rocks on Mars: Noachian crust/volcanism [117, 118, 137–144] or impact melting from large impact basins [145, 146]. Noachian/early crust on Mars can contain evidence for its formation and crustal modification afterward [118]. Mg-rich olivine got exposed on the wall/rim of Degana-A crater. McSween et al. (2006) suggested that Mg-enriched olivine on Mars likely indicates ancient primitive magmatic rock. Thus, the exposures of more mafic rocks in this region has implications for the magmatic history of the region. The exposed olivine and LCP in the uplifted rim of Degana-A provide a piece of direct evidence for the materials present in the interior of the volcanic dome. This strongly reveals that the materials exposed by the Degana outcrops represent either pristine Noachis crust and/or volcanic deposits sourced by a primitive mantle [141, 142, 147–150].

4.4.2 The fate of water at Degana crater

Earlier studies suggest regional glacial deposits in the southern highlands poleward of 30°S [31, 133, 151–157]. While the glacial deposits around the Tharis volcanoes have got attention for the Amazonian equatorial ice [13, 158], several craters located in low to mid-latitude (~5° to 60°) regions on Mars host young landforms on their floors and walls, which potentially indicate involvement of ice-rich material with lobate tongues and arcuate ridges [29, 83, 132, 133, 159–161].

Thus like other craters the local deposition of atmospheric ice occurred within the Degana. The moraines observed within Degana-A crater, which is situated at 23°S latitude, provide crucial evidence of equatorward glacial deposits during Amazonian period. Global climate models for the equatorial highlands region of Mars shows the possibility of snow accumulation and melting over the low and mid-latitudes, which would enable fan formation by snowmelt hypothesis [14, 103]. However, there is no umambiguous observation of glacial deposits connected to the alluvial fans. While the interpreted glacial landforms postdate the alluvial fans at Degana, the fact that glacial ice was able to be deposited during the Amazonian shows that this location was once favorable to snow precipitation during this period reinforcing a snowmelt scenario. Average ratio of basal stress to density for Degana glacier(s) (i.e. ~4 m^2/s2) in comparision to terrestrial values of pure ice glaciers (40-100 m^2/s^2) is one order of magnitude lower, but not so much lower than values of 3.7 to 44.5 m^2/s^2 found by Hartmann et al. (2014) at Greg crater. These low values are likely explained by the fact that these moraines underestimate the actual thickness of the past glaciers, but are consistent with pure-ice glaciers, while rock glaciers would show higher values and a partial filling by the residual material [134].

Morgan et al. (2014) documented distributaries within Saheki crater’ fans as observed on Degana’ fans (Figure 4.8), which are downslope oriented and show radiating outward patterns from the fan apex. Many other studies [32, 162, 163] reported similar ridges over the fans within many martian craters, which were interpreted as inverted channels or fan distributary ridges. Morgan et al. (2014) documented layered sediments within Saheki crater and interpreted that overbank flows, which might have been sourced from multiple flows within the distributaries, have deposited these layered sediments. Distributaries have spread across the fans in Degana-A crater (Figure 7), and they were the potential source for layered sediments, as suggested by Morgan et al. (2014). The flanks of the discontinuous distributaries (Figures 4.9d,4.10) with layers are records of possible long duration flow events in the region. Additionally, Morgan et al. (2014) suggested that such layers were exposed by aeolian erosion. Exposures of layers on both sides of the distributary (Figure 4.10) indicate that erosion occurred possibly due to the wind-driven activity**.** In Saheki crater, a similar distributary with exposed layers and bluish clasts in the HiRISE RGB-images suggested the presence of different materials [93]. Within fan f3 of Degana-A, the HiRISE image shows bluish clasts on the distributary (Figure 4.10) that are possibly comparable to Saheki crater ridge. However, this part of fan f3 lacks mineralogical data (CRISM) to assess the composition.

The rim breaching of Degana-A crater and fan f1 formation is closely associated to the valleys over the eastern wall of Degana crater. In addition, the valleys that incise the outer rim of Degana-A (black arrows in **f**igure 4.11) cut through a layered wall material on eastern side of Degana (Figure 4.11b). This layered material to be residual deposits from an initial fan that formed on the outer rim of Degana-A, similar to fans f5 to f9. Then, the breach through the rim produced a change in the base level of the deposits, starting to build the fan f1. In this scenario, the fact that a breach formed here rather than for the other fans f5 to f9 is likely due to the large watershed (Figure 4.14). An important implication of this scenario is that the fans f5-f9 would have formed coeval to the fans f1 to f4 inside Degana-A crater (see section 3.5). Several embedded craters are present on the fans (Figure 4.19), these possibly display evidence of interbedding within the crater [98]. From the observations of fan f1 to estimate the flow velocity and discharge quantitatively. Following Morgan et al. (2014), the value of maximum discharge is determined as ~84 m^3/s (Table 4.3). Based on this, the supply rate of water is determined, which is the maximum discharge per total area of source catchment and found that the source catchment would have supplied the water at a rate of ~2.25 mm/hr.

Studies on the deposition of large equatorial alluvial fans and deltas show the role of enhanced precipitation by rainfall or snow/ice melting followed by runoff [32, 91, 101, 102, 104, 105]. Although many alluvial fans are evident within Degana (Figure 4.7), due to limited CRISM coverage, hydrated mineral formation cannot be ruled out within the craters. The polygonal patterns display characteristics consistent with the patterns observed in aqueous sedimentary layers containing clay minerals that formed by contraction either from desiccation or from enhanced cold temperatures during their exhumation [164, 165]**.** The major hypotheses for polygon formation on Mars are thermal contraction and desiccation of sediments either enabled by ground ice or by sediments containing absorbed water such as in clay minerals [164–168]. Although the polygons were observed on alluvial fans, however, they are not interpreted as lava-related cooling cracks. Polygon patterns are generally defined by four factors: shape, size, boundary type, and intersection pattern [169]. They can be characterized by an elevated ridge boundary or a depressed trough along the boundary. The pattern of intersection can be orthogonal, random orthogonal or random [165, 169, 170]. The rectangular shape and size of the polygon in this study area form an orthogonal pattern indicative of desiccation cracks [164–166, 168] and/or thermal contracted sediments, i.e., potentially ice-wedge or sand-wedge polygons [170–173]. Desiccation generally forms nested polygons that display many secondary fractures [165]. Therefore desiccation is less likely than thermal contracted ice-wedge polygons over potential periglacial terrain [174] formed by ice/snow deposition as indicated by the presence of moraines. Two types of ice-wedge polygons were suggested based on thermal stability: 1) a low centered polygon and 2) high centered polygon [175, 176]. It was suggested that differences in their morphology potentially reflect a change in climatic conditions [57, 176–179]. In contrast to high-centered polygons, polygons in figure 4.17c show ridges along the boundary, implying low centered polygons. Those polygons do not have a regular shape and follow a more random geometry. They are consistent with networks of veins (also named boxwork deposits, [180]), which are formed by groundwater circulation and precipitations along fractures. Their presence may imply a period of groundwater circulation during or after the alluvial fan formation period. Alternatively, another possible reason can be deposition and cementation of sand/dust in cracks formed by thermal contraction and further erosion of the material inside polygons [165]. On the other hand, the preservation of olivine-rich outcrops means that no prolonged aqueous activity took place at this location, or outcrops have been covered and therefore protected from alteration until relatively recently. Thus, the presence of alteration minerals cannot be conclusively demonstrated, but a well-developed chemical alteration seems unlikely. To decipher the fate of water-related deposits within Degana it is assumed that the crater was once covered by ice before the formation of Degana-A. With this assumption, three scenarios may explain following observations: (A) An episodic climatic warming, perhaps related to obliquity variations [98]**,** (B) fluvial activity related to volcanic heat, possibly related to Alba Patera or Ceraunius Tholus [15, 16, 18], or (C) the role of the Degana-A impact whose heat release may have helped to melt snow and trigger fluvial activity. Scenario (A) requires to have favorable climatic warming relatively recently in the Amazonian era. This is possible according to recent studies [98], but speculative, lacking other evidence for warming, at least regionally. For instance, the older crater located in the east of Degana (Figure 4.3c) shows only ancient erosion by valleys, but no pristine alluvial fans as reported in Degana, while its size and wall hillslopes look quite similar. This comparison suggests that the alluvial fans formed at Degana are local. Scenario (B) is unlikely because Degana-A is far younger than the volcanic activity, and no volcanic landforms are observed inside either Degana or Degana-A craters. Regarding hypothesis (C), it has been shown that hot ejecta emplaced over an ice-rich surface could have generated local melting [97, 181, 182] possibly explaining some of the Amazonian age fluvial activity inside craters [17]. Ejecta temperatures for craters of diameter range between 5 km to 150 km were determined by Weiss and Head (2016) to be up to 490K. Snow melting due to ejecta emplacement produced by the Degana-A impact would have deposited sediments for fan f1. Maximum and minimum values for flow velocity and discharge rate for fan f1 in Degana crater wre also determined**.** The maximum value for the flow velocity is ~2 m/s whereas the discharge rate is estimated as ~2.25 mm/hr. These values are lower than the estimated flow velocity and discharge rate by Kite et al. (2013) and Morgan et al. (2014). These results support the interpretation regarding snow melting and the formation of fan f1. The breach of the ~1 km wide and ~900 m high eastern rim wall of Degana-A crater also indicates the long-lasting melting of snow/ice due to Degana-A impact. At least five valleys (Figure 4.11a) converge around the eastern wall region of Degana-A, which might have provided sufficient sediments to breach the crater rim. Figure 4.14 shows the catchment area associated with these five valleys. Large catchment area (Figure 4.14) and positive relief of the dome lead us to envisage high possibility of atmospheric snow/ice precipitation. This suggests that sufficient ice melt occurred to form the fan deposits within the craters. Thus, local atmospheric snow/ice precipitation is interpreted as the most likely source for fluvial activity within the craters.

4.4.3 Geological history of the Degana crater region and its implications for the geological history of Mars

The overall geologic interpretation and the sequence of events are based on the stratigraphic and chronological relationships. The sequence of geological events that occurred in the Degana region aids in deciphering the Martian surface processes, and climatic conditions that prevailed over this region. A schematic scenario is shown in figure 4.20, which represents the activities that took place in this region.

(1) Apparent model ages derived from crater size-frequency measurements by Xiao et al. (2012) suggest the volcanic dome formed around 4 Ga ago, during the Early to Mid-Noachian epochs (Figure 4.20a).

(2) Degana impact crater formed on the volcanic dome and exposed the dome interior down to ~2 km. Apparent model ages suggest that Degana crater formed in the early Hesperian 3.7 Ga +0.04/-0.16 or close to the Noachian-Hesperian boundary (Figure 4.18b). No volcanic-origin flows were observed within the crater. Therefore, it suggests that dome-related volcanic activity had ceased around 3.7 Ga.

(3) Degana-A crater superposed Degana crater after an unknown period. It is difficult to estimate the age of Degana-A's formation because a lot of its ejecta were likely sequestered inside Degana crater. Degana-A further exposed the interior of the dome or the underlying Noachian crust by another ~0.7 km. In total, both craters excavated ~2.7 km deep into the volcanic dome. However, the floor of the crater is covered by four large depositional fans (Figure 4.7) whose tentative crater retention epoch is early Amazonian.

(4) Multiple valleys on the wall, and floor of Degana crater, and several fan deposits within Degana-A (Figures 4.7b,4.21**)** provide strong evidence for fluvial activity. Although the length of time over which the fans formed is uncertain, two scenarios were evaluated. The orthogonal coalesced alluvial fans (Figure 4.7b), inverted channels/distributaries, and the discharge rate for fan f1 suggest that the fans were formed by steady discharges over a long period, possibly millions of years [12]**.**

This result suggest that the widespread occurrence of fans within Degana required snow/ice precipitation [32, 91, 105], followed by snowmelt within Degana to help the rim breaching of Degana-A. This suggests that sufficient ice deposition by mantling has occurred at least since the formation of the Degana crater. On Degana-A southern floor, possibly all the fans coalesced at their toe region and eroded (Figures 4.7b, 4.21). Thus, it is proposed that Degana-A was affected by snow/ice cover over Degana emplaced at some point after its formation around ~3.7 Ga and the ejecta from Degana-A played a role in melting the deposited snow/ice over the shattered dome, a scenario that had already been proposed for other locations on Mars [181].

(5) At the last stage, during the Amazonian or post fan formation [98], moraine-like ridges are formed. The glacial activities in lower latitudes reported to be more likely on the pole-facing walls of the craters [17, 183]. The presence of moraine-like ridges on the pole facing northern wall of Degana (Figures 4.15, 4.21) provides comprehensive evidence for the glacial activity that occurred up to lower mid-latitude [29]**.** Moraine-like ridges superposed over fans f2 and f3 (Figure 4.15) imply their post fan formation. This also suggests that the atmosphere-derived snow/ice was possible up to this latitude during the Amazonian period (Figures 4.20, 4.21).

Overall, the major implications from this study are that the craters excavated into a Noachian volcanic edifice and exposed pristine early Martian minerals, which is similar to earlier studies at different location of Mars [142, 148–150]. Degana crater also hosts significant evidence for post-Noachian fluvial activities. This means that they formed under climatic conditions more favorable to sustain runoff, which was capable to breach the Degana-A rim. Notably, no delta deposits like those formed in Jezero crater [34] were observed in the Degana.

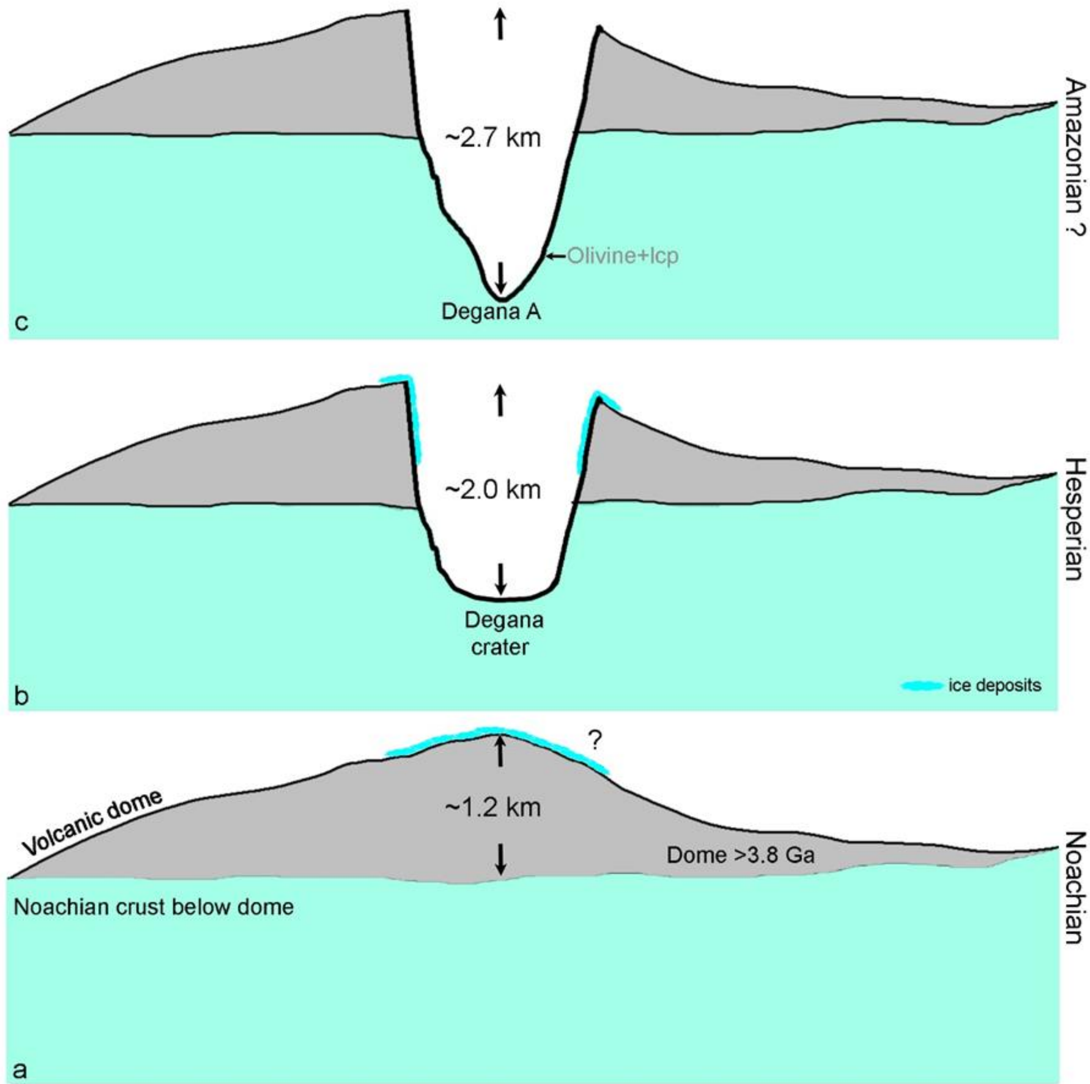

Figure 4.20: Schematic perspective outlining the tentative sequence of events. a) Volcanic dome formation at ~4.0 Ga with an elevation of ~1.2 km above the surrounding surface (baseline of the dome). b) Formation of Degana crater at ~3.7 Ga excavating ~2 km of the volcanic dome. c) Formation of Degana-A in Degana crater and additional ~0.7 km of excavation. In total, both the craters excavate material from ~2.7 km deep. The crater size frequency distribution for all the fans suggests an Amazonian crater retention age.

This implies that the condition during fan formations in Degana-A did not involve steady water [184] for the delta formation. This indicates that the climatic conditions were suited for alluvial fan deposits only which might be due to limited liquid water availability due to low temperatures, lack of moisture, and/or insufficient atmospheric pressure. However, this climatic condition varied over the Hesperian-Amazonian. This suggests that during the Hesperian-Amazonian, the ice accumulation at this latitude considerably reduced, which enabled moraine-forming glacial activity during the Amazonian, but no more (glacio-) fluvial activity. Thus, this area is one of the regions on Mars, which witnessed the transition from fan-forming fluvial activity in the Hesperian to moraine-building glacial activity in the Amazonian.

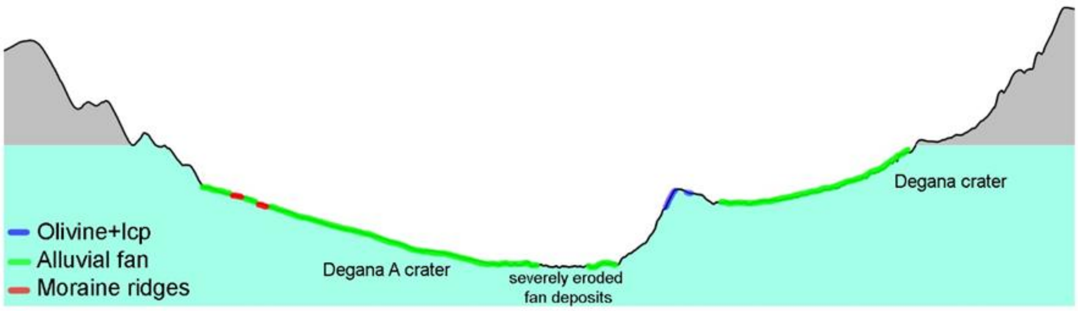

Figure 4.21: Schematic diagram showing the current state of Degana and Degana-A craters. Locations of mafic minerals, and fluvial and glacial landforms are marked.

4.5 Conclusions

A detailed topographical, morphological, mineralogical, and chronological analysis of impact craters Degana and Degana-A was carried out in this study. The results reveal the diverse geologic activities, which are:

- Degana and Degana-A craters formed on a ~1.2 km high Noachian volcanic dome. Both impacts excavated up to ~2.7 km deep, i.e., ~1.5 km deep in the Noachian crust located below the base of the volcanic dome. These impacts exposed pristine Noachian mafic minerals (Mg-rich olivine and low-calcium pyroxene) on the walls of Degana-A crater. Xiao et al. (2012) mentioned that true composition of these ancient Noachian aged volcanoes is not known, as most of these volcanoes are heavily dust covered and no in-situ observations were taken yet. Thus, this study provide likely composition of one of the ancient volcanoes on Mars.

- Both crater floors are covered by depositional fans, and especially Degana-A crater fans show distinguishable ridges, stratigraphic layers, and coalesced deposits. A notable ~1 km wide rim breach on the eastern rim of Degana-A crater and the hydrological estimation over this region suggest water flowed with a velocity of ~2 m/s and with a discharge rate of ~2.25 mm/hr. In support, Kite et al. (2019) reported discharge rate of 3 mm/hr for globally present channels on Mars.

- The moraine-like ridges linked to glacial activities superposed the alluvial fans. Such moraine-like ridges are observed only on the pole-facing walls of Degana crater. The fluvial fan deposits and the glacial moraine ridges are non-coeval events. They reveal comprehensive evidence for snow/ice deposition towards the lower latitudes of Mars during Hesperian-Amazonian epochs suggesting local climate change on Mars. Thus, Degana is one of the important locations that report lower latitudes (23°S) glacial activities on Mars [158].

- Based on the dome elevation, the formation of fluvial/glacial deposits within the impact craters and the latitudinal location, the atmospheric snow/ice precipitation is interpreted as the possible source.

Thus, Degana is a unique location on Mars has mid-Noachian aged mafic minerals, Hesperian-Amazonian aged fluvial and glacial deposits.

Chapter 5 Craters in the vicinity of Valles Marineris region, Mars: Chronological implications to the graben and pits activities

5.1 Introduction

A system of troughs along the equator of Mars formed a grand canyon, which is known as Valles Marineris (VM). It is one of the longest spatial features on the surface of Mars. VM covers an area up to ~4000 km in length, ~100 to 500 km in width, and has an average depth of 10 km [7, 8, 185–187]. Its formation possibly occurred over a large time period ranges from ~200 million to billions of years [7, 186–188]. The surrounding region of the VM is dominated by graben and pits. These graben and pits are considered as primordial features of the formation of VM troughs [40, 185, 188–192]. Their presence in the vicinity of VM are one of the markers to understand VM formation and its likely extension [2, 7, 8, 40, 185, 188–192]. Carr and Head (2010) stated that it is difficult to determine the age of the VM troughs and the canyon as a whole, as they are spatially large and wide in context. Many studies predicted the period of formation of VM, which was predicted to be of late Noachian because of its large extent [2, 3, 188, 193]. Studies suggest that VM formation is most likely related to the Tharsis tectonic and volcanic activities [2, 3, 188, 193]. Faults in the vicinity of VM region are reported to form during the Late Noachian epoch [193]. Additionally, uplift and rifting considered to have happened during the Early to Late Hesperian [188]**.** The graben that formed along the length of VM probably formed during the Late Noachian to Early Hesperian [43]. However, ridge plains proposed to form during Hesperian [194] and their relationship with the wall/boundary of VM suggests that most of the VM opening happened after the early Hesperian epoch [195, 196]. Also, graben which are oriented perpendicular to the VM and terminate against its wall were suggested to form before the VM opening [197]. Many studies suggest that the broadening of the VM varied with location and time, and the rate of broadening may vary over the time [191, 198–200]. This pose a question for the period of VM opening and its spatial and temporal development in the surrounding region.

Thus, the duration of formation and modification of VM remain an outstanding question. Also, which regions around the VM have been modified, and how is this observed over the surface, and how does this modification vary spatially as well as chronologically? Analyzing the graben and pits that are formed in the vicinity of VM will possibly allow us to decipher the history of their development and modification. Chronologically, there is no detailed study on these graben and pits, which are closely associated with the exterior part of the VM region. Spatially, there is no detailed study on how they varied over the time. This study used the relationship of graben and pits with the craters (assessing superposition and/or cross-cut relations) to determine the possible period up to which the extension/modification occurred in and around the VM region [40, 189]. In this study 1) a detailed investigation of craters having superposition and/or cross-cut relationship with graben/pits/troughs was carried out, 2) estimated the age of the craters which are located within 100 km vicinity of VM region to infer how the vicinity region modified over time.

5.2 Data used

For the analysis of regional morphology, Mars Odyssey (MO)-THermal EMission Imaging System (THEMIS) ortho-projected daytime infrared (IR) data at 100 m/pixel resolution was used [46, 201]. MRO-CTX individual images at a resolution of 6 m/pixel [48], CTX mosaic images [202] and MOM-MCC image at ~20 m/pixel resolution [47] are used for the morphological analysis. Mars Global Surveyor (MGS)-Mars Orbiter Laser Altimeter (MOLA) Precision Experiment Data Record (PEDR) individual altimetry readings and a digital elevation model (DEM) mosaic at ~463 m/pixel resolution are used for the topographical analysis [51].

For determining the absolute model ages, the CraterTools was used. For this purpose, Neukum-Ivanov (2001) system containing the production function of Ivanov (2001) and the chronology function of Hartmann and Neukum (2001) is used. Epoch boundaries from Michael (2013) is used to determine the ages. Due to less number of craters in many areas, Poisson timing analysis [136] is used to determine the ages more accurately and to support the ages determined using the cumulative fit of Neukum-Ivanov (2001) system. Dust cover over many regions hinder the ejecta boundary, however, it was taken care by demarcated the ejecta boundary from multiple images (Figures 5.1-5.4). Highly clustered and ordered secondary craters are carefully excluded in counting regions of this study to minimize the error. However, there are few craters with no visible ejecta boundary, in such cases the craters on their floor are used to determine the relative ages. Using cumulative crater size-frequency distribution, absolute model ages for all the selected craters were obtained using Neukum-Ivanov (2001) system (Table 5.1).

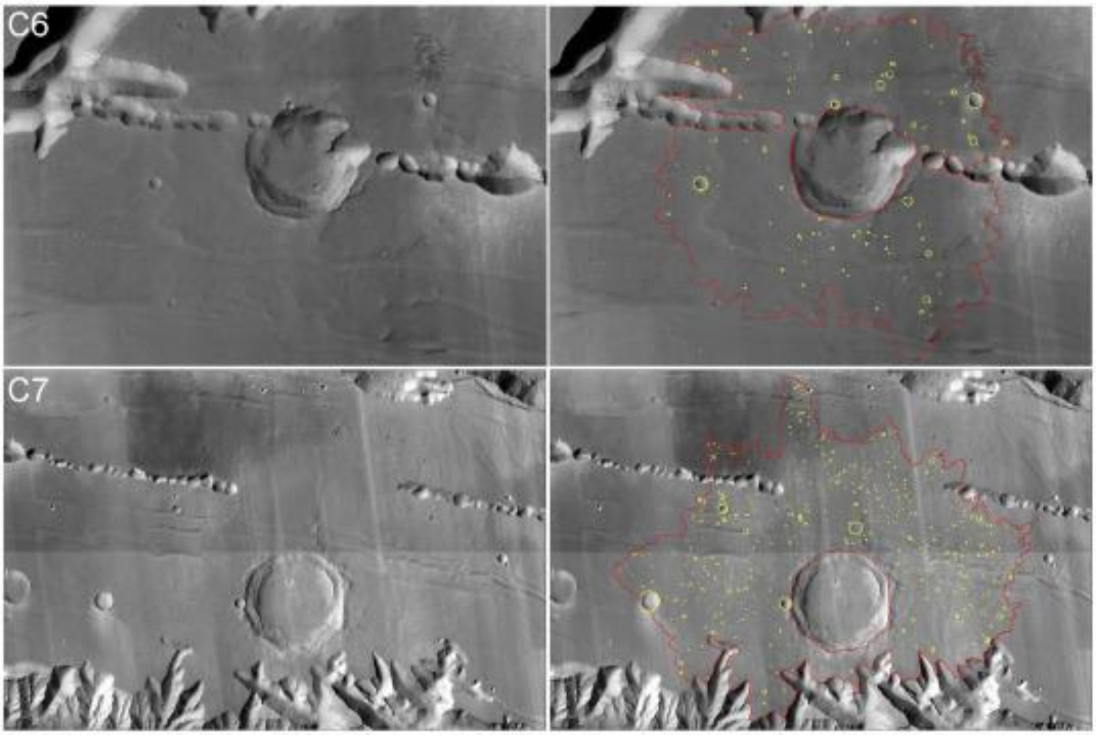

Figure 5.1: Ejecta boundary and crater counts for craters C6 and C7. Left panel - unmarked and right panel - boundaries marked and counted craters. Ejecta boundary (red) and counted craters (yellow). CTX mosaic (downloaded using Dickson et al., 2018) is used as the base data in the images.

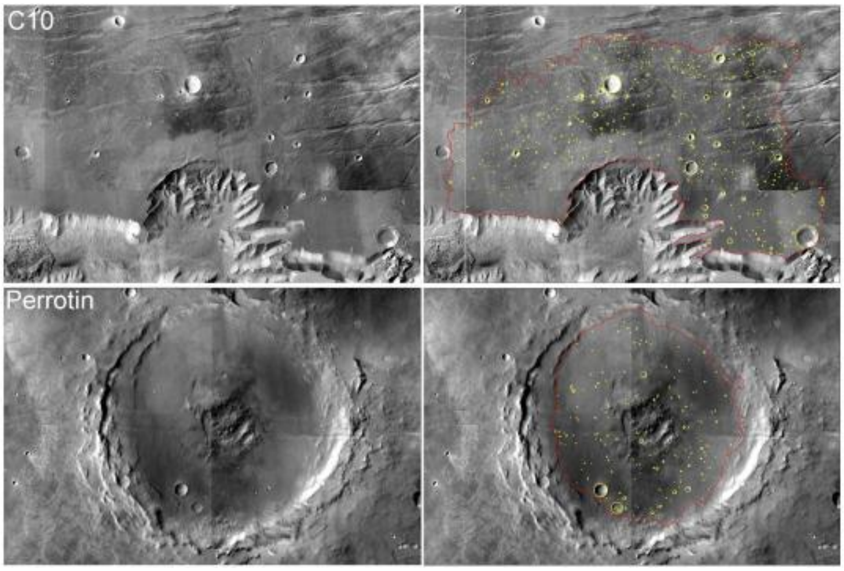

Figure 5.2: Ejecta boundary and crater counts for craters C10 and Perrotin. Left panel - unmarked and right panel - boundaries marked and counted craters. Ejecta/floor boundary (red) and counted craters (yellow). CTX mosaic (downloaded using Dickson et al., 2018) is used as the base data in the images.

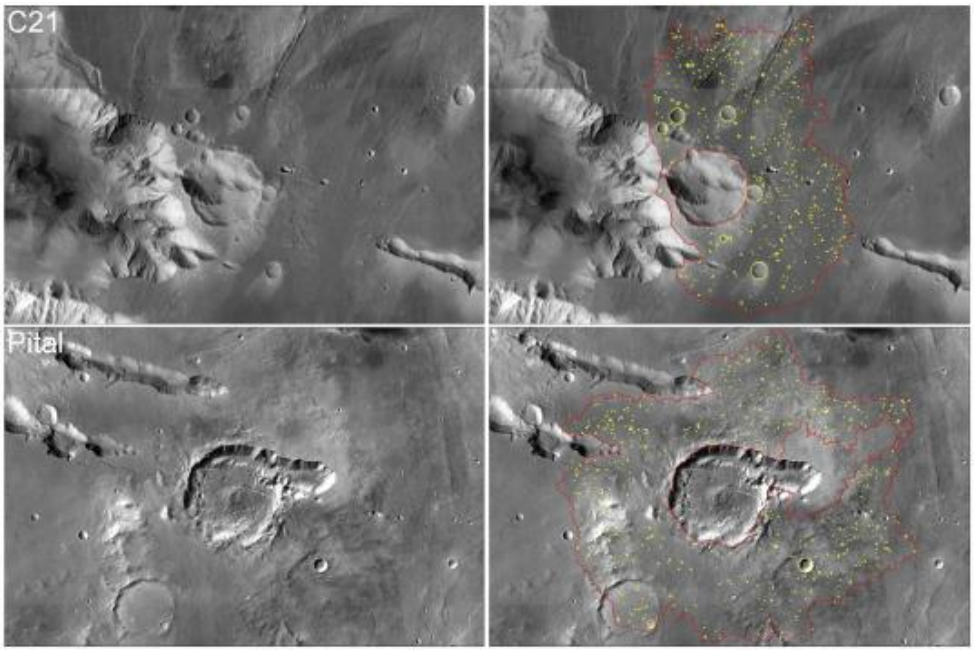

Figure 5.3: Ejecta boundary and crater counts for craters C21 and Pital. Left panel – unmarked and right panel – boundaries marked and counted craters. Ejecta boundary (red) and counted craters (yellow). CTX mosaic (downloaded using Dickson et al., 2018) is used as the base data in the images.

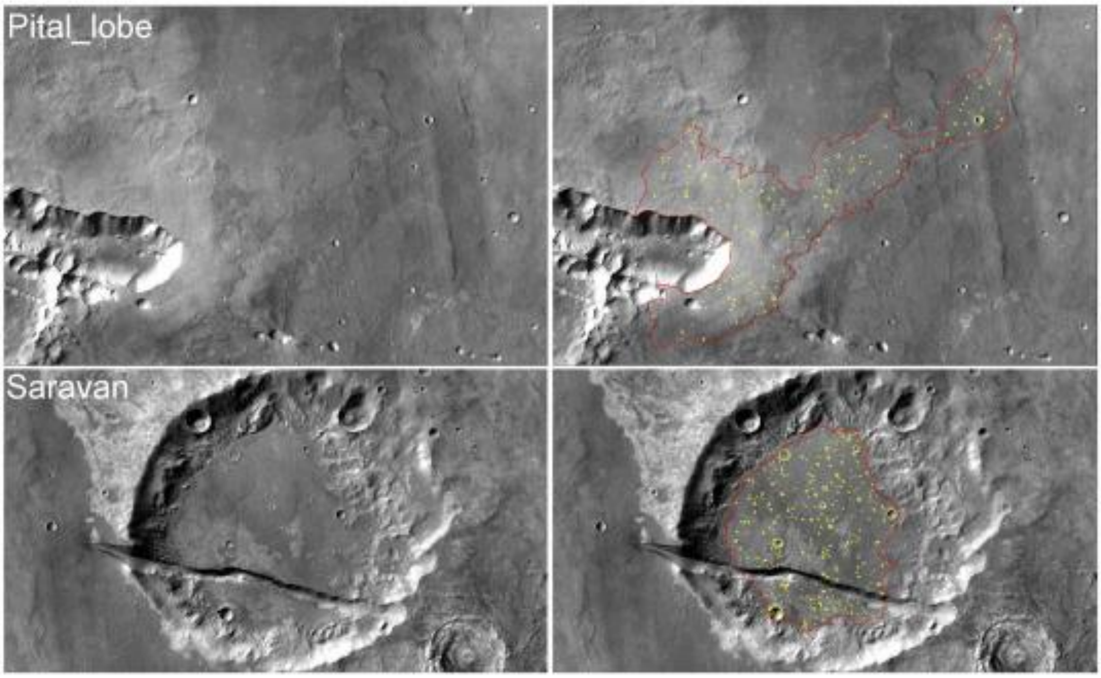

Figure 5.4: Ejecta boundary and crater counts for Pital_lobe and Saravan crater floor. Left panel - unmarked and right panel - boundaries marked and counted craters. Boundary (red) and counted craters (yellow). CTX mosaic (downloaded using Dickson et al., 2018) is used as the base data in the images.

Table 5.1: Crater chronology for craters/lobe in the vicinity of Valles Marineris.

Name	Coordinates [˚]		Diameter [km]	Area [km^2]	Total no. craters	D[km] in fit range		No. craters in fit range	Age[1]			N_{cum}(1 km)/10^6 km^2 of fitted isochron	Epoch		Geological unit on which crater superposed
this study	Latitude	Longitude				D_{min}	D_{max}		best fit	error +	-		this study[2]	Tanaka[3]	
C6	-83.99	-5.41	17.78	1706.7	98	1.0	12.0	8	3.60	0.09	0.17	3980	lH	AHi	eHh
C7	-81.89	-6.27	32.19	7515.1	502	1.6	7.8	9	3.63	0.08	0.12	4480	eH	AHi	eHh
C10	-84.54	-4.19	56.29	16205.5	830	1.8	7.8	19	3.71	0.04	0.05	8650	eH	AHi	eHh
Perrotin	-77.95	-2.81	78.79	36010.2	587	2.7	5.5	2	3.70	0.17	0.83	6620	eH	AHi	eHh
C21	-69.68	-4.60	27.02	4809.1	582	4.0	20.0	5	3.92	0.07	0.08	22400	mN	-	eHv
Pital	-62.30	-9.22	38.50	10968.2	597	1.0	11.0	14	2.61	0.45	0.54	1270	eA	AHi	eHv
Saravan	-54.01	-16.93	45.99	582.9	337	1.1	3.6	4	3.76	0.09	0.16	8340	lN	-	mNh
Pital_lobe	-61.24	-8.58		1100.0	170	0.39	2.70	17	1.14	0.29	0.25	556	mA	-	eHv

[1]Absolute model ages are derived using the poisson timing analysis of Michael et al., (2016) in the chronology system of Neukum-Ivanov, 2001 [production function of Ivanov (2001) and the chronology function of Hartmann and Neukum (2001).

[2]Epoch boundaries in the Neukum chronology system as recalculated in table 2 of Michael (2013).

[3]Tanaka et al., 2014.

5.3 Graben

In the VM region, the most notable features are troughs, chasmata, graben, pits, collapsed pits, pit chains, valleys, interior layered deposits and landslides [7, 39, 40, 43, 185–187, 189, 192, 199]. Among these, graben are linear depressions having very high length to depth ratio on the order of 10^5 [188]. Martian graben are classified as simple and complex graben on the basis of their morphology and relief [43]. Graben having lengths of tens to hundreds of kilometers and widths of less than five kilometers are classified as simple graben [204–206], whereas complex graben are having more widths ranging between tens to hundreds of kilometers and depths up to a few kilometers [43, 207, 208]. On Mars, simple graben are more dominant and their rate of formation decreases over the time in comparison to other extensional tectonic features, such as complex graben, rifts, tension cracks and troughs [43]. Many studies mapped the distribution of graben surrounding the VM region[43, 204, 209–211]**.** Many studies considered VM troughs as large graben [40, 189, 190, 212]. Schultz (1998) suggested that different sequential processes occurred post to the graben formation finally caused the formation of Valles Marineris. Overall, the vast distribution of graben along the VM hints their role in the formation of VM trough [40].

5.4 Pits

Pits are commonly circular to elliptical depressions, plausibly shaped by tectonics and/or volcanism and they commonly witnessed to associate with the graben and parallel to border faults [39, 42, 213]. Pits on Mars typically have concave up geometry with high slope steep walls [39]. They are primarily found in alignments or chains and reported collinear with normal faults [39, 40, 189]. Pits are depressions analogous to impact craters. However, impact craters are distinguished from pits based on the following [39]: 1) Craters are usually circular, whereas pits are generally elliptical (Figure 5.5), 2) Craters are surrounded by ejecta, whereas pits do not have ejecta, 3) Craters generally have elevated rim, whereas pits don't show elevated rim in most cases (Figure 5.5), 4) Craters are shallower than the similar size pit (Figure 5.5).

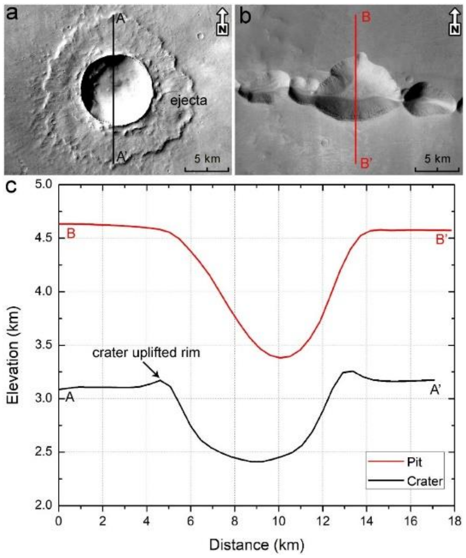

Figure 5.5: Detailed comparison between a similar size crater and pit. a) Crater shows circular shape, uplifted rim and ejecta all around it. b) Pit shows elliptical shape, and no uplifted rim and ejecta is visible around the pit. c) Elevation profile across the crater and pit shows that similar size pit is almost two times deep as compare two the crater.

Wyrick et al. (2004a) reported elliptical-shaped pits with the long axis parallel to the chain. These pits are enlarged by collapse and later coalesce to form a linear feature termed as trough [40]. Smaller pits are having size less than 2 km, while the size of larger pits ranges between 4-10 km. These pits are also discriminated based on their morphologies [214]. Smaller pits have a regular circular shape and in most cases they are contained within graben, while larger pits have an irregular shape and are coalesced within each other [214]. Some of the pits have stratified layers on their walls, and their walls are differentially eroded[39]**.** In the VM region, the pits are reported to superpose or crosscut the graben and suggests that the pits formed post to the graben formation [42]. Pits on Mars also occur as continuous pit crater chains and they are strongly associated with graben or faults [39]. There are many pit crater chains and coalesced pits located almost parallel to VM, including Tithoniae Catenae, Ganges Catena, Ophir Catenae and Coprates Catena [215].

5.5 Amphitheater-headed valley

The periphery of VM is surrounded by several amphitheater-headed valleys [216, 217]. Box-shaped planform geometry was suggested for these valleys/troughs and they generally have steep, stubby headwalls, and flat floors [216]. These valleys, appear to follow the path of previously formed graben running parallel-subparallel to the VM, are believed to form by headward erosion due to preferential weathering through groundwater sapping, springs, or overland flows [216–221]. However, they are also defined as collapse structures that trend parallel to the blunt end of the trough, which may be the planes of weakness generated due to minor tectonic activity and collapse [187]. Recently, Schmidt et al. (2018) reported long U-shaped valleys with amphitheater-shaped heads as graben and they appear to extend from the chasma. Hence, amphitheater-headed valleys are referred as troughs in this study.

5.6 Selection of craters

Around the VM region, a 100 km buffer was made and craters within this boundary from the wall are more likely to be affected [7]. A rigorous scouting around this buffer region found that 1516 craters are having diameter ≥1 km. Only those craters which demonstrate 1) a clear association with graben and pits such that clearly showing superimposing and/or crosscutting relationship and 2) discernible ejecta or adequate floor for the estimation of age are selected in this study (Figure 5.6). As the craters of diameter less than 3 km do not have evident ejecta and the area of the ejecta/floor unit is not ample for age interpretation [222], for this reason, these craters were not selected in this study. Of the 1516 scouted craters, 1228 of them have a diameter less than 3 km. Out of the remaining 288 craters, only 48 craters likely show a clear association with graben and/or pits. The selected 48 craters are allied (superposed/crosscut) with the graben, pits, and troughs. In this study, the superposition relationship is deduced based on: 1) graben/pits superpose/crosscuts the crater rim, 2) graben/pits dissects or superposed the crater ejecta, 3) graben/pits forming within the floor region of the crater, and 4) craters and/or their ejecta superposing the graben/pits. Figure 5.6 displays the distribution of all 1516 craters within the ~100 km vicinity of VM region, and the 48 craters selected in this study are studied in detail.

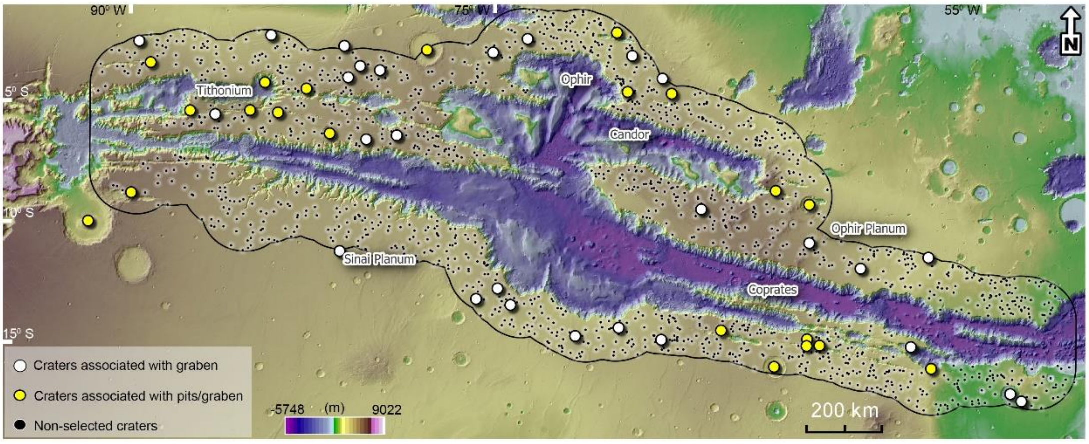

Figure 5.6: Color shaded-relief map derived from MOLA topography (20°S to 0°N) of the Valles Marineris region, and distribution of craters within ~100 km vicinity. The location of 1516 craters within ~100 km vicinity used for analysis around the Valles Marineris region.

These 48 craters were classified in two classes: (1) craters that exhibit an association with only graben and 2) craters that are associated with both graben and pits. Very few craters are associated with catenae/troughs, which have either crosscut the rim or have formed near to the crater rim. Figure 5.7 demonstrates examples of above mentioned crater types. Figure 5.7a shows a clear association with graben and has distinguishable ejecta blanket around the crater. Among the selected 48 craters, graben are commonly observed in association with the crater ejecta, except for a few craters where they are observed to reach upto the crater floor (Figure 5.6). At some locations, graben are observed to pass near to the rim of the crater (Figure 5.7), while at other locations they passes near to the crater’s ejecta. In these scenarios, either the ejecta has been emplaced over the graben or vice versa. However, the craters' ejecta and their association with graben are analysed carefully to determine their superposition relationship. Figure 5.7b displays one more selected crater in this study, which demonstrates crater association with both graben and pits. Figure 5.7c displays the Pital crater that is associated with pits chains and one big catena, where the catena appears to crosscuts the northeast rim of the Pital crater.

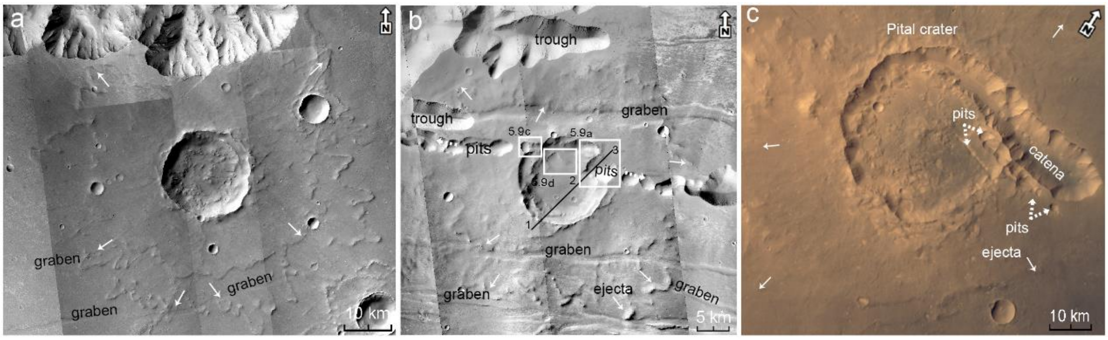

Figure 5.7: Example craters having association with graben and pits in the 100 km vicinity from the VM wall. a) Craters associated with graben and emplacement of ejecta over the graben or vice-versa). b) Craters associated with graben and pits, and rim of the crater crosscut by pit. c) Pital crater with superposed pits, pit chains and **catena.** ***The northeastern rim of the Pital crater is crosscut by catena. (MOM-MCC image id: MCC_MRR_20150423T072306117_G_D32). (White arrows – ejecta, dashed arrow – pit chains).***

Craters selected in this study are also inferred based on their regional locations. The selected 48 craters are distributed primarily over the regions of Tithonium (22 craters), Ophir (11 craters), and Coprates (15 craters) Chasmatas (Figure 5.6). Among these craters, ~60% craters are located to the north of VM, whereas ~40% craters are located in the south of VM. Figure 5.8 displays the spatial distribution of selected craters, their association with graben/pits, and variation in topography that observed in the vicinity of VM, particularly over the three above mentioned regions. Pits/graben are not mapped regionally and only those pits/graben that are associated with the selected craters are mapped in figure 5.8. In the Tithonium region (TR), crater C10 and surrounding craters located at relatively low elevated terrain than the adjoining Perrotin crater which located on a relatively elevated terrain (Figures 5.6, 5.8). In the Ophir region (OR) near to the Pital crater, the topography demonstrates terrains with gentle slope from south to north and also toward the northeast (Figures 5.6, 5.8). In the Coprates region (CR), craters in the vicinity of Arima crater are located on a relatively elevated topography, while craters adjacent to Saravan crater are located on a relatively low elevated topography (Figures 5.6, 5.8). The topographical analysis is carried out to understand the topography effects, if any, on graben and pits activity. This analysis suggests that the selected craters are located spatially apart and sited on different elevated terrains.

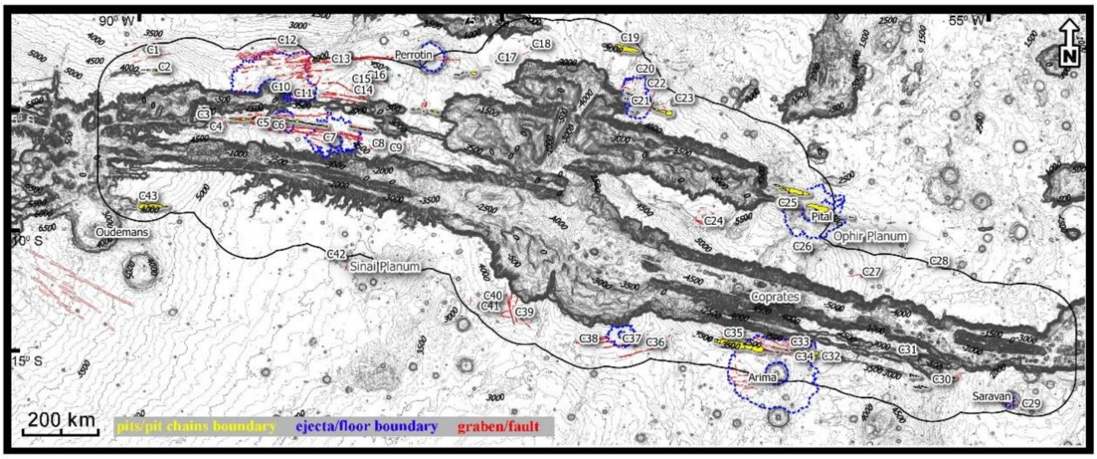

Figure 5.8: MOLA DEM derived contour map of the VM region with a contour interval at of 100 m. The contour map also shows the distribution of graben/faults, pit/pit chains, and crater ejecta/floor boundary. The location of marked 48 craters represent the craters selected for this study.

5.7 Observations and interpretations:

5.7.1 Craters in Tithonium region

In the TR, four craters (C6, C7, C10, and Perrotin) are focussed which are having clear association with graben, pits, coalesced pits, and troughs.

Crater C6: Crater C6 (Figure 5.8) is centered at -5.41°, -83.99°. It is ~17 km in diameter and ~1 km deep. The ejecta of this crater spreads over more than two crater radii from the crater's rim. Within crater C6 it is witnessed that pits are emplaced over the crater at three locations (Figure 5.7b). The easternmost pit has carved into the crater rim (Figure 5.9a), with an extent of ~6.8 km along the major axis and depth of ~1.17 km. It is observed that this pit has dug below the crater floor, thus, pit depth is relatively more than the crater (Figure 5.9b). The other ~200 m deep pit is observed to emplace over the western part of the rim (Figure 5.9c). These two pits jointly covers ~10 % area of the crater rim. The third pit is observed to emplace over the crater floor (Figure 5.9d). The extent of this pit is almost half of the easternmost pit that carved into the crater rim. The crater's floor appears to be dust-covered and the pit emplaced over the floor is likely aligned along the line of pits chain located over the crater's wall (Figure 5.9d). Also, a plausible buried pit over the floor is observed which is mantled by the dust (Figure 5.9d). These evidence renders the superposed emplacement of pits over the crater C6. Here pits of varying lengths and depths have formed within and around the crater. Outside the crater, pits are observed in chains which are oriented in W-E side (Figure 5.7b). In the east of the crater, coalesced pits were observed to emplace within the plausible graben (Figure 5.7b). Within the ejecta boundary, the maximum length and depth of pits are ~7 km and ~1.2 km respectively.

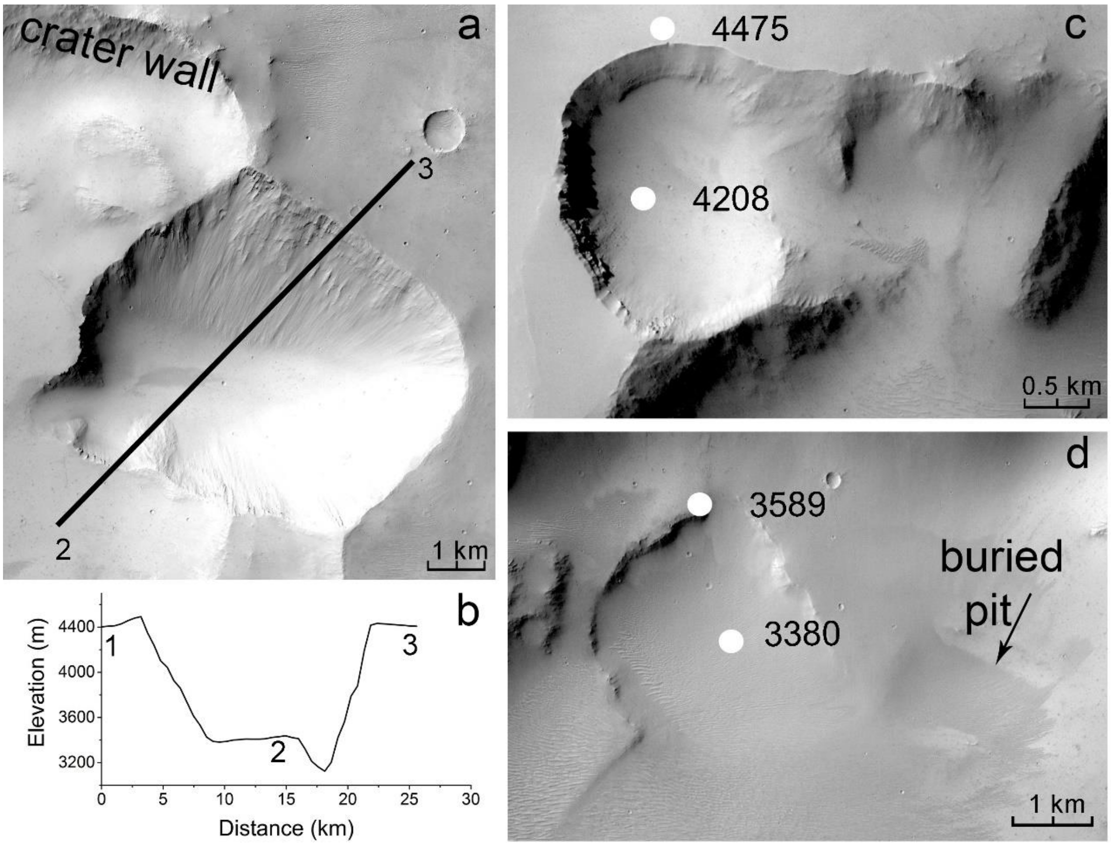

Figure 5.9: Pits associated with crater C6 in Tithonium region, a) typical example of superposed pit over the crater eastern rim (CTX id: P18_007931_1737_XN_06S083W), b) elevation profile cross-section of pit, note that the pit depth is more in comparison to the crater floor depth (full profile is shown in figure 5.7b), c) pit formed over the western rim, which is smaller in size and depth when compared to pit on eastern side (4a) (CTX id: J10_048703_1754_XI_04S084W 2016-12-16), d) pit present over the crater floor mantled by dust cover, Adjacent to this pit, a buried pit is present (black arrow) (CTX id: P08_004160_1736_XN_06S084W 2007-6-16). (White dot: MOLA elevation values in meter; for location refer to Figure 5.7b).

In figure 5.7b, the northwest side of the crater hosts an elongated depression marked as trough. The trough is observed within the crater ejecta blanket and it is located parallel to the western pit chain. Both, the trough and pits chain are observed to line up along the graben (Figure 5.7b). However, there is no clear evidence of whether trough superposes the crater ejecta or vice versa due to the dust cover, over this region (Figure 5.7b). On observing the graben associated with this crater, it is found that the ejecta is emplaced over the graben and determined that they are likely superposed by the crater ejecta (Figures 5.7b, 5.10). The features associated with this crater (e.g. pits, pit chains, troughs and graben) are observed to vary in their spatial extent and pits provide clear evidence for their superposed presence.

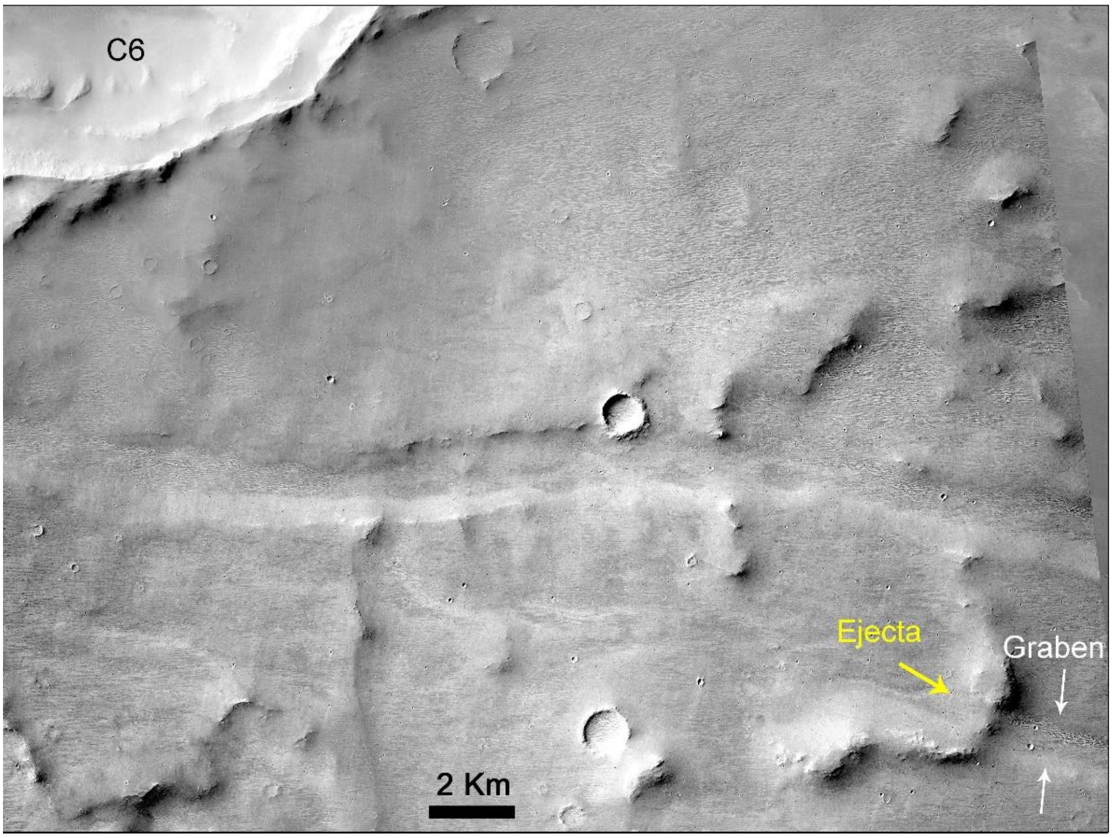

Figure 5.10: Crater C6 ejecta superposed over the graben.

Crater C7: Crater C7 is centered at -6.27°, -81.89° (Figure 5.8) and having diameter and depth as ~32 km and ~1.2 km respectively. The ejecta of the crater spreads radially outward up to a distance of ~60 km, except in the south of the crater, where the troughs have formed and hinders the ejecta information (Figure 5.11a). Crater C7 shows clear association with parallel and sub-parallel graben which are trending in W-E and NW-SE directions (Figure 5.11a). Notable evidence are witnessed for the emplacement of the crater over the parallel graben based on their discontinuity. This recommends that the graben are superposed by the crater. Another associated feature with this crater is the elongated troughs that are present in the south of the crater (Figure 5.11b). The heads of the troughs are sited ~5 km away from the southern rim of crater C7 and the tails of the troughs are connected with the walls of VM (Figure 5.11a). These troughs have multiple branches with varying extent and depth (Figure 5.11b). The trough's heads located close to the rim are rounded and visually appear smooth. Within the ~10 km limit from the crater's rim, only three troughs were observed whose heads are close to the southern crater wall (Figure 5.11b). However, as no discernible ejecta is observed within the trough heads, it is difficult to decide their superposition relationship with the crater solely based on the ejecta emplacement. As an alternative, it is witnessed that around the crater rim there are raised hummocky surface due to rim formation (Figure 5.11b). This raised hummocky surface is observed within ~0.5 crater radii in all directions except in the southern side. In addition, though few troughs are very close (~5 km) to the crater's rim, they are still intact and are not affected due to the crater formation. If the troughs are pre-existing than the formation of C7 crater, then they should be affected due to the formation of a ~32 km diameter crater C7 atleast upto ~5 km distance if not more. Overall, these observations renders that the troughs are likely superposed over the ejecta of crater C7. Within the very close vicinity of the crater C7, the extent of the troughs ranges from few kilometers to tens of kilometers (~2 to ~11 km) and depth can be up to ~1 km. The depth of troughs are found to increase away from their heads and they are comparatively deeper than the depth of C7 crater (Figure 5.11b).

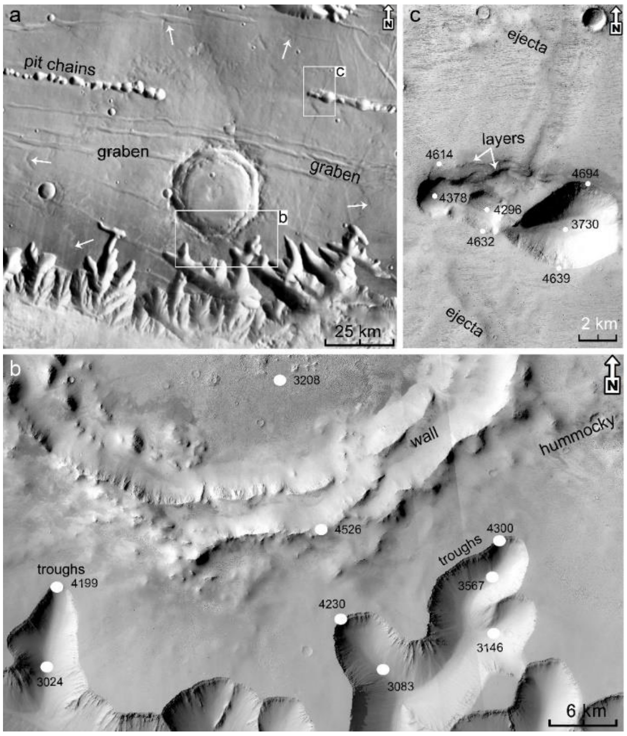

Figure 5.11: a) THEMIS daytime infrared controlled mosaic image of the crater C7 with the distribution of graben, pits, pit chains (NW and NE) and troughs (South) in Tithonium region, b) The southern part of the crater dominated by troughs, whose width and depth are varying widely. The closest head trough from the southern wall is ~5 km. Outside the crater rim, hummocky and elevated terrain due to the impact is observed over the SE part, whereas such hummocky uplift is absent over the southern side where troughs are emplaced (CTX id: J03_045789_1724_XN_07S081W 2016-5-3, J05_046923_1731_XI_06S081W 2016-7-30), c) Pits in the NE side of crater ejecta, likely formed with underlying graben. These pits also exposes layers or multiple collapses (CTX id: P16_007364_1733_XN_06S081W 2008-2-21). (White dot: MOLA elevation values in meter; White arrow: C7 ejecta boundary).

It is also observed that most of the troughs are formed and aligned along the graben as shown in figure 5.11a. On observing the pits, the NW side of the crater ejecta holds pit chains that are possibly aligned to the pits chain linked to the crater C6 (Figure 5.8). ~30 km long pits chain is observed within the ejecta blanket of crater C7 (Figure 5.11a). The other pits chain is observed in the NE of the crater C7, having an overall spatial extent of ~60 km. However, only ~35% of this pits chain is observed to fall within the ejecta of the C7 crater. The pits chain is emplaced within a graben, which is surrounded by other multiple cross-cutting graben (Figures 5.8, 5.11a). Parallel to this pit chain, scarps and layers were observed within the troughs (Figure 5.11c). Hauber et al. (2009) also reported scarps parallel to a long linear vent (fissure) and deduced that such scarps indicate a multi-stage collapse. On interpreting the superposition relationship of the pits with the C7 crater, only two likelihoods exist: 1) the ejecta might have been deposited and emplaced over the underlying structures or 2) pits were formed over the ejecta. However, the dust cover obstructs the stratigraphic evaluation of the pits to the north of crater C7, but the troughs around the southern side render evidence for their post crater formation.

<u>Crater C10:</u> Crater C10 (Figure 5.8) is centered at -4.19°, -84.54° and having a diameter of ~40 km. The southern rim and floor of the crater are completely obliterated as shown in figure 5.12a. This feature is identified as an impact crater on the basis of: 1) the discernible and radially-out spread ejecta on the northern part, 2) raised rim in the northern side and 3) the geologic map of Mars by Tanaka et al. (2014). This crater is surrounded by graben, pits and troughs (Figure 5.12a). Troughs are observed to cut through the entire eastern crater wall (Figure 5.12b, c), and completely obliterated it.

These troughs have variable extent and depth. The longest trough is ~35 km in length, with a maximum width of ~5 km and has an average depth of ~3 km (Figure 5.12b). Figure 5.12b also displays elevation points over the trough’s floor and adjacent VM’s floor, and the difference of ~700 m has been observed between the two. In addition to the eastern rim, the troughs have also dissected the western part of the crater rim (Figure 5.12d), however, the extent is relatively less as compared to the troughs that dissected in the eastern rim. Though most of the troughs have been observed to be oriented towards the east, still a few are observed to be oriented towards the southwest (Figure 5.12b, d). In the northern side, there are few troughs that are observed to dissect within the crater wall and floor (Figure 5.12c). These troughs are observed to partially degrade the rim of the crater and suggest their cross-cut relationship with the C10 crater. On observing the graben in the vicinity of this crater, it is found that the northern region hosts several graben (Figure 5.12a). The crater’s ejecta is observed to be emplaced over the graben (Figure 5.12a). The graben over this region have been mapped by earlier studies [43, 211], and they also reported discontinuous graben over this region because of the crater formation.

N-S trending topographic profile passing through the C10 crater and the VM’s wall (Figure 5.12e) clearly indicates ~3 km elevation difference between the hummocky crater’s floor and the adjoining VM’s floor. Figure 5.12e displays another elevation profile trending W-E direction and found that the floor of the crater and troughs have a significant elevation difference. The crater depth measured using the

MOLA DEM is in the range of ~2 to 3 km due to the hummocky floor. While, the empirically derived depth for a similar diameter crater is ~2.4 km [44].

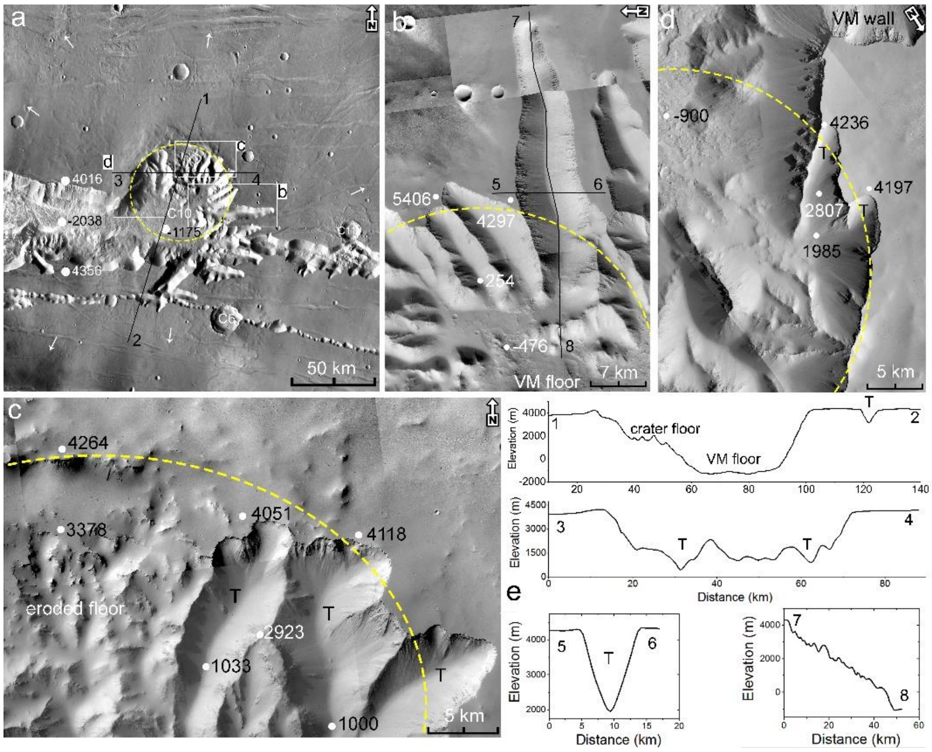

Figure 5.12: a) THEMIS daytime infrared image of degraded crater C10 with presence of graben (to its north), pits, pit chains (to its south) and troughs (over east, west and south side), b) troughs dissected the eastern rim of crater, whose spatial extent and depth are varying diversely (CTX id: P08_004160_1736_XN_06S084W, P18_007931_1737_XN_06S083W, P07_003949_1738_XN_06S083W, G06_020695_1777_XN_02S084W), c) preserved crater rim and terraced wall over the northern side, however, towards the floor side, the surface is eroded and hummocky. The NE side is dissected by a trough, which extends towards the floor (CTX id: F03_036835_1757_XN_04S084W, F19_043178_1748_XI_05S083W), d) troughs dissected the crater rim and the orientation is different from other troughs present within the crater. Over the western side a part of the crater wall shares the boundary with the Valles Marineris wall region (CTX id: F18_042888_1751_XI_04S084W), e) elevation profiles taken along the N-S direction where the crater floor and VM floor show ~3 km elevation difference. The elevation profile along the W-E direction shows a hummocky crater floor with multiple troughs. Elevation cross profile along a trough on the eastern side (profile location in figure 5.12b) shows trough depth is ~2 km, whereas the elevation along the trough varies up to ~4 km representing slope variation. (White dot- MOLA elevation values in meter; White arrow- C10 ejecta boundary; dashed yellow line- the tentative boundary of crater C10; T- trough).

The depth of Tithonium chasma in the immediate west of the crater C10 were also determined (Figure 5.12a), which is ~6 km and almost equal to the depth of chasma in the southern side of the crater C10 (Figure 5.12e). The significant correlation between the depth of chasma situated in the southern side of the C10 crater and the adjoining chasma in the west suggests that it could be a continuous feature. From this, it is inferred that the chasma likely existed before the formation of crater C10. Topographic profiles along and across a trough (Figure 5.12b, e) is also extracted, which indicate that the trough is more than 2 km deep and the depth is increasing away from the head of the trough.

<u>Perrotin crater:</u> From crater C10, it is inferred that the entire eastern part of the rim is dissected by the troughs, which is one of the strong evidence for their cross-cut superposed activity. Some of the graben that are observed in north of C10 crater (Figure 5.8) show extension towards the western side of Perrotin crater. Perrotin crater (centered at -2.81°, -77.95°) is ~80 km in diameter with a depth of ~1 km and has a central pit over its floor (Figure 5.13a). The surface over which the two craters (C10 and Perrotin craters) are located have an elevation difference of ~600 m. Perrotin crater is mainly surrounded by graben (Figure 5.13a). Some of the graben are observed over the crater’s floor and the others are observed outside the crater mainly towards the western and eastern sides (Figure 5.13a). These graben have dissected the crater floor as well as the rim from eastern and western sides (Figure 5.13b, c). The dissection of crater’s floor and rim by graben is a direct evidence for their superposed emplacement. Here, it is difficult to interpret whether the full length of the graben formed at the same

time or if they are reactivated and interlinked to one other in the later stages. However, the observation is limited within the crater floor and rim, which are clearly cross-cut by graben (Figure 5.13b, c).

Graben within the floor is ~ 82 km long (partially covered the crater along W-E), ~1 to 2.5 km wide and ~50 m deep. In the east of the crater, graben traversed ~1.5 km of elevation difference (Figure 5.13b), whereas in the west of crater, the surface elevation declines to ~1 km (Figure 5.13c). Perrotin crater ejecta is not distinguishable as the dust cover is significant over this part. Thus, the superposed graben over the crater floor and wall are used for further analysis (Figure 5.13b, c). As parallel and sub-parallel graben spread out for hundreds of kilometers in the TR [43], thus, graben observed around the Perrotin crater are considerably advantageous in untangling the widespread formation scenario over this region.

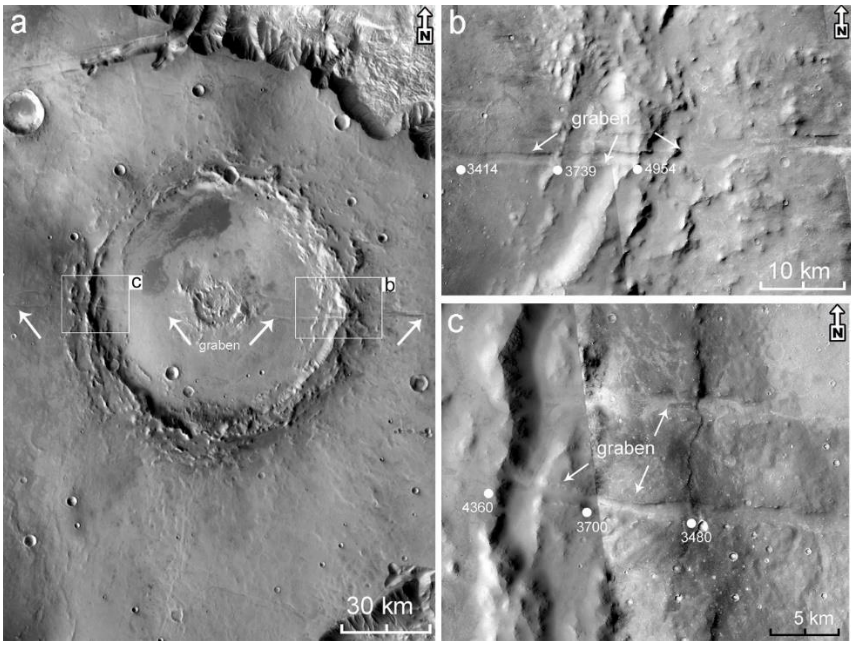

Figure 5.13: a) THEMIS daytime infrared image of Perrotin crater in the Tithonium region. The presence of graben over its floor and rim is indicated by white arrows, b)

graben crosscutting the eastern rim part and extended over the crater floor (CTX id: D22_035793_1751_XN_04S076W, P15_007087_1779_XN_02S077W), c) graben crosscutting the western rim at two places and extended over the crater floor (CTX id: B03_010726_1785_XI_01S078W, G05_020141_1769_XN_03S078W). (White dot- MOLA elevation values in meter).

5.7.2 Craters in Ophir region

The Ophir region of VM is recognised for interior layered deposits, landslides, and faults [191, 200, 224]. In OR, two craters (C21 and Pital) are analyzed in detail. Crater C21: This crater is centered at -4.60°, -69.68° (Figure 5.8), whose diameter and depth are ~27 km and ~1.5 km respectively. The ejecta of this crater spread out ~40 km radially from the crater rim in all directions, except in the western side (Figure 5.14a). The crater is associated with graben, pits and pit chains (Figure 5.14a). Pits are present both within and outside the crater (Figure 5.14b). Over the western wall and floor of crater C21, a circular depression of diameter ~15 km was observed (Figure 5.14a). The circular depression is having raised rim, and therefore it is interpreted as a superposed crater. Many other depressions on the crater floor and the eastern rim are observed to be pits (Figure 5.14b) as they lack raised rim. The pits are observed to locate at different floor elevations such as ~1 km and ~2.2 km (Figure 5.14b). Additionally, pits are observed to crosscut through the northern and western side rim of the crater (Figure 5.14b, c). The pits located on the floor have covered more than ~15% of the floor's area and the pits located on the rim carved ~10% of the crater's rim (Figure 5.14a). Few discontinuous pits are also observed in the north, north-west and north-east side of the crater's rim (Figure 5.14a). The southwest crater's wall is located ~3 km away from the wall of VM (Figure 5.14c). This raises the question of whether any extension of VM's wall occurred towards the crater. To untangle this observation, the pits on the western wall that are located in between the crater and VM's wall are analysed further (Figure 5.14c). The presence of these pits render evidence for their superposition over the crater's rim and their association with VM's wall indicates post modification after the formation of crater C21.

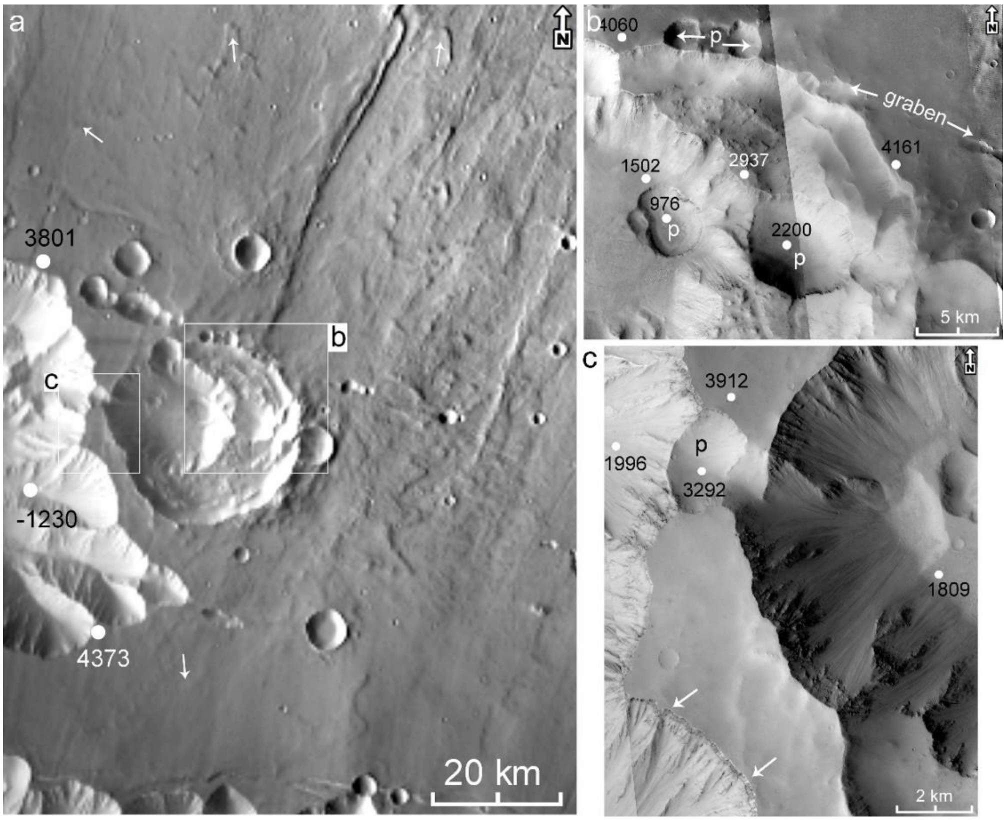

Figure 5.14: Crater C21 in the Ophir region a) THEMIS day time infrared image of pits and graben, which formed adjacent to VM wall, b) northern part of crater superposed by multiple pits, formed at a different elevations and with different depth and size. Over the northern rim, few pits emplaced over the region. This is evidence for their superposed presence after C21 formation (CTX id: P09_004410_1733_XI_06S069W), c) Pit likely formed in between the VM wall and crater wall. The C21 crater rim uplifted hummocky surface adjacent over the SW side is likely obliterated by the VM wall (CTX id: F10_039736_1740_XI_06S069W). (White dot- MOLA elevation values in meter; White arrow- C21 ejecta boundary; black arrow- graben/pit or VM wall).

The crater's rim and floor superposed by east-west trending set of pits. On observing the pits outside the crater's rim, it was found that they have likely association with the graben (Figure 5.14b), whereas the pits located over the crater's floor are observed without any association to graben. In the southern side of C21 crater, an elongated catena is present but with some discontinuity with the Ophir Chasma (Figure 5.14a). However, its relationship with the crater is hindered due to dust cover over this region. Along with pits, there is a long, narrow and shallow graben that is trending parallel and perpendicular to the VM (Figure 5.8). These narrow and shallow graben are located very near to the crater wall (Figure 5.14b) and still they are unaffected by the crater formation. In addition, they lacks any clear emplacement of the crater's ejecta over them. These observations render evidence for superposed graben formation over the crater. Overall, it is observed that both pits and graben are superposed over the crater C21 at multiple places (Figure 5.14).

<u>Pital crater:</u> Pital crater is centered at -9.22°, -62.30° that is having a diameter of ~39 km and has a depth of ~1.8 km (Figures 5.7c, 5.8). The ejecta of this crater spreads out radially to more than one crater radii from the crater's rim (Figure 5.15a). This crater hosts pit chains, catenae, a lobe-shaped deposit [225], and graben over the crater's floor, rim and in the periphery of ejecta blanket (Figures 5.15a-c,5.16a-d). The striking observation in the vicinity of Pital crater is the presence of W-E oriented elongated coalesced pit or catena like depression [225], which crosscuts through the NE rim (Figure 5.15b). This coalesced-pit like structure observed to be narrower and shallower from the western side but has become broader and deeper towards the east side (Figure

5.15b). This opening is referred as catena [225], and evidence clearly substantiates the cross-cut nature of catena through the crater's rim and floor. The catena is found to be ~50 km long (W-E side), and ~14 km wide (N-S side) and ~2 km deep (Figure 5.15b). This catena is comparatively deeper than the plausible catena in the west of the Pital crater (Figure 5.15d) and the Pital crater as well (Figure 5.15e). The regional topography of the catena is declining towards the eastern side (Figure 5.6). The catena is is observed in alignment with the adjacent Candor Chasma [225].

Several pits and pit chains of variable sizes are observed within the periphery of Pital crater. In the immediate south of catena, a series of pits chains are formed within and outside of the crater (Figure 5.15c). Pits within this pits chain (Figure 5.15c) are continuous, and their maximum extent and depth are ~5 km and ~500 m respectively. These pits chains share the wall with the W-E aligned catena. To farther south of this pits chain, one more pits chain, comparatively smaller in size and width, is observed that covers from the crater's floor to the wall flank of the crater (Figure 5.16c). The overall extent of this pits chain is ~15 km (Figure 5.16b). Spatially, these two pit chains are ~2 km apart but both host pits of different sizes and depth. This suggests that within such close vicinity the extent of pit formation varied (Figures 5.15c, 5.16c). Figure 5.16d displays several pits that are located within the floor of catena. These pits are located ~2 km below than the adjoining surface (Figures 5.15b, 5.16d). The catena and the pits that superposed and cross-cut through the crater's floor and rim are aligned in parallel to the VM, which is tending towards the W-E side.

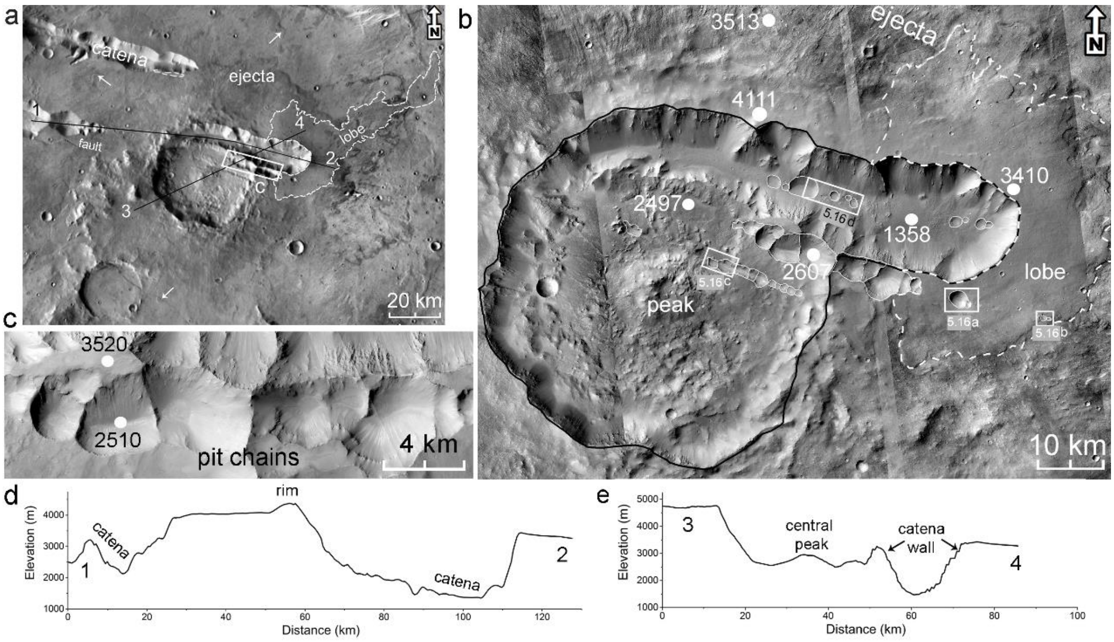

Figure 5.15: Pital crater in the Ophir region, a) THEMIS day time infrared image of Pital crater with presence of pits, catena, lobe deposits on NE side and graben. b) CTX mosaic of Pital crater, with distinguishable lobe deposits associated with the catena, which dissected the NE crater rim. The catena to its eastern side is broadened and deeper when compared to the western side. Multiple pits were observed within the catena. The lobe associated to the catena is only present towards the NE side where the topography is also inclined in this direction (Figure 5.8) (CTX id: J18_051867_1724_XI_07S062W, J04_046408_1711_XN_08S062W, J18_051946_1715_XN_08S061W, B19_016923_1696_XN_10S061W, G02_018980_1713_XN_08S061W), c) A portion pit chain interpreted to superpose over the floor and rim of the crater (CTX id: F22_044298_1719_XN_08S062W). The size and depth of the pit chains varies throughout its length, d) elevation profile along the W-E direction, note that the catena on western sided is relatively less deep than the catena crosscut the Pital NE rim, e) elevation profile along the rim-central peak and catena suggest that the catena is relatively deeper than the Pital crater.

In close association and to NE of this catena, a lobe-shaped deposit has formed (Figure 5.15a), which is emplaced over the Pital crater ejecta and mantled more than 10% of the crater ejecta. This lobe-shaped deposit is extended up to ~70 km from the catena NE end, and the average thickness of the lobe-deposit is reported as ~50 m [225].

The lobe suggested to form either during the formation of catena or before the formation of the catena [225]. Pits in the Tharsis region of Mars are likely interpreted to associate with the lava flows in the volcanic plains [223]. If the radial pattern of lava flows is present in association to a pit then that could indicate effusive volcanic conduits [226]. The flow direction of the lobe is in agreement with the regional topography, which is declining towards SW-NE (Figures 5.6, 5.8). In this study, this lobe deposit was used to interpret the relative chronology of the pit forming activities. Remarkably, few pits are clearly visible over this lobe deposit (Figures 5.15b, 5.16a,b). The stratigraphic emplacement between the crater's ejecta, the lobe and superposed pits is used to interpret the series of events that happened in this region. Figure 5.16a demonstrates a pit located over the lobe that is ~3 km long, ~2 km wide and ~200 m deep. This pit suggests its youngest formation when compared to Pital crater's ejecta and catena associated lobe deposits. The two-more smaller continuous pits that are superposed over the lobe (Figure 5.16b). Overall, the evidences provided are the clear indicators of the superposition of pits over the lobe deposit.

Towards the west and NW side of the Pital crater, two-more broad and elongated pits or catenae are located [225] that are partially bound within the boundary of Pital crater's ejecta (Figure 5.15a). The upper catena is associated with small lobe-like deposits that are emplaced over the Pital crater's ejecta (Figure 5.15a). This suggest plausible superposed emplacement of the upper catena over the ejecta. The lower catena contains pits of various size and this catena is potentially emplaced within a graben or fault (Figure 5.15a). Overall, it was observed that the Pital crater and its ejecta host superposed features like catenae and pits, which predominantly altered the eastern part of the crater.

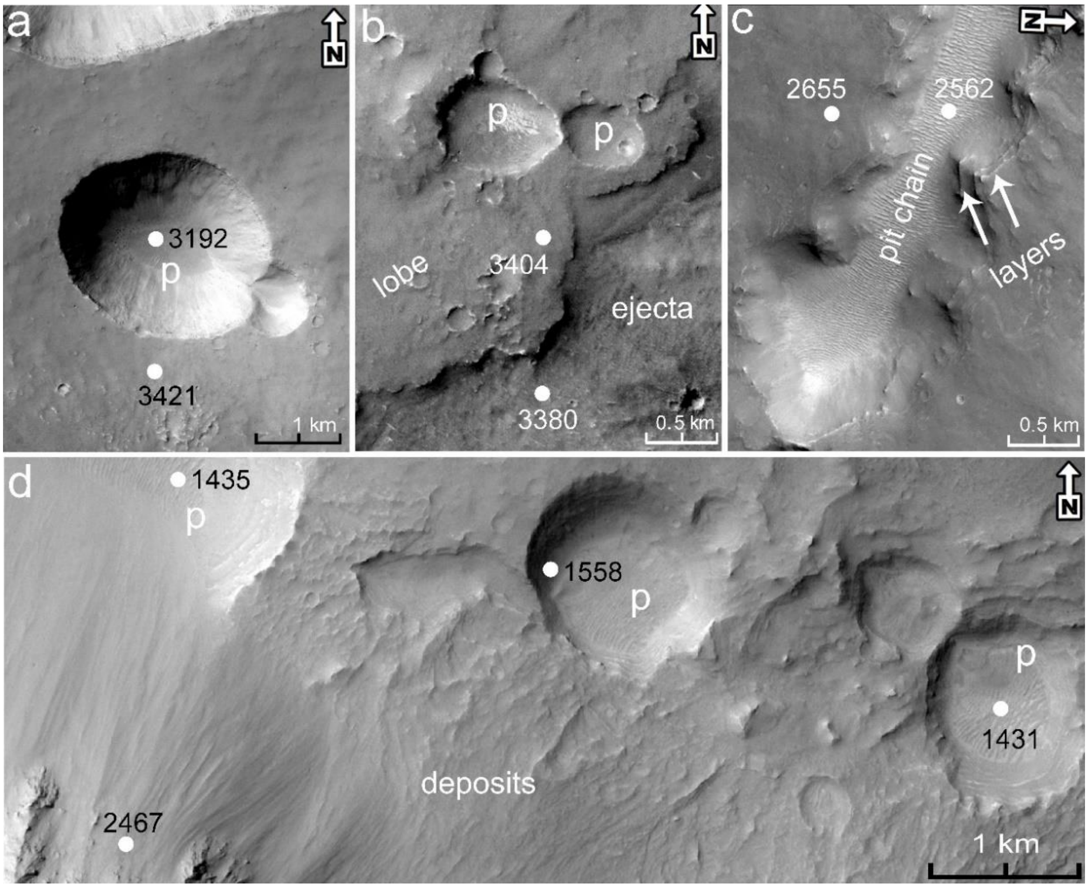

Figure 5.16: Pits associated with Pital crater, a) A ~2 km wide pit emplaced over the lobe deposits associated with the catena. This pit and lobe are emplaced above the Pital crater ejecta. This suggests that stratigraphically the pit is the youngest feature in this region (CTX id: J18_051946_1715_XN_08S061W), b) continuous pit observed at the termini of the lobe deposit, note that the Pital ejecta is underlying below the pit (CTX id: B19_016923_1696_XN_10S061W), c) pit chains with collapsed nature formed within the crater floor and with possible exposure of layers over their walls. This pit chain emplaced over the wall continued till the flank of the crater rim (Figure 5.15b) is evidence for their superposed activity after crater formation (CTX id: J07_047542_1708_XN_09S062W), d) pits formed within the catena and they are further mantled by wall origin deposits. The pits within catena are found to be of different depth and size. These pits have formed ~2 km below than those formed over the lobe/ejecta deposits (5.16a). The fan-shaped deposits from the southern wall of catena likely have an abrupt end at the pit. Note the visible distinguishable layers within the pit over this region (CTX id: J18_051946_1715_XN_08S061W).

5.7.3 Craters in Coprates region

The craters selected in the CR are sited in the south of the VM (Figure 5.6). In this region, two craters are associated with pits, troughs, and graben.

<u>Saravan crater:</u> This crater is centered at -16.93°, -54.01°, which is ~46 km in diameter, ~2 km deep and exhibits no discernible ejecta blanket (Figures 5.8, 5.17). A ~50 km long elongated trough was observed in the southern floor that carved through the crater's floor from west to east (Figure 5.17).

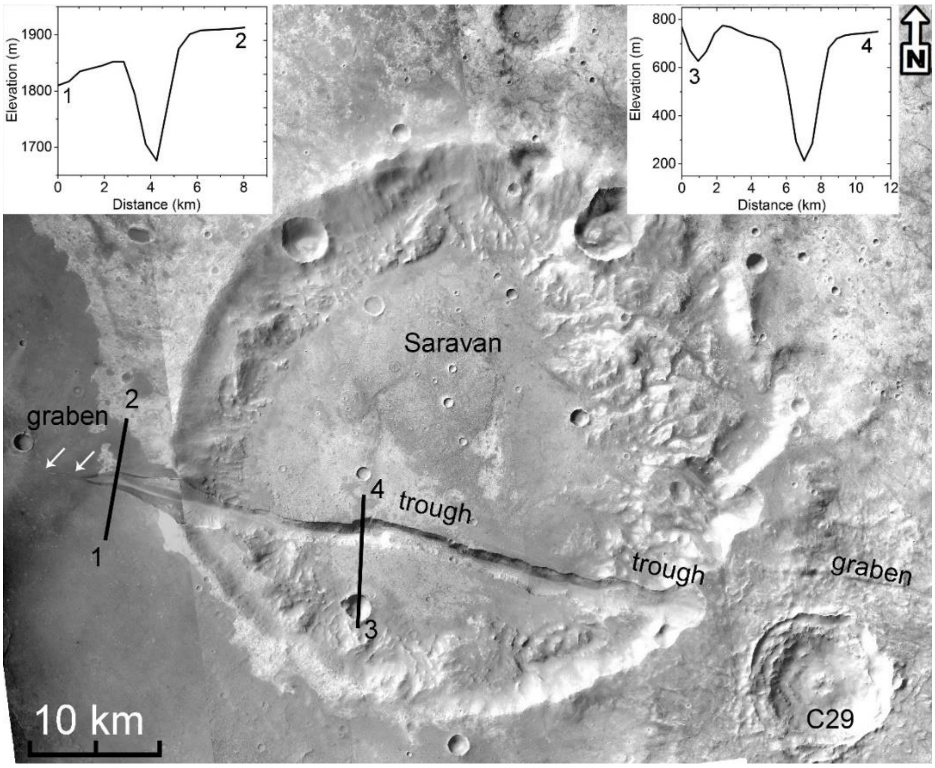

Figure 5.17: CTX mosaic of Saravan crater located in the Coprates region with a graben associated trough in the floor. The crater floor hosts a long trough, which dissects the rim and suggests superposed activity after crater formation. Inset images show the elevation profiles across the trough and indicates their variation in width and depth. The trough is relatively deeper than a small crater located on the southern side of Saravan crater. (CTX id: D04_028751_1641_XN_15S054W, P11_005438_1649_XN_15S053W, B16_016026_1643_XN_15S054W, B19_016870_1633_XN_16S054W).

The maximum width and depth of the trough are determined as ~2.4 km and ~0.5 km respectively. The trough eastern end, which has carved through the eastern side rim, is comparatively more circular and deep than the western end. It is more linear and shallow in the west (Figure 5.17). The trough, which carved through the eastern side rim of the Saravan crater, is mantled by the ejecta of crater C29 (Figure 5.17). The superposed trough located within the Saravan crater clearly indicates evidence for post trough formation activity in the southern side of the VM.

<u>Crater C34:</u> This crater is centered at -14.99°, -62.32° and having ~6 km in diameter and ~1.3 km deep (Figures 5.8, 5.18). As the northern part of the crater is entirely degraded, based on the following it is interpreted as an impact crater: 1) the ejecta emplacement in the southern side of the crater and 2) the raised southern rim (Figure 5.18). However, it is not clear that the crater formed over the pit or vice-versa. To deduce the likely emplacement scenario, a pit with lobe-shaped deposit emplaced in the western side of the C34 crater was analysed further (Figure 5.18). The spread of the lobe-shaped deposit is estimated up to ~4.5 km distance from the pit's rim (Figure 5.18). The lobe is further examined to decipher its association with the crater C34. It is observed that the lobe is possibly superposed over some portion of the ejecta of crater C34 (Figure 5.17). Similar deposits are reported adjacent to the catenae that are located in the Ophir region [225], and they are observed to superpose over the ejecta of Pital crater (Figure 5.15a).

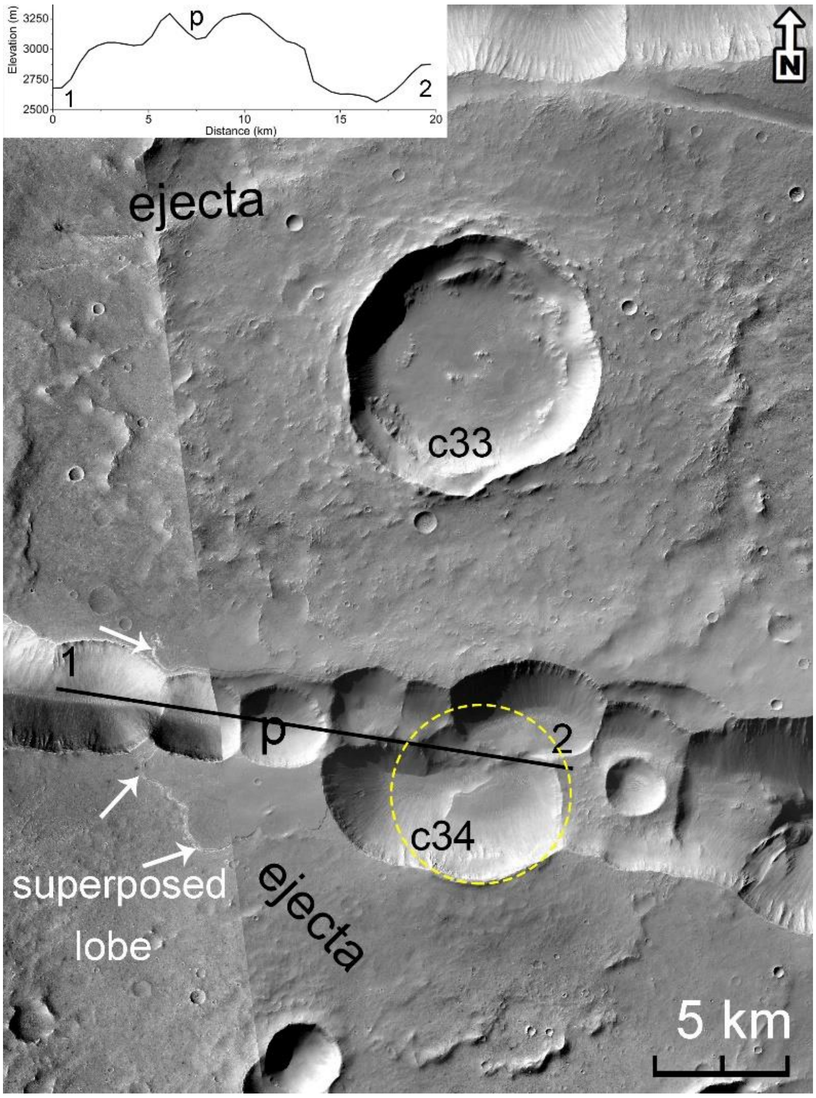

Figure 5.18: CTX mosaic of two craters over the Coprates region, in which one of the craters is degraded (C34). The pit chains over this region are having a wide variation in depth and width, as inferred from the elevation profile along the pit chain. The yellow dashed line indicates the possible crater C34 rim. Towards the western side of C34, the lobe-like deposit emplaced over its ejecta and has closely associated with one of the pits. The lobe deposits superposed the C34 ejecta blanket and suggests their post activity. However, note that this lobe-shaped deposit is only observed adjacent to only one pit. (P-pits; White arrow- superposed location of lobe deposits over the ejecta; CTX id: B20_017556_1659_XN_14S062W, J05_046619_1666_XN_13S062W).

Therefore, in the CR if the lobe is associated with the pits, then these pits likely represent a superposition association with the crater. Topographic profile extracted along the pits chain in the W-E direction demonstrates variation in pits' depth (Figure 5.18). Overall, the crosscut trough and the superposed pits over the discussed craters (Saravan and C34 crates respectively) are used to decipher their spatial and chronological variations in the VM region.

5.8 Discussion

In this study, the interpretation of the chronological relationship is limited for only those craters, which has the following: 1) crater formed before graben, pits/pit chains, catena, and trough and 2) that are having significant count area to get an absolute model crater age. Based on this limit, the estimated ages of seven craters are shown in figure 5.19.

<u>Tithonium region:</u> The TR and the plateaus its surrounding have been marked as early Hesperian highland units [4]**.** In this region, pits superposed the crater C6 (Figure 5.9) and troughs cut through the rim of the crater C10 (Figure 5.12), however, the period of these activities in the TR cannot be well constrained by stratigraphy alone. Therefore, the absolute model ages were determined for four example craters that are superposed and cross-cut by graben, pits, and troughs. The estimated ages (Figure 5.19a, Table 5.1) for the C6 (Figure 5.9), C7 (Figure 5.13), C10 (Figure 5.12), and Perrotin crater (Figure 5.13) are the upper age limits for the formation of features associated to them (Figure 5.20). For crater C6, where pit chains superposed over the crater rim (Figure 5.9), the obtained absolute model age as ~3.6 Ga or Early Hesperian epoch (Figure 5.19a, Table

5.1). This model age recommends that the pit chains have developed post to Early Hesperian epoch (Figure 5.20).

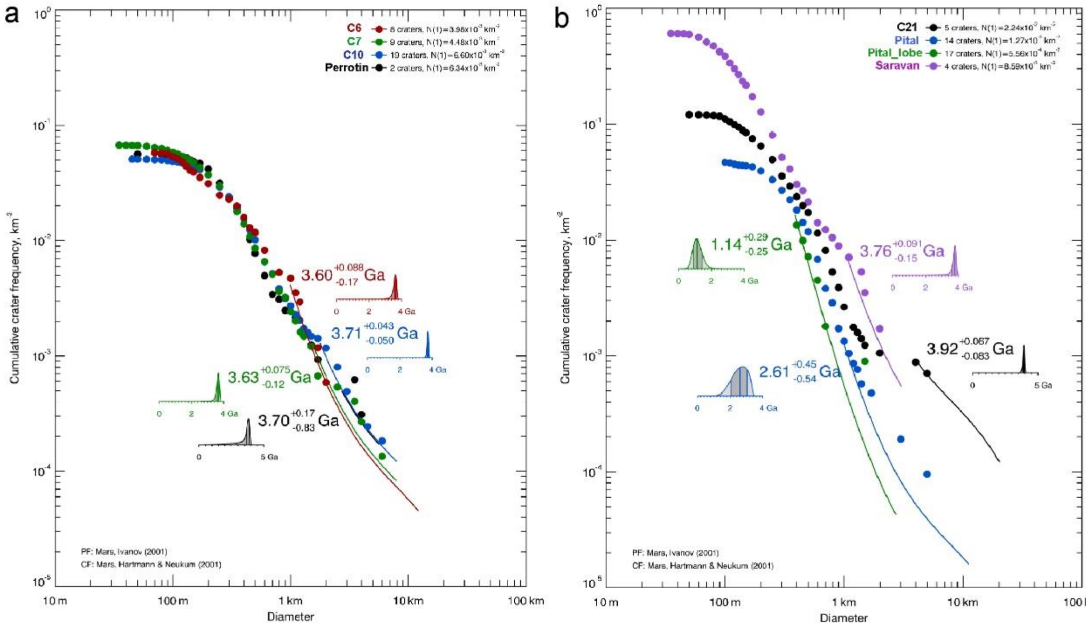

Figure 5.19: Crater size-frequency distribution for craters superposed by pits, graben, catena. The model ages obtained for seven craters and one lobe deposits are given for craters from a) Tithonium region and b) Ophir and Coprates region.

For crater C10, where the rim is crosscut at multiple places by the troughs (Figure 5.12b), an age of ~3.71 Ga is estimated (Figure 5.19). This age clearly indicates that the troughs are preferably formed after the Early Hesperian epoch (Figure 5.20, Table 5.1). The other crater in the TR is Perrotin but its ejecta is indistinguishable from CTX or THEMIS datasets (Figure 5.13), which led to estimate the absolute model age using the crater's floor. This crater is known for the superposed and cross-cut graben over the wall and floor region (Figure 5.13b, c), and stratigraphically indicates their post activity. The crater retention age of the Perrotin crater' floor is estimated as ~3.70 Ga

(Early Hesperian) (Figure 5.19a). Additionally, superposed craters within one crater diameter from the Perrotin rim were counted. Here, buffered crater count is used to validate craters' age (2 out of 48 craters) of those craters where the ejecta is not discernible for the counting of superposed craters. The ages are estimated by considering one diameter circle form the craters' rim and counting all the craters located within the circle. The estimated model age of the Perrotin crater using one-diameter circle is almost equal to model age estimated using the floor of the crater that tends to the Early Hesperian epoch. The notable point from the analysis of two craters (Perrotin and crater C10) is that they are likely associated with the same graben. Combined analysis of C10 and Perrotin craters helps to infer the following: 1) the ejecta of crater C10 is superposed over the graben that is located in north of the crater (Figure 5.12a) and suggests that graben are older than ~3.71 Ga, and 2) these graben extend up to Perrotin crater with a discontinuity and cross-cut the Perrotin crater' floor and rim, and suggests that the graben are younger than ~3.70 Ga (Figure 5.19a, Table 5.1). Thus, the graben in the TR are likely developed over the time, which is clearly evident from observations and chronological analysis in this study. However, it is not interpreted that the formation period of the graben is ~0.01 Ga, rather as an alternative it is interpreted that they are regionally varying over time, which is consistent with morphological and other earlier interpretations [43]. In the TR, the superposition, cross-cutting and chronological relationships between the features and the craters suggest that the formation of pits, troughs and graben varied widely and likely formed on or post to Early Hesperian epoch (Figure 5.20).

Ophir region: Tanaka et al. (2014) mapped the OR as the Early Hesperian highland unit. Two craters (C21 and Pital) in the OR renders clear evidence for: 1) superposed pits (Figures 5.14b, 5.15c), 2) catena cutting through the Pital rim (Figure 5.15b) and 3) coalesced pits in association with VM walls (Figures 5.14c, 5.15a). For crater C21, where pits superposed the crater's floor and wall (Figure 5.14b), the crater count statistics over the ejecta provide an absolute model age of ~3.92 Ga that indicates Mid to Late Noachian epoch on Mars (Table 5.1, Figure 5.19b). Thus, the pits located on the crater's floor and wall should have formed on or post to the Mid-Noachian epoch (Figure 5.20). Also, the western pits (Figure 5.14b) that are directly connected with the VM wall indicate that they also formed after the formation of crater C21 (Figure 5.20). Other crater in the OR is Pital and crater count statistics over the ejecta of Pital crater provide an absolute model age ~2.61 Ga, which denotes the Early Amazonian epoch on Mars (Figure 5.19b, Table 5.1). Pital crater is the best example for Early to Mid-Amazonian activities in the VM region, which is in favour of Carr and Head (2010). The determined absolute model age for the lobe-shaped deposit emplaced over the Pital ejecta (Figure 5.19b) tends to ~1.14 Ga (Middle Amazonian) (Figure 5.19b). Marra et al. (2015) also mapped this lobe and determined the age that is similar to estimated age in this study. The origin of such lobes was studied previously and likely interpreted them as fluvial lobes, however, the study didn't deny the role of lava in the formation of lobe and argued that the elliptical features (pits) could be related to volcanic activity [225]. The lobe shown in figure 5.15b cannot be younger than the associated catena/pits and may have formed during the formation of pits [225]. In addition, pits that superposed over the Pital' lobe (Figure 5.16a, b) led to the interpretation that they have formed after ~1.14 Ga and host evidence of one of the youngest pit related activities in the VM region (Figure 5.20). Thus, the Ophir region of VM hosts the youngest pits that formed during Mid to Late Amazonian epoch.

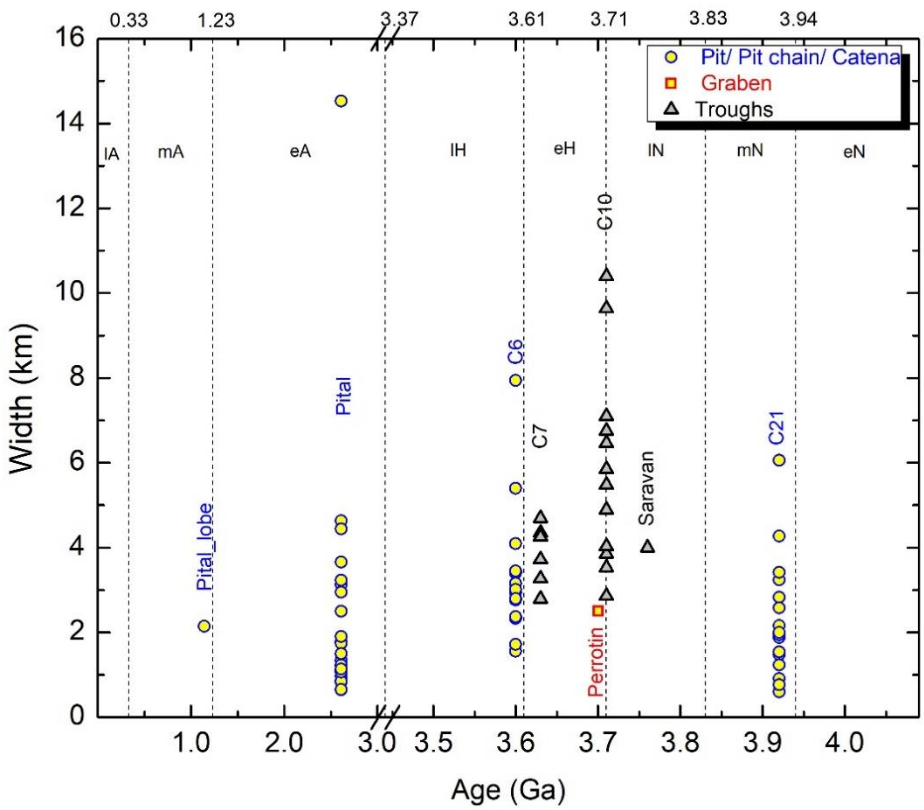

Figure 5.20: Model absolute ages for seven craters and Pital lobe versus the pits, graben, trough, and catena width. Perrotin crater provides an evidence for graben formation on or post late Noachian epoch. Pit formation over the VM widely varied spatially and chronologically, with the pit formed over crater C21 on or post to middle Noachian, whereas the youngest pit is ~2 km in size and formed during middle Amazonian. Pital crater catena possibly formed during the early Amazonian and is nearly one-tenth of Candor Chasma width. Troughs are observed within the Saravan crater and close to craters C10 and C7, which widely observed on or post to the late Noachian epoch.

Coprates region: The Coprates region is mapped as Early Hesperian highland unit [4]. In this region, mainly the chronological relationship for two craters (Saravan and C34 crater) has been discussed (Figures 5.17, 5.18). The ejecta of Saravan crater is not discernible, therefore crater count statistics was carried out on the crater floor. The estimated age of Saravan crater tends to ~3.76 Ga or Late Noachian epoch (Figure 5.19b, Table 5.1). Hence, the elongated trough that cut through the crater's floor and rim (Figure 5.17) indicates that it probably formed on or later than the Late Noachian epoch.

For crater C34 (Figure 5.8) the crater count samples a small area as ejecta in the south of the crater is only available for crater counting. This leads to an age ~414 Ma (Late Amazonian) for the formation of crater C43 (Table 5.1). If the lobe, which likely superposed over the ejecta of crater C34, is associated with the pits (Figure 5.18), then pit forming activity has occurred during the Late Amazonian epoch in this region.

Figure 5.21 renders the regional context of seven craters and their chronological variation around the VM region. This reveals that the pits and trough activities are varying chronologically over the large spatial extent of the VM. Figure 5.22 renders the ages determined for all the 48 craters; however, these ages are provided for completeness. Three more craters (Oudemans, Arima, C30 craters) also demonstrate association with pits, however, the superposition relationship between the craters and pits is unclear (Figures 5.23-5.25).

Thus, no conclusion has made from these craters. Note here that for interpretation mainly those pits and troughs are considered which are superposed over the crater rim (C6 (Figure 5.9), Pital (Figure 5.15), and C10 (Figure 5.12)). If the pits/troughs are superposed over the crater, then they are post-event relative to formation of the crater. Also, their reactivation is not contested here as superposed pits/troughs can be modified over time. It is difficult to address such ambiguities fully, therefore, in this study the current state of pits/troughs have been considered.

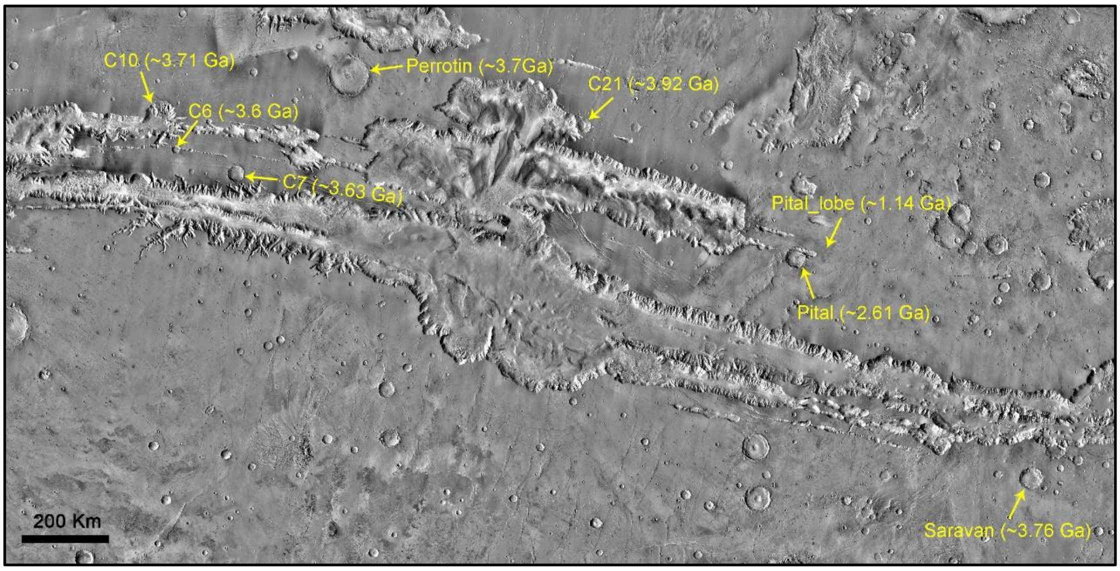

Figure 5.21: The chronological age for seven craters and one lobe deposits around the VM region. The pits, graben and trough activities varied chronologically over the spatial extent of VM region.

5.9 Conclusions

A comprehensive survey of craters associated with graben, pits, and troughs around the VM is carried out to understand the chronological and spatial modification of these features. Chronologically, pits and pit chains are superposed over several craters, among them the oldest pit to be formed on or post to ~3.92 Ga (Middle

Noachian) and the youngest pit to be formed on or post to ~1.14 Ga (Middle Amazonian) (Figure 5.20). Spatially, the formation of pits occurred over a wide extent that spans to different regions of the VM and pits of variable sizes (length, width, and depth) are witnessed within the craters and among the regions.

<u>Tithonium region:</u> From the Tithonium region, the Perrotin crater offers evidence for post-Noachian graben formation that are evident on the crater's floor and cut through the crater's rim. Analysis from this study are in agreement with Sharp (1973). The crater C10 offers evidence for Hesperian aged multiple troughs dissecting through the crater's rim and also suggest a clear association with the VM wall. Moreover, pits associated with the crater C6 provide evidence for post Hesperian aged pit activities in this region of the VM.

<u>Ophir region:</u> In the Ophir region, Pital crater and the surrounding region have preserved stratigraphic events that are as follows: 1) formation of ~2.61 Ga old Pital crater 2) catena formation (~14 km wide on or after ~2.61 Ga), 3) this is followed by lobe deposition (~1.14 Ga) and 4) formation of pit (~2 km wide) on the lobe that possibly occurred during Mid to Late Amazonian. Thus, Pital crater is one typical location on Mars to infer the spatially diverse pit activities around a crater that are formed at different epochs. Pital crater also revealed that on or after the Early Amazonian epoch, this region of Mars was capable to form one of the longest reported catena formation activity. The mean width of this catena appears to be one-tenth to the width of Candor Chasma of VM, which is located in the west of the Pital crater. In concurrence to this, the orientation of Pital' catena matches with the Candor Chasma,

suggesting that the Pital' catena could have a potential association with the Candor Chasma but it is formed during the younger epoch. Results from this study provide evidence in favor of Carr and Head (2010)**,** which stated that the transition of individual pits to chains of coalescing pits and later to continuous canyons by surface material collapse over graben took place over a wide range of scale and time.

Inter comparison between regions in VM periphery: On comparing the Tithonium and Ophir regions that are ~700 km apart, superposed graben, pits, and troughs were observed. From the regional comparison, it is evident that these features not only varied chronologically among the regions, but also varied in size and extent. The presence of graben, pits, and troughs on the surface, and their spatial and chronological variations are likely records of the internal activity of Mars. The acquisition of more HiRISE and CRISM datasets can be used to study small notable features and their mineralogical variations. Overall, the superposition and/or crosscutting relationships of these graben and pits with craters vis-à-vis chronological interpretation, revealed that the VM region likely witnessed the modification till the Middle Amazonian epoch, which is much later than what is generally presumed.

Chapter 6 Summary and Future Work

6.1 Summary and synthesis of the thesis work

Mars is one of the most intriguing body in our Solar System as diverse geological activities and climatic conditions occurred throughout its history. Diverse geological activities that prevailed on Mars include tectonic, magmatic, volcanic, fluvial, glacial and impact cratering. Among these, impact cratering is one of the continuous process which is ongoing from oldest time to till today, though, the frequency decreases over the time. These large number of craters present on the surface of Mars provide a proxy to study the diverse geological activities from Amazonian to Noachian period. Therefore, in this thesis work, impact craters are used as a fingerprint to study the climatic conditions and diverse geological activities occurred from the recent few million years to billions of years ago.

<u>Impact crater exposing water-ice:</u> The northern mid latitudes on Mars are mostly known for its water/dry ice deposits. The impact craters in the higher latitudes are the potential traps to have the water-ice deposits and they act as a fingerprint to study recent snow deposition. To date, only one northern mid-latitude crater is reported with exposed water-ice [22]. Therefore, it is indeed important to discover more locations which host

near-surface water-ice to understand their spatial distribution. Two craters located in the Northern Hemisphere were identified in this study. These craters worked as a host for recent snow deposition and accumulation over the walls and floor. Over time, the scarps formed by erosion within the craters walls/floors aid to expose the accumulated and preserved water-ice deposits. In that line, the two unnamed craters (UC1 and UC2) discovered in the northern mid-latitude with preserved water-ice is spatially ~5000 km apart from each other. This study revealed that the snow was accumulated over the pole-facing wall of UC1 and equator-facing wall of UC2 crater. These observations have strong implication for the snow deposition phenomena, as general understanding of Mars suggest that pole-facing wall of the craters are more likely to host the ice at the mid-latitudes. This study revealed that at such latitude the deposition occurred both in pole and non-pole facing walls. Using crater-size frequency distribution it is substantiated that the snow accumulation have occurred within the last tens to hundreds of million years, whereas, the water-ice get exposed within the last one-million year. Additionally, strong temporal spectral evidence for the exposed water-ice is obtained from the CRISM spectral signatures. The exposed water-ice remains preserved atleast for a week on Mars in the steep walls of the scarps. Discovery of late Amazonian craters with exposed water-ice using photo-geological and spectral evidence substantiate that they are widely distributed in the near-surface of Mars. This study reveals that the younger craters are the potential zones to explore for recent water-ice exposures. However, the key scientific challenge that need to address in near future is to quantify the near-surface exposed water-ice on Mars. The quantification of water-ice is indeed important for the upcoming missions to mars, more importantly to the human missions to Mars.

<u>Impact crater over a volcanic dome with post fluvial and glacial activity:</u> Mars is known for its widespread glacial, fluvial and volcanic activities. Preserved evidence of all these three major geological activities within a region will provide crucial information about the crustal and climatic evolution of Mars. The study of two superposed impact craters (Degana and Degana-A) revealed information about the volcanic, fluvial and glacial activities happened in different epoch, but at the same location. Degana-A projectile impacted within the Degana crater, and in total both the craters excavated ~2.7 km deep into the Noachian dome. The two superposed craters helped to excavate the Noachian volcanic dome (~ 1.5 km high and ~4.0 Ga old) and mafic minerals like olivine and low-calcium pyroxene are excavated by these impacts. Within these two craters nine alluvial fans are formed; five fans within the Degana crater and four fans within the superposed crater Degana-A. Modelled absolute ages of these fans were found to be similar and suggested that all the fans were formed during the Hesperian period. On two alluvial fans in the northern part of the crater, superposed linear ridge-like features are present. These linear features are glacial originated moraines, hence, provide evidence for glacial activity within the crater which superposed the volcanic dome. The analysis revealed that the glacial activities were followed post to the fan formation activity that is during the Amazonian period. This study reveals that the possible source for the fan formation within the crater is due to the snow melting that accumulated over the wall of Degana crater. The impact of Degana-A within the Degana crater and the ejecta associated with Degana-A contributed to melt the snow/ice deposits. Thus, the

location of Degana and Degana-A craters are distinctive on Mars as they expose the Noachian aged mafic minerals, and host the Hesperian aged fluvial deposits and early-Amazonian aged glacial deposits. All these activities make Degana crater an important region and revealed this region witnessed diverse climatic conditions over the time. However, the key scientific problem that need to address in near future is to have a detailed mineralogy of Degana crater. The crater's floor is mostly covered with alluvial fans, thus, the crater can be a potential site to host clay minerals. However, the dust cover can cause challenges in detecting and interpreting the minerals that can be present in Degana crater. Overall, a detailed mineralogy of the crater can be indeed important to increase the possibility of Degana crater as one of the future potential landing site on Mars.

<u>Impact craters with superposed pits and graben:</u> The widespread craters around the Valles Marineris region were used to decipher how the periphery of the VM undergone spatial and temporal modifications. The impact craters around the VM regions were used as a proxy to understand the tectonic and possible magmatic activities. In total, there are ~1516 craters of diameter greater than 3 km in the ~100 km vicinity of the VM boundary. Out of these craters, 48 craters have clear association with graben/pits and they are superposed over these craters or vice-versa. The absolute modelled ages of these selected craters found to be from Mid-Noachian to Mid-Amazonian period. This suggest that the periphery region of VM was plausibly undergoing modification over a large period at different places around the VM. Graben in this region have formed post to Hesperian epoch, whereas, pits have formed post to Noachian period and they were also formed during the mid-Amazonian epoch. A major result from this study is

a ~14 km wide catena crosscut the Pital crater NE rim. The age of the Pital crater is ~2.6 Ga and the crosscut catena revealed its post formation. This catena is one of the largest and youngest around the VM periphery. This catena is ~1/15th size of VM width. Therefore, the craters in the surrounding of VM provided strong evidence for the record of internal activities (pits/graben). Finally, these impact craters substantiated that the VM modification was ongoing during or post to mid-Amazonian period. Therefore, spatial and temporal modification of graben and pits in the vicinity of VM is directly related to the modification of VM and is linked with the internal activity of the Mars. However, the key scientific challenge that need a focus study in near future is to focus on the modification and formation of catenae along the boundary of Valles Marineris. This remain unanswered and challenging that what cause the formation of the catenae and did they form in a single event or multiple episodes of event cause their formation.

Overall, this thesis work used impact craters as fingerprints to understand the diverse geological activities on Mars. In one region, impact craters help to study the recent near-surface water-ice deposition and its spatial distribution on Mars, whereas, at other locations they help to understand volcanic, fluvial, glacial, tectonic and collapse processes on Mars.

6.2 Future work

In the future work, the plan is to extend the rigorous search for exposed near-surface water-ice globally on Mars with a more focus to mid-latitude craters in the southern highland of Mars. It is proposed to use the available CRISM and HiRISE datasets for this study. Along with the manual search, the plan is to use machine learning to detect potential sites. These sites will provide a global distribution of near-surface water-ice on Mars. Identification of more such locations are indeed important for future robotic and manned missions to Mars. Followed by this, it is proposed to start the photogeological analysis of all the HiRISE images available in the mid-high southern highlands (~45° to 60°S). Thus, initially the plan is to target those locations where coordinated HiRISE and CRISM datasets are available, which later can be extended to individual HiRISE and CRISM datasets.

Another encouraging direction of future study is understanding about the subsurface structure of Mars and its implication for geological history of the planet Mars. This will include the identification of ice and lava layers in the subsurface of Mars. For such type of studies, I am planning to use SHAllow RADar (SHARAD) and Mars Advanced Radar for Subsurface and Ionosphere Sounding (MARSIS) data, which will give subsurface information. The study of subsurface structure of Mars will provide evidence for buried lava and ice deposits, which are crucial to understand the lava and ice-rich history of the planet Mars. First step is to identify the locations that host buried lava or ice deposits globally on Mars. Next, determining the thickness of the deposits is one of the important target of this study. Thus, I propose to determine the thickness by correlating SHARAD and HiRISE datasets. This can be done by identifying lava and/or ice layers in radar analysis with SHARAD and in image analysis with HiRISE. Therefore, in the near future the plan is to target thick and/or exposed deposits within the walls of a crater, pit, and graben or fosssae on Mars. Also, I'm interested to study the interaction between the two (lava and ice) on the surface of Mars.

Bibliography

1. Mitchell, K. L., & Wilson, L. (2003). Mars: a geologically active planet. *Astronomy & Geophysics*, *44*(4), 4.16-4.20. https://doi.org/10.1046/j.1468-4004.2003.44416.x

2. Carr, M. H., & Head, J. W. (2010). Geologic history of Mars. *Earth and Planetary Science Letters*, *294*(3), 185–203. https://doi.org/10.1016/j.epsl.2009.06.042

3. Carr, M. H. (2012). The fluvial history of Mars. *Philosophical Transactions of the Royal Society A: Mathematical, Physical and Engineering Sciences*, *370*(1966), 2193–2215. https://doi.org/10.1098/rsta.2011.0500

4. Tanaka, K. L., Skinner, J. A., Dohm, J. M., Irwin III, R. P., Kolb, E. J., Fortezzo, C. M., … Hare, T. M. (2014). *Geologic map of Mars* (USGS Numbered Series No. 3292). *Geologic map of Mars* (Vol. 3292, p. 48). Reston, VA: U.S. Geological Survey. https://doi.org/10.3133/sim3292

5. Ehlmann, B. L., Mustard, J. F., Swayze, G. A., Clark, R. N., Bishop, J. L., Poulet, F., … Murchie, S. L. (2009). Identification of hydrated silicate minerals on Mars using MRO-CRISM: Geologic context near Nili Fossae and implications for aqueous alteration. *Journal of Geophysical Research: Planets*, *114*(E2). https://doi.org/10.1029/2009JE003339

6. de Pater, I., & Lissauer, J. J. (2010). Planetary Sciences. *Planetary Sciences, by Imke de Pater , Jack J. Lissauer, Cambridge, UK: Cambridge University Press, 2010*. Retrieved from http://adsabs.harvard.edu/abs/2010plsc.book.....D

7. Andrews-Hanna, J. C. (2012). The formation of Valles Marineris: 1. Tectonic architecture and the relative roles of extension and subsidence. *Journal of Geophysical Research: Planets*, *117*(E3). https://doi.org/10.1029/2011JE003953

8. Brustel, C., Flahaut, J., Hauber, E., Fueten, F., Quantin, C., Stesky, R., & Davies, G. R. (2017). Valles Marineris tectonic and volcanic history inferred from dikes in eastern Coprates Chasma. *Journal of Geophysical Research: Planets*, *122*(6), 1353–1371. https://doi.org/10.1002/2016JE005231

9. Werner, S. C., & Tanaka, K. L. (2011). Redefinition of the crater-density and absolute-age boundaries for the chronostratigraphic system of Mars. *Icarus*, *215*(2), 603–607. https://doi.org/10.1016/j.icarus.2011.07.024

10. Michael, G. G., & Neukum, G. (2010). Planetary surface dating from crater size–frequency distribution measurements: Partial resurfacing events and statistical age uncertainty. *Earth and Planetary Science Letters*, *294*(3), 223–229. https://doi.org/10.1016/j.epsl.2009.12.041

11. Michael, G. G. (2013). Planetary surface dating from crater size–frequency distribution measurements: Multiple resurfacing episodes and differential isochron fitting. *Icarus*, *226*(1), 885–890. https://doi.org/10.1016/j.icarus.2013.07.004

12. Moore, J. M., Howard, A. D., Dietrich, W. E., & Schenk, P. M. (2003). Martian Layered Fluvial Deposits: Implications for Noachian Climate Scenarios. *Geophysical Research Letters*, *30*(24). https://doi.org/10.1029/2003GL019002

13. Forget, F., Haberle, R. M., Montmessin, F., Levrard, B., & Head, J. W. (2006). Formation of Glaciers on Mars by Atmospheric Precipitation at High Obliquity. *Science*, *311*(5759), 368–371. https://doi.org/10.1126/science.1120335

14. Wordsworth, R., Forget, F., Millour, E., Head, J. W., Madeleine, J.-B., & Charnay, B. (2013). Global modelling of the early martian climate under a denser CO2 atmosphere: Water cycle and ice evolution. *Icarus*, *222*(1), 1–19. https://doi.org/10.1016/j.icarus.2012.09.036

15. Gulick, V. C. (2001). Origin of the valley networks on Mars: a hydrological perspective. *Geomorphology*, *37*(3), 241–268. https://doi.org/10.1016/S0169-555X(00)00086-6

16. Hauber, E., van Gasselt, S., Ivanov, B., Werner, S., Head, J. W., Neukum, G., … HRSC Co-Investigator Team. (2005). Discovery of a flank caldera and very young glacial activity at Hecates Tholus, Mars. *Nature*, *434*(7031), 356–361. https://doi.org/10.1038/nature03423

17. Williams, K. E., Toon, O. B., Heldmann, J. L., & Mellon, M. T. (2009). Ancient melting of mid-latitude snowpacks on Mars as a water source for gullies. *Icarus*, *200*(2), 418–425. https://doi.org/10.1016/j.icarus.2008.12.013

18. Ansan, V., & Mangold, N. (2013). 3D morphometry of valley networks on Mars from HRSC/MEX DEMs: Implications for climatic evolution through

time. *Journal of Geophysical Research: Planets*, *118*(9), 1873–1894. https://doi.org/10.1002/jgre.20117

19. Melosh, H. J. (1989). *Impact cratering: a geologic process*. New York : Oxford: Oxford University Press ; Clarendon Press.

20. Osinski, G. R., & Pierazzo, E. (2012). *Impact Cratering: Processes and Products* (1st edition.). Wiley-Blackwell.

21. Bevan M. French. (1999). Traces of catastrophe: a handbook of shock-metamorphic effects in terrestrial meteorite impact structures. *Choice Reviews Online*, *36*(10), 36-5704-36–5704. https://doi.org/10.5860/CHOICE.36-5704

22. Dundas, C. M., Bramson, A. M., Ojha, L., Wray, J. J., Mellon, M. T., Byrne, S., … Holt, J. W. (2018). Exposed subsurface ice sheets in the Martian mid-latitudes. *Science*, *359*(6372), 199–201. https://doi.org/10.1126/science.aao1619

23. Lefort, A., Russell, P. S., Thomas, N., McEwen, A. S., Dundas, C. M., & Kirk, R. L. (2009). Observations of periglacial landforms in Utopia Planitia with the High Resolution Imaging Science Experiment (HiRISE). *Journal of Geophysical Research: Planets*, *114*(E4). https://doi.org/10.1029/2008JE003264

24. Bandfield, J. L. (2007). High-resolution subsurface water-ice distributions on Mars. *Nature*, *447*(7140), 64–67. https://doi.org/10.1038/nature05781

25. Head, J. W., Mustard, J. F., Kreslavsky, M. A., Milliken, R. E., & Marchant, D. R. (2003). Recent ice ages on Mars. *Nature*, *426*(6968), 797–802. https://doi.org/10.1038/nature02114

26. Piqueux, S., Buz, J., Edwards, C. S., Bandfield, J. L., Kleinböhl, A., Kass, D. M., & Hayne, P. O. (2019). Widespread Shallow Water Ice on Mars at High Latitudesand Midlatitudes. *Geophysical Research Letters*, *46*(24), 14290–14298. https://doi.org/10.1029/2019GL083947

27. Souness, C., & Hubbard, B. (2012). Mid-latitude glaciation on Mars. *Progress in Physical Geography: Earth and Environment*, *36*(2), 238–261. https://doi.org/10.1177/0309133312436570

28. Nazari-Sharabian, M., Aghababaei, M., Karakouzian, M., & Karami, M. (2020). Water on Mars—A Literature Review. *Galaxies*, *8*(2), 40. https://doi.org/10.3390/galaxies8020040

29. Shean, D. E. (2010). Candidate ice-rich material within equatorial craters on Mars. *Geophysical Research Letters*, *37*(24). https://doi.org/10.1029/2010GL045181

30. Conway, S. J., Butcher, F. E. G., de Haas, T., Deijns, A. A. J., Grindrod, P. M., & Davis, J. M. (2018). Glacial and gully erosion on Mars: A terrestrial perspective. *Geomorphology*, *318*, 26–57. https://doi.org/10.1016/j.geomorph.2018.05.019

31. Scanlon, K. E., Head, J. W., Wilson, L., & Marchant, D. R. (2014). Volcano–ice interactions in the Arsia Mons tropical mountain glacier deposits. *Icarus*, *237*, 315–339. https://doi.org/10.1016/j.icarus.2014.04.024

32. Moore, J. M., & Howard, A. D. (2005). Large alluvial fans on Mars. *Journal of Geophysical Research: Planets*, *110*(E4). https://doi.org/10.1029/2004JE002352

33. Vijayan, S., & Sinha, R. K. (2017). Amazonian fluvial outflow channels in Jovis Tholus region, Mars. *Journal of Geophysical Research: Planets*, *122*(5), 927–949. https://doi.org/10.1002/2016JE005237

34. Goudge, T. A., Milliken, R. E., Head, J. W., Mustard, J. F., & Fassett, C. I. (2017). Sedimentological evidence for a deltaic origin of the western fan deposit in Jezero crater, Mars and implications for future exploration. *Earth and Planetary Science Letters*, *458*, 357–365. https://doi.org/10.1016/j.epsl.2016.10.056

35. Grant, J. A., & Wilson, S. A. (2019). Evidence for Late Alluvial Activity in Gale Crater, Mars. *Geophysical Research Letters*, *46*(13), 7287–7294. https://doi.org/10.1029/2019GL083444

36. Fassett, C. I., & Head, J. W. (2008). The timing of martian valley network activity: Constraints from buffered crater counting. *Icarus*, *195*(1), 61–89. https://doi.org/10.1016/j.icarus.2007.12.009

37. Goudge, T. A., Mustard, J. F., Head, J. W., & Fassett, C. I. (2012). Constraints on the history of open-basin lakes on Mars from the composition and timing of

volcanic resurfacing. *Journal of Geophysical Research: Planets*, *117*(E12). https://doi.org/10.1029/2012JE004115

38. Goudge, T. A., Aureli, K. L., Head, J. W., Fassett, C. I., & Mustard, J. F. (2015). Classification and analysis of candidate impact crater-hosted closed-basin lakes on Mars. *Icarus*, *260*, 346–367. https://doi.org/10.1016/j.icarus.2015.07.026

39. Wyrick, D., Ferrill, D. A., Morris, A. P., Colton, S. L., & Sims, D. W. (2004). Distribution, morphology, and origins of Martian pit crater chains. *Journal of Geophysical Research: Planets*, *109*(E6). https://doi.org/10.1029/2004JE002240

40. Tanaka, K. L., & Golombek, M. P. (1989). Martian tension fractures and the formation of grabens and collapse features at Valles Marineris. In *Lunar and Planetary Science Conference Proceedings* (Vol. 19, pp. 383–396).

41. Hauber, E., & Kronberg, P. (2005). The large Thaumasia graben on Mars: Is it a rift? *Journal of Geophysical Research: Planets*, *110*(E7). https://doi.org/10.1029/2005JE002407

42. Mège, D., Cook, A. C., Garel, E., Lagabrielle, Y., & Cormier, M.-H. (2003). Volcanic rifting at Martian grabens. *Journal of Geophysical Research: Planets*, *108*(E5). https://doi.org/10.1029/2002JE001852

43. Anderson, R. C., Dohm, J. M., Golombek, M. P., Haldemann, A. F. C., Franklin, B. J., Tanaka, K. L., … Peer, B. (2001). Primary centers and secondary concentrations of tectonic activity through time in the western

hemisphere of Mars. *Journal of Geophysical Research: Planets*, *106*(E9), 20563–20585. https://doi.org/10.1029/2000JE001278

44. Robbins, S. J., & Hynek, B. M. (2012). A new global database of Mars impact craters ≥1 km: 1. Database creation, properties, and parameters. *Journal of Geophysical Research: Planets*, *117*(E5). https://doi.org/10.1029/2011JE003966

45. Xiao, L., Huang, J., Christensen, P. R., Greeley, R., Williams, D. A., Zhao, J., & He, Q. (2012). Ancient volcanism and its implication for thermal evolution of Mars. *Earth and Planetary Science Letters*, *323–324*, 9–18. https://doi.org/10.1016/j.epsl.2012.01.027

46. Christensen, P. R., Jakosky, B. M., Kieffer, H. H., Malin, M. C., McSween, H. Y., Nealson, K., … Ravine, M. (2004). The Thermal Emission Imaging System (THEMIS) for the Mars 2001 Odyssey Mission. *Space Science Reviews*, *110*(1), 85–130. https://doi.org/10.1023/B:SPAC.0000021008.16305.94

47. Arya, A. S., Sarkar, S. S., Srinivas, A. R., Manthira Moorthi, S., Patel, V. D., Singh, R. B., … Kiran Kumar, A. S. (2015). Mars Colour Camera: the payload characterization/calibration and data analysis from Earth imaging phase. *Current Science*, *109*(6), 1076. https://doi.org/10.18520/cs/v109/i6/1076-1086

48. Malin, M. C., Bell, J. F., Cantor, B. A., Caplinger, M. A., Calvin, W. M., Clancy, R. T., … Wolff, M. J. (2007). Context Camera Investigation on board the Mars Reconnaissance Orbiter. *Journal of Geophysical Research: Planets*, *112*(E5). https://doi.org/10.1029/2006JE002808

49. McEwen, A. S., Eliason, E. M., Bergstrom, J. W., Bridges, N. T., Hansen, C. J., Delamere, W. A., … Weitz, C. M. (2007). Mars Reconnaissance Orbiter's High Resolution Imaging Science Experiment (HiRISE). *Journal of Geophysical Research: Planets*, *112*(E5). https://doi.org/10.1029/2005JE002605

50. Edwards, C. S., Nowicki, K. J., Christensen, P. R., Hill, J., Gorelick, N., & Murray, K. (2011). Mosaicking of global planetary image datasets: 1. Techniques and data processing for Thermal Emission Imaging System (THEMIS) multi-spectral data. *Journal of Geophysical Research: Planets*, *116*(E10). https://doi.org/10.1029/2010JE003755

51. Smith, D. E., Zuber, M. T., Frey, H. V., Garvin, J. B., Head, J. W., Muhleman, D. O., … Sun, X. (2001). Mars Orbiter Laser Altimeter: Experiment summary after the first year of global mapping of Mars. *Journal of Geophysical Research: Planets*, *106*(E10), 23689–23722. https://doi.org/10.1029/2000JE001364

52. Fergason, R. L, Hare, T. M., & Laura, J. (2018). HRSC and MOLA Blended Digital Elevation Model at 200m v2. Astrogeology PDS Annex, U.S. Geological Survey. http://bit.ly/HRSC_MOLA_Blend_v0

53. Beyer, R. A., Alexandrov, O., & McMichael, S. (2018). The Ames Stereo Pipeline: NASA's Open Source Software for Deriving and Processing Terrain Data. *Earth and Space Science*, *5*(9), 537–548. https://doi.org/10.1029/2018EA000409

54. Murchie, S., Arvidson, R., Bedini, P., Beisser, K., Bibring, J.-P., Bishop, J., … Wolff, M. (2007). Compact Reconnaissance Imaging Spectrometer for Mars (CRISM) on Mars Reconnaissance Orbiter (MRO). *Journal of Geophysical Research: Planets*, *112*(E5). https://doi.org/10.1029/2006JE002682

55. Hartmann, W. K., & Neukum, G. (2001). Cratering Chronology and the Evolution of Mars. *Space Science Reviews*, *96*(1), 165–194. https://doi.org/10.1023/A:1011945222010

56. Mangold, N., Maurice, S., Feldman, W. C., Costard, F., & Forget, F. (2004). Spatial relationships between patterned ground and ground ice detected by the Neutron Spectrometer on Mars. *Journal of Geophysical Research: Planets*, *109*(E8). https://doi.org/10.1029/2004JE002235

57. Mellon, M. T., Arvidson, R. E., Sizemore, H. G., Searls, M. L., Blaney, D. L., Cull, S., … Zent, A. P. (2009). Ground ice at the Phoenix Landing Site: Stability state and origin. *Journal of Geophysical Research: Planets*, *114*(E1). https://doi.org/10.1029/2009JE003417

58. Cull, S., Arvidson, R. E., Mellon, M. T., Skemer, P., Shaw, A., & Morris, R. V. (2010). Compositions of subsurface ices at the Mars Phoenix landing site. *Geophysical Research Letters*, *37*(24). https://doi.org/10.1029/2010GL045372

59. Mellon, M. T., & Jakosky, B. M. (1995). The distribution and behavior of Martian ground ice during past and present epochs. *Journal of Geophysical Research: Planets*, *100*(E6), 11781–11799. https://doi.org/10.1029/95JE01027

60. Mellon, M. T., Jakosky, B. M., & Postawko, S. E. (1997). The persistence of equatorial ground ice on Mars. *Journal of Geophysical Research: Planets*, *102*(E8), 19357–19369. https://doi.org/10.1029/97JE01346

61. Mellon, M. T., Feldman, W. C., & Prettyman, T. H. (2004). The presence and stability of ground ice in the southern hemisphere of Mars. *Icarus*, *169*(2), 324–340. https://doi.org/10.1016/j.icarus.2003.10.022

62. Chamberlain, M. A., & Boynton, W. V. (2007). Response of Martian ground ice to orbit-induced climate change. *Journal of Geophysical Research: Planets*, *112*(E6). https://doi.org/10.1029/2006JE002801

63. Schorghofer, N., & Forget, F. (2012). History and anatomy of subsurface ice on Mars. *Icarus*, *220*(2), 1112–1120. https://doi.org/10.1016/j.icarus.2012.07.003

64. Aharonson, O., & Schorghofer, N. (2006). Subsurface ice on Mars with rough topography. *Journal of Geophysical Research: Planets*, *111*(E11). https://doi.org/10.1029/2005JE002636

65. Vincendon, M., Mustard, J., Forget, F., Kreslavsky, M., Spiga, A., Murchie, S., & Bibring, J.-P. (2010). Near-tropical subsurface ice on Mars. *Geophysical Research Letters*, *37*(1). https://doi.org/10.1029/2009GL041426

66. Quantin-Nataf, C., Lozac'h, L., Thollot, P., Loizeau, D., Bultel, B., Fernando, J., … Harrisson, S. (2018). MarsSI: Martian surface data processing information system. *Planetary and Space Science*, *150*, 157–170. https://doi.org/10.1016/j.pss.2017.09.014

67. Viviano-Beck, C. E., Seelos, F. P., Murchie, S. L., Kahn, E. G., Seelos, K. D., Taylor, H. W., … Morgan, M. F. (2014). Revised CRISM spectral parameters and summary products based on the currently detected mineral diversity on Mars. *Journal of Geophysical Research: Planets*, *119*(6), 1403–1431. https://doi.org/10.1002/2014JE004627

68. Zent, A. P., Hecht, M. H., Hudson, T. L., Wood, S. E., & Chevrier, V. F. (2016). A revised calibration function and results for the Phoenix mission TECP relative humidity sensor. *Journal of Geophysical Research: Planets*, *121*(4), 626–651. https://doi.org/10.1002/2015JE004933

69. Viviano-Beck, C. E. (2015). MRO CRISM type spectra library. *NASA Planetary Data System*.

70. Keszthelyi, L., Jaeger, W., McEwen, A., Tornabene, L., Beyer, R. A., Dundas, C., & Milazzo, M. (2008). High Resolution Imaging Science Experiment (HiRISE) images of volcanic terrains from the first 6 months of the Mars Reconnaissance Orbiter Primary Science Phase. *Journal of Geophysical Research: Planets*, *113*(E4). https://doi.org/10.1029/2007JE002968

71. Bramson, A. M., Byrne, S., & Bapst, J. (2017). Preservation of Midlatitude Ice Sheets on Mars. *Journal of Geophysical Research: Planets*, *122*(11), 2250–2266. https://doi.org/10.1002/2017JE005357

72. Kreslavsky, M. A., & Head, J. W. (2002). Mars: Nature and evolution of young latitude-dependent water-ice-rich mantle. *Geophysical Research Letters*, *29*(15), 14-1-14–4. https://doi.org/10.1029/2002GL015392

73. Levy, J. S., Head, J. W., & Marchant, D. R. (2011). Gullies, polygons and mantles in Martian permafrost environments: cold desert landforms and sedimentary processes during recent Martian geological history. *Geological Society, London, Special Publications*, *354*(1), 167–182. https://doi.org/10.1144/SP354.10

74. Dundas, C. M., & Byrne, S. (2010). Modeling sublimation of ice exposed by new impacts in the martian mid-latitudes. *Icarus*, *206*(2), 716–728. https://doi.org/10.1016/j.icarus.2009.09.007

75. Berman, D. C., Crown, D. A., & Bleamaster, L. F. (2009). Degradation of mid-latitude craters on Mars. *Icarus*, *200*(1), 77–95. https://doi.org/10.1016/j.icarus.2008.10.026

76. Schorghofer, N., & Edgett, K. S. (2006). Seasonal surface frost at low latitudes on Mars. *Icarus*, *180*(2), 321–334. https://doi.org/10.1016/j.icarus.2005.08.022

77. Hartmann, W. K. (2005). Martian cratering 8: Isochron refinement and the chronology of Mars. *Icarus*, *174*(2), 294–320. https://doi.org/10.1016/j.icarus.2004.11.023

78. Viola, D. (2020). Age-Dating of Ice-Rich Mid-Latitude Mantle Deposits on Mars, *51*, 2872. Presented at the Lunar and Planetary Science Conference.

79. Laskar, J., Correia, A. C. M., Gastineau, M., Joutel, F., Levrard, B., & Robutel, P. (2004). Long term evolution and chaotic diffusion of the insolation quantities of Mars. *Icarus*, *170*(2), 343–364. https://doi.org/10.1016/j.icarus.2004.04.005

80. Viola, D., McEwen, A. S., Dundas, C. M., & Byrne, S. (2015). Expanded secondary craters in the Arcadia Planitia region, Mars: Evidence for tens of Myr-old shallow subsurface ice. *Icarus*, *248*, 190–204. https://doi.org/10.1016/j.icarus.2014.10.032

81. Dickson, J. L., Head, J. W., & Fassett, C. I. (2012). Patterns of accumulation and flow of ice in the mid-latitudes of Mars during the Amazonian. *Icarus*, *219*(2), 723–732. https://doi.org/10.1016/j.icarus.2012.03.010

82. Feldman, W. C., Boynton, W. V., Tokar, R. L., Prettyman, T. H., Gasnault, O., Squyres, S. W., … Reedy, R. C. (2002). Global Distribution of Neutrons from Mars: Results from Mars Odyssey. *Science*, *297*(5578), 75–78. https://doi.org/10.1126/science.1073541

83. Sinha, R. K., & Vijayan, S. (2017). Geomorphic investigation of craters in Alba Mons, Mars: Implications for Late Amazonian glacial activity in the region. *Planetary and Space Science*, *144*, 32–48. https://doi.org/10.1016/j.pss.2017.05.014

84. Fisher, D. A. (2005). A process to make massive ice in the martian regolith using long-term diffusion and thermal cracking. *Icarus*, *179*(2), 387–397. https://doi.org/10.1016/j.icarus.2005.07.024

85. Sizemore, H. G., Zent, A. P., & Rempel, A. W. (2015). Initiation and growth of martian ice lenses. *Icarus*, *251*, 191–210. https://doi.org/10.1016/j.icarus.2014.04.013

86. Schon, S. C., Head, J. W., & Milliken, R. E. (2009). A recent ice age on Mars: Evidence for climate oscillations from regional layering in mid-latitude mantling deposits. *Geophysical Research Letters*, *36*(15). https://doi.org/10.1029/2009GL038554

87. Jakosky, B. M., Mellon, M. T., Varnes, E. S., Feldman, W. C., Boynton, W. V., & Haberle, R. M. (2005). Mars low-latitude neutron distribution: Possible remnant near-surface water ice and a mechanism for its recent emplacement. *Icarus*, *175*(1), 58–67. https://doi.org/10.1016/j.icarus.2004.11.014

88. Dundas, C. M., Byrne, S., McEwen, A. S., Mellon, M. T., Kennedy, M. R., Daubar, I. J., & Saper, L. (2014). HiRISE observations of new impact craters exposing Martian ground ice. *Journal of Geophysical Research: Planets*, *119*(1), 109–127. https://doi.org/10.1002/2013JE004482

89. Kraal, E. R., Asphaug, E., Moore, J. M., Howard, A., & Bredt, A. (2008). Catalogue of large alluvial fans in martian impact craters. *Icarus*, *194*(1), 101–110. https://doi.org/10.1016/j.icarus.2007.09.028

90. Blair, T. C., & McPherson, J. G. (2009). Processes and Forms of Alluvial Fans. In A. J. Parsons & A. D. Abrahams (Eds.), *Geomorphology of Desert Environments* (pp. 413–467). Dordrecht: Springer Netherlands. https://doi.org/10.1007/978-1-4020-5719-9_14

91. Grant, J. A., & Wilson, S. A. (2011). Late alluvial fan formation in southern Margaritifer Terra, Mars. *Geophysical Research Letters*, *38*(8). https://doi.org/10.1029/2011GL046844

92. Morgan, A. M., Beyer, R. A., Howard, A. D., & Moore, J. M. (2012). The Alluvial Fans of Saheki Crater, *43*, 2815. Presented at the Lunar and Planetary Science Conference.

93. Morgan, A. M., Howard, A. D., Hobley, D. E. J., Moore, J. M., Dietrich, W. E., Williams, R. M. E., … Matsubara, Y. (2014). Sedimentology and climatic environment of alluvial fans in the martian Saheki crater and a comparison with terrestrial fans in the Atacama Desert. *Icarus*, *229*, 131–156. https://doi.org/10.1016/j.icarus.2013.11.007

94. Bristow, T. F., Rampe, E. B., Achilles, C. N., Blake, D. F., Chipera, S. J., Craig, P., … Yen, A. S. (2018). Clay mineral diversity and abundance in sedimentary rocks of Gale crater, Mars. *Science Advances*, *4*(6), eaar3330. https://doi.org/10.1126/sciadv.aar3330

95. Carter, J., Poulet, F., Bibring, J.-P., Mangold, N., & Murchie, S. (2013). Hydrous minerals on Mars as seen by the CRISM and OMEGA imaging spectrometers: Updated global view. *Journal of Geophysical Research: Planets*, *118*(4), 831–858. https://doi.org/10.1029/2012JE004145

96. Mangold, N., Adeli, S., Conway, S., Ansan, V., & Langlais, B. (2012). A chronology of early Mars climatic evolution from impact crater degradation. *Journal of Geophysical Research: Planets*, *117*(E4). https://doi.org/10.1029/2011JE004005

97. Mangold, N., Kite, E. S., Kleinhans, M. G., Newsom, H., Ansan, V., Hauber, E., … Tanaka, K. (2012). The origin and timing of fluvial activity at

Eberswalde crater, Mars. *Icarus*, *220*(2), 530–551. https://doi.org/10.1016/j.icarus.2012.05.026

98. Kite, E. S., Sneed, J., Mayer, D. P., & Wilson, S. A. (2017). Persistent or repeated surface habitability on Mars during the late Hesperian - Amazonian. *Geophysical Research Letters*, *44*(9), 3991–3999. https://doi.org/10.1002/2017GL072660

99. Milton, D. J. (1973). Water and processes of degradation in the Martian landscape. *Journal of Geophysical Research (1896-1977)*, *78*(20), 4037–4047. https://doi.org/10.1029/JB078i020p04037

100. Hoke, M. R. T., & Hynek, B. M. (2009). Roaming zones of precipitation on ancient Mars as recorded in valley networks. *Journal of Geophysical Research: Planets*, *114*(E8). https://doi.org/10.1029/2008JE003247

101. Achille, G. di, & Hynek, B. M. (2010). Deltas and valley networks on Mars. In *Lakes on Mars* (pp. 223–248). Elsevier. https://doi.org/10.1016/B978-0-444-52854-4.00008-8

102. Di Achille, G., & Hynek, B. M. (2010). Ancient ocean on Mars supported by global distribution of deltas and valleys. *Nature Geoscience*, *3*(7), 459–463. https://doi.org/10.1038/ngeo891

103. Kite, E. S., Halevy, I., Kahre, M. A., Wolff, M. J., & Manga, M. (2013). Seasonal melting and the formation of sedimentary rocks on Mars, with predictions for the Gale Crater mound. *Icarus*, *223*(1), 181–210. https://doi.org/10.1016/j.icarus.2012.11.034

104. Armitage, J. J., Warner, N. H., Goddard, K., & Gupta, S. (2011). Timescales of alluvial fan development by precipitation on Mars. *Geophysical Research Letters*, *38*(17). https://doi.org/10.1029/2011GL048907

105. Grant, J. A., & Wilson, S. A. (2012). A possible synoptic source of water for alluvial fan formation in southern Margaritifer Terra, Mars. *Planetary and Space Science*, *72*(1), 44–52. https://doi.org/10.1016/j.pss.2012.05.020

106. Flahaut, J., Mustard, J. F., Quantin, C., Clenet, H., Allemand, P., & Thomas, P. (2011). Dikes of distinct composition intruded into Noachian-aged crust exposed in the walls of Valles Marineris. *Geophysical Research Letters*, *38*(15). https://doi.org/10.1029/2011GL048109

107. Salvatore, M. R., Mustard, J. F., Wyatt, M. B., & Murchie, S. L. (2010). Definitive evidence of Hesperian basalt in Acidalia and Chryse planitiae. *Journal of Geophysical Research: Planets*, *115*(E7). https://doi.org/10.1029/2009JE003519

108. Pelkey, S. M., Mustard, J. F., Murchie, S., Clancy, R. T., Wolff, M., Smith, M., … Gondet, B. (2007). CRISM multispectral summary products: Parameterizing mineral diversity on Mars from reflectance. *Journal of Geophysical Research: Planets*, *112*(E8). https://doi.org/10.1029/2006JE002831

109. Sun, V. Z., & Milliken, R. E. (2014). The geology and mineralogy of Ritchey crater, Mars: Evidence for post-Noachian clay formation. *Journal of Geophysical Research: Planets*, *119*(4), 810–836. https://doi.org/10.1002/2013JE004602

110. McCauley, J. F. (1978). Geologic map of the Coprates Quadrangle of Mars. Retrieved December 27, 2020, from https://pubs.er.usgs.gov/publication/i897

111. Scott, D., & Tanaka, K. (1999). Mars Geologic Map of the Western Equatorial Region | USGS Astrogeology Science Center. Retrieved December 27, 2020, from https://astrogeology.usgs.gov/search/map/Mars/Geology/year-1990/Mars-Geologic-Map-of-the-Western-Equatorial-Region

112. Adams, J. B. (1974). Visible and near-infrared diffuse reflectance spectra of pyroxenes as applied to remote sensing of solid objects in the solar system. *Journal of Geophysical Research (1896-1977)*, *79*(32), 4829–4836. https://doi.org/10.1029/JB079i032p04829

113. Cloutis, E. A., Gaffey, M. J., Jackowski, T. L., & Reed, K. L. (1986). Calibrations of phase abundance, composition, and particle size distribution for olivine-orthopyroxene mixtures from reflectance spectra. *Journal of Geophysical Research: Solid Earth*, *91*(B11), 11641–11653. https://doi.org/10.1029/JB091iB11p11641

114. Cloutis, E. A., & Gaffey, M. J. (1991). Pyroxene spectroscopy revisited: Spectral-compositional correlations and relationship to geothermometry. *Journal of Geophysical Research: Planets*, *96*(E5), 22809–22826. https://doi.org/10.1029/91JE02512

115. Klima, R. L., Pieters, C. M., & Dyar, M. D. (2007). Spectroscopy of synthetic Mg-Fe pyroxenes I: Spin-allowed and spin-forbidden crystal field bands in the

visible and near-infrared. *Meteoritics & Planetary Science*, *42*(2), 235–253. https://doi.org/10.1111/j.1945-5100.2007.tb00230.x

116. Huang, J., Edwards, C. S., Horgan, B. H. N., Christensen, P. R., Kraft, M. D., & Xiao, L. (2012). Identification and mapping of dikes with relatively primitive compositions in Thaumasia Planum on Mars: Implications for Tharsis volcanism and the opening of Valles Marineris. *Geophysical Research Letters*, *39*(17). https://doi.org/10.1029/2012GL052523

117. Mustard, J. F., Poulet, F., Gendrin, A., Bibring, J.-P., Langevin, Y., Gondet, B., … Altieri, F. (2005). Olivine and Pyroxene Diversity in the Crust of Mars. *Science*, *307*(5715), 1594–1597. https://doi.org/10.1126/science.1109098

118. Skok, J. R., Mustard, J. F., Tornabene, L. L., Pan, C., Rogers, D., & Murchie, S. L. (2012). A spectroscopic analysis of Martian crater central peaks: Formation of the ancient crust. *Journal of Geophysical Research: Planets*, *117*(E11). https://doi.org/10.1029/2012JE004148

119. Clénet, H., Pinet, P., Daydou, Y., Heuripeau, F., Rosemberg, C., Baratoux, D., & Chevrel, S. (2011). A new systematic approach using the Modified Gaussian Model: Insight for the characterization of chemical composition of olivines, pyroxenes and olivine–pyroxene mixtures. *Icarus*, *213*(1), 404–422. https://doi.org/10.1016/j.icarus.2011.03.002

120. Burns, R. G. (1970). Crystal field spectra and evidence of cation ordering in olivine minerals. *American Mineralogist*, *55*(9–10), 1608–1632.

121. King, T. V. V., & Ridley, W. I. (1987). Relation of the spectroscopic reflectance of olivine to mineral chemistry and some remote sensing implications. *Journal of Geophysical Research: Solid Earth*, *92*(B11), 11457–11469. https://doi.org/10.1029/JB092iB11p11457

122. Sunshine, J. M., & Pieters, C. M. (1998). Determining the composition of olivine from reflectance spectroscopy. *Journal of Geophysical Research: Planets*, *103*(E6), 13675–13688. https://doi.org/10.1029/98JE01217

123. Ody, A., Poulet, F., Bibring, J.-P., Loizeau, D., Carter, J., Gondet, B., & Langevin, Y. (2013). Global investigation of olivine on Mars: Insights into crust and mantle compositions. *Journal of Geophysical Research: Planets*, *118*(2), 234–262. https://doi.org/10.1029/2012JE004149

124. Sunshine, J. M., Pieters, C. M., & Pratt, S. F. (1990). Deconvolution of mineral absorption bands: An improved approach. *Journal of Geophysical Research: Solid Earth*, *95*(B5), 6955–6966. https://doi.org/10.1029/JB095iB05p06955

125. Wilson, S. A., & Zimbelman, J. R. (2004). Latitude-dependent nature and physical characteristics of transverse aeolian ridges on Mars. *Journal of Geophysical Research: Planets*, *109*(E10). https://doi.org/10.1029/2004JE002247

126. Berman, D. C., Balme, M. R., Rafkin, S. C. R., & Zimbelman, J. R. (2011). Transverse Aeolian Ridges (TARs) on Mars II: Distributions, orientations, and ages. *Icarus*, *213*(1), 116–130. https://doi.org/10.1016/j.icarus.2011.02.014

127. Blair, T. C., & McPherson, J. G. (1994). Alluvial fans and their natural distinction from rivers based on morphology, hydraulic processes, sedimentary processes, and facies assemblages. *Journal of Sedimentary Research*, *64*(3a), 450–489. https://doi.org/10.1306/D4267DDE-2B26-11D7-8648000102C1865D

128. Kleinhans, M. G. (2005). Flow discharge and sediment transport models for estimating a minimum timescale of hydrological activity and channel and delta formation on Mars. *Journal of Geophysical Research: Planets*, *110*(E12). https://doi.org/10.1029/2005JE002521

129. Costa, J. E. (1998). Rheologic, geomorphic, and sedimentologic differentiation of water floods, hyperconcentrated flows, and debris flows, in Baker, V.R., Kochel, R.C., and Patton, P.C., eds. Flood geomorphology. Retrieved December 27, 2020, from https://dggs.alaska.gov/pubs/id/29798

130. Ferguson, R. (2007). Flow resistance equations for gravel- and boulder-bed streams. *Water Resources Research*, *43*(5). https://doi.org/10.1029/2006WR005422

131. Lamb, M. P., Dietrich, W. E., & Sklar, L. S. (2008). A model for fluvial bedrock incision by impacting suspended and bed load sediment. *Journal of Geophysical Research: Earth Surface*, *113*(F3). https://doi.org/10.1029/2007JF000915

132. Arfstrom, J., & Hartmann, W. K. (2005). Martian flow features, moraine-like ridges, and gullies: Terrestrial analogs and interrelationships. *Icarus*, *174*(2), 321–335. https://doi.org/10.1016/j.icarus.2004.05.026

133. Scanlon, K. E., Head, J. W., & Marchant, D. R. (2015). Volcanism-induced, local wet-based glacial conditions recorded in the Late Amazonian Arsia Mons tropical mountain glacier deposits. *Icarus*, *250*, 18–31. https://doi.org/10.1016/j.icarus.2014.11.016

134. Hartmann, W. K., Ansan, V., Berman, D. C., Mangold, N., & Forget, F. (2014). Comprehensive analysis of glaciated martian crater Greg. *Icarus*, *228*, 96–120. https://doi.org/10.1016/j.icarus.2013.09.016

135. Paterson, W. S. B. (1994). Physics of Glaciers - 3rd Edition. Retrieved December 27, 2020, from https://www.elsevier.com/books/physics-of-glaciers/paterson/978-0-08-051386-7

136. Michael, G. G., Kneissl, T., & Neesemann, A. (2016). Planetary surface dating from crater size-frequency distribution measurements: Poisson timing analysis. *Icarus*, *277*, 279–285. https://doi.org/10.1016/j.icarus.2016.05.019

137. Hamilton, V. E., & Christensen, P. R. (2005). Evidence for extensive, olivine-rich bedrock on Mars. *Geology*, *33*(6), 433. https://doi.org/10.1130/G21258.1

138. Tornabene, L. L., Moersch, J. E., McSween, H. Y., Hamilton, V. E., Piatek, J. L., & Christensen, P. R. (2008). Surface and crater-exposed lithologic units of the Isidis Basin as mapped by coanalysis of THEMIS and TES derived data products. *Journal of Geophysical Research: Planets*, *113*(E10). https://doi.org/10.1029/2007JE002988

139. Poulet, F., Bibring, J.-P., Langevin, Y., Mustard, J. F., Mangold, N., Vincendon, M., … Platevoet, B. (2009). Quantitative compositional analysis of

martian mafic regions using the MEx/OMEGA reflectance data 1. Methodology, uncertainties and examples of application. *Icarus*, *201*(1), 69–83. https://doi.org/10.1016/j.icarus.2008.12.025

140. Poulet, F., Mangold, N., Platevoet, B., Bardintzeff, J.-M., Sautter, V., Mustard, J. F., … Aléon-Toppani, A. (2009). Quantitative compositional analysis of martian mafic regions using the MEx/OMEGA reflectance data: 2. Petrological implications. *Icarus*, *201*(1), 84–101. https://doi.org/10.1016/j.icarus.2008.12.042

141. Flahaut, J., Quantin, C., Clenet, H., Allemand, P., Mustard, J. F., & Thomas, P. (2012). Pristine Noachian crust and key geologic transitions in the lower walls of Valles Marineris: Insights into early igneous processes on Mars. *Icarus*, *221*(1), 420–435. https://doi.org/10.1016/j.icarus.2011.12.027

142. Quantin, C., Flahaut, J., Clenet, H., Allemand, P., & Thomas, P. (2012). Composition and structures of the subsurface in the vicinity of Valles Marineris as revealed by central uplifts of impact craters. *Icarus*, *221*(1), 436–452. https://doi.org/10.1016/j.icarus.2012.07.031

143. Rogers, A. D., Warner, N. H., Golombek, M. P., Head, J. W., & Cowart, J. C. (2018). Areally Extensive Surface Bedrock Exposures on Mars: Many Are Clastic Rocks, Not Lavas. *Geophysical Research Letters*, *45*(4), 1767–1777. https://doi.org/10.1002/2018GL077030

144. Viviano, C. E., Murchie, S. L., Daubar, I. J., Morgan, M. F., Seelos, F. P., & Plescia, J. B. (2019). Composition of Amazonian volcanic materials in Tharsis

and Elysium, Mars, from MRO/CRISM reflectance spectra. *Icarus*, *328*, 274–286. https://doi.org/10.1016/j.icarus.2019.03.001

145. Mustard, J. F., Poulet, F., Head, J. W., Mangold, N., Bibring, J.-P., Pelkey, S. M., … Neukum, G. (2007). Mineralogy of the Nili Fossae region with OMEGA/Mars Express data: 1. Ancient impact melt in the Isidis Basin and implications for the transition from the Noachian to Hesperian. *Journal of Geophysical Research: Planets*, *112*(E8). https://doi.org/10.1029/2006JE002834

146. Palumbo, A. M., & Head, J. W. (2018). Impact cratering as a cause of climate change, surface alteration, and resurfacing during the early history of Mars. *Meteoritics & Planetary Science*, *53*(4), 687–725. https://doi.org/10.1111/maps.13001

147. McSween, H. Y., Wyatt, M. B., Gellert, R., Bell, J. F., Morris, R. V., Herkenhoff, K. E., … Zipfel, J. (2006). Characterization and petrologic interpretation of olivine-rich basalts at Gusev Crater, Mars. *Journal of Geophysical Research: Planets*, *111*(E2). https://doi.org/10.1029/2005JE002477

148. Mustard, J. F., Ehlmann, B. L., Murchie, S. L., Poulet, F., Mangold, N., Head, J. W., … Roach, L. H. (2009). Composition, Morphology, and Stratigraphy of Noachian Crust around the Isidis basin. *Journal of Geophysical Research: Planets*, *114*(E2). https://doi.org/10.1029/2009JE003349

149. Skok, J. R., Mustard, J. F., Murchie, S. L., Wyatt, M. B., & Ehlmann, B. L. (2010). Spectrally distinct ejecta in Syrtis Major, Mars: Evidence for environmental change at the Hesperian-Amazonian boundary. *Journal of Geophysical Research: Planets*, *115*(E2). https://doi.org/10.1029/2009JE003338

150. Baratoux, D., Toplis, M. J., Monnereau, M., & Sautter, V. (2013). The petrological expression of early Mars volcanism. *Journal of Geophysical Research: Planets*, *118*(1), 59–64. https://doi.org/10.1029/2012JE004234

151. Kargel, J. S., & Strom, R. G. (1992). Ancient glaciation on Mars. *Geology*, *20*(1), 3–7. https://doi.org/10.1130/0091-7613(1992)020<0003:AGOM>2.3.CO;2

152. Head, J. W., & Pratt, S. (2001). Extensive Hesperian-aged south polar ice sheet on Mars: Evidence for massive melting and retreat, and lateral flow and ponding of meltwater. *Journal of Geophysical Research: Planets*, *106*(E6), 12275–12299. https://doi.org/10.1029/2000JE001359

153. Ghatan, G. J., & Head, J. W. (2002). Candidate subglacial volcanoes in the south polar region of Mars: Morphology, morphometry, and eruption conditions. *Journal of Geophysical Research: Planets*, *107*(E7), 2-1-2–19. https://doi.org/10.1029/2001JE001519

154. Fastook, J. L., Head, J. W., Marchant, D. R., Forget, F., & Madeleine, J.-B. (2012). Early Mars climate near the Noachian–Hesperian boundary: Independent evidence for cold conditions from basal melting of the south polar

ice sheet (Dorsa Argentea Formation) and implications for valley network formation. *Icarus*, *219*(1), 25–40. https://doi.org/10.1016/j.icarus.2012.02.013

155. Head, J. W., & Marchant, D. R. (2014). The climate history of early Mars: insights from the Antarctic McMurdo Dry Valleys hydrologic system. *Antarctic Science*, *26*(6), 774–800. https://doi.org/10.1017/S0954102014000686

156. Fastook, J. L., & Head, J. W. (2015). Glaciation in the Late Noachian Icy Highlands: Ice accumulation, distribution, flow rates, basal melting, and top-down melting rates and patterns. *Planetary and Space Science*, *106*, 82–98. https://doi.org/10.1016/j.pss.2014.11.028

157. Kress, A. M., & Head, J. W. (2015). Late Noachian and early Hesperian ridge systems in the south circumpolar Dorsa Argentea Formation, Mars: Evidence for two stages of melting of an extensive late Noachian ice sheet. *Planetary and Space Science*, *109–110*, 1–20. https://doi.org/10.1016/j.pss.2014.11.025

158. Shean, D. E., Head, J. W., & Marchant, D. R. (2005). Origin and evolution of a cold-based tropical mountain glacier on Mars: The Pavonis Mons fan-shaped deposit. *Journal of Geophysical Research: Planets*, *110*(E5). https://doi.org/10.1029/2004JE002360

159. Head, J. W., Neukum, G., Jaumann, R., Hiesinger, H., Hauber, E., Carr, M., … HRSC Co-Investigator Team. (2005). Tropical to mid-latitude snow and ice accumulation, flow and glaciation on Mars. *Nature*, *434*(7031), 346–351. https://doi.org/10.1038/nature03359

160. Hartmann, W. K., Thorsteinsson, T., & Sigurdsson, F. (2002). Comparison of Icelandic and Martian Hillside Gullies, *33*. Presented at the Lunar and Planetary Science Conference. Retrieved from http://adsabs.harvard.edu/abs/2002LPI....33.1904H

161. Hartmann, W. K., Thorsteinsson, T., & Sigurdsson, F. (2003). Martian hillside gullies and icelandic analogs. *Icarus*, *162*(2), 259–277. https://doi.org/10.1016/S0019-1035(02)00065-9

162. Irwin, R. P., Wray, J. J., Mest, S. C., & Maxwell, T. A. (2018). Wind-Eroded Crater Floors and Intercrater Plains, Terra Sabaea, Mars. *Journal of Geophysical Research: Planets*, *123*(2), 445–467. https://doi.org/10.1002/2017JE005270

163. Boatwright, B. D., & Head, J. W. (2019). Fluvial Geology of the Northwest Hellas Region, Mars: Evidence for Localized Drainage and Terrain Inversion, *50*, 2688. Presented at the Lunar and Planetary Science Conference.

164. El Maarry, M. R., Kodikara, J., Wijessoriya, S., Markiewicz, W. J., & Thomas, N. (2012). Desiccation mechanism for formation of giant polygons on Earth and intermediate-sized polygons on Mars: Results from a pre-fracture model. *Earth and Planetary Science Letters*, *323–324*, 19–26. https://doi.org/10.1016/j.epsl.2012.01.016

165. Oehler, D. Z., Mangold, N., Hallet, B., Fairén, A. G., Deit, L. L., Williams, A. J., … Martínez-Frías, J. (2016). Origin and significance of decameter-scale

polygons in the lower Peace Vallis fan of Gale crater, Mars. *Icarus*, *277*, 56–72. https://doi.org/10.1016/j.icarus.2016.04.038

166. Neal, J. T., Langer, A., & Kerr, P. (1968). Giant Desiccation Polygons of Great Basin Playas. https://doi.org/10.1130/0016-7606(1968)79[69:GDPOGB]2.0.CO;2

167. Levy, J., Head, J., & Marchant, D. (2009). Thermal contraction crack polygons on Mars: Classification, distribution, and climate implications from HiRISE observations. *Journal of Geophysical Research: Planets*, *114*(E1). https://doi.org/10.1029/2008JE003273

168. Maarry, M. R. E., Markiewicz, W. J., Mellon, M. T., Goetz, W., Dohm, J. M., & Pack, A. (2010). Crater floor polygons: Desiccation patterns of ancient lakes on Mars? *Journal of Geophysical Research: Planets*, *115*(E10). https://doi.org/10.1029/2010JE003609

169. Yoshikawa, K. (2003). Origin of the polygons and the thickness of Vastitas Borealis Formation in Western Utopia Planitia on Mars. *Geophysical Research Letters*, *30*(12). https://doi.org/10.1029/2003GL017165

170. Mangold, N. (2005). High latitude patterned grounds on Mars: Classification, distribution and climatic control. *Icarus*, *174*(2), 336–359. https://doi.org/10.1016/j.icarus.2004.07.030

171. Hallet, B., Sletten, R., Stewart, W., Williams, R., Mangold, N., Schieber, J., … Kocurek, G. (2013). Fracture Networks, Gale Crater, Mars. *LPI Contributions*, *1719*, 3108.

172. Kerber, L., Dickson, J. L., Head, J. W., & Grosfils, E. B. (2017). Polygonal ridge networks on Mars: Diversity of morphologies and the special case of the Eastern Medusae Fossae Formation. *Icarus*, *281*, 200–219. https://doi.org/10.1016/j.icarus.2016.08.020

173. Brooker, L. M., Balme, M. R., Conway, S. J., Hagermann, A., Barrett, A. M., Collins, G. S., & Soare, R. J. (2018). Clastic polygonal networks around Lyot crater, Mars: Possible formation mechanisms from morphometric analysis. *Icarus*, *302*, 386–406. https://doi.org/10.1016/j.icarus.2017.11.022

174. Soare, R. J., Conway, S. J., & Dohm, J. M. (2014). Possible ice-wedge polygons and recent landscape modification by “wet” periglacial processes in and around the Argyre impact basin, Mars. *Icarus*, *233*, 214–228. https://doi.org/10.1016/j.icarus.2014.01.034

175. Washburn, A. L. (1980). Geocryology, A Survey of Periglacial Processes and Environments. *Geological Magazine*, *117*(5), 503–504. https://doi.org/10.1017/S0016756800028703

176. Mackay, J. (2002). Thermally induced movements in ice-wedge polygons, western arctic coast: a long-term study. https://doi.org/10.7202/004846AR

177. Lachenbruch, A. H. (1966). *CONTRACTION THEORY OF ICE-WEDGE POLYGONS: A QUALITATIVE DISCUSSION*. in: Proc Int Permafrost Conf.

178. Jorgenson, M. T., Shur, Y. L., & Pullman, E. R. (2006). Abrupt increase in permafrost degradation in Arctic Alaska. *Geophysical Research Letters*, *33*(2). https://doi.org/10.1029/2005GL024960

179. Abolt, C. J., Young, M. H., Atchley, A. L., & Harp, D. R. (2018). Microtopographic control on the ground thermal regime in ice wedge polygons. *The Cryosphere*, *12*(6), 1957–1968. https://doi.org/10.5194/tc-12-1957-2018

180. Siebach, K. L., Grotzinger, J. P., Kah, L. C., Stack, K. M., Malin, M., Léveillé, R., & Sumner, D. Y. (2014). Subaqueous shrinkage cracks in the Sheepbed mudstone: Implications for early fluid diagenesis, Gale crater, Mars. *Journal of Geophysical Research: Planets*, *119*(7), 1597–1613. https://doi.org/10.1002/2014JE004623

181. Mangold, N. (2012). Fluvial landforms on fresh impact ejecta on Mars. *Planetary and Space Science*, *62*(1), 69–85. https://doi.org/10.1016/j.pss.2011.12.009

182. Weiss, D. K., & Head, J. W. (2016). Impact ejecta-induced melting of surface ice deposits on Mars. *Icarus*, *280*, 205–233. https://doi.org/10.1016/j.icarus.2016.07.007

183. de Haas, T., Hauber, E., Conway, S. J., van Steijn, H., Johnsson, A., & Kleinhans, M. G. (2015). Earth-like aqueous debris-flow activity on Mars at high orbital obliquity in the last million years. *Nature Communications*, *6*(1), 7543. https://doi.org/10.1038/ncomms8543

184. Fassett, C. I., & Head, J. W. (2008). Valley network-fed, open-basin lakes on Mars: Distribution and implications for Noachian surface and subsurface hydrology. *Icarus*, *198*(1), 37–56. https://doi.org/10.1016/j.icarus.2008.06.016

185. McCauley, J. F., Carr, M. H., Cutts, J. A., Hartmann, W. K., Masursky, H., Milton, D. J., … Wilhelms, D. E. (1972). Preliminary mariner 9 report on the geology of Mars. *Icarus*, *17*(2), 289–327. https://doi.org/10.1016/0019-1035(72)90003-6

186. Andrews-Hanna, J. C. (2012). The formation of Valles Marineris: 2. Stress focusing along the buried dichotomy boundary. *Journal of Geophysical Research: Planets*, *117*(E4). https://doi.org/10.1029/2011JE003954

187. Andrews-Hanna, J. C. (2012). The formation of Valles Marineris: 3. Trough formation through super-isostasy, stress, sedimentation, and subsidence. *Journal of Geophysical Research: Planets*, *117*(E6). https://doi.org/10.1029/2012JE004059

188. Schultz, R. A. (1998). Multiple-process origin of Valles Marineris basins and troughs, Mars. *Planetary and Space Science*, *46*(6), 827–834. https://doi.org/10.1016/S0032-0633(98)00030-0

189. Sharp, R. P. (1973). Mars: Troughed terrain. *Journal of Geophysical Research (1896-1977)*, *78*(20), 4063–4072. https://doi.org/10.1029/JB078i020p04063

190. Frey, H. (1979). Thaumasia: A fossilized early forming tharsis uplift. *Journal of Geophysical Research: Solid Earth*, *84*(B3), 1009–1023. https://doi.org/10.1029/JB084iB03p01009

191. Lucchitta, B. K., Isbell, N. K., & Howington-Kraus, A. (1994). Topography of Valles Marineris: Implications for erosional and structural history. *Journal of*

Geophysical Research: Planets, *99*(E2), 3783–3798. https://doi.org/10.1029/93JE03095

192. Okubo, C. H., & Schultz, R. A. (2005). Evidence of Normal Faulting and Dike Intrusion at Valles Marineris from Pit Crater Topography, *36*. Presented at the 36th Annual Lunar and Planetary Science Conference. Retrieved from http://adsabs.harvard.edu/abs/2005LPI....36.1008O

193. Dohm, J. M., & Tanaka, K. L. (1999). Geology of the Thaumasia region, Mars: plateau development, valley origins, and magmatic evolution. *Planetary and Space Science*, *47*(3), 411–431. https://doi.org/10.1016/S0032-0633(98)00141-X

194. Greeley, R., & Guest, J. (1987). Geologic map of the eastern equatorial region of Mars.

195. Webb, B. M., & Head, J. W., III. (2002). Terrestrial Analogs for Noachian Tectonics of the Tharsis Rise and Thaumasia Plateau, Mars, *33*. Presented at the Lunar and Planetary Science Conference. Retrieved from http://adsabs.harvard.edu/abs/2002LPI....33.1825W

196. Montgomery, D. R., Som, S. M., Jackson, M. P. A., Schreiber, B. C., Gillespie, A. R., & Adams, J. B. (2009). Continental-scale salt tectonics on Mars and the origin of Valles Marineris and associated outflow channels. *GSA Bulletin*, *121*(1–2), 117–133. https://doi.org/10.1130/B26307.1

197. Hager, A., Schedl, A. D., & Ukiwo, O. (2018). Ages of Fault Structures Adjacent and Running Subparallel to Parallel to Valles Marineris, *49*, 2062. Presented at the Lunar and Planetary Science Conference.

198. Baker, V. R., Carr, M. H., Gulick, V. C., Williams, C. R., & Marley, M. S. (1992). Channels and valley networks. *Mars*, 493–522.

199. Quantin, C., Allemand, P., Mangold, N., & Delacourt, C. (2004). Ages of Valles Marineris (Mars) landslides and implications for canyon history. *Icarus*, *172*(2), 555–572. https://doi.org/10.1016/j.icarus.2004.06.013

200. Fueten, F., Flahaut, J., Deit, L. L., Stesky, R., Hauber, E., & Gwinner, K. (2011). Interior layered deposits within a perched basin, southern Coprates Chasma, Mars: Evidence for their formation, alteration, and erosion. *Journal of Geophysical Research: Planets*, *116*(E2). https://doi.org/10.1029/2010JE003695

201. Fergason, R. L., Lee, E. M., & Weller, L. (2013). THEMIS Geodetically Controlled Mosaics of Mars, *44*, 1642. Presented at the Lunar and Planetary Science Conference.

202. Dickson, J. L., Kerber, L. A., Fassett, C. I., & Ehlmann, B. L. (2018). A Global, Blended CTX Mosaic of Mars with Vectorized Seam Mapping: A New Mosaicking Pipeline Using Principles of Non-Destructive Image Editing, *49*, 2480. Presented at the Lunar and Planetary Science Conference.

203. Ivanov, B. A. (2001). Mars/Moon Cratering Rate Ratio Estimates. *Space Science Reviews*, *96*(1), 87–104. https://doi.org/10.1023/A:1011941121102

204. Tanaka, K. L., & Davis, P. A. (1988). Tectonic history of the Syria Planum province of Mars. *Journal of Geophysical Research: Solid Earth*, *93*(B12), 14893–14917. https://doi.org/10.1029/JB093iB12p14893

205. Tanaka, K. L., Golombek, M. P., & Banerdt, W. B. (1991). Reconciliation of stress and structural histories of the Tharsis region of Mars. *Journal of Geophysical Research: Planets*, *96*(E1), 15617–15633. https://doi.org/10.1029/91JE01194

206. Davis, P. A., Tanaka, K. L., & Golombek, M. P. (1995). Topography of Closed Depressions, Scarps, and Grabens in the North Tharsis Region of Mars: Implications for Shallow Crustal Discontinuities and Graben Formation. Retrieved from https://trs.jpl.nasa.gov/handle/2014/29504

207. Plescia, J. B., & Saunders, R. S. (1982). Tectonic history of the Tharsis Region, Mars. *Journal of Geophysical Research: Solid Earth*, *87*(B12), 9775–9791. https://doi.org/10.1029/JB087iB12p09775

208. Banerdt, W. B., Golombek, M. P., & Tanaka, K. L. (1992). Stress and tectonics on Mars, Mars HH Kieffer, et al., 249–297, Univ. of Ariz. *Press, Tucson*.

209. Golombek, M. P. (1979). Structural analysis of lunar grabens and the shallow crustal structure of the Moon. *Journal of Geophysical Research: Solid Earth*, *84*(B9), 4657–4666. https://doi.org/10.1029/JB084iB09p04657

210. Tanaka, K. L. (1990). Tectonic history of the Alba Patera-Ceraunius Fossae region of Mars. In *Lunar and Planetary Science Conference Proceedings* (Vol. 20, pp. 515–523).

211. Senthil Kumar, P., Krishna, N., Prasanna Lakshmi, K. J., Raghukanth, S. T. G., Dhabu, A., & Platz, T. (2019). Recent seismicity in Valles Marineris, Mars: Insights from young faults, landslides, boulder falls and possible mud volcanoes. *Earth and Planetary Science Letters*, *505*, 51–64. https://doi.org/10.1016/j.epsl.2018.10.008

212. Hartmann, W. K. (1973). Martian surface and crust: Review and synthesis. *Icarus*, *19*(4), 550–575. https://doi.org/10.1016/0019-1035(73)90083-3

213. Vamshi, G. T., Martha, T. R., & Vinod Kumar, K. (2014). Origin of collapsed pits and branched valleys surrounding the Ius chasma on Mars. In *ISPRS - International Archives of the Photogrammetry, Remote Sensing and Spatial Information Sciences* (Vol. XL–8, pp. 485–491). Presented at the ISPRS Technical Commission VIII Symposium (Volume XL-8) - 09–12 December 2014, Hyderabad, India, Copernicus GmbH. https://doi.org/10.5194/isprsarchives-XL-8-485-2014

214. Scott, E. D., & Wilson, L. (2002). Plinian eruptions and passive collapse events as mechanisms of formation for Martian pit chain craters. *Journal of Geophysical Research: Planets*, *107*(E4), 4-1-4–11. https://doi.org/10.1029/2000JE001432

215. Witbeck, N. E., Tanaka, K. L., & Scott, D. H. (1991). Geologic map of the Valles Marineris region, Mars. *IMAP*. https://doi.org/10.3133/i2010

216. Lamb, M. P., Howard, A. D., Dietrich, W. E., & Perron, J. T. (2007). Formation of amphitheater-headed valleys by waterfall erosion after large-scale

slumping on Hawai‘i. *GSA Bulletin*, *119*(7–8), 805–822. https://doi.org/10.1130/B25986.1

217. Schmidt, G., Fueten, F., Stesky, R., Flahaut, J., & Hauber, E. (2018). Geology of Hebes Chasma, Mars: 1. Structure, Stratigraphy, and Mineralogy of the Interior Layered Deposits. *Journal of Geophysical Research: Planets*, *123*(11), 2893–2919. https://doi.org/10.1029/2018JE005658

218. Sharp, R. P., & Malin, M. C. (1975). Channels on Mars. *GSA Bulletin*, *86*(5), 593–609. https://doi.org/10.1130/0016-7606(1975)86<593:COM>2.0.CO;2

219. Pieri, D. C. (1980). Martian Valleys: Morphology, Distribution, Age, and Origin. *Science*, *210*(4472), 895–897. https://doi.org/10.1126/science.210.4472.895

220. Howard, A. D. (1986). Groundwater sapping on Mars and Earth. In *Proc., and Field Guide, NASA Groundwater Sapping Conf., AD Howard, RC Kochel, and HE Holt, Eds., National Aeronautics and Space Administration, Flagstaff, Ariz., pp. vi–xiv*.

221. Mangold, N., Quantin, C., Ansan, V., Delacourt, C., & Allemand, P. (2004). Evidence for Precipitation on Mars from Dendritic Valleys in the Valles Marineris Area. *Science*, *305*(5680), 78–81. https://doi.org/10.1126/science.1097549

222. Warner, N. H., Gupta, S., Calef, F., Grindrod, P., Boll, N., & Goddard, K. (2015). Minimum effective area for high resolution crater counting of martian terrains. *Icarus*, *245*, 198–240. https://doi.org/10.1016/j.icarus.2014.09.024

223. Hauber, E., Bleacher, J., Gwinner, K., Williams, D., & Greeley, R. (2009). The topography and morphology of low shields and associated landforms of plains volcanism in the Tharsis region of Mars. *Journal of Volcanology and Geothermal Research*, *185*(1), 69–95. https://doi.org/10.1016/j.jvolgeores.2009.04.015

224. Chojnacki, M., Jakosky, B. M., & Hynek, B. M. (2006). Surficial properties of landslides and surrounding units in Ophir Chasma, Mars. *Journal of Geophysical Research: Planets*, *111*(E4). https://doi.org/10.1029/2005JE002601

225. Marra, W. A., Hauber, E., de Jong, S. M., & Kleinhans, M. G. (2015). Pressurized groundwater systems in Lunae and Ophir Plana (Mars): Insights from small-scale morphology and experiments. *GeoResJ*, *8*, 1–13. https://doi.org/10.1016/j.grj.2015.08.001

226. Cushing, G. E., Okubo, C. H., & Titus, T. N. (2015). Atypical pit craters on Mars: New insights from THEMIS, CTX, and HiRISE observations. *Journal of Geophysical Research: Planets*, *120*(6), 1023–1043. https://doi.org/10.1002/2014JE004735

List of Publications

1. **Harish,** Vijayan S., Nicolas Mangold, and Anil Bhardwaj, Water-ice exposing scarps within the northern mid-latitude craters on Mars, Geophysical Research Letters, 2020.

   https://doi.org/10.1029/2020GL089057
2. **Harish,** Vijayan S., and Nicolas Mangold, Evidence for fluvial and glacial activities within impact craters exposing a Noachian volcanic dome on Mars, Icarus, 361, 114397, 2021.

   https://doi.org/10.1016/j.icarus.2021.114397
3. **Harish** and Vijayan S., Craters in the vicinity of Valles Marineris region, Mars: Chronological implications to the graben and pits activities, Icarus, 343, 113704, 2020.

   https://doi.org/10.1016/j.icarus.2020.113704
4. Vijayan, S., Rishitosh K. Sinha, **Harish** and Ritu Anilkumar, Evidence for Multiple Superposed Fluvial Deposits within Reuyl Crater, Mars, JGR-Planets, 125, e2019JE006136, 2020.

   https://doi.org/10.1029/2019JE006136
5. R.K. Sinha, Vijayan S**.,** M. Bhatt, **Harish,** N. Kumari, N. Srivastava, I. Varatharajan, D. Ray, C. Wohler, and A. Bhardwaj, Geological characterization of Chandrayaan-2 landing site in the southern high latitudes

of the Moon, Icarus, 337, 113449, 2020.
https://doi.org/10.1016/j.icarus.2019.113449

6. E. Shivakarthik, J.K. Meka, **Harish**, V.S. Surendra, K.K. Rahul, R. Thombre, H. Hill, S. Vijayan, and B. Sivaraman, Sticking of dust/ micrometeorite particles on to ices at high impact velocities -Implications for astrochemical ice enrichment, Planetary and Space Science, 104972, 2020.
https://doi.org/10.1016/j.pss.2020.104972
7. A. J. Gawronska, N. Barrett, S. J. Boazman, C. M. Gilmour, S. H. Halim, **Harish,** K. McCanaan, A. V. Satyakumar, J. Shah, H. M. Meyer, and D. A. Kring, Geologic Context and Potential EVA Targets at the Lunar South Pole, Advance in Space Research, 66, 1247-1264, 2020.
https://doi.org/10.1016/j.asr.2020.05.035
8. S. H. Halim, N. Barrett, S. J. Boazman, C. M. Gilmour, A. J. Gawronska, **Harish,** K. McCanaan, A. V. Satyakumar, J. Shah, and D. A. Kring, Numerical modeling of the formation of Shackleton crater at the lunar South Pole, Icarus, 354, 113992, 2021. https://doi.org/10.1016/j.icarus.2020.113992D

Conference Proceedings

1. **Harish,** Kimi KB, Tuhi Saumya, and Vijayan S., “Cerberus Fossae region, Mars: Insights into subsurface lava layers using SHARAD and HiRISE analysis”. 2nd Indian Planetary Science Conference, 2021.

2. **Harish,** Vijayan S., and Nicolas Mangold, "Degana crater, Mars: Evidence for fluvial and glacial landforms on a volcanic dome". 51st Proc. of Lunar and Planetary Science Conference, 2020.
3. **Harish,** N. Barrett, S. J. Boazman, A. J. Gawronska, C. M. Gilmour, S. H. Halim, K. McCanaan, A. V. Satyakumar, J. Shah, and D. A. Kring, "Two types of terrain exposed in the upper crater wall of Shackleton crater, lunar south pole: Implications for future landings". 51st Proc. of Lunar and Planetary Science Conference, 2020.
4. **Harish a**nd Vijayan S., "Evidence for volcanic resurfacing in thesurrounding region ofRavi Vallis,Mars", 1st Indian Planetary Science Conference (IPSC), 2020.
5. **Harish** and Vijayan S., "Understanding chronological evolution of Valles Marineris vicinity region on Mars through grabens, pits and craters". 50th Proc. of Lunar and Planetary Science Conference, 2019.
6. **Harish** and Vijayan S., "Chronological evolution of Valles Marineris vicinity region on Mars through impact craters", National Space Science Symposium (NSSS), 2019.

Publications attached with this thesis

1. **Harish,** Vijayan S., Nicolas Mangold, and Anil Bhardwaj, Water-ice exposing scarps within the northern mid-latitude craters on Mars, Geophysical Research Letters, 2020.

   https://doi.org/10.1029/2020GL089057

2. **Harish,** Vijayan S., and Nicolas Mangold, Evidence for fluvial and glacial activities within impact craters exposing a Noachian volcanic dome on Mars, Icarus, in press, 2021.

   https://doi.org/10.1016/j.icarus.2021.114397

3. **Harish** and Vijayan S., Craters in the vicinity of Valles Marineris region, Mars: Chronological implications to the graben and pits activities, Icarus, 343, 113704, 2020.

   https://doi.org/10.1016/j.icarus.2020.113704

ADVANCING EARTH AND SPACE SCIENCE

Geophysical Research Letters

RESEARCH LETTER
10.1029/2020GL089057

Key Points:
- We report newly identified water-ice deposits exposed by scarps within craters in the northern midlatitude on Mars
- Ice accumulated within last 25 Myr over the pole-facing and 95 Myr over equator-facing walls and exposure time is expected to be ~1 Myr
- Temporal spectral evidence reveals conserved water-ice reservoirs on Mars associated with both pole/equator-facing wall deposits

Supporting Information:
- Supporting Information S1

Correspondence to:
Harish,
harishnandal77@gmail.com

Citation:
Harish, Vijayan, S., Mangold, N., & Bhardwaj, A. (2020). Water-ice exposing scarps within the northern midlatitude craters on Mars. *Geophysical Research Letters*, *47*, e2020GL089057. https://doi.org/10.1029/2020GL089057

Received 27 MAY 2020
Accepted 29 JUN 2020
Accepted article online 8 JUL 2020

Water-Ice Exposing Scarps Within the Northern Midlatitude Craters on Mars

Harish[1,2], S. Vijayan[1], N. Mangold[3], and Anil Bhardwaj[1]

[1]Planetary Science Division, Physical Research Laboratory, Ahmedabad, India, [2]Discipline of Earth Sciences, Indian Institute of Technology, Gandhinagar, India, [3]Laboratoire de Planétologie et Géodynamique, Nantes, CNRS UMR6112, Université de Nantes, Université d'Angers, Nantes, France

Abstract We report new exposures of water ice along the scarps wall located within craters in the northern midlatitude region of Mars using high-resolution imagery and spectral data of Mars Reconnaissance Orbiter. The exposed water-ice deposits are shallower and exhibit 1.5 and 2 μm absorption. These scarps are located on the pole-facing walls and equator-facing wall origin floor deposits which formed over the latitude dependent mantle. Our observations advance in bracketing the younger ice deposits through the crater size-frequency distributions of host craters, which formed around ~25 and ~95 Myr and exposed around ~1 Myr. This reveals that ice transportation, accumulation, compaction, and ice-dust mixing occurred in recent epochs. Our study complements the earlier studies that shallow water ice is spatially widespread and consistent with subsurface water-ice detection by neutron spectrometer. We interpret the ice remnants likely to preserve in craters pole-facing wall and equator-facing wall-associated floor deposits, which demonstrates widespread water-ice resources on Mars.

Plain Language Summary One third of the planet Mars is rich in water ice which is mostly preserved a few meters below the surface. Identification of new water-ice-rich regions is indeed required to understand their spatial spread across Mars. Identification of new water-ice-rich locations will have a vital role in identifying future landing/robotic missions on Mars and even for the in situ resource utilization. Recent high-resolution visible images and infrared wavelength-dependent spectral signature provide more diagnostic evidence for water ice. In this study, we have reported water-ice exposure within two craters located in the northern hemisphere of Mars. These exposures are found in the crater wall and over the crater floor deposits. We found that on one location, the exposed ice is stable after 1 week of interval, this gives a direct proof for the stable exposed ice. We determined that these craters are formed a few tens of million years ago, and deposits occurred likely over a few million years, but the ice deposits within a crater is exposed within a million year ago. We append our new locations to the existing list of identified water-ice deposits and ensure the widespread of water ice few meters below the surface of Mars.

1. Introduction

Water ice on Mars is a vital source for identifying and determining the aqueous history of the planet. The occurrence of shallow ground water ice can be used to infer the snow accumulation processes and related climatic conditions that prevailed on Mars. Also, these shallow water-ice-rich locations can be prime target sites for future missions to Mars (Bandfield, 2007; Dundas et al., 2018; Head et al., 2003; Piqueux et al., 2019) specifically the northern midlatitude regions because of their low elevation and smooth terrain (Piqueux et al., 2019). Precipitation, accumulation, and compaction of snow would have caused formation of massive (few meters to hundreds of meters thick) water-ice layers during the high obliquity (>30°) periods of Mars (Bandfield, 2007; Dundas et al., 2018; Head et al., 2003; Mangold et al., 2004). These compacted shallow water-ice layers are located few meters to tens of meters below the surface and suggested to cover one third of the planet Mars (Bandfield, 2007; Dundas et al., 2018; Mangold et al., 2004).

Shallow ground water ice on Mars can be found in the form of pore filling or massive, nearly pure water ice (Bandfield, 2007; Cull et al., 2010; Dundas et al., 2018; Mangold et al., 2004; Mellon et al., 2009). Dundas et al. (2018) reported exposures of pure water-ice deposits in cliff scarps at eight locations, predominant over the southeastern side of the Hellas basin, and only one location in the northern lowlands within the Milankovič crater. Piqueux et al. (2019) reported widespread shallow water ice in the high latitude and

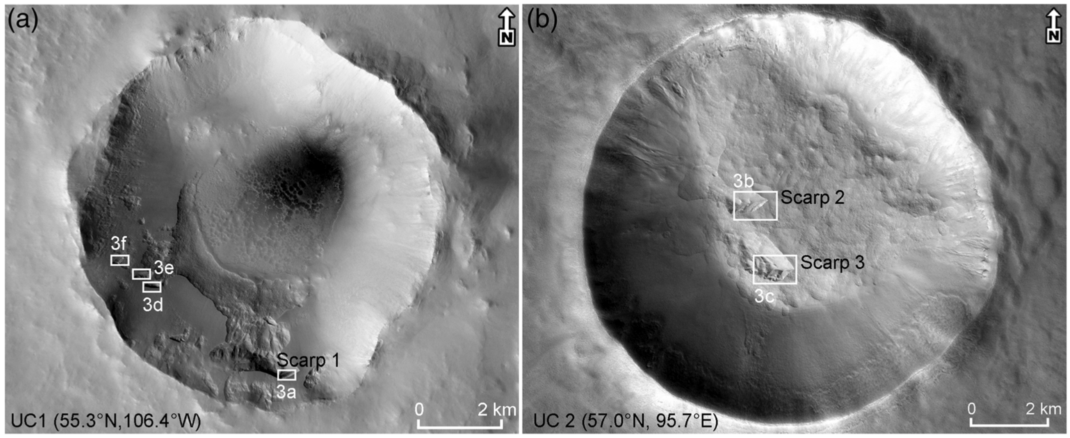

Figure 1. Two unnamed craters (UC1 and UC2) located in the northern lowlands of Mars. (a) UC1 crater with scarps on pole-facing wall. (b) UC2 crater with scarps on its floor.

midlatitude up to 35°N/45°S of Mars based on trends of seasonal surface temperature. However, direct spectral observations of spatially distributed shallow ground water ice in the northern midlatitude are limited. Along with that, earlier studies (Bandfield, 2007; Chamberlain & Boynton, 2007; Jakosky et al., 2005; Mellon & Jakosky, 1995; Mellon et al., 1997, 2004; Schorghofer & Forget, 2012) suggested instability of surface water ice in midlatitude; however, stable ground water ice favored below a dust cover (Dundas et al., 2018; Head et al., 2003; Mangold et al., 2004). Based on the slope orientation, Aharonson and Schorghofer (2006) and Dundas et al. (2018) suggested that water ice can be more preserved over the pole-facing walls of the craters on Mars. Independent of the pole-facing scenario, Vincendon et al. (2010) suggested that shallow ground water ice in the midlatitude region of Mars can survive throughout the whole year. However, the period of accumulation of water ice in the midlatitude regions and its preservation on equator-facing crater walls are not known.

The craters in the midlatitude regions record the history of snow transport across regions, and those craters could be the potential reservoirs to refine our understanding of the recent climatic conditions. We have identified two unnamed craters (UC1 and UC2) in the northern lowlands of Mars (Figures 1 and S1 in the supporting information) with a clear signature of water-ice exposures. The identification of new craters with preserved exposure of water-ice deposits at different spatial extent is indeed important to support the widespread global interpretation of shallow water ice and use as a resource in future manned exploration, landing site, and in situ resource utilization.

2. New Observation and Results

The two unnamed craters identified in this study are shown in Figure 1 (Malin et al., 2007). Figure S1 displays the locations of these two craters along with the other locations of shallow ground water-ice deposits reported by Dundas et al. (2018). Both the craters are ~11 km in diameter, where UC1 is ~1.1 km deep and UC2 is ~800 m deep, with preserved layered ejecta. The Crater UC1 is located to the north of Alba mons (Figures 1a and S1), whereas the Crater UC2 is located to the west of Utopia Planitia (Figures 1b and S1). Spatially, these craters are located ~5,100 km apart but located almost in the same latitude and with exposed scarps (Figure 1). Scarps on Mars are known as erosional features which are interpreted to retreating actively due to the ice sublimation (Dundas et al., 2018). They generally have steep walls (slope > 40°) and reveal the vertical structure of the shallow ground (Dundas et al., 2018). Within the UC1 southern wall, there are four major scarps, few small scarps, and one large scarp with collapsed nature (Figure 1a). Crater UC2 has two scarps, both are located on top of the wall origin floor deposits (Figure 1b).

2.1. Spectral Analysis

The CRISM (Murchie et al., 2007) color composite maps are generated by using the summary product BD_1500 derived similarly to Viviano-Beck et al. (2014). These derived false-color composite images for

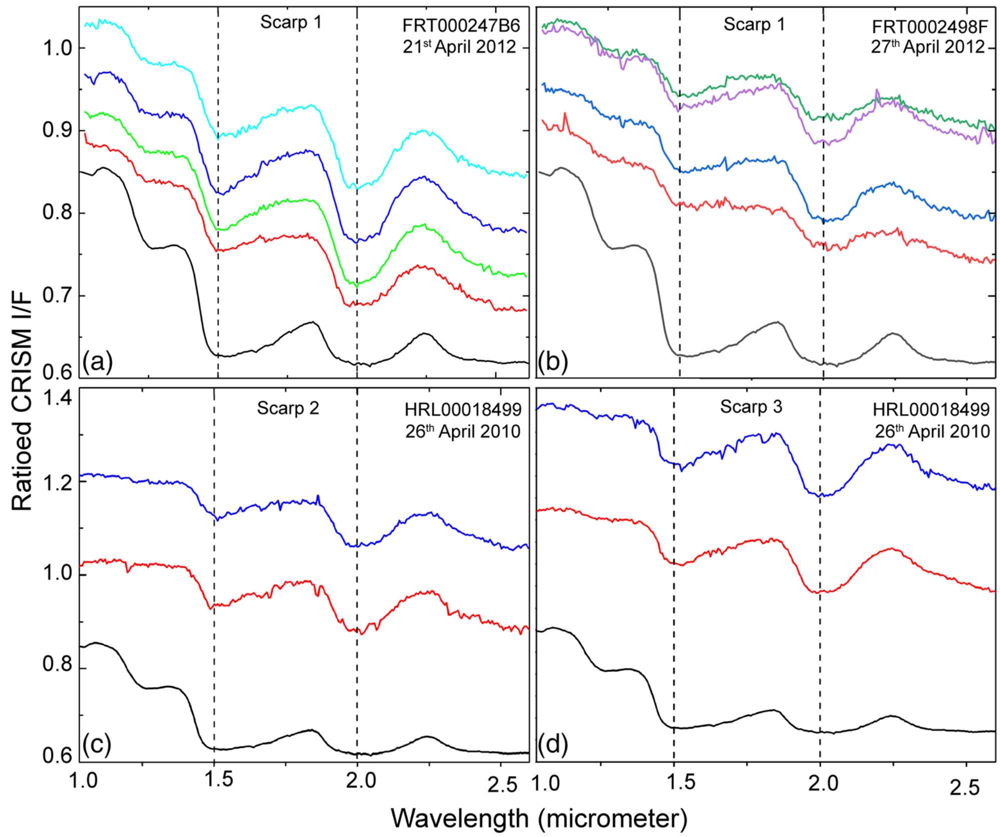

Figure 2. CRISM spectrum. (a) Spectrum for water ice from the scarp1. (b) Spectrum of water ice of the same scarp1 from 1-week temporal CRISM image. (c) Spectrum of water ice from scarp2. (d) Spectrum of water ice from scarp3 (for spectrum locations, refer Figures S4 and S5). (black line) The reference spectrum from MRO-CRISM spectral library (Viviano-Beck et al., 2015).

Craters UC1 (Figure S2) and UC2 (Figure S3) are used to decipher the water-ice regions. From the BD_1500 highlighted water-ice regions (Figure S2b, S2d, and S3b), we extracted the water-ice spectra from 12 regions of interest (Tables S1 and S2), which falls within the scarps (colored boxes in Figures S4 and S5). Figures 2a and 2b show ratioed CRISM spectra from scarp1, located on the pole-facing wall of Crater UC1, using temporal images (Table S1). The spectra extracted from the scarp1 have absorptions near 1.5 and 2 μm wavelength which indicates water ice (Dundas et al., 2018; Viviano-Beck et al., 2015). Apart from the scarp1, no significant signature of water-ice spectra is seen within the Crater UC1 (Figure S2). The possible reasons for the absence of ice signatures could be poor signal-to-noise ratio, location of their exposure, high dust cover, and/or sublimation of ice partially or completely masking the water ice and old scarps with longer exposure time (Cull et al., 2010; Dundas et al., 2018).

Figures 2c and 2d show CRISM spectra for scarp2 and scarp3, which are located on the floor of the Crater UC2 and are characterized by 1.5 and 2 μm absorption which confirms the water-ice deposits. In scarp2, the observed water-ice spectral signatures are spatially spread a few tens of meters along the wall (Figure S5) suggesting their wide exposure within the scarp. In scarp3, the spectral signature of water ice are observed to spread a few tens of meters vertically or across the scarp wall. Though the scarp2 and scarp3 are formed over the floor deposits (Figure 1b), however, these floor deposits originated from the equator-facing wall of Crater UC2 (see section 2.2). Our study reports the unique exposure of water ice from the crater floor deposits, thus providing the evidence for crater floor preserving the ice deposits.

In temporal CRISM spectral signatures (Figures 2a and 2b), variations can be observed in terms of absorptions depth. A shallower absorption is seen in the spectrum after a week (Figure 2b). These images were acquired in MY 31 during the last phase of northern spring similar to Dundas et al. (2018). It may be

10.1029/2020GL089057

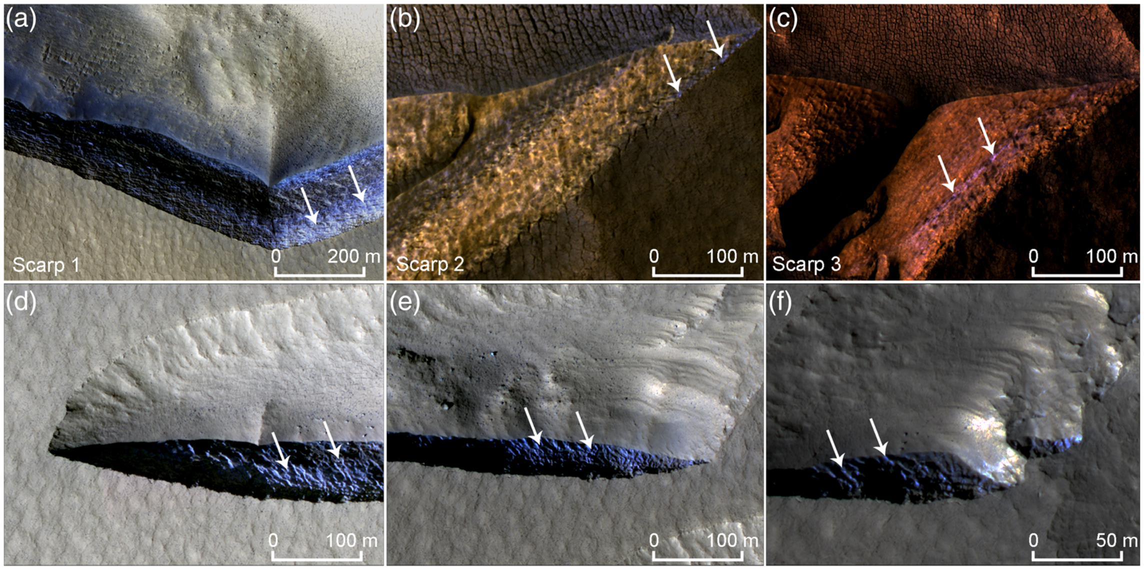

Figure 3. False-colored HiRISE images with bluish-white contrast represent the water-ice-rich regions (a–c), and spectrum shown in Figure 2 were extracted from these scarps. (d)–(f) also show bluish-white color but no prominent water-ice spectra. North is up, and sunlight is from the left in all figures.

noted that though the spectra shown in Figures 2a and 2b are taken from the scarp1, they are not exactly from the same pixels. The factors like dust mixing into ice, difference in pixel, 1-week temporal image, and viewing geometry may be the possible reasons that cause variations in the reflectance spectra. Overall, the small temporal variations of water-ice spectrums provide vital evidence that the exposed water ice can probably last for a certain duration on Mars.

2.2. HiRISE Observations

Figure 3 shows the HiRISE (McEwen et al., 2007) false-color RGB images (Table S3) for water-ice scarps present within both the craters. There are three major scarps (Figures 3a–3c) in which we observed spectral evidence for water ice (Figure 2). In Crater UC1, the scarps are formed over the pole-facing wall (Figure 1a), and scarp1 is located nearly 1 km downward from the southern rim. Figure S6(Quantin-Nataf et al., 2018) shows the vertical structure of the pole-facing crater wall, over which the scarp1 is located, whose steep-sided wall has a slope of ~45° with exposed ice. Crater topographic profile across the scarp1 reveals its steep slope (~45°) at the location where the ice is exposed which is much higher than the average slope of the crater wall (~15°) (Figure S7a). Within the scarp1 (Figure 3a), we observed three layers: an uppermost bluish-white layer similar to Dundas et al. (2018), a middle dark-toned layer appears as dust-covered with non-ice deposits, and a lowermost layer with bluish-white color again. From the uppermost layer, we obtained the water-ice spectral signature (Figures 2a and 2b). We determined the elevation of scarp1 is ~2 km below the Martian geoid. We estimate the uppermost exposed water-ice deposit thickness to be at least ~20 m, whereas the exposed scarp total vertical length is ~150 m after correcting for the regional slope. Due to the absence of the CRISM water-ice spectrum, it is difficult to identify the lowermost bluish layer in HiRISE false color as a water-ice deposit (Figure 3a). The viewing geometry and high slope make it difficult to get any spectrum from this bottommost layer. Hence, we are left out to make photogeological interpretation with HiRISE images. Keszthelyi et al. (2008) reported that the dust deposits may also result in the blue color in the HiRISE imagery. The western part of scarp1 and the adjoining floors are blue which is due to dust mantling (Keszthelyi et al., 2008). However, the third bottommost layer is more toward bluish-white tone, whereas the immediate floor lacks such bluish-white color. This interpretation resulted in hypothesizing that this layer could be one ice layer. Thus, the scarp1 over the pole-facing wall exposed the possible layered ice deposits as anticipated in earlier studies (Dundas et al., 2018; Piqueux et al., 2019). This suggests that the current to past climatic conditions could have formed internal layering (Bramson et al., 2017; Schorghofer & Forget, 2012), and these may be exposed on the scarp1 walls.

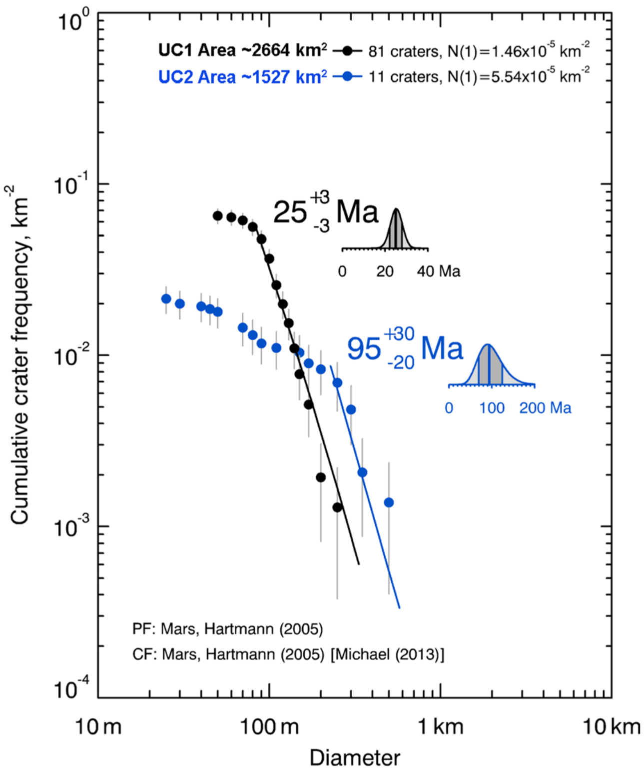

Figure 4. Crater size-frequency distribution ages for the UC1 and UC2 craters using Poisson analysis (Michael, 2013) tend to ~25 and ~95 Ma.

Figure 3b shows the false and enhanced HiRISE color image of scarp2 within the Crater UC2 with very little bluish-white contrast in the upper part of the scarp. The strong spectral signature from this location (Figure 2c) coincides with the HiRISE observations and demonstrates this bluish-white layer as potential water ice. Scarp3 (Figure 3c) within the UC2 crater also shows a thin bluish-white color and has a strong water-ice spectral signature (Figure 2d). The coordinated HiRISE interpretation in scarp2 and scarp3 are highly supported by CRISM spectral signatures (Figures 2c and 2d) and reveal that such a small quantity of ice exposures, if not covered by dust, is capable of being detected by CRISM.

Apart from the spectrally distinguishable water-ice signature within scarps, we observed few scarps with bluish-white tone in UC1 from HiRISE images (Figures 3d–3f). However, these scarps (Figures 3d–3f) do not have any distinguishable spectral signatures from CRISM. These scarps have a bluish-white tone that is notably different from the blue color due to the dust cover (Keszthelyi et al., 2008). We propose that these scarps (Figures 3d–3f) host possible water-ice exposures based on their close vicinity to water-ice-rich scarp1. Moreover, all the scarps are located over the bumpy-textured latitude-dependent-mantled (LDM) unit (Head et al., 2003; Kreslavsky & Head, 2002; Levy et al., 2011). Figure S8 shows the preserved LDM unit over the southern wall, whereas the rest of the southern wall is eroded. Moreover, all the exposed scarps share boundaries with the LDM unit (Figure S8). Therefore, we likely interpret that all the scarps shown in Figures 3d–3f may contain water-ice signatures. However, the role of ice sublimed over a long period (Dundas & Byrne, 2010) is not contested, and these exposures may partially be covered by dust.

In Crater UC2, both the scarps are located within the floor deposits (Figure 1b), The two scarps within UC2 are spatially separated by ~2 km from each other and have an elevation difference of ~100 m. Scarp2 is located on the middle of the floor deposit, whereas scarp3 is located at the toe of the deposits (Figure S7b) (Fergason et al., 2018). Topographic profile across the Crater UC2 and through the scarp2 and scarp3 (Figure S7b) shows a higher slope over the pole-facing wall (~13°) than the equator-facing wall (~9°). This we interpret as that the material from the equator-facing wall deposited over the floor (Berman et al., 2009). The water-ice deposits which currently rest on the crater floor are originated from the equator-facing wall with due erosion of wall material. Based on the UC2 crater observation, we infer that not only the pole-facing wall (Figure S7a) host the ice deposits but also the equator-facing wall origin floor deposits (Figure S7b) host buried ice. Our study provides evidence that both the pole- and equator-facing walls of craters are likely for snow accumulation and preservation of water ice.

Other scarps within the UC1 crater (Figure S9) that are located near the smooth LDM unit (Kreslavsky & Head, 2002) lack HiRISE bluish-white tone and water-ice signature. The possible reason could be that these scarps are older exposures, where the ice could have sublimed over the time (Dundas & Byrne, 2010; Vincendon et al., 2010) and currently appear as dry scarp. These dry scarps are different from the water-ice-rich scarps as they lack a bluish-white tone in the HiRISE images (Dundas et al., 2018). Dry scarps with complete lack of water ice (Figure S9) could be used to infer that whether the ice reported within the scarp1 is exposed or seasonal deposits (Schorghofer & Edgett, 2006).

2.3. Chronological Relationship

Crater ejecta is used to estimate the upper ages for the ice exposures. Crater size-frequency distribution for Crater UC1 (Figures 4 and S10) tends $n = 101$, whose diameter ranges from ~60 to ~300 m. The derived best fit model age for Crater UC1 formation is ~25 Myr by fitting 81 craters with diameter >85 m (Figure 4). This age represents the crater formation age, whereas all the scarps formed over the wall will be younger than the smooth LDM unit. The tentative age of the smooth unit is estimated to infer the possible time frame after which the scarps have formed. The smooth unit surrounding the scarp1 (Figure S8) lacks superposed craters even at HiRISE resolution. In this regard, we utilized tens of meter-scale bumpy texture (Head et al., 2003; Levy et al., 2011) of the smooth unit (Figure S8), which formed due to the ice mantling. Such texture could hide or have deformed the small craters <20 m in diameter. Thus, considering this limit, we have determined that the crater density would be given by the presence of one crater of typical size 20-30 m and plotted the same in the differential plot of Hartmann (2005). The plot shows (Figure S11) that it is statistically likely that the tentative age of the smooth unit is ~1 Myr or younger (Viola, 2020), and the scarp1 could have exposed the water ice in last 1 Myr.

For Crater UC2, crater count statistics over the ejecta tend $n = 31$, and the diameter of the craters ranges from ~30 to ~515 m. We obtained the best fit model age as ~95 Myr, by fitting 11 craters whose diameter is greater than ~200 m (Figure 4). This crater floor is hummocky and lacks superposed craters. Thus, we limited our chronological interpretation only from crater ejecta. We infer that the Crater UC2 either represents an older ice deposit (postcrater formation) contained within the wall deposits that are exposed more recently or it represents a younger material accumulated more recently during the high obliquity of Mars (Laskar et al., 2004; Viola et al., 2015). Irrespective of any scenario, UC2 reveals that within the last 95 Myr, the obliquity and climatic conditions favored equator-facing wall deposits within the midlatitude craters on Mars (Dickson et al., 2012). Crater UC1 provides evidence for ice precipitation and accumulation over the pole-facing wall occurred within the last 25 Myr (Viola et al., 2015). Regardless of the crater formation age, the ice deposits exposed in these two craters reveal that these scarps are formed recently compared to impact craters age, due to which they are capable of retaining the exposed water-ice till present.

3. Discussion

Water-ice deposits have been identified in the northern plains of Mars using Neutron spectroscopy (Feldman et al., 2002; Mangold et al., 2004) and seasonal surface temperature variations (Bandfield, 2007; Piqueux et al., 2019), suggesting they will be shallow (<1- to 2-m depth). Figure S12 reveals the correlation between the locations of water ice in the middle-to-high latitudes (Mangold et al., 2004), and our reported craters match unprecedentedly. Hence, our results are consistent with orbital detection of hydrogen at shallow depth (Bandfield, 2007; Dundas et al., 2018; Feldman et al., 2002; Mangold et al., 2004), but we add to this story that both pole- and equator-facing (Aharonson & Schorghofer, 2006; Sinha & Vijayan, 2017) deposits within the craters could host significantly preserved water ice. The water-ice/glacial origin deposits are predominantly observed only in the pole-facing walls within craters (Aharonson & Schorghofer, 2006; Dundas et al., 2018; Sinha & Vijayan, 2017). In contrast, deposits over the equator-facing walls remain an enigma. The equator-facing walls are more prevalent to the gully and glacial origin landforms with preserved ice deposits between ~45° and 60° (Berman et al., 2009; Dickson et al., 2012) during the Amazonian period. In UC2, we anticipate that ice possibly accumulated all over the crater wall and this is evident from the LDM mantling (Figure 1b). Dickson et al. (2012) suggested that net accumulation of ice occurs on all surfaces within craters poleward of ~45°. The UC2 crater floor hosts a thick deposit (>100 m) with a continuous association with the N-NE wall. Using the topographic profile (Figure S7b), we interpreted that this deposit has been eroded from the equator-facing wall and settled over the floor. Thus, a significant contribution of floor material is obtained from the equator-facing wall deposits (Figure S7b), where it remains preserved until younger epochs. Such a scenario can be explained by the obliquity trends on Mars that change over time (Laskar et al., 2004; Viola et al., 2015).

In this scenario, the adjoining question that arises is whether all the wall deposits will host water ice. It is anticipated that these two craters are spatially apart by 5,100 km and similar water-ice deposits are reported in previous studies which suggested a global middle- to high- latitude distribution of ice on Mars (Bandfield, 2007; Dundas et al., 2018; Mangold et al., 2004). To infer whether the water-ice deposits within craters are subsurface exposures or they are related to seasonal frost, we interpreted that (1) the water-ice-rich scarp1 (Figure 1a) and the dry scarps (Figure S9) are located only ~1 km apart and located within the same elevation range. If seasonally driven topographically controlled ice mantled on the scarp1, then such deposits are anticipated in these nearby scarps (Figure S9). However, no spectral or geomorphic evidence for water ice is found in these dry scarps. (2) The average temperature value at the scarp1 (minimum 228 K; Table S4) (Christensen et al., 2004) is above the likely frost point of water (Dundas et al., 2018).

Therefore, in line to the previous evidence (Dundas et al., 2018), we suggest that the ice exposed by the scarps is subsurface ice rather than persistent seasonal frost (Dundas et al., 2018). The following mechanisms can be possible for this subsurface ice: (1) snow accumulation and compaction (Dundas et al., 2018), (2) water-vapor diffusion (Fisher, 2005), and (3) growth of ice lenses (Sizemore et al., 2015). Dundas et al. (2018) reported that the last two mechanisms usually occur only at shallow depth and they are slow processes. The interpretation of LDM units mantled around the craters suggests the snow accumulation and compaction (Head et al., 2003; Schon et al., 2009) with dust as the most likely process responsible for the ice deposits. It is likely that initially ice/snow would have accumulated by the atmospheric precipitation and later vapor diffusion process (Fisher, 2005) cannot be ruled out.

Scarps within the crater floor and walls reveal the preserved vertical structure of young ice deposits at midlatitudes. The 1-week interval spectral signatures provide evidence that the current temperature and pressure conditions on Mars are not subliming the ice or that the sublimation rate is slow (Chamberlain & Boynton, 2007; Jakosky et al., 2005; Schorghofer & Forget, 2012). Though the temporal difference is short, it provides spectral evidence that the ice on Mars can be exposed on the surface for quite a long time (Dundas et al., 2014; Vincendon et al., 2010). The possible layered ice deposits within the scarp1 (Figure 3a) over the pole-facing wall and UC2 crater equator-facing wall origin floor-ice deposits likely indicate multiple cycles of deposition of ice-rich mantles or linked to obliquity conditions (Berman et al., 2009; Dickson et al., 2012).

4. Conclusions

We demonstrated the sustainability of shallow ground water-ice deposits on Mars using spectral observations of CRISM and morphological observations of HiRISE. We have shown strong evidence that the pole-facing wall deposits and equator-facing wall-associated floor deposits within the craters at midlatitudes contain buried shallow water ice. Our study provides evidence for the water-ice deposits preserved and exposed on the crater floor which originated from the equator-facing wall. The exposure of water-ice deposits on the floor specifically implies that the midlatitude craters with pole/equator facing deposits can be potential reservoirs for water ice which depends on the period and obliquity of Mars. Our chronological analysis reveals evidence for snow precipitation, accumulation, and compaction of water ice within the last 25 Myr and expose by scarps within the last 1 Myr in UC1 crater. Thus, we interpret that the pole-facing walls and equator-facing wall origin deposits within northern midlatitude craters are more likely to preserve shallow ground water ice, which can be of prime interest for future robotic/human missions to Mars and vital for understanding the climatic conditions that prevailed at different epochs.

Data Availability Statement

All the data used are available online (http://ode.rsl.wustl.edu/mars and http://global-data.mars.asu.edu/bin/themis.pl).

Acknowledgments

The work at the Physical Research Laboratory was supported by the Department of Space, India. N. M. acknowledges the support from the Centre National d'Etudes Spatiales (CNES), France. We thank one anonymous reviewer, Selby Hearth, and the Editor Andrew J. Dombard for constructive suggestions. We thank the MRO and MO mission team for acquiring the CTX, HiRISE, CRISM, and THEMIS images. We thank the NASA AMES Stereo Pipeline and MarsSI for developing CTX-DEM.

References

Aharonson, O., & Schorghofer, N. (2006). Subsurface ice on Mars with rough topography. *Journal of Geophysical Research*, *111*, E11007. https://doi.org/10.1029/2005JE002636

Bandfield, J. L. (2007). High-resolution subsurface water-ice distributions on Mars. *Nature*, *447*(7140), 64–67. https://doi.org/10.1038/nature05781

Berman, D. C., Crown, D. A., & Bleamaster, L. F. III (2009). Degradation of mid-latitude craters on Mars. *Icarus*, *200*(1), 77–95. https://doi.org/10.1016/j.icarus.2008.10.026

Bramson, A. M., Byrne, S., & Bapst, J. (2017). Preservation of mid-latitude ice sheets on Mars. *Journal of Geophysical Research: Planets*, *122*, 2250–2266. https://doi.org/10.1002/2017JE005357

Chamberlain, M. A., & Boynton, W. V. (2007). Response of Martian ground ice to orbit-induced climate change. *Journal of Geophysical Research*, *112*, E06009. https://doi.org/10.1029/2006JE002801

Christensen, P. R., Jakosky, B. M., Kieffer, H. H., Malin, M. C., McSween, H. Y., Nealson, K., et al. (2004). The Thermal Emission Imaging System (THEMIS) For The Mars 2001 Odyssey Mission. *Space Science Reviews*, *110*, 85–130. https://doi.org/10.1023/B:SPAC.0000021008.16305.94

Cull, S., Arvidson, R. E., Mellon, M. T., Skemer, P., Shaw, A., & Morris, R. V. (2010). Compositions of subsurface ices at the Mars Phoenix landing site. *Geophysical Research Letters*, *37*, L24203. https://doi.org/10.1029/2010GL045372

Dickson, J. L., Head, J. W., & Fassett, C. I. (2012). Patterns of accumulation and flow of ice in the mid-latitudes of Mars during the Amazonian. *Icarus*, *219*(2), 723–732. https://doi.org/10.1016/j.icarus.2012.03.010

Dundas, C. M., Bramson, A. M., Ojha, L., Wray, J. J., Mellon, M. T., Byrne, S., et al. (2018). Exposed subsurface ice sheets in the Martian mid-latitudes. *Science*, *359*(6372), 199–201. https://doi.org/10.1126/science.aao1619

Dundas, C. M., & Byrne, S. (2010). Modeling sublimation of ice exposed by new impacts in the martian mid-latitudes. *Icarus*, *206*(2), 716–728. https://doi.org/10.1016/j.icarus.2009.09.007

Dundas, C. M., Byrne, S., McEwen, A. S., Mellon, M. T., Kennedy, M. R., Daubar, I. J., & Saper, L. (2014). HiRISE observations of new impact craters exposing Martian ground ice. *Journal of Geophysical Research: Planets*, *119*, 109–127. https://doi.org/10.1002/2013JE004482

Feldman, W. C., Boynton, W. V., Tokar, R. L., Prettyman, T. H., Gasnault, O., Squyres, S. W., et al. (2002). Global distribution of neutrons from Mars: Results from Mars Odyssey. *Science*, *297*(5578), 75–78. https://doi.org/10.1126/science.1073541

Fergason, R. L., Hare, T. M., & Laura, J. (2018). HRSC and MOLA Blended Digital Elevation Model at 200 m v2, Astrogeology PDS Annex, U.S. Geological Survey, http://bit.ly/HRSC_MOLA_Blend_v0

Fisher, D. A. (2005). A process to make massive ice in the Martian regolithusing long-term diffusion and thermal cracking. *Icarus*, *179*(2), 387–397. https://doi.org/10.1016/j.icarus.2005.07.024

Hartmann, W. K. (2005). Martian cratering 8: Isochron refinement and chronology of Mars. *Icarus*, *174*(2), 294–320. https://doi.org/10.1016/j.icarus.2004.11.023

Head, J. W., Mustard, J. F., Kreslavsky, M. A., Milliken, R. E., & Marchant, D. R. (2003). Recent ice ages on Mars. *Nature*, *426*(6968), 797–802. https://doi.org/10.1038/nature02114

Jakosky, B. M., Mellon, M. T., Varnes, E. S., Feldman, W. C., Boynton, W. V., & Haberle, R. M. (2005). Mars low-latitude neutron distribution: Possible remnant near-surface water-ice and a mechanism for its recent emplacement. *Icarus*, *175*(1), 58–67. https://doi.org/10.1016/j.icarus.2004.1011.1014

Keszthelyi, L., Jaeger, W., McEwen, A., Tornabene, L., Beyer, R. A., Dundas, C., & Milazzo, M. (2008). High-Resolution Imaging Science Experiment (HiRISE) images of volcanic terrains from the first 6 months of the Mars Reconnaissance Orbiter primary science phase. *Journal of Geophysical Research*, *113*, E04005. https://doi.org/10.1029/2007JE002968

Kreslavsky, M. A., & Head, J. W. (2002). Mars: Nature and evolution of young latitude-dependent water-ice-rich mantle. *Geophysical Research Letters*, *29*(15), 1719. https://doi.org/10.1029/2002GL015392

Laskar, J., Correia, A. C., Gastineau, M., Joutel, F., Levrard, B., & Robutel, P. (2004). Long term evolution and chaotic diffusion of the insolation quantities of Mars. *Icarus*, *170*(2), 343–364. https://doi.org/10.1016/j.icarus.2004.04.005

Levy, J. S., Head, J. W., & Marchant, D. R. (2011). *Gullies, polygons, and mantles in Martian permafrost environments: Cold desert landforms and sedimentary processes during recent Martian geological history*, *Special Publications* (Vol. 354, pp. 167–182). London: Geological Society. https://doi.org/10.1144/SP354.10

Malin, M. C., Bell, J. F. III, Cantor, B. A., Caplinger, M. A., Calvin, W. M., Clancy, R. T., et al. (2007). Context Camera investigation onboard the Mars Reconnaissance Orbiter. *Journal of Geophysical Research*, *112*, E05S04. https://doi.org/10.1029/2006JE002808

Mangold, N., Maurice, S., Feldman, W. C., Costard, F., & Forget, F. (2004). Spatial relationships between patterned ground and ground ice detected by the neutron spectrometer on Mars. *Journal of Geophysical Research*, *109*, E08001. https://doi.org/10.1029/2004JE002235

McEwen, A. S., Eliason, E. M., Bergstrom, J. W., Bridges, N. T., Hansen, C. J., Delamere, W. A., et al. (2007). Mars Reconnaissance Orbiter's High-Resolution Imaging Science Experiment (HiRISE). *Journal of Geophysical Research*, *112*, E05S02. https://doi.org/10.1029/2005JE002605

Mellon, M. T., Arvidson, R. E., Sizemore, H. G., Searls, M. L., Blaney, D. L., Cull, S., et al. (2009). Ground ice at the Phoenix landing site: Stability state and origin. *Journal of Geophysical Research*, *114*, E00E07. https://doi.org/10.1029/2009JE003417

Mellon, M. T., Feldman, W. C., & Prettyman, T. H. (2004). The presence and stability of ground ice in the southern hemisphere of Mars. *Icarus*, *169*(2), 324–340. https://doi.org/10.1016/j.icarus.2003.10.022

Mellon, M. T., & Jakosky, B. (1995). The distribution and behavior of Martian ground ice during past and present epochs. *Journal of Geophysical Research*, *100*(E6), 11,781–11,799. https://doi.org/10.1029/95JE01027

Mellon, M. T., Jakosky, B. M., & Postawko, S. E. (1997). The persistence of equatorial ground ice on Mars. *Journal of Geophysical Research*, *102*(E8), 19,357–19,369. https://doi.org/10.1029/97JE01346

Michael, G. G. (2013). Planetary surface dating from crater size-frequency distribution measurements: Multiple resurfacing episodes and differential isochron fitting. *Icarus*, *226*(1), 885–890. https://doi.org/10.1016/j.icarus.2013.07.004

Murchie, S., Arvidson, R., Bedini, P., Beisser, K., Bibring, J. P., Bishop, J., et al. (2007). Compact Reconnaissance Imaging Spectrometer for Mars (CRISM) on Mars Reconnaissance Orbiter (MRO). *Journal of Geophysical Research*, *112*, E05S03. https://doi.org/10.1029/2006JE002682

Piqueux, S., Buz, J., Edwards, C. S., Bandfield, J. L., Kleinböhl, A., Kass, D. M., Hayne, P. O., The MCS, & THEMIS Teams (2019). Widespread shallow water ice on mars at high latitudes and midlatitudes. *Geophysical Research Letters*, *46*, 14,290–14,298. https://doi.org/10.1029/2019GL083947

Quantin-Nataf, C., Lozac'h, L., Thollot, P., Loizeau, D., Bultel, B., Fernando, J., et al. (2018). MarsSI: Martian surface data processing information system. *Planetary and Space Science*, *150*, 157–170. https://doi.org/10.1016/j.pss.2017.09.014

Schon, S. C., Head, J. W., & Milliken, R. E. (2009). A recent ice age on Mars: Evidence for climate oscillations from regional layering in mid-latitude mantling deposits. *Geophysical Research Letters*, *36*, L15202. https://doi.org/10.1029/2009GL038554

Schorghofer, N., & Edgett, K. S. (2006). Seasonal surface frost at low latitudes on Mars. *Icarus*, *180*(2), 321–334. https://doi.org/10.1016/j.icarus.2005.08.022

Schorghofer, N., & Forget, F. (2012). History and anatomy of subsurface ice on Mars. *Icarus*, *220*(2), 1112–1120. https://doi.org/10.1016/jicarus.2012.07.003

Sinha, R. K., & Vijayan, S. (2017). Geomorphic investigation of craters in Alba Mons, Mars: Implications for Late Amazonian glacial activity in the region. *Planetary and Space Science*, *144*, 32–48. https://doi.org/10.1016/j.pss.2017.05.014

Sizemore, H. G., Zent, A. P., & Rempel, A. W. (2015). Initiation and growth of Martian ice lenses. *Icarus*, *251*, 191–210. https://doi.org/10.1016/j.icarus.2014.04.013

Vincendon, M., Mustard, J., Forget, F., Kreslavsky, M., Spiga, A., Murchie, S., & Bibring, J.-P. (2010). Near-tropical subsurface ice on Mars. *Geophysical Research Letters*, *37*, L01202. https://doi.org/10.1029/2009GL041426

Viola, D. (2020). Age-dating of ice-rich mid-latitude mantle deposits on Mars. 51st Lunar and Planetary Science Conference, abstract#2872.

Viola, D., McEwen, A. S., Dundas, C. M., & Byrne, S. (2015). Expanded secondary craters in the Arcadia Planitia region, Mars: Evidence for tens of Myr-old shallow subsurface ice. *Icarus*, *248*, 190–204. https://doi.org/10.1016/j.icarus.2014.10.032

Viviano-Beck, C. E., Seelos, F. P., Murchie, S. L., Kahn, E. G., Seelos, K. D., Taylor, H. W., et al. (2014). Revised CRISM spectral parameters and summary products based on the currently detected mineral diversity on Mars. *Journal of Geophysical Research: Planets*, *119*, 1403–1431. https://doi.org/10.1002/2014JE004627

Viviano-Beck, C. E. et al. (2015). MRO CRISM Type Spectra Library, NASA Planetary Data System. https://crismtypespectra.rsl.wustl.edu

Icarus 361 (2021) 114397

Contents lists available at ScienceDirect

Icarus

journal homepage: www.elsevier.com/locate/icarus

Evidence for fluvial and glacial activities within impact craters that excavated into a Noachian volcanic dome on Mars

Harish [a,b], S. Vijayan [a,*], N. Mangold [c]

[a] Planetary Science Division, Physical Research Laboratory, Ahmedabad 380009, India
[b] Discipline of Earth Sciences, Indian Institute of Technology, Gandhinagar, India
[c] Laboratoire de Planétologie et Géodynamique, Nantes, CNRS UMR6112, Université de Nantes, Université d'Angers, 44322 Nantes, France

A B S T R A C T

Impact craters on Mars preserve diverse records of volcanic, fluvial, and glacial activities. Enigmatically, the preservation of these major activities or records altogether within impact craters is rare. We report one such new observation of impact craters that formed on a volcanic dome studied using data from the Mars Reconnaissance Orbiter's (MRO) Context Camera (CTX), High-Resolution Imaging Science Experiment (HiRISE), and Compact Reconnaissance Imaging Spectrometer for Mars (CRISM), Mars Global Surveyor's Mars Orbiter Laser Altimeter (MOLA), and Mars Express' High-Resolution Stereo Camera (HRSC). A ~ 20 km diameter impact crater, informally named as Degana-A, is formed within the ~50 km diameter impact crater Degana. Mineralogical analysis reveals exposures of low-calcium pyroxene and olivine deposits, which occupy Degana-A's eastern walls, leading to the idea that pristine Noachian bedrocks might be exposed from beneath the volcanic dome. Degana-A floor is completely covered by alluvial fans from all sides with distributaries. Within Degana crater, multiple fans are observed along its eastern to southern side only. The most likely source of water was the accumulation of snow on Degana crater walls, which possibly melted as a result of the impact of Degana-A. We observed a ~ 1 km wide breach on the eastern wall of Degana-A and the estimated maximum flow velocity is ~2 m/s and a run-off ~2.25 mm/h. Over the south-facing walls, multiple moraine-like ridges superposed the fans, which suggests overprinting by glacial activities. The presence of fans and superposed moraine-like ridges located at the mid-latitudes (~23°S) implies atmosphere-derived snow/ice precipitation was possible. Chronologically, the dome is of Noachian age, whereas Degana crater formed in the Hesperian period and crater retention on the fans indicates late Hesperian to Amazonian ages. Overall, the preserved Noachian crustal material underneath a volcanic dome is rarely exposed in its pristine context, which offers a rare window into early igneous processes. This intriguing location also witnessed a climatic transition as implied by water/ice derived landforms formed by non-coeval events.

1. Introduction

Sedimentary deposits on Mars retain the record of ancient environments and prevailing climatic conditions (Moore and Howard, 2005; Kraal et al., 2008; Blair and McPherson, 2009; Grant and Wilson, 2011; Morgan et al., 2012; Morgan et al., 2014; Wilson et al., 2021). Sedimentary deposits are more developed in the Late Noachian and Early Hesperian epochs, where they are frequently associated with widespread mineralogical assemblages as observed in-situ at Gale crater (e.g., Bristow et al., 2018) and from orbit (e.g., Carter et al., 2013). However, among the various sedimentary deposits observed on Mars, mid-latitude alluvial fans date predominantly from the Late Hesperian-Early Amazonian epochs, so they are of great interest as they represent fluvial activity that occurred after a potential climatic optimum of the Noachian (Moore and Howard, 2005; Kraal et al., 2008; Grant and Wilson, 2011; Morgan et al., 2012; Mangold et al., 2012a, 2012b; Kite et al., 2017; Wilson et al., 2021). Although many studies have described alluvial fans, their origin remains debated among several hypotheses: snowmelt versus rainfall (e.g. Milton, 1973; Hoke and Hynek, 2009; Di Achille and Hynek, 2010a, 2010b; Wordsworth et al., 2013; Kite et al., 2013; Vijayan et al., 2020), transient or stable climatic conditions (Moore and Howard, 2005; Armitage et al., 2011; Grant and Wilson, 2011, 2012; Kite et al., 2017), the role of impact or volcanic activity in melting water ice (e.g., Gulick, 2001; Hauber et al., 2005; Williams et al., 2009; Ansan and Mangold, 2013). Thus, finding key locations to better understand these processes is an important challenge to provide answers on Martian climate change.

In this context, we present new observations of fluvial and glacial landforms in Degana crater (23.72°S, 314.50°E), an impact crater that formed on a volcanic dome (Xiao et al., 2012) (Fig. 1). Xiao et al. (2012) mapped almost all the ancient volcanoes on Mars, excluding the Tharsis region. Their study identified the region over which Degana crater is located as a huge Noachian-age volcanic dome. They suggested these domes are mostly conical in shape and lack calderas. However, no direct observation has yet been made to show that they host fluvial deposits and glacial landforms. Likewise, no mineralogical analysis has been

* Corresponding author at: Planetary Science Division, Physical Research Laboratory, Ahmedabad 380009, India.
E-mail address: vijayan@prl.res.in (S. Vijayan).

https://doi.org/10.1016/j.icarus.2021.114397
Received 13 February 2020; Received in revised form 17 February 2021; Accepted 18 February 2021
Available online 25 February 2021
0019-1035/

carried out over this volcanic dome to decipher the Noachian mineralogy. Thus, this region offers a unique chance to observe volcanic, impact, glacial, and fluvial landforms in the same location, assessing whether the processes that formed them occurred in concert or not. In addition, the composition of such Noachian volcanoes is critical to understand the evolution of ancient volcanic crust on Mars (Xiao et al., 2012). In this study, we will provide new information about the geological context and bedrock composition and characterize the morphology of the fluvial and glacial landforms. We established the relative stratigraphic relationships between the volcanic dome, impact craters, fluvial deposits, and glacial landforms within both impact craters. Then, we performed quantitative analysis on the fluvial and glacial landforms to constrain their extent and timing. Also, using crater-size frequency analysis, we determined the apparent ages of these processes. At last, we discuss the formation hypothesis for the fluvial and glacial deposits and the climatic evolution of Mars.

2. Data and methods

For the geomorphological analysis, we used ~6 m/px Mars Reconnaissance Orbiter (MRO)-Context Camera (CTX), and ~ 25 cm/px MRO-High-Resolution Imaging Science Experiment (HiRISE) images (Malin et al., 2007; McEwen et al., 2007). For the topographic analyses, we used ~463 m/px Mars Global Surveyor (MGS)-Mars Orbiter Laser Altimeter (MOLA) DEM (Smith et al., 2001), and the ~200 m/px Mars Express (MEX)-High-Resolution Stereo Camera (HRSC) – MGS MOLA blended DEM (Fergason et al., 2018). We also used high-resolution CTX DEM and HiRISE DEMs (wherever available), generated using the open-source pipeline of MarsSI (Quantin-Nataf et al., 2018).

For the mineralogical analysis, we used data by the MRO-Compact Reconnaissance Imaging Spectrometer for Mars (CRISM), a hyperspectral camera (Murchie et al., 2007). CRISM used two detectors with 544 channels in the visible to the near-infrared spectral region (0.4 to 4.0 μm) (Murchie et al., 2007). In this study, CRISM data analysis was performed using both S-detector (VNIR) and L-detector (IR) datasets (Murchie et al., 2007). The short wavelength (VNIR) data ranges from 0.36 to 1.05 μm, while the long-wavelength (IR) data ranges from 1.0 to 3.92 μm. The analysis was performed using the CRISM Analysis Toolkit (CAT) plug-in added to ENVI 4.5. CRISM observations were converted into I/F reflectances by applying corrections for instrumental artifacts (Murchie et al., 2007). Degana crater includes only one full resolution targeted (FRT00023F32), which was processed to correct for photometric, and atmospheric noise in the spectral data using the method suggested by Murchie et al. (2007) and Flahaut et al. (2010).

For identifying the composition, we used the spectral parameters OLINDEX2, LCPINDEX, and HCPINDEX mentioned in Viviano-Beck et al. (2014). OLINDEX2 is the modified olivine parameter that measures olivine's 1.0 μm band depth in the presence of spectral slopes (Salvatore et al., 2010). LCPINDEX and HCPINDEX are the low Calcium-pyroxene and high Calcium-pyroxene parameters, respectively, that measure the pyroxene's 1.0 μm and 2.0 μm band depth (Pelkey et al., 2007). The regions highlighted in spectral parameters were examined in more detail to get a diagnostic spectral signature. Areas with strong spectral absorption signatures were used to determine the region of interest (ROI) and spectra were taken from ROIs of several pixels. We used a minimum of 3*3 pixels ROI for each average spectrum considered in this study (Table 1). We used spectral data in the wavelength range from 0.5 to 2.6 μm by integrating the VNIR and IR data to confirm the mineral absorptions of the Fe-bearing phases, which generally turned up around 1 μm (Sun and Milliken, 2015). The selected ROI spectra were ratioed with the neutral spectra, mostly a dust-rich area obtained from the same column (Ehlmann et al., 2009) to enhance the spectral features. We calculated the ratioed spectra for each detector (VNIR and IR) separately and then integrated them. We also removed the overlapping spectral data from 1.0 to 1.05 μm in the S-detector and L-detector datasets as suggested by Murchie et al. (2007).

Table 1
Details of center pixel and the number of pixels used for the spectra shown in Fig. 4b,c.

Labels	Center pixel/Pixels	Number of pixels
Fig. 4b		
P1 (numerator); (denominator)	X:551, Y:344; X:551, Y:301	5*5
P2 (numerator); (denominator)	X:370, Y:358; X:370, Y:149	3*3
P3 (numerator); (denominator)	X:575, Y:338; X:575, Y:282	5*5
P4 (numerator); (denominator)	X:323, Y:283; X:323, Y:96	3*2
P5 (numerator); (denominator)	X:581, Y:101; X:581, Y:83	3*3
P6 (numerator); (denominator)	X:524, Y:410; X:524, Y:100	5*5
Fig. 4c		
O1 (numerator); (denominator)	X:615, Y:117; X:615, Y:10	6*3
O2 (numerator); (denominator)	X:547, Y:99; X:547, Y:8	5*5
O3 (numerator); (denominator)	X:581, Y:42; X:581, Y:12	9*7

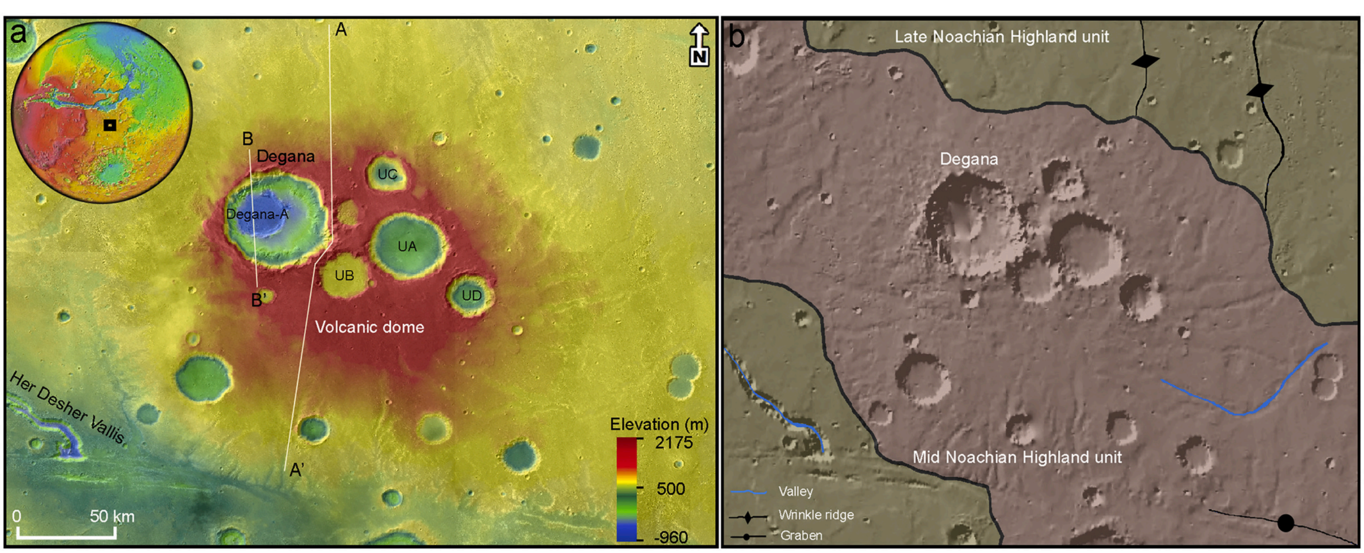

Fig. 1. Location map of Degana crater, Mars. Image is MOLA DEM. a) Topographic map of Degana crater and its surrounding region. b) Geologic map from Tanaka et al. (2014) indicates the terrain is Noachian in age.

3. Observations and interpretations

3.1. Geologic context and bedrock composition

3.1.1. Geologic context and volcanic dome

The study area (Fig. 1a) is located at the easternmost side of the Coprates quadrangle in the southern highlands of Mars (McCauley, 1978). Fig. 1a shows the geologic context of the area of study, which shows an elevated area similar to a dome. This dome extends more than 200 km in diameter (Fig. 2a). Many impact craters of varying diameters superimpose the dome (Fig. 1). The largest crater on the western flank of the volcanic dome is the Degana crater whose diameter and depth are ~50 km and ~ 2 km, respectively. Another impact within the Degana crater leads to form a ~20 km diameter crater, and depth of ~0.7 km, which is named in this study as 'Degana-A' (Fig. 2b).

Degana crater and its surrounding region are mapped as Mid-Noachian highland units (Fig. 1b), which hosts undifferentiated materials formed by volcanic and impact activity (Scott and Tanaka, 1986; Tanaka et al., 2014). Also, this unit is identified as moderately to heavily degraded, heavily cratered, hosts dense valleys, grabens, and wrinkle ridges (Scott and Tanaka, 1986; Tanaka et al., 2014). Xiao et al. (2012) categorized this dome structure as a shield volcano. The dome is embayed on its edge by Late Noachian volcanic plains, which contain wrinkle ridges as typically observed in Late Noachian and Hesperian plains of Coprates Planum (Tanaka et al., 2014). Tanaka et al. (2014) have mapped two valley networks in the region. The valley network in the south-west is Her Desher Vallis, whereas the other valley network has been mapped on the eastern flank of the dome (Fig. 1b).

An elevation profile AA' (north to south) taken along this volcanic dome shows typical domical topography (Fig. 2a). The elevated dome stands ~1.2 km above the adjoining plain surface (Fig. 2a), whereas, the craters Degana (Fig. 3a) and Degana-A (Fig. 3b) have excavated ~1.5 km below the regional baseline defined by the reference elevation of the plain surface adjacent to the dome. Overall, the two craters in combination penetrated ~2.7 km deep into the dome (Fig. 2b). Considering the surrounding plains, the surface elevation at the time of dome formation might be ~500 m. It means Degana-A reached a terrain deeper than the surface that exists before dome formation, i.e. an outcrop could be exhumed from the primitive crust below the volcanic dome or from a crystallized magma chamber beneath the dome. If the surrounding plains are thicker than 1.5 km, the outcrop would be exhumed from the deep part of the volcanic dome. In both cases, this observation provides an opportunity to analyze the pristine bedrock of Mars, which is preserved from the middle-Noachian epoch (Xiao et al., 2012). Apart from Degana and Degana-A craters, the other circular features atop the dome (Fig. 1) are unnamed craters marked in Robbins and Hynek (2012)'s impact crater database. These four large craters are superposed over the volcanic dome, as shown in (Fig. 3). The diameter of these craters ranges from ~20 km to 40 km. In this study, the four craters are named unnamed craters A, B, C, and D (hereafter referred to as UA, UB, UC, and UD) (Fig. 1a). Fig. 3c-f shows the four individual craters with their raised rims and relatively distinguishable ejecta from two of them (Fig. 3e,f). Based on their raised rims and ejecta, we interpret these craters as impact craters (Figs. 1a,3) and not as volcanic features.

3.1.2. Bedrock mineralogy

The exposed bedrock material from the two superposed craters is analyzed using CRISM data. Before analyzing the individual CRISM spectra, we derived the CRISM color composite map or spectral parameter map according to Viviano-Beck et al. (2014) by using the OLINDEX2, LCPINDEX, and HCPINDEX. This derived color composite image is overlaid over the CTX-DEM (Fig. 4a) to assess the compositional variation observed within the crater. This RGB combination of spectral parameters (OLINDEX2, LCPINDEX, and HCPINDEX) shown in Fig. 4a highlights potential olivine-rich regions in red color, low-calcium pyroxene (LCP) regions as green/cyan and high-calcium pyroxene (HCP) regions as blue color as suggested by Viviano-Beck et al. (2014).

From these highlighted regions, we have chosen spectra from 9 ROIs (Fig. 4a), which are mostly located on the northeastern and southeastern wall/rim of Degana-A. The locations of all the numerator spectra, denominator spectra, and the ROI sizes are given in Table 1. These are the locations where the diagnostic absorption features in the spectra are distinguishable. Spectra signature from the northeastern rim of Degana-A shows (Fig. 4b) a broad absorption near 1 μm and 2 μm wavelength. Absorptions around 1 and 2 μm are spectrally identified as pyroxene, where the band centers strongly dependent on the Ca content (Adams, 1974; Cloutis et al., 1986; Cloutis and Gaffey, 1991; Klima et al., 2007). All the colored spectra from the green/cyan region (Fig. 4a,b) exhibit a strong absorption feature between 0.8 and 1.0 μm, indicating that the ferrous phase is plausibly low-calcium pyroxene (LCP) (Huang et al., 2012). An additional broad absorption before 2 μm (Fig. 4b) implies the presence of low-calcium pyroxene as distinguished elsewhere on Mars (Mustard et al., 2005; Skok et al., 2012; Clenet et al., 2011). We have observed that LCP is widespread over this part of the north-eastern rim (Fig. 4a,b). Among the six identified locations of LCP detections, spectra P1, P2, and P6 are located on the northeastern rim. LCP identified in locations P3 and P4 is exposed along the eroded walls of the valleys, which are connected to the east rim of Degana-A. The LCP spectra obtained from P5 are located on the south-eastern wall of Degana-A crater (Fig. 4a). The LCP ratioed CRISM I/F reflectance spectra obtained from the six ROIs matches with RELAB (Viviano-Beck et al., 2015) representative spectra of low-calcium pyroxene (Fig. 4b).

The other diagnostic spectra are obtained from the south-eastern wall of Degana-A crater. Fig. 4c shows a broad absorption around 1 μm and no other diagnostic absorption at other wavelengths. A broad absorption around 1 μm in the near-infrared region and a lack of

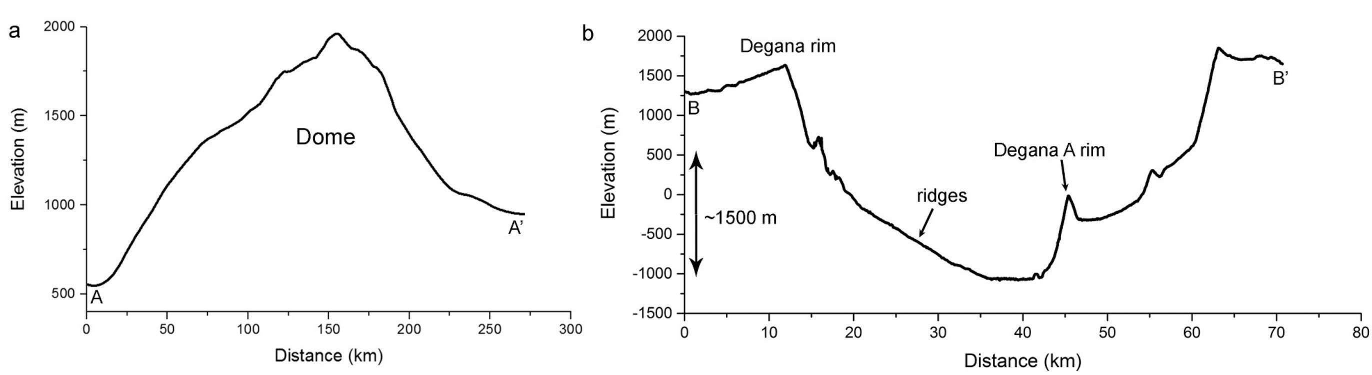

Fig. 2. MOLA DEM-derived topographic profiles a) profile is taken across the dome, which has a bell curve shape. This dome stands ~1.2 km high from its surroundings. b) Profile taken across Degana and Degana-A craters. Both impacts occurred on the dome and they have excavated ~1.5 km deep material from the base of the dome. (For profiles refer to Fig. 1a).

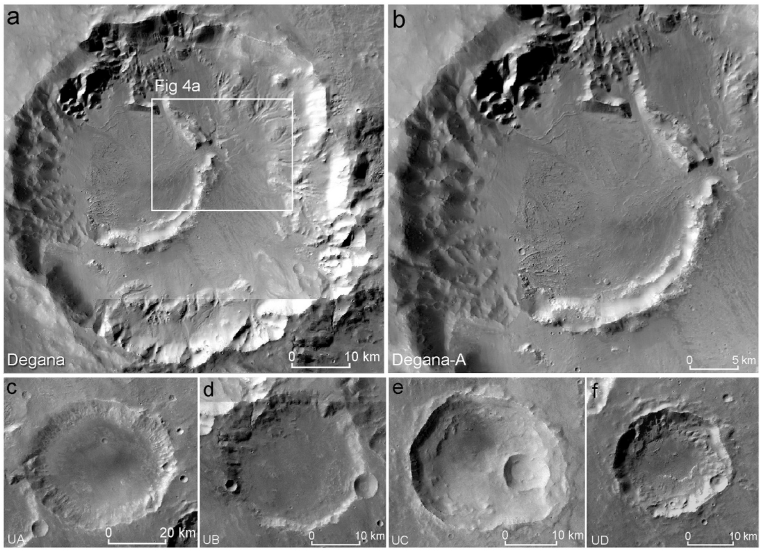

Fig. 3. Impact craters located on top of the volcanic dome. a) Degana crater, the largest on the dome. b) Degana-A crater, which superposed Degana crater. c) Unnamed crater- UA, with no distinguishable ejecta. d) Unnamed crater-UB located to the southeast of Degana. e) Unnamed crater-UC, with distinguishable raised rim and another smaller crater superposing its eastern wall. f) Unnamed crater-UD, located at the flank of the dome. The location of all the impact craters is marked in Fig. 1a. (CTX mosaic by Dickson et al. (2018) is used and north is up in all the images).

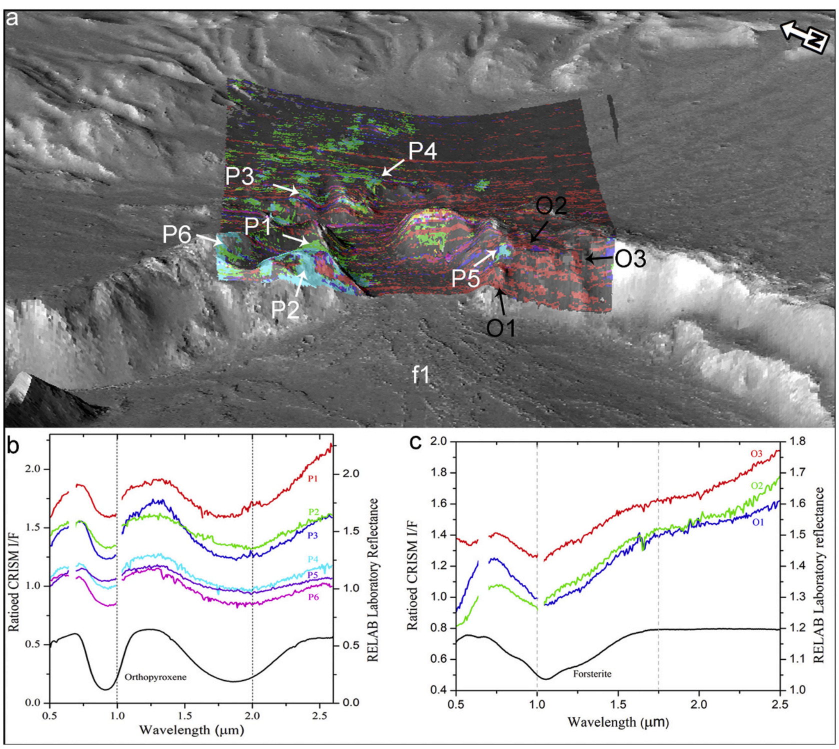

Fig. 4. a) MRO-CRISM derived summary parameters overlaid on CTX mosaic around the eastern wall of Degana-A crater. Summary parameters are calculated for CRISM image FRT00023F32. The summary parameter colors indicate: Red - Olivine, Cyan/green – LCP, Blue – HCP (Viviano-Beck et al., 2014). b) CRISM ratioed spectra for low- Calcium pyroxene identified with diagnostic 1 μm and 2 μm spectral features. A laboratory spectra from the RELAB library is shown below for comparison. Locations P1 to P6 indicate from where the spectras are extracted. c) CRISM ratioed spectra for olivine, identified with diagnostic 1 μm spectral features. RELAB laboratory-derived spectrum for forsterite is given below for comparison. Locations O1 to O3 indicates from where the spectras are extracted. (For interpretation of the references to color in this figure legend, the reader is referred to the web version of this article.)

absorption around 2 μm is indicative of olivine where the band center is dependent on the relative content of Fe and Mg (Burns, 1970; King and Ridley, 1987; Sunshine and Pieters, 1998). The spectra shown in Fig. 4c indicate absorption around shorter wavelengths (<1 μm), which is due to an increase in Mg content (Ody et al., 2013). In addition, the absence of strong absorption between 1.2 and 1.4 μm (Fig. 4b) also indicates that the olivine is richer in Mg (e.g., Huang et al., 2012). This suggests that this potential olivine outcrop is consistent with Mg-rich olivine (Fig. 4c). Spectra O1 and O2 in Fig. 4c exhibit olivine signatures within Degana crater, whereas, the spectra shown in black is the lab spectrum of Mg-rich olivine (Forsterite) from RELAB (Viviano-Beck et al., 2015). We have observed similar absorptions at location O3 (Fig. 4a). Although the olivine mineral exposures are spatially prevalent on the south-eastern wall of Degana-A, isolated patches have also been observed on the north-eastern wall in the color composite image (Fig. 4a). We have also used the CRISM CAT tool associated Modified Gaussian Model (MGM) to estimate the cation compositions of the pyroxene mineral (Sunshine et al., 1990). Using MGM we determined the normalized LCP/(LCP + HCP) ratio, which remains high (>70%) in most of the locations, as shown in Fig. S1. This analysis suggests that the proportion of LCP is high within Degana crater in comparison to other mafic minerals. Overall, the minerals identified using CRISM are dominated by primary mafic minerals (e.g. Viviano-Beck et al., 2015). However, we have not detected any hydrated minerals within the fan deposits or along the eroded walls of valleys. The complete lack of hydrated minerals is possibly caused by dust mantling on the floor, or by the limited area covered by the single CRISM cube, so the presence of hydrated minerals cannot be ruled out.

Fig. 5 shows the HiRISE RGB and greyscale images locations where CRISM mineral spectra were obtained. Fig. 5a,b shows the locations of LCP exposures in false-color images by HiRISE, as indicated by cyan coloring (Sun and Milliken, 2015). We have also observed distinct spectral absorptions over the light-toned outcrop (Fig. 5c), which is identified as a possible olivine exposure (Fig. 4c) on the inner crater wall. In addition, olivine exposures were identified along the inner crater wall of Degana-A (Fig. 5d) in the greyscale HiRISE images. Interestingly, all the LCP and olivine detected within the craters are linked to either the inner crater wall or the proximal part of the valley. Overall, the notable mafic signatures are observed along the rim of Degana-A crater, where the slope is high enough (>30°) to expose these signatures. This suggests that the elevated region of the inner crater wall and the adjoining valley wall exposed the mafic minerals due to their steep slope and possible erosion. It also suggests that a significant portion of the mafic minerals is blanketed by alluvial deposits in other areas. The presence of LCP on the northeastern and southeastern wall of Degana-A crater indicates a continuous layer along the rim that was exposed by the impact. This small exposure, although dust-covered, allows us to infer the mineral composition exposed within this dome. Thus, we infer these exposed mineral units to be pristine Noachian crust uplifted by volcanic dome formation.

3.2. *Morphology of fan deposits*

We mapped the occurrence and extent of fan deposits, valleys, and ridges within the crater (Fig. 6). The four fan deposits within Degana-A crater cover the entire floor area (Fig. 6a,b). The fan deposits are also observed on the floor of Degana crater, especially in the southwestern quadrant of the crater (Fig. 6b). Fig. 6b shows the geomorphic map of the impact craters and their diverse features. Fig. 7 shows six prominent fan deposits formed within Degana-A and Degana craters, and their corresponding area, fan length, and slope gradient are given in Table 2.

We observed several channels with positive relief on the fans (Fig. 7). These channels are consistent with original distributary, where the positive relief likely formed as a result of the finer surrounding material being removed by the wind. The fans within Degana crater (Fig. 7) host several distributaries. Some of these distributaries present on the fans' surface are marked by white arrows (Fig. 7). We observed that these distributaries are mostly radiating away from the fan apex (Fig. 7). The toe regions of the fans located within Degana-A fused with each other (Figs. 6,7). Within fans (f1–f4), multiple distributaries are observed and they vary in their extent and width. These distributaries are few kilometers long and a couple of meters wide (Fig. 7). The fans within the Degana-A are of low gradients in the range of 2° to 4° (Table 2), and the four fans have almost equal areas (Table 2). In almost every fan deposit (Fig. 7a–d), near the apex region, the distributaries appear in a cluster, whereas away from the apex region towards the downstream, they are apart from each other and observed to follow the typical topographic driven flow. The distributaries are oriented downslope, and they are aligned along with the fan orientation (Fig. 7d). The fans located on the floor of Degana crater (Fig. 7e,f) did not show as many sharp distributaries as observed on the fans located within Degana-A. The distributaries are observed only at the termini of fans f5 and f6 (Fig. 7 e, f), and they are mantled by a dust cover. Interestingly, Fig. 7e shows the possible coalescing of two fans in the toe region. Dust cover and transverse aeolian ridges (TAR) (Wilson and Zimbelman, 2004; Berman et al., 2011) were observed to fill the intermediate troughs within the fan deposits.

Fig. 8a shows the HiRISE DEM of surface features of fan f1, where the prominent distributaries are radiating from the fan apex. The elevation gradient along the distributaries can be seen in the HiRISE DEM. Though all the distributaries are sourced from the apex points, some of them are discontinuous. Fig. 8b shows a topographic profile with varying elevations along a distributary within fan f1, which has a relief of ~10 m. Fig. 8c shows distributaries on fan f1, which are often stacked, exhibiting crosscutting and superposition relationships. We have also observed that the width of these distributaries decreases as we move farther from the apex (Fig. 8c). These distributaries over the Degana fans are up to 10s of meters thick. The observed crosscutting of the distributaries is the most prominent intersection at an acute angle that occurred within fan f1 (Fig. 8c). The distal portion of this distributary is discontinuous (Fig. 8b) and terminates abruptly.

Apart from distributaries, the fans in Degana-A, particularly fans f1 and f3 (Fig. 8c,d) exhibit surface textures with noticeable bedding/layered sediments. Fan f1 hosts many distinguishable stratigraphies (Fig. 8c,d) observed at the distributary termini and along the intermediate region between the distributaries. Fig. 8d also shows that the

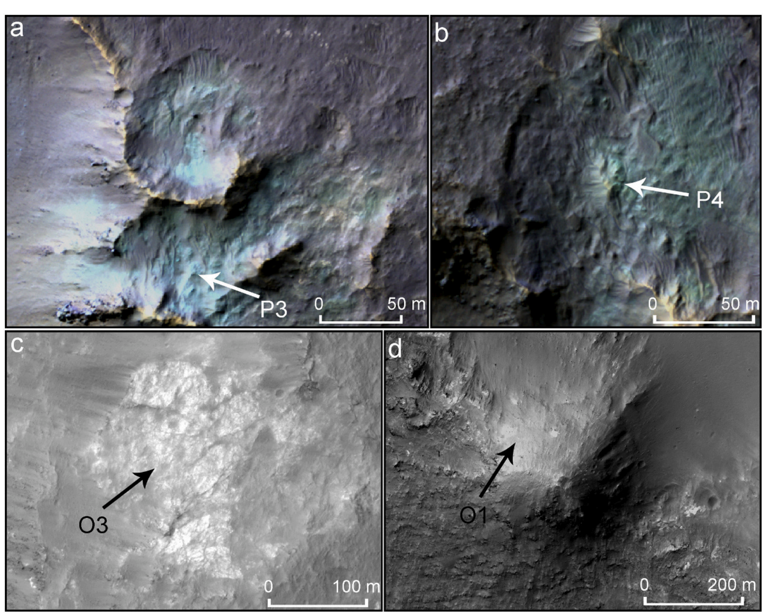

Fig. 5. Examples of locations in HiRISE false color image for a) pyroxene on the elevated rim, b) pyroxene along topmost part of the eroded valley (HiRISE ESP_026522_1560). Example location for c) olivine detected along the eastern wall with light-toned exposure and d) olivine signature along the eastern wall (HiRISE ESP_16540_1560).

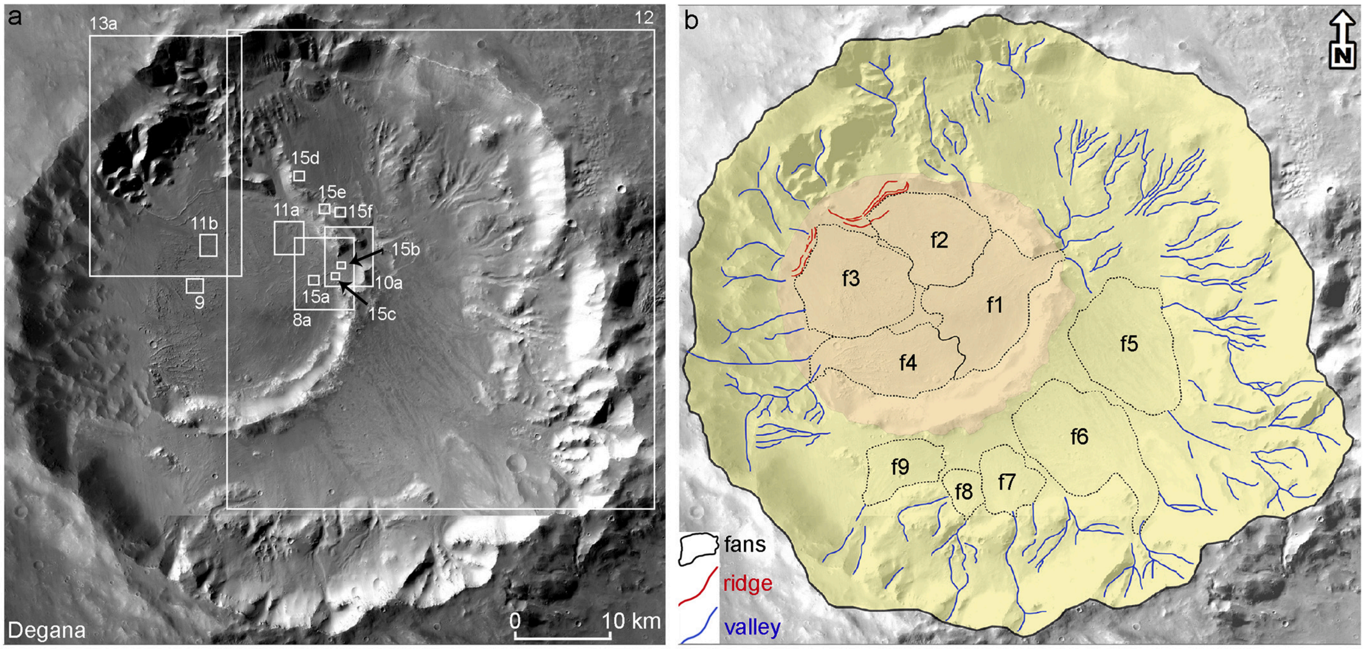

Fig. 6. a) CTX mosaic of Degana and superposed Degana-A crater. b) Geomorphological map of Degana and Degana-A craters overlaid at 80% transparency on the CTX mosaic. The predominant mapped units are fan deposits, valleys over the crater rim, and moraine-like ridges.

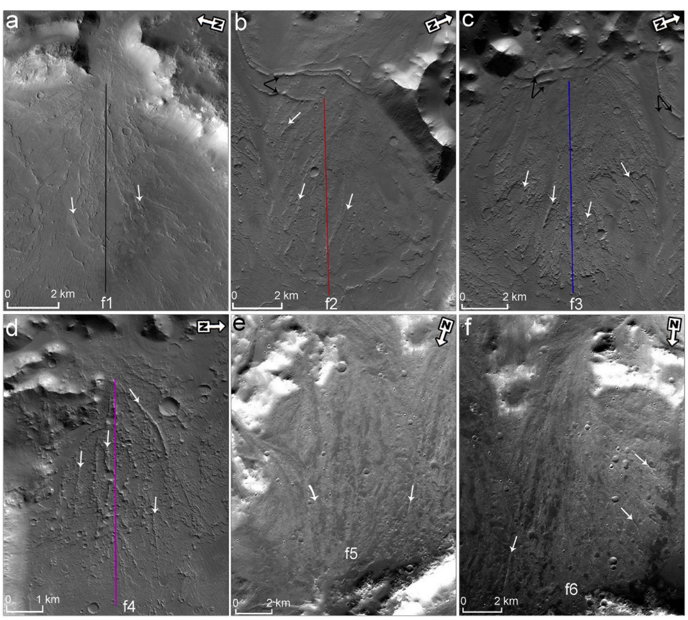

Fig. 7. Distribution of fan deposits within Degana-A crater, a) Fan f1, located on the eastern wall, whose apex region is situated on the breached rim. Individual ridges and dendritic distributaries are present over the fan surface. b) Fan f2, from the northern wall. c) Fan f3 from the northwestern side, with distinguishable ridges at its toe side. d) Fan f4 from the southwest side, with deposits and distinguishable ridges. Distribution of fan deposits within Degana crater, e) Fan f5, the largest fan within both craters. The toe region of this fan merges with another adjacent small fan deposit. f) Fan f6, from the southeastern wall with broad fan-shaped deposits at the toe region. The toe region of the fan deposits terminated at the walls of Degana-A crater. Colored lines over the fans indicate the traverses of topographic profile Fig. S3, White arrows - distinguishable distributaries over the fans. (CTX IDs a-d: G02_018874_1561_XN_23S045W, and e-f: D19_034592_1579_XN_22S045W).

Table 2
Details of all the fans mapped within Degana crater with length, area, and slope.

Fan name	Approx. fan length (along major axis) (in km)	Approx. area (in km^2)	Slope (degrees)
f1	13.39	70.06	2.62
f2	9.09	60.36	2.47
f3	10.21	76.00	2.71
f4	10.10	52.11	3.81
f5	11.10	79.22	2.32
f6	11.98	85.05	2.50
f7	5.67	25.65	2.98
f8	4.22	10.11	2.75
f9	7.63	27.44	2.59

layering is evident along the flanks of the distributaries located on the fan f1. These layers are 100 s of meters long, and the entire sequence is 10s of meters thick. Also, the source area of fan f3 on the western crater wall (Fig. 9) shows well-exposed layers along the flanks of the distributary. The distributary flank hosts notable small boulders resolvable in HiRISE color images (Fig. 9).

On observing fan f1 apex region, a significant part of the crater rim was breached and this breach is associated with five valleys, which originated from Degana's crater wall (Fig. 10a). Over this part of the Degana-A crater rim, we observed that the rim height is ~800 m towards the northern side, whereas it is ~920 m towards the southern side. We observed ~800 m of the wall has been eroded and made as an inlet for the fan f1 deposits. Nearly all five valleys converge outside the eastern

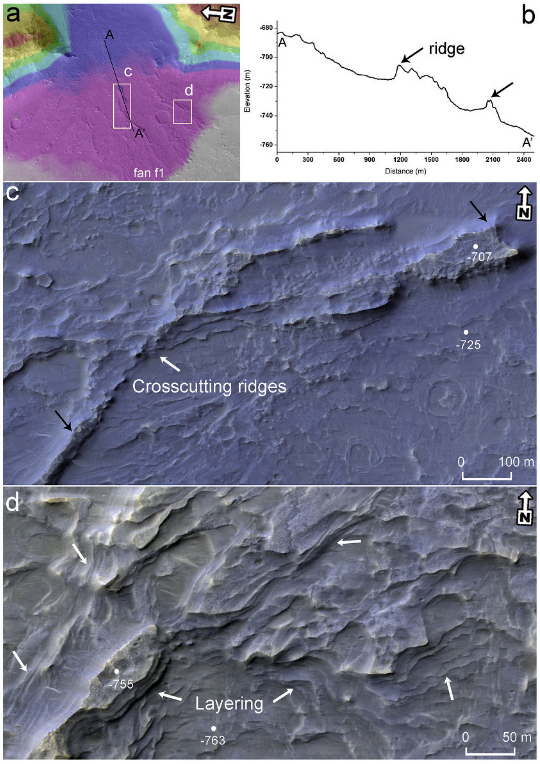

Fig. 8. a) HiRISE stereo pair (ESP_016540_1560 and ESP_016039_1560) derived DEM image for fan f1. b) Elevation profile (AA') taken along a discontinuous distributary ridge, note the height variation within the ridge c) HiRISE false-color image shows some parts of the discontinuous ridge. At the downslope side, crosscutting ridges are observed with exposed stratigraphic deposits (HiRISE ID: ESP_016540_1560). This false-color image also highlights the multiple distinguishable layers within the fan deposits. The black arrows display the locations marked on the elevation profile in Fig. 7b. d) HiRISE false-color image (ESP_016540_1560) over the toe region of fan f1. The eroded ridges expose multiple stratigraphic layers located at different elevations (marked by white arrow). These layers likely hint at multiple stages of deposition within Degana-A crater. (White dot shows elevation value at that particular location.)

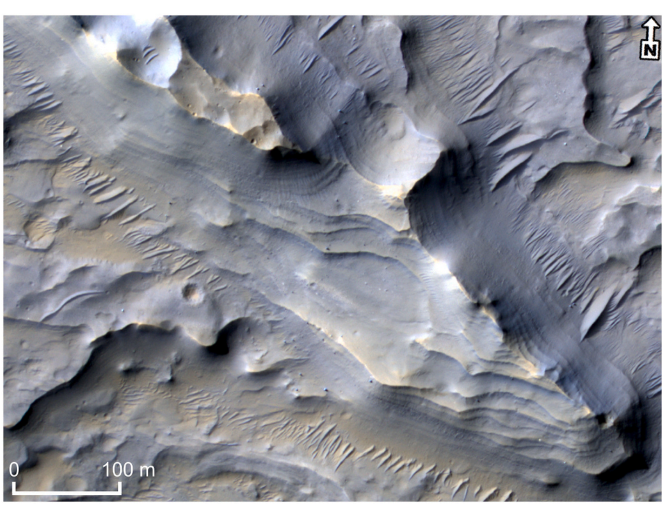

Fig. 9. HiRISE color image ESP_018874_1560 reveals details of ridges with interbedded fine sediments and exposed stratigraphy. The layers are exposed all around the ridge and they are individually distinguishable. The ridge is surrounded by aeolian deposits, TARs, and mantled by dust showcasing the role of wind in eroding the ridge and exposing layers. Towards the toe side of the ridge, it is narrow and exposed more distinct light-toned layers, which are ~3–5 m thick.

wall of Degana-A crater (Fig. 10a) and breach this part to form the f1 fan deposits. Fig. 10b shows one of the valleys from the Degana eastern wall with exposed layering in the HiRISE color image. This we observe as the earlier deposited sediments over the eastern floor of Degana were incised, possibly during the Degana-A rim breaching.

On observing the distal fan f2, we found that it has coalesced with the toe part of fan f1 (Fig. 11a). Layers are observed at the toe region of both the fans f1 and f2, whereas at their coalescing part, hummocky materials are observed (Fig. 11a). The region of coalescing can be identified by a rough-textured surface with an absence of distributaries (Fig. 11a). Fig. 11b shows distributaries (marked by black arrow) and layering (marked by white arrow) on fan f2. Fan f3 also shows evidence of distributaries (Fig. 11b) and layering that are distinguishable (Fig. 9). All the four fans within Degana-A have coalesced at their toe region or by their sides.

We also observed fan deposits over the walls of Degana crater (f5 to f9), which mostly terminate at the rim of the Degana-A crater (Fig. 6b). The slopes of these fans are in the range of 2° to 3°. Apparently, they have formed in the south and southeast of Degana-A and connected with the valleys presented on the wall of Degana (Fig. 6b). Out of fans f5-f9, the smallest fan (f8) is ~4 km long and covers an area of ~10 km^2, while the largest fan (f6) is ~12 km long and covers an area of ~85 km^2. Fan f5 is the second-largest fan within Degana crater though it is formed by deposits from multiple valleys (Table 2).

Based on Blair and McPherson's (1994, 2009) definition, alluvial fans are semi-conical depositional landforms that develop through a channel, and branching spreads the sediments across the surface. In general, alluvial fans are hundreds of meters to few kilometers long along their major axis and fed by constrained catchments. This definition applies well to the observed fan deposits (Fig. 7) inside Degana and Degana-A craters.

3.3. Ridges

In Degana-A crater, we observed arcuate or wide U-shaped ridges located over fans f2 and f3 (Fig. 13). Photo-geological observations and profiles across these ridges indicate positive relief features with knobs (Figs. 13,14). They were observed to drape over the eroded wall and fan of the Degana-A crater (Fig. 13). These ridges are 10s of kilometers long and 100 s of meters wide. Two ridges in the center over fan f2 have merged and formed a thick ridge towards the west (Fig. 13). Further to the west, we observed a discontinuity along this merged ridge (Fig. 13). The ridges in Degana-A appear more degraded towards the eastern side (Fig. 13). This ridge is relatively thicker in its center and the thickness decreases towards both of its frontal lobes (Fig. 13). We have also observed that fan f2 is oriented from northwest to southeast, whereas these ridges are oriented in a northeast-southwest direction (Fig. 13). Similar, but only 5 km long, ridges are also observed on the alluvial fan f3 (Fig. 13). Interestingly, the ridges superposed the fan deposits and are observed on the pole-facing wall of Degana crater. The ridges in Degana and their characteristics such as convex geometry, an arcuate shape, and knobs are consistent with other moraines observed on Mars (Arfstrom and Hartmann, 2005; Shean, 2010; Scanlon et al., 2015).

We analyzed elevation profiles along north-south directions using the CTX DEM across the ridges located on fan f2 (no HiRISE DEM is available for this location). Four profiles were examined for which we determined the average thicknesses. The limited resolution of the CTX DEM does not allow extracting precise thicknesses for some of the ridges (Fig. 14). These measured thicknesses vary from 8 m (BB') to 51 m (CC') (Fig. 14, Table 4), and we have taken these values as a range for the possible ridge thickness. Further, we followed the approach by Hartmann et al. (2014), to estimate the ratio of basal stress (ζ) to density (ρ), which provides information about the nature of a glacier. To calculate this ratio, we used Paterson's (1994) relation, which suggests a relationship between basal stress and the density given as:

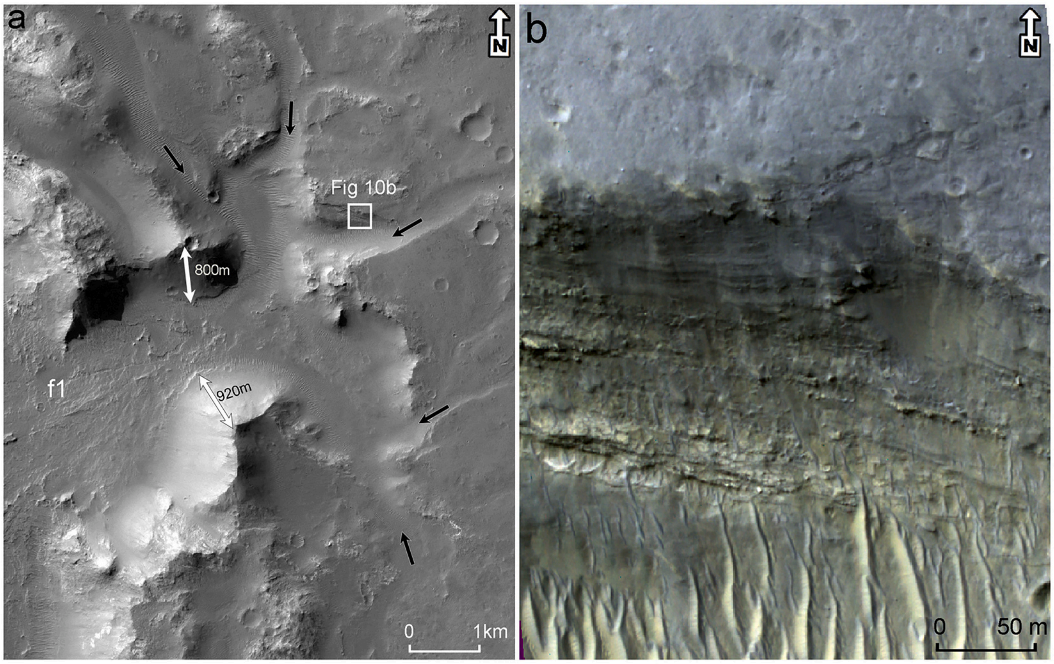

Fig. 10. a) The apex region of fan f1 located over the breached rim region of Degana-A. Towards the north, the rim height is ~800 m, whereas, towards the south, it is much higher at ~920 m. This suggests that the ~900 m high and ~ 1 km wide rim is breached by fan f1 deposits. Over this part, nearly five valleys from the Degana crater wall converge, which suggests the possible source for the rim breaching. Black arrows display the valleys, which fed fan f1. b) HiRISE color image ESP_026522_1560_COLOR of one of the eroded walls of the valley shows distinguishable layers. We interpret this exposed stratigraphy as earlier deposits within the Degana eastern wall, which later got breached by the valley associated with the rim breaching.

$$\zeta = \rho\, g\, h \tan \alpha \quad (7)$$

where g is the gravity (3.72 m/s^2), h is the height/thickness, and α is the slope in degrees (Paterson, 1994; Hartmann et al., 2014). The average and maximum thickness (h) measured for moraine-like ridges over fan f2 are estimated as ~22 m and 51 m, respectively. The average and the maximum values are used because this region could have undergone erosion after their formation. Slope (α) values were also determined, along with all the profiles that are considered for thickness measurements (Table 3). We obtained the average ratio of basal stress to density for Degana glacier(s) as ~4 m^2/s^2 (Table 3).

3.4. Small polygonal patterns

Within the Degana crater and on the fan deposits, several polygonal-shaped features are observed (Fig. 15). Polygonal patterns are observed, especially on the fans in Degana-A, and also on the inner and outer eastern wall of Degana-A crater (Fig. 15). The majority of polygons' boundaries or fractures observed on the fans appear irregular (Fig. 15 a–c), whereas polygons over the Degana-A walls visually appear regular or organized to each other (Fig. 15 d–f). These polygons are 10s of meters wide and the fracture length varies accordingly. Fig. 15b shows polygons over the fan f1, with fractures cutting through several layers. The polygonal fractures are well distinguishable over the fan f1 and within the vertically exposed stratigraphy (Fig. 15b). We have observed that over the fans (Fig. 15 a,b) and the wall (Fig. 15 d–e), most of the polygons are negative relief features. In contrast, Fig. 15c shows a distinct style of polygons with filled ridges and positive reliefs in some areas on fan f1. Polygons in the wall of Degana-A (Fig. 15d) are distinct from the polygons observed on the fans (Fig. 15a–c) in terms of the slope at which they formed. Polygons shown in Fig. 15a–c have formed on the relatively level floor (<10°), whereas polygons shown in Fig. 15d have formed on the more inclined wall (>30°).

Overall, polygons on the fans suggest a potential involvement of volatiles potentially ice or adsorbed water in clay minerals, in their formation and, which would imply a periglacial environment postdating the deposition of the pile of sediments.

3.5. Crater size-frequency distributions

Xiao et al. (2012) estimated the age of the volcanic dome as ~4 Ga. In this study, we used a Poisson timing analysis (Michael et al., 2016) to estimate the absolute model ages. We mapped the best visible ejecta boundary of Degana crater and counted the superposed craters over the ejecta (Fig. 16a). Our crater count statistics over the ejecta (area ~ 6546 km^2) resulted in a total of 362 craters from ~100 m to 20 km. We obtained the best fit model age by fitting 17 craters, whose diameter is greater than 1.3 km (Fig. 16b). From this, the age of Degana crater is ~3.7 Ga (early Hesperian) (Michael, 2013). Further, we analyzed the ejecta of Degana-A; however, it is very difficult to distinguish the ejecta, which is degraded by mass movement processes within the host crater Degana. The floor of Degana-A is almost entirely covered by sediment deposits (Fig. 6) from all around the wall, occupying an area of ~313 km^2. Hence, we counted all the possible superposed and embedded craters (Fig. S2) over these alluvial fans (f1–f4) and determined cumulative (Fig. 16c) and differential (Fig. 16d) crater size-frequency distributions. The cumulative and differential fan-derived crater size-frequency distribution for Degana-A is early Amazonian (Michael, 2013). This age is not the formation age of the fan deposits within Degana-A; rather, it is estimated from the craters retained after their formation. Also, the diverse erosion of fan ridges observed (Fig. 11) shows the difficulty in determining the model fan age. We want to clarify here that this age is the crater retention age for all the alluvial fans and can only suggest a possible lower bound to the deposits within Degana-A. In addition, we estimated cumulative (Fig. 16c) and differential (Fig. 16d) fan-derived crater size-frequency distributions for the four fans (f5 to f9) located over the walls of Degana crater. The obtained age is also early Amazonian. This suggests that the fan deposits observed within both craters (Degana and Degana-A) are likely Amazonian.

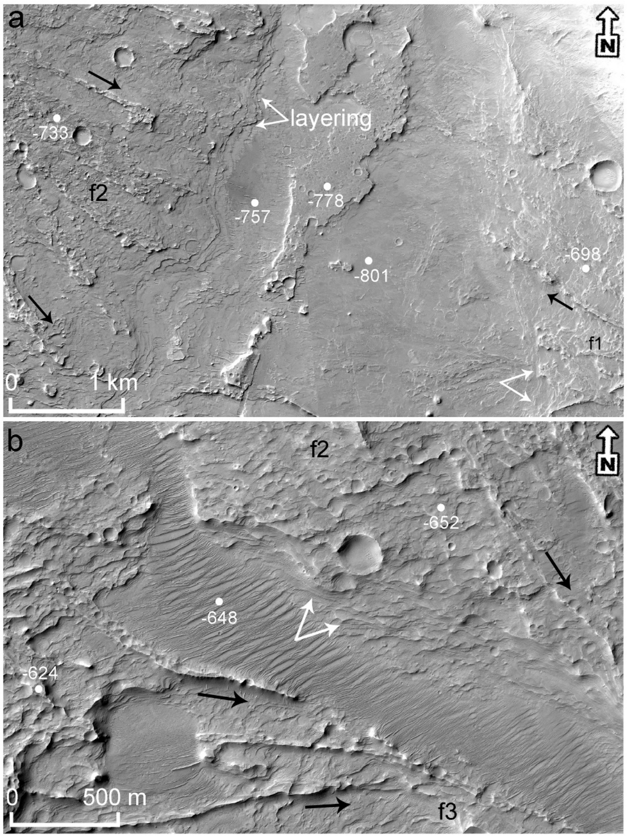

Fig. 11. Example locations of intersecting fan deposits within Degana-A crater. a) Region of convergence of fan f1 and f2, with marked distributaries (black arrow, aligned in the direction of the fan). Layers were identified at the front scarp of both the fans. The hummocky patch located at the termini region of both the fans (f1 and f2) is ~20 m elevated. On both sides of this hummocky surface, the fan deposits expose the layers at their front scarp (HiRISE ID ESP_016039_1560 and ESP_035159_1560). b) Region of convergence between fan f2 and f3, with marked distributaries (black arrows, aligned in the direction of the fan). Layers were identified at the termini region of fan f2. The dust mantled the trough in between the fan deposits. The orientation of both fan deposits are different, which crosscut/superpose each other nearly orthogonal (HiRISE ID ESP_018874_1560).

Table 3
Geometric characteristics of moraine-like ridges on the northern wall of Degana-A.

Profile ID	Maximum height of moraine-like ridges (m)	Slope (in degrees) α	Basal stress/ density (m^2/s^2)
AA'	20	3.49	4.5
BB'	8	3.0	1.6
CC'	51	2.74	9.1
DD'	8	2.24	1.2
Average	22		4.1

4. Discussion

4.1. Evidence for exposure of pristine Noachian crust

The presence of mafic minerals in well-exposed outcrops within Degana crater indicates igneous lithology or basaltic/volcanic subsurface layers (e.g., Skok et al., 2012) exposed by the Degana and Degana-A impact. The following mechanisms have been proposed for the origin of olivine and LCP bearing rocks on Mars: Noachian crust/volcanism (Mustard et al., 2005; Hamilton and Christensen, 2005; Tornabene et al., 2008; Poulet et al., 2009a, 2009b; Flahaut et al., 2012; Quantin et al., 2012; Skok et al., 2012; Rogers et al., 2018; Viviano-Beck et al., 2019) or impact melting from large impact basins (Mustard et al., 2007; Palumbo and Head, 2017). Noachian/early crust on Mars can contain evidence for its formation and crustal modification afterward (Skok et al., 2012). Mg-rich olivine got exposed on the wall/rim of Degana-A crater. McSween et al. (2006) suggested that Mg-enriched olivine on Mars likely indicates ancient primitive magmatic rock. Thus, the exposure of more mafic rocks in this region has implications for the magmatic history of the region. The exposed olivine and LCP in the uplifted rim of Degana-A provide a piece of direct evidence for the materials present in the interior of the volcanic dome. This strongly reveals that the materials exposed by the Degana outcrops represent either pristine Noachis crust and/or volcanic deposits sourced by a primitive mantle (McSween et al., 2006; Mustard et al., 2009; Skok et al., 2010; Flahaut et al., 2012; Quantin et al., 2012; Baratoux et al., 2013).

4.2. The fate of water at Degana crater

Earlier studies suggest regional glacial deposits in the southern highlands poleward of 30°S (Kargel and Strom, 1992; Head and Pratt, 2001; Ghatan and Head, 2002; Fastook et al., 2012; Scanlon et al., 2014; Head and Merchant, 2014; Fastook and Head, 2015; Kress and Head, 2015; Scanlon et al., 2015). While the glacial deposits around the Tharis volcanoes have got attention for the Amazonian equatorial ice (Shean et al., 2005; Forget et al., 2006), several craters located in low to mid-latitude (~5° to 60°) regions on Mars host young landforms on their floors and walls, which potentially indicate the involvement of ice-rich material with lobate tongues and arcuate ridges (Arfstrom and Hartmann, 2005; Head et al., 2005; Shean, 2010; Scanlon et al., 2015; Sinha and Vijayan, 2017; Hartmann et al., 2002, 2003).

Thus like other craters, the local deposition of atmospheric ice occurred within the Degana. The moraines observed within Degana-A crater, which is situated at 23°S latitude, provide crucial evidence of equatorward glacial deposits during the Amazonian period. Global climate models for the equatorial highlands region of Mars show the possibility of snow accumulation and melting over the low and mid-latitudes, which would enable fan formation by snowmelt hypothesis (Wordsworth et al., 2013; Kite et al., 2013). However, there is no unambiguous observation of glacial deposits connected to the alluvial fans. While the interpreted glacial landforms postdate the alluvial fans at Degana, the fact that glacial ice was able to be deposited during the Amazonian shows that this location was once favorable to snow precipitation in the past. The average ratio of basal stress to density for Degana glacier(s) (i.e. ~4 m^2/s2) in comparison to terrestrial values of pure ice glaciers (40–100 m^2/s^2) is one order of magnitude lower, but not so much lower than values of 3.7 to 44.5 m^2/s^2 found by Hartmann et al. (2014) at Greg crater. These low values are likely explained by the fact that these moraines underestimate the actual thickness of the past glaciers, but are consistent with pure-ice glaciers, while rock glaciers would show higher values and a partial filling by the residual material (Hartmann et al., 2014).

Morgan et al. (2014) documented distributaries within Saheki crater' fans as observed on Degana' fans (Fig. 7), which are downslope oriented and show radiating outward patterns from the fan apex. Many other studies (Moore and Howard, 2005; Irwin et al., 2018; Boatwright and Head, 2019) reported similar ridges over the fans within many martian craters, which were interpreted as inverted channels or fan distributary ridges. Morgan et al. (2014) documented layered sediments within the Saheki crater and interpreted that overbank flows, which might have been sourced from multiple flows within the distributaries, have deposited these layered sediments. Distributaries have spread across the fans in Degana-A crater (Fig. 7), and they were the potential source for layered sediments, as suggested by Morgan et al. (2014). The flanks of the discontinuous distributaries (Figs. 8d,9) with layers are records of possible long-duration flow events in the region. Additionally, Morgan et al. (2014) suggested that such layers were exposed by aeolian erosion.

Exposures of layers on both sides of the distributary (Fig. 9) indicate that erosion occurred possibly due to wind-driven activity. In the Saheki crater, a similar distributary with exposed layers and bluish clasts in the HiRISE RGB-images suggested the presence of different materials (Morgan et al., 2014). Within fan f3 of Degana-A, the HiRISE image shows bluish clasts on the distributary (Fig. 9) that are possibly comparable to Saheki crater ridge. However, this part of fan f3 lacks mineralogical data (CRISM) to assess the composition.

The rim breaching of Degana-A crater and fan f1 formation is closely associated with the valleys over the eastern wall of Degana crater. In addition, the valleys that incise the outer rim of Degana-A (black arrows in Fig. 10) cut through a layered wall material on the eastern side of Degana (Fig. 10b). This layered material might be residual deposits from an initial fan that formed on the outer rim of Degana-A, similar to fans f5 to f9. Then, the breach through the rim produced a change in the base level of the deposits, starting to build fan f1. In this scenario, the fact that a breach formed here rather than for the other fans f5 to f9 is likely due to the large watershed (Fig. 12). An important implication of this scenario is that the fans f5-f9 would have formed coevally to the fans f1 to f4 inside Degana-A crater (see Section 3.5). We also identified embedded craters on the fans (Fig. S2), these possibly display evidence of interbedding within the crater (Kite et al., 2017). We use observations of fan f1 to estimate the flow velocity and discharge quantitatively (see supplementary file). Following Morgan et al. (2014), we determined the value of maximum discharge as ~84 m^3/s (Table S1). Based on this, we also determined the supply rate of water, which is the maximum discharge per total area of source catchment, and found that the source catchment would have supplied the water at a rate of ~2.25 mm/h.

Studies on the deposition of large equatorial alluvial fans and deltas show the role of enhanced precipitation by rainfall or snow/ice melting followed by runoff (Moore and Howard, 2005; Di Achille and Hynek, 2010a, 2010b; Armitage et al., 2011; Grant and Wilson, 2011, 2012; Wilson et al., 2021). Although many alluvial fans are evident within Degana (Fig. 6), due to limited CRISM coverage, we cannot rule out hydrated mineral formation within the craters. The polygonal patterns display characteristics consistent with the patterns observed in aqueous sedimentary layers containing clay minerals that formed by contraction either from desiccation or from enhanced cold temperatures during their exhumation (Elmaarry et al., 2012; Oehler et al., 2016). The major hypotheses for polygon formation on Mars are thermal contraction and desiccation of sediments either enabled by ground ice or by sediments containing absorbed water such as in clay minerals (Neal et al., 1968; Levy et al., 2009; Elmaarry et al., 2010, 2012; Oehler et al., 2016). Although the polygons were observed on alluvial fans, which are located within the volcanic dome, we do not interpret them as lava-related cooling cracks. Polygon patterns are generally defined by four factors: shape, size, boundary type, and intersection pattern (Yoshikawa, 2003). They can be characterized by an elevated ridge boundary or a depressed trough along the boundary. The pattern of intersection can be orthogonal, random orthogonal, or random (Yoshikawa, 2003; Mangold, 2005; Oehler et al., 2016). The rectangular shape and size of the polygon in our study area form an orthogonal pattern indicative of desiccation cracks (Neal et al., 1968; Elmaarry et al., 2010, 2012; Oehler et al., 2016) and/or thermal contracted sediments, i.e., potentially ice-wedge or sand-wedge polygons (Mangold, 2005; Hallet et al., 2013; Kerber et al., 2017; Brooker et al., 2018). Desiccation generally forms nested polygons that display many secondary fractures (Oehler et al., 2016). Therefore desiccation is less likely than thermal contracted ice-wedge polygons over potential periglacial terrain (Soare et al., 2014) formed by ice/snow deposition as indicated by the presence of moraines. Two types of ice-wedge polygons were suggested based on thermal stability: 1) a low centered polygon and 2) a high centered polygon (Washburn, 1980; Mackay, 2000). It was suggested that differences in their morphology potentially reflect a change in climatic conditions (Lachenbruch, 1963; Mackay, 2000; Jorgenson et al., 2006; Mellon et al., 2009; Abolt et al., 2018). In contrast to high-centered polygons, polygons in Fig. 15c show

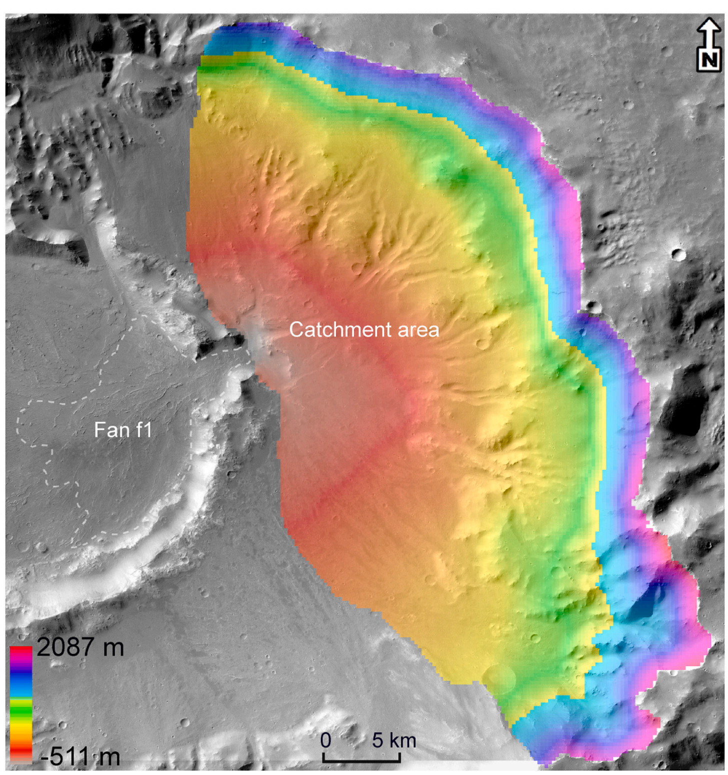

Fig. 12. MGS MOLA- MEX HRSC blended DEM overlaid on the CTX image in the eastern side of Degana crater. This part is the possible catchment area for the five valleys, which played a role in breaching the Degana-A eastern rim. The elevation of the catchment area ranges from −511 to 2087 m. The boundary of fan f1 is marked with a dotted gray line. The estimated catchment area is larger in comparison to the area of fan f1.

ridges along the boundary, implying low-centered polygons. Those polygons do not have a regular shape and follow a more random geometry. They are consistent with networks of veins (also named box work deposits, Siebach and Grotzinger, 2014), which are formed by groundwater circulation and precipitations along the fractures. Their presence may imply a period of groundwater circulation during or after the alluvial fan formation period. Alternatively, another possible reason can be deposition and cementation of sand/dust in cracks formed by thermal contraction and further erosion of the material inside polygons (Oehler et al., 2016). On the other hand, the preservation of olivine-rich outcrops means that no prolonged aqueous activity took place at this location, or outcrops have been covered and therefore protected from alteration until relatively recently. Thus, the presence of alteration minerals cannot be conclusively demonstrated, but a well-developed chemical alteration seems unlikely. To decipher the fate of water-related deposits within Degana we are assuming that the crater was once covered by ice before the formation of Degana-A. With this assumption, three scenarios may explain our observations: (A) An episodic climatic warming, perhaps related to obliquity variations (e.g., Kite et al., 2017), (B) fluvial activity related to volcanic heat, possibly related to Alba Patera or Ceraunius Tholus (e.g., Gulick, 2001; Hauber et al., 2005; Ansan and Mangold, 2013), or (C) the role of the Degana-A impact whose heat release may have helped to melt snow and trigger fluvial activity. Scenario (A) requires to have favorable climatic warming relatively recently in the Amazonian era. This is possible according to recent studies (e.g., Kite et al., 2017), but speculative, lacking other evidence for warming, at least regionally. For instance, the older crater located in the east of Degana (Fig. 3c) shows only ancient erosion by valleys, but no pristine alluvial fans as reported in Degana, while its size and wall hillslopes look quite similar. This comparison suggests that the alluvial fans formed at Degana are local. Scenario (B) is unlikely because Degana-A is far younger than the volcanic activity, and no volcanic landforms are observed inside either Degana and Degana-A craters. Regarding hypothesis (C), it has been shown that hot ejecta emplaced over an ice-rich surface could have generated local melting (Mangold, 2012; Mangold et al., 2012c; Weiss and Head, 2016) possibly explaining some of the Amazonian age fluvial activity inside craters (e.g., Williams et al., 2009). Ejecta temperatures for craters of diameter range between 5 km to 150 km were determined by Weiss and Head (2016) to be up to 490 K. Snow melting due to ejecta emplacement produced by the Degana-A impact would have deposited sediments for fan f1. We also determined maximum and minimum values for flow velocity and discharge rate for fan f1 in Degana crater. The maximum value for the flow velocity is ~2 m/s whereas the discharge rate is estimated as ~2.25 mm/h. These values are lower than the estimated flow velocity and discharge rate by Kite et al. (2013) and Morgan et al. (2014). These results support our interpretation regarding snow melting and the formation of fan f1. The breach of the ~1 km wide and ~ 900 m high eastern rim wall of Degana-A crater also indicates the long-lasting melting of snow/ice due to Degana-A impact. At least five valleys (Fig. 10a) converge around the eastern wall region of Degana-A, which might have provided sufficient sediments to breach the crater rim. Fig. 12 shows the catchment area associated with these five valleys. Large catchment area (Fig. 12) and positive relief of the dome lead us to envisage a high possibility of atmospheric snow/ice precipitation. This suggests that sufficient ice melt occurred to form the fan deposits within the craters. Thus, we interpret local atmospheric snow/ice precipitation as the most likely source for fluvial activity within the craters.

4.3. *Geological history of the Degana crater region and its implications for the geological history of Mars*

The overall geologic interpretation and the sequence of events are based on stratigraphic and chronological relationships. The sequence of geological events that occurred in the Degana region aids in deciphering the Martian surface processes, and climatic conditions that prevailed over this region. A schematic scenario is shown in Fig. 17, which represents the activities that took place in this region.

(1) Apparent model ages derived from crater size-frequency measurements by Xiao et al. (2012) suggest the volcanic dome formed around 4 Ga ago, during the Early to Mid-Noachian epochs (Fig. 17a).

(2) Degana impact crater formed on the volcanic dome and exposed the dome interior down to ~2 km. Apparent model ages suggest that Degana crater formed in the early Hesperian 3.7 Ga $+0.04/-0.16$ or close to the Noachian-Hesperian boundary (Fig. 16b). No volcanic-origin flows were observed within the crater. Therefore, we suggest that dome-related volcanic activity had ceased around 3.7 Ga.

(3) Degana-A crater superposed Degana crater after an unknown period. It is very difficult to estimate the age of Degana-A's formation because a lot of its ejecta were likely sequestered inside Degana crater. Degana-A further exposed the interior of the dome or the underlying Noachian crust by another ~0.7 km. In total, both craters excavated ~2.7 km deep into the volcanic dome. However, the floor of the crater is covered by four large depositional fans (Fig. 6) whose tentative crater retention epoch is early Amazonian.

(4) Multiple valleys on the wall, and floor of Degana crater, and several fan deposits within Degana-A (Figs. 6b,18) provide strong evidence for fluvial activity. Although the length of time over which the fans formed is uncertain, we evaluate two scenarios. The orthogonal coalesced alluvial fans (Fig. 6b), inverted channels/distributaries, and the discharge rate for fan f1 suggest that the fans were formed by steady discharges over a very long period, possibly millions of years (Moore et al., 2003). We suggest that the widespread occurrence of fans within Degana required snow/ice precipitation (Moore and Howard, 2005; Grant and Wilson, 2011, 2012), followed by snowmelt within Degana to help the rim breaching of Degana-A. This suggests that sufficient ice deposition by mantling has occurred at least since the formation of the Degana crater. On Degana-A southern floor, possibly all the fans coalesced at their toe region and eroded (Figs. 6b, 18). Thus, we propose that Degana-A was affected by snow/ice cover over Degana emplaced at some point after its formation around ~3.7 Ga. We infer the ejecta from Degana-A played a role in melting the deposited snow/ice over the shattered dome, a scenario that had already been proposed for other locations on Mars (Mangold, 2012).

(5) At the last stage, during the Amazonian or post fan formation (Kite et al., 2017), moraine-like ridges are formed. The glacial activities in lower latitudes were reported to be more likely on the pole-facing walls of the craters (Williams et al., 2009; de Haas et al., 2015). The presence of moraine-like ridges on the pole facing northern wall of Degana (Figs. 13, 18) provides comprehensive evidence for the glacial activity that occurred up to lower mid-latitude (Shean, 2010). Moraine-like ridges superposed over fans f2 and f3 (Fig. 13) imply their post fan formation. This also suggests that the atmosphere-derived snow/ice was possible up to this latitude during the Amazonian period (Figs. 17, 18).

Overall, the major implications from our study are that the craters excavated into a Noachian volcanic edifice and exposed pristine early Martian minerals, which is similar to earlier studies at different location of Mars (Mustard et al., 2009; Skok et al., 2010; Quantin et al., 2012; Baratoux et al., 2013). Degana crater also hosts significant evidence for post-Noachian fluvial activities. This means that they formed under climatic conditions more favorable to sustain runoff, which was capable to breach the Degana-A rim. Notably, no delta deposits like those formed in the Jezero crater (e.g., Goudge et al., 2017) were observed in the Degana. This implies that the fans in Degana-A were not deposited into a standing body of water (Fassett and Head, 2008). This indicates that the climatic conditions were suited for alluvial fan deposits only which might be due to limited liquid water availability due to low temperatures, lack of moisture, and/or insufficient atmospheric pressure. However, this climatic condition varied over the Hesperian-Amazonian. This suggests that during the Hesperian-Amazonian, the ice accumulation at this latitude considerably reduced, which enabled moraine-forming glacial activity during the Amazonian, but no more (glacio-)

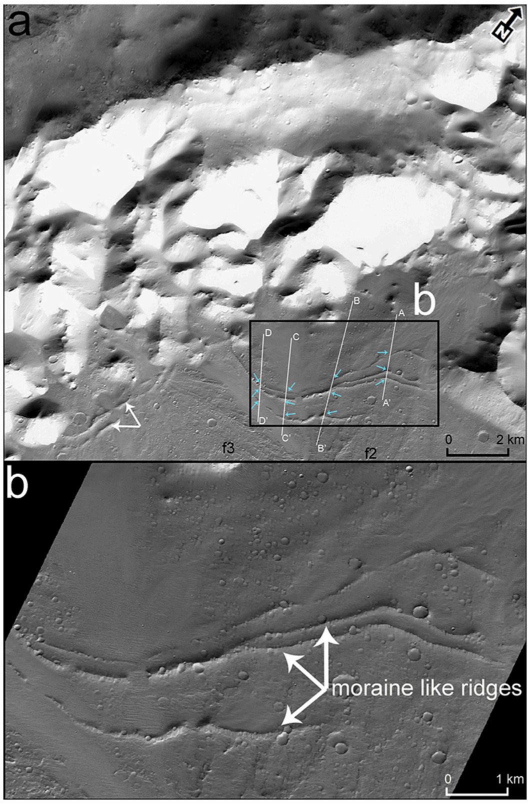

Fig. 13. a) CTX image (G02_018874_1561_XN_23S045W) of the northern wall of Degana crater showing moraine-like ridges (marked with black arrow). These moraine-like ridges occur on the pole-facing wall. These ridges superposed over two fan deposits (f2 and f3). b) four distinguishable moraine-like ridges formed on fan f2. The thickness and the relative height of the ridges vary.

fluvial activity. Thus, this region is one of the locations on Mars, which witnessed the transition from fan-forming fluvial activity in the Hesperian to moraine-building glacial activity in the Amazonian.

5. Conclusions

We carried out a detailed topographical, morphological, mineralogical, and chronological analysis of impact craters Degana and Degana-A. Our results reveal the diverse geologic activities, which are:

- Degana and Degana-A craters formed on a ~ 1.2 km high Noachian volcanic dome. Both impacts excavated up to ~2.7 km deep, i.e., ~1.5 km deep in the Noachian crust located below the base of the volcanic dome. These impacts exposed pristine Noachian mafic minerals (Mg-rich olivine and low-calcium pyroxene) on the walls of Degana-A crater. Xiao et al., 2012 mentioned that the true composition of these ancient Noachian-aged volcanoes is not known, as most of these volcanoes are heavily dust-covered and no in-situ observations were taken yet. Thus, this study provides the likely composition of one of the ancient volcanoes on Mars.
- Both crater floors are covered by depositional fans, and especially Degana-A crater fans show distinguishable ridges, stratigraphic layers, and coalesced deposits. A notable ~1 km wide rim breach on the eastern rim of Degana-A crater and the hydrological estimation over this region suggest water flowed with a velocity of ~2 m/s and with a discharge rate of ~2.25 mm/h. This is in agreement with Kite et al. (2019) that reported a discharge rate of 3 mm/h for globally present channels on Mars.
- Moraine-like ridges linked to glacial activities superposed the alluvial fans. Such moraine-like ridges are observed only on the pole-facing walls of Degana crater. The alluvial fan deposits and the glacial moraine ridges are non-coeval events. They strongly indicate evidence for snow/ice deposition towards the lower latitudes of Mars during Hesperian-Amazonian epochs suggesting local climate change on Mars. Thus, Degana is one of the important locations that

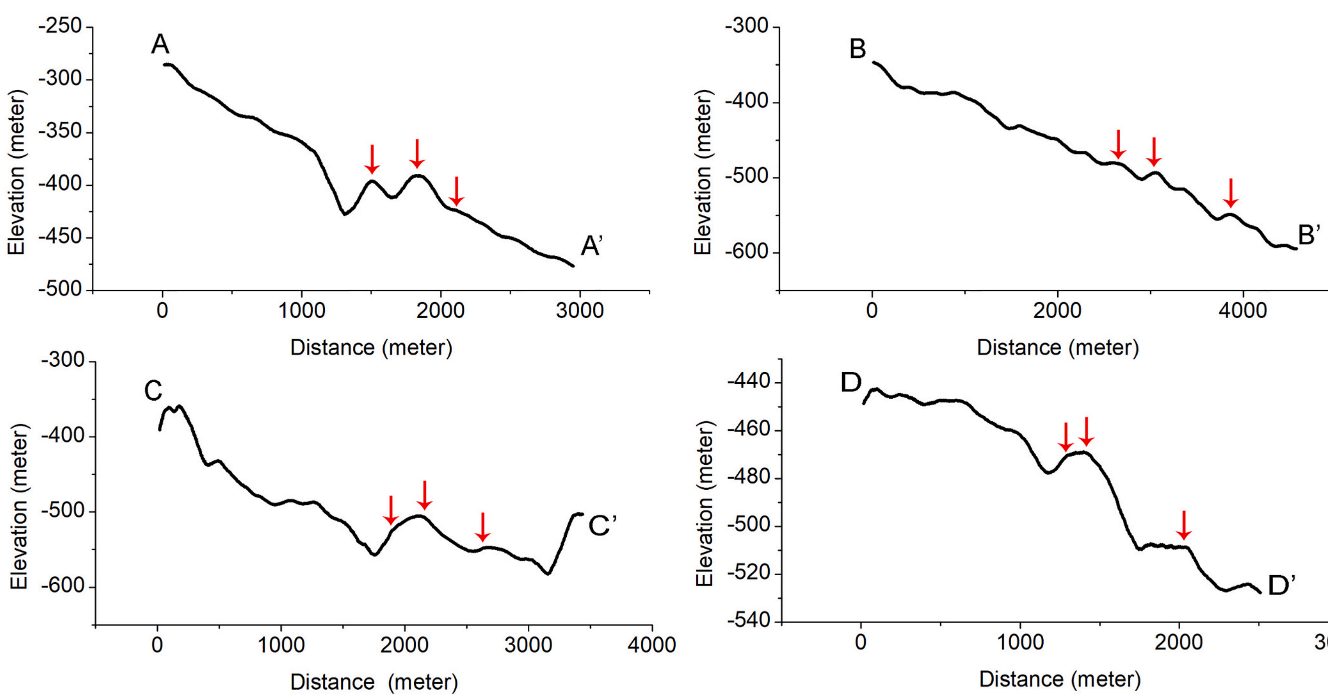

Fig. 14. Example elevation profiles used to determine the thickness of moraine-like ridges extracted from CTX DEM (stereo-pair CTX_016540_1579_034592_1579). Red is the location of ridges. The height of some of the ridges is unresolvable in the CTX DEM. (For interpretation of the references to color in this figure legend, the reader is referred to the web version of this article.)

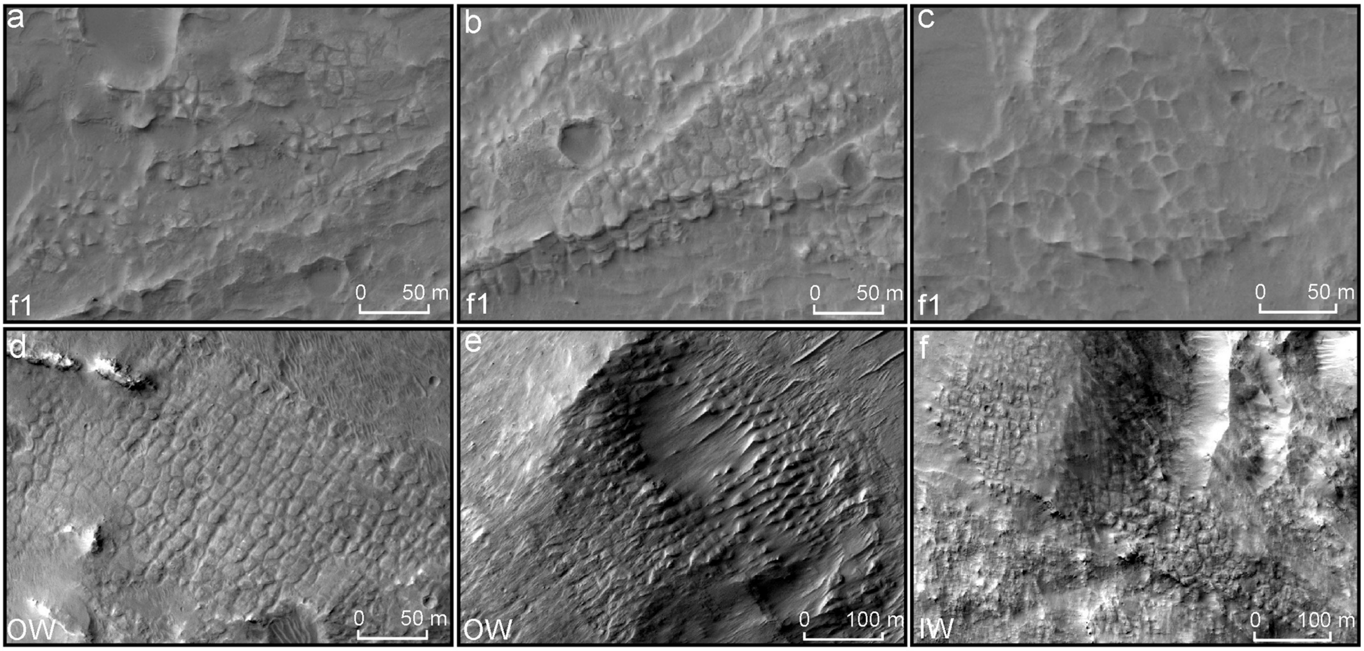

Fig. 15. Examples of polygons within the Degana-A fan deposits. a) Trough boundary type polygons on fan f1. b) Polygons formed over the layered ridges. The size and extent of the polygons vary around the ridge. c) Ridge boundary type polygon with hollows at the center and raised ridges at the boundaries. Examples of polygons within the walls of Degana crater. d) Polygons over the raised northern outer wall (OW) of Degana-A crater with varying sizes. e) Polygons with dust mantling over the OW of Degana-A crater. f) Polygons on the inner walls (IW) of Degana crater. All the polygons on the walls are observed along the topmost part of the rim only. (HiRISE ID ESP_016540_1560).

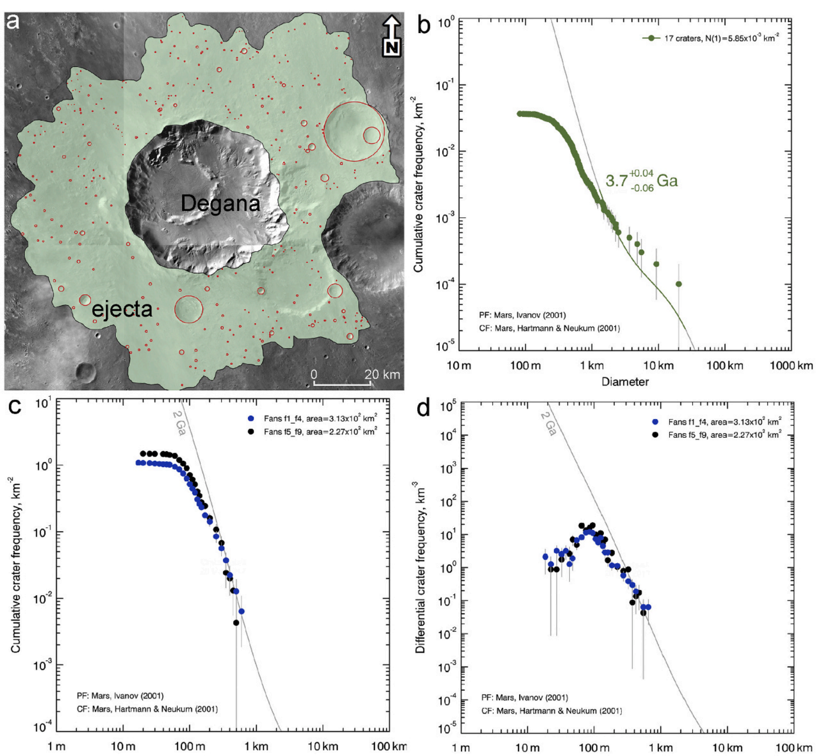

Fig. 16. a) Degana crater and its ejecta boundary with superposed craters considered for crater chronology. Counts (red circles) were conducted using CTX images. b) Relative ages were determined using the production function of Ivanov (2001) and chronology function of Hartmann and Neukum (2001). The apparent model age of Degana crater is ~3.7 Gyr. c) Cumulative crater size-frequency distribution for all the fans within both craters. d) Differential crater size-frequency distribution for all the fans within both craters. (For interpretation of the references to color in this figure legend, the reader is referred to the web version of this article.)

report lower latitudes (23°S) glacial activities on Mars (Shean et al., 2005).

- Based on the dome elevation, the formation of fluvial/glacial deposits within the impact craters, and the latitudinal location, we suggest atmospheric snow/ice precipitation as the possible source.

Thus, Degana is a unique location on Mars that has mid-Noachian aged mafic minerals, Hesperian-Amazonian aged fluvial and glacial deposits.

Supplementary data to this article can be found online at https://doi.org/10.1016/j.icarus.2021.114397.

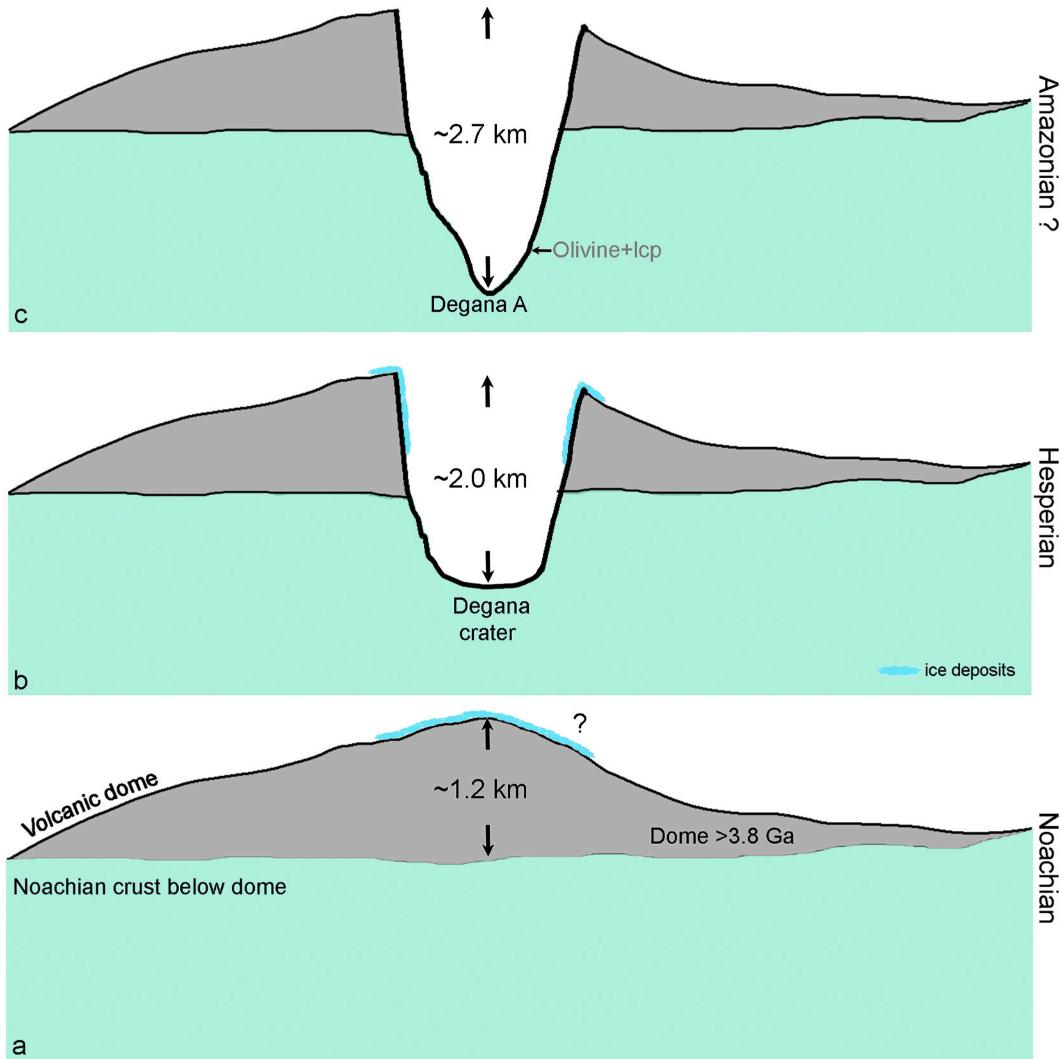

Fig. 17. Schematic perspective outlining the tentative sequence of events. a) Volcanic dome formation at ~4.0 Ga with an elevation of ~1.2 km above the surrounding surface (baseline of the dome). b) Formation of Degana crater at ~3.7 Ga excavating ~2 km of the volcanic dome. c) Formation of Degana-A in Degana crater and additional ~0.7 km of excavation. In total, both the craters excavate ~2.7 km. The crater size-frequency distribution for all the fans suggests an Amazonian crater retention age.

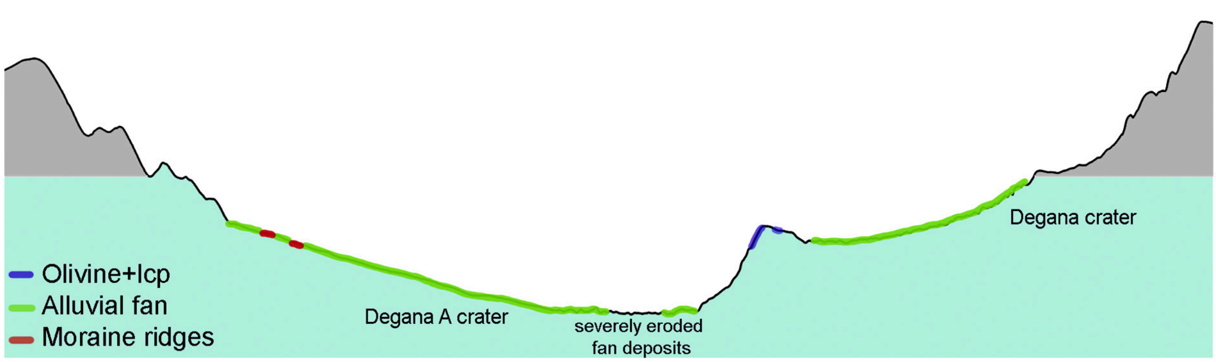

Fig. 18. Schematic diagram of the current state of Degana and Degana-A. Locations of mafic minerals, fluvial and glacial landforms are marked within the exposed surface.

Declaration of Competing Interest

None.

Acknowledgment

We thank Hannes Bernhardt of Arizona State University and an anonymous reviewer for the constructive suggestions. We thank Physical Research Laboratory, Department of Space, India, for supporting our work. NM acknowledges the support from the Centre National d'Etudes Spatiales (CNES), France. We thank the CRISM, HiRISE and CTX team for the availability of the required datasets used in this study, which were downloaded from the PDS (https://ode.rsl.wustl.edu/mars/).

References

Abolt, C.J., Young, M.H., Atchley, A.L., Harp, D.R., 2018. Microtopographic control on the ground thermal regime in ice-wedge polygons. Cryosphere 12, 1957–1968. https://doi.org/10.5194/tc-12-1957-2018.

Adams, J.B., 1974. Visible and near-infrared diffuse reflectance: spectra of pyroxenes as applied to remote sensing of solid objects in the solar system. J. Geophys. Res. 79, 4829–4836. https://doi.org/10.1029/JB079i032p04829.

Ansan, V., Mangold, N., 2013. 3D morphometry of valley networks on Mars from HRSC/MEX DEMs: implications for climatic evolutionthrough time. J. Geophys. Res. Planets 118, 1873–1894. https://doi.org/10.1002/jgre.20117.

Arfstrom, J., Hartmann, W.K., 2005. Martian flow features, moraine-like ridges, and gullies: terrestrial analogs and interrelationships. Icarus 174 (2), 321–335. https://doi.org/10.1016/j.icarus.2004.05.026.

Armitage, J.J., Warner, N.H., Goddard, K., Gupta, S., 2011. Timescales of alluvial fan development by precipitation on Mars. Geophys. Res. Lett. 38, L17203 https://doi.org/10.1029/2011GL048907.

Baratoux, D., Toplis, M.J., Monnereau, M., Sautter, V., 2013. The petrological expression of early Mars volcanism. J. Geophys. Res. Planets 118, 59–64. https://doi.org/10.1029/2012JE004234.

Berman, D.C., Balme, M.R., Rafkin, S.C.R., Zimbelman, J.R., 2011. Transverse Aeolian Ridges (TARs) on Mars II: distributions, orientations, and ages. Icarus 213, 116–130. https://doi.org/10.1016/j.icarus.2011.02.014.

Blair, T.C., McPherson, J.G., 1994. Alluvial fans and their natural distinction from rivers based on morphology, hydraulic processes, sedimentary processes, and facies assemblages. J. Sediment. Res. 64 (3a), 450–489.

Blair, T.C., McPherson, J.G., 2009. Processes and forms of alluvial fans. In: Parsons, A.J., Abrahams, A.D. (Eds.), Geomorphology of Desert Environments. Springer Science+Business Media B.V, pp. 413–466.

Boatwright, B.D., Head, J.W., 2019. Fluvial Geology of the Northwest Hellas Region, Mars: Evidence for Localized Drainage and Terrain Inversion. In: Lunar and Planetary Science Conference, p. 2688.

Bristow, T.F., Rampe, E.B., Achilles, C.N., Blake, D.F., Chipera, S.J., Craig, P., et al., 2018. Clay mineral diversity and abundance in sedimentary rocks of Gale crater, Mars. Sci. Adv. 4 (6), eaar3330. https://doi.org/10.1126/sciadv.aar3330.

Brooker, L.M., et al., 2018. Clastic polygonal networks around Lyot Crater, Mars: possible formation mechanisms from morphometric analysis. Icarus 302, 386–406.

Burns, R.G., 1970. Crystal field spectra and evidence of cation ordering in olivine minerals. Am. Mineral. 55, 1608–1632.

Carter, J., et al., 2013. Hydrous minerals on Mars as seen by the CRISM and OMEGA imaging spectrometers: Updated global view. J. Geophys. Res. (Planets) 118 (2013), 831–858.

Clenet, H., Pinet, P.C., Daydou, Y., Heuripeau, F., Rosemberg, C., Baratoux, D., Chevrel, S., 2011. A new systematic approach using the Modified Gaussian Model: insight for the characterization of chemical composition of olivines, pyroxenes, and olivine–pyroxene mixtures. Icarus 213, 404–422. https://doi.org/10.1016/j.icarus.2011.03.002.

Cloutis, E.A., Gaffey, M.J., 1991. Pyroxene spectroscopy revisited: spectral composition correlations and relationship to geothermometry. J. Geophys. Res. 96, 22,809–22,826. https://doi.org/10.1029/91JE02512.

Cloutis, E.A., Galley, M.J., Jackowski, T.L., Reed, R.L., 1986. Calibrations of phase abundance, composition, and particle size distributions for olivine-orthopyroxene mixtures from reflectance spectra. J. Geophys. Res. 91, 11,641–11,653. https://doi.org/10.1029/JB091iB11p11641.

de Haas, T., Hauber, E., Conway, S.J., van Steijn, H., Johnsson, A., Kleinhans, M.G., 2015. Earth-like aqueous debris-flow activity on Mars at high orbital obliquity in the last million years. Nat. Commun. 6 https://doi.org/10.1038/ncomms.

Di Achille, G., Hynek, B.M., 2010a. Deltas and valley networks on Mars: implications for a global hydrosphere. In: Lakes on Mars edited by N. Cabrol and E. Grin. Chap. 8, Elsevier, New York.

Di Achille, G., Hynek, B.M., 2010b. Ancient ocean on Mars supported by global distribution of deltas and valleys. Nat. Geosci. 3, 459–463. https://doi.org/10.1038/NGEO891.

Dickson, J.L., Kerber, L.A., Fassett, C.I., Ehlmann, B.L., 2018. A global, blended CTX mosaic of Mars with vectorized seam mapping: a new mosaicking pipeline using principles of non-destructive image editing. In: Proc. Lunar Planet. Sci. Conf. 49th, abstract#2480.

Ehlmann, B.L., et al., 2009. Identification of hydrated silicate minerals on Mars using MRO-CRISM: Geologic context near Nili Fossae and implications for aqueous alteration. J. Geophys. Res. 114, E00D08. https://doi.org/10.1029/2009JE003339.

Elmaarry, M.R., Markiewicz, W.J., Mellon, M.T., et al., 2010. Crater floor polygons: Desiccation patterns of ancient lakes on Mars? J. Geophys. Res.-Planets 115. https://doi.org/10.1029/2010JE0. E10 0 06. 03609.

Elmaarry, M.R., Kodikara, J., Wijessoriya, S., Markiewicz, W.J., Thomas, N., 2012. Desiccation mechanism for formation of giant polygons on earth and intermediate-sized polygons on Mars: results from a pre-fracture model. Earth Planet. Sci. Lett. 323–324, 19–26.

Fassett, C.I., Head, J.W., 2008. The timing of martian valley network activity: constraints from buffered crater counting. Icarus 195, 61–89. https://doi.org/10.1016/j.icarus.2007.12.009.

Fastook, J.L., Head, J.W., 2015. Glaciation in the Late Noachian icy highlands: ice accumulation, distribution, flow rates, basal melting, and top-down melting rate sand patterns. Planet. Space Sci. 106, 82–98.

Fastook, J.L., Head, J.W., Marchant, D.R., Forget, F., Madeleine, J.-B., 2012. Early Mars climate near the Noachian–Hesperian boundary: independent evidence for cold conditions from basal melting of the south polar ice sheet (Dorsa Argentea Formation) and implications for valley network formation. Icarus 219 (1), 25–40. https://doi.org/10.1016/j.icarus.2012.02.013.

Fergason, R.L., Hare, T.M., Laura, J., 2018. HRSC and MOLA Blended Digital Elevation Model at 200 m v2, Astrogeology PDS Annex. U.S. Geological Survey. http://bit.ly/HRSC_MOLA_Blend_v0.

Flahaut, J., Mustard, J.F., Quantin, C., Clenet, H., Allemand, P., Thomas, P., 2010. Dikes of distinct composition intruded into Noachian-aged crust exposed in the walls of Valles Marineris. Geophys. Res. Lett. 38, 15.

Flahaut, J., Quantin, C., Clenet, H., Allemand, P., Mustard, J.F., Thomas, P., 2012. Pristine Noachian crust and key geologic transitions in the lower walls of Valles Marineris: insights into early igneous processes on Mars. Icarus 221, 420–435.

Forget, F., Haberle, R.M., Montmessin, F., Levrard, B., Head, J.W., 2006. Formation of glaciers on Mars by atmospheric precipitation at high obliquity. Science 311 (5759), 368–371.

Ghatan, G.J., Head, J.W., 2002. Candidate subglacial volcanoes in the south polar region of Mars: morphology, morphometry, and eruption conditions. J. Geophys. Res. 107, E7.

Goudge, T.A., Milliken, R.E., Head, J.W., Mustard, J.F., Fassett, C.I., 2017. Sedimentological evidence for a deltaic origin of the western fan deposit in Jezero crater, Mars and implications for future exploration. Earth Planet. Sci. Lett. 458, 357–365. https://doi.org/10.1016/j.epsl.2016.10.056.

Grant, J.A., Wilson, S.A., 2011. Late alluvial fan formation in southern Margaritifer Terra. Mars. Geophys. Res. Lett. 38, L08201 https://doi.org/10.1029/2011GL046844.

Grant, J.A., Wilson, S.A., 2012. A possible synoptic source of water for alluvial fan formation in Southern Margaritifer Terra. Mars. Planet. Space Sci. 72 (1), 44–52.

Gulick, V.C., 2001. Origin of the valley networks on Mars: a hydrological perspective. Geomorphology 37, 241–268. https://doi.org/10.1016/S0169-555X(00)00086-6.

Hallet, B., Sletten, R.S., Stewart, W., et al., 2013. Fracture networks, Gale Crater, Mars. In: Proceedings of 44th LPSC. #Abstract No. 3108.

Hamilton, V.E., Christensen, P.R., 2005. Evidence for extensive, olivine-rich bedrock on Mars. Geology 33 (6), 433–436. https://doi.org/10.1130/G21258.1.

Hartmann, W.K., Neukum, G., 2001. Cratering chronology and the evolution of Mars. Space Sci. Rev. 96, 165–194. https://doi.org/10.1023/A:1011945222010.

Hartmann, W.K., Thorsteinsson, T., Sigurdsson, F., 2002. Comparison of Icelandic and martian hillside gullies. In: Lunar and Planet. Sci. XLIII. Abstract #1904.

Hartmann, W.K., Thorsteinsson, T., Sigurdsson, F., 2003. Martian hillside gullies and Icelandic analogs. Icarus 162, 259–277.

Hartmann, W.K., Ansan, V., Berman, D.C., Mangold, N., Forget, F., 2014. Comprehensive analysis of glaciated Martian crater Greg. Icarus 228, 96–120. https://doi.org/10.1016/j.icarus.2013.09.016.

Hauber, E., Gasselt, S.V., Ivanov, B., Werner, S., Head, J.W., Neukum, G., Jaumann, R., Greeley, R., Mitchell, L.K., Muller, P., The HRSC Co-Investigator Team, 2005. Discovery of a flank caldera and very young glacial activity at Hecatus Tholus, Mars. Nature 434, 356–361. https://doi.org/10.1038/nature03423.

Head, J.W., Merchant, D.R., 2014. The climate history of early Mars: insights from the Antarctic McMurdo Dry Valleys hydrologic system. Antarct. Sci. 26 (6), 774–800.

Head, J.W., Pratt, S., 2001. Extensive Hesperian-aged south polar ice sheet on Mars: Evidence for massive melting and retreat, and lateral flow and ponding of meltwater. J. Geophys. Res. 106 (E6), 12275–12299. https://doi.org/10.1029/2000JE001359.

Head, J., et al., 2005. Tropical to mid-latitude snow and ice accumulation, flow, and glaciation on Mars. Nature 434, 346–351.

Hoke, M.R.T., Hynek, B.M., 2009. Roaming zones of precipitation on ancient Mars as recorded in valley networks. J. Geophys. Res. 114, E08002 https://doi.org/10.1029/2008JE003247.

Huang, J., Edwards, C.S., Horgan, B.H.N., Christensen, P.R., Kraft, M.D., Xiao, L., 2012. Identification and mapping of dikes with relatively primitive compositions in Thaumasia Planum on Mars: implications for Tharsis volcanism and the opening of Valles Marineris. Geophys. Res. Lett. 39, L17201 https://doi.org/10.1029/2012GL052523.

Irwin, R.P., Wray, J.J., Mest, S.C., Maxwell, T.A., 2018. Wind-eroded crater floors and intercrater plains, Terra Sabaea, Mars. J. Geophys. Res. Planets 123 (2), 445–467. https://doi.org/10.1002/2017JE005270.

Ivanov, B.A., 2001. Mars/Moon cratering rate ratio estimates. Space Sci. Rev. 96, 87–104. https://doi.org/10.1023/A:1011941121102.

Jorgenson, M.T., Shur, Y.L., Pullman, E.R., 2006. Abrupt increase in permafrost degradation in Arctic Alaska. Geophys. Res. Lett. 33, L02503 https://doi.org/10.1029/2005GL024960.

Kargel, J.S., Strom, R.G., 1992. Ancient glaciation on Mars. Geology 20 (1), 3–7.

Kerber, L., Dickson, J.L., Head, J.W., Grosfils, E.B., 2017. Polygonal ridge networks on Mars: diversity of morphologies and the special case of the Eastern Medusae Fossae Formation. Icarus 281, 200–219. https://doi.org/10.1016/j.icarus.2016.08.020.

King, T.V.V., Ridley, W.I., 1987. Relation of the spectroscopic reflectance of olivine to mineral chemistry and some remote sensing implications. J. Geophys. Res. 92, 11,457–11,469. https://doi.org/10.1029/JB092iB11p11457.

Kite, E.S., Harvey, I., Kahre, M.A., Wolff, M.J., Manga, M., 2013. Seasonal melting and the formation of sedimentary rocks on Mars, with predictions for the Gale crater mound. Icarus 223, 131–210. https://doi.org/10.1016/j.icarus.2012.11.034.
Kite, E.S., Sneed, J., Mayer, D.P., Wilson, S.A., 2017. Persistent or repeated surface habitability on Mars during the late Hesperian – Amazonian. Geophys. Res. Lett. 44, 3991–3999. https://doi.org/10.1002/2017GL072660.
Kite, E.S., Mayer, D.P., Wilson, S.A., Davis, J.M., Lucas, A.S., de Quay, G.S., 2019. Persistence of intense, climate-driven runoff late in Mars history, 5(3), eaav7710. Science Advances 5 (3), eaav7710. https://doi.org/10.1126/sciadv.aav7710.
Klima, R.L., Pieers, C.M., Dyar, M.D., 2007. Spectroscopy of synthetic Mg-Fe pyroxenes I: spin-allowed and spin-forbidden crystal field bands in the visible and near-infrared. Meteorit. Planet. Sci. 42, 235–253. https://doi.org/10.1111/j.1945-5100.2007.tb00230.x.
Kraal, E.R., Asphaug, E., Moore, J.M., Howard, A., Bredt, A., 2008. Catalogue of large alluvial fans in Martian impact craters. Icarus 194, 101–110. https://doi.org/10.1016/j.icarus.2007.09.028.
Kress, A.M., Head, J.W., 2015. Late Noachian and early Hesperian ridge systems in the south circumpolar Dorsa Argentea Formation, Mars: evidence for two stages of melting of an extensive late Noachian ice sheet. Planet. Space Sci. 109-110, 1–20. https://doi.org/10.1016/j.pss.2014.11.025.
Lachenbruch, A.H., 1963. Contraction theory of ice-wedge polygons: a qualitative discussion. In: Proceedings of International Permafrost Conference, Proceedings, Lafayette, Indiana. National Academy of Sciences, National Research Council Publication No. 1287, pp. 63–71.
Levy, J.S., Head, J., Marchant, D., 2009. Thermal contraction crack polygons on Mars: classification, distribution, and climate implications from HiRISE observations. J. Geophys. Res. 114 https://doi.org/10.1029/2008JE0 03273.
Mackay, J.R., 2000. Thermally induced movements in ice-wedge polygons, western arctic coast: a long-term study. Geogr. Phys. Quat. 54, 41–68.
Malin, M.C., et al., 2007. Context Camera investigation onboard the Mars Reconnaissance Orbiter. J. Geophys. Res. 112, E05S04. https://doi.org/10.1029/2006JE002808.
Mangold, N., 2005. High latitude patterned grounds on Mars: classification, distribution, and climatic control. Icarus 174, 336–359.
Mangold, N., 2012. Fluvial landforms on fresh impact ejecta on Mars. Planet. Space Sci. 62, 69–85.
Mangold, N., Adeli, S., Conway, S., Ansan, V., Langlais, B., 2012a. A chronology of early Mars climatic evolution from impact crater degradation. J. Geophys. Res.-Planets 117, E4. https://doi.org/10.1029/2011JE004005.
Mangold, N., Carter, J., Poulet, F., Dehouck, E., Ansan, V., Loizeau, D., 2012b. Late Hesperian aqueous alteration at Majuro crater, Mars. Planet. Space Sci. 72, 18–30.
Mangold, N., Kite, E.S., Kleinhans, M.G., Newsom, H., Ansan, V., Hauber, E., Kraal, E., Quantin, C., Tanaka, K., 2012c. The origin and timing of fluvial activity at Eberswalde crater, Mars. Icarus 220, 530–551.
McCauley, J.F., 1978. Geologic map of the Coprates quadrangle of Mars. https://doi.org/10.3133/i897.
McEwen, A.S., et al., 2007. Mars Reconnaissance Orbiter's High-Resolution Imaging Science Experiment (HiRISE). J. Geophys. Res. 112, E05S02. https://doi.org/10.1029/2005JE002605.
McSween, H.Y., et al., 2006. Characterization and petrologic interpretation of olivine-rich basalts at Gusev Crater, Mars. J. Geophys. Res. 111, E02S10. https://doi.org/10.1029/2005JE002477.
Mellon, M.T., et al., 2009. Ground ice at the Phoenix Landing Site: Stability state and origin. J. Geophys. Res. 114, E00E07. https://doi.org/10.1029/2009JE003417.
Michael, G.G., 2013. Planetary surface dating from crater size-frequency distribution measurements: multiple resurfacing episodes and differential isochron fitting. Icarus 226, 885–890.
Michael, G.G., Kneissl, T., Neesemann, A., 2016. Planetary surface dating from crater size-frequency distribution measurements: Poisson timing analysis. Icarus 227, 279–285.
Milton, D.J., 1973. Water and processes of degradation in the Martian landscape. J. Geophys. Res. 78, 4037–4047.
Moore, J.M., Howard, A.D., 2005. Large alluvial fans on Mars. J. Geophys. Res. 110, E04005 https://doi.org/10.1029/2004JE002352.
Moore, J.M., Howard, A.D., Dietrich, W.E., Schenk, P.M., 2003. Martian layered fluvial deposits: implications for Noachian climate scenarios. Geophys. Res. Lett. 30 (24), 2292. https://doi.org/10.1029/2003GL019002.
Morgan, A.M., Beyer, R.A., Howard, A.D., Moore, J.M., 2012. The alluvial fans of Saheki crater. Lunar Planet. Sci. 43. Abstract #2815.
Morgan, A.M., Howard, A.D., Hobley, D.E., Moore, J.M., Dietrich, W.E., Williams, R.M., Burr, D.M., Grant, J.A., Wilson, S.A., Matsubara, Y., 2014. Sedimentology and climatic environment of alluvial fans in the Martian Saheki crater and a comparison with terrestrial fans in the Atacama Desert. Icarus 229, 131–156.
Murchie, S., et al., 2007. Compact Reconnaissance Imaging Spectrometer for Mars (CRISM) on Mars Reconnaissance Orbiter (MRO). J. Geophys. Res. 112, E05S03. https://doi.org/10.1029/2006JE002682.
Mustard, J.F., Poulet, F., Gendrin, A., Bibring, J.-P., Langevin, Y., Gondet, B., Mangold, N., Bellucci, G., Altieri, F., 2005. Olivine and pyroxene diversity in the crust of Mars. Science 307, 1594–1597.
Mustard, J.F., Poulet, F., Head, J.W., Mangold, N., Bibring, J.-P., Pelkey, S.M., et al., 2007. Mineralogy of the Nili Fossae region with OMEGA/Mex data: 1 ancient impact melt in the Isidis basin and implications for the transition from the Noachian to Hesperian. J. Geophys. Res. 112, E08S03.
Mustard, J.F., Ehlmann, B.L., Murchie, S.L., Poulet, F., Mangold, N., Head, J.W., Bibring, J.P., Roach, L.H., 2009. Composition, Morphology, and Stratigraphy of Noachian Crust around the Isidis basin. J. Geophys. Res. 114, E00D12. https://doi.org/10.1029/2009JE003349.
Neal, J.T., Langer, A.M., Kerr, P.F., 1968. Giant desiccation polygons of Great Basin playas. Geol. Soc. Am. Bull. 79 (1), 69–90.
Ody, A., Poulet, F., Bibring, J.P., Loizeau, D., Carter, J., Gondet, B., Langevin, Y., 2013. Global investigation of olivine on Mars: insights into crust and mantle compositions. J. Geophys. Res. 118, 234–262.
Oehler, D.Z., Mangold, N., Hallet, B., Fairén, A.G., Le Deit, L., Williams, A.J., Sletten, R. S., Martínez-Frías, J., 2016. Origin and significance of decameter-scale polygons in the lower Peace Vallis fan of Gale crater, Mars. Icarus 277, 56–72.
Palumbo, A., Head, J.W., 2017. Impact cratering as a cause of climate change, surface alteration, and resurfacing during the early history of Mars. Meteorit. Planet. Sci. https://doi.org/10.1111/maps.13001.
Paterson, W.S.B., 1994. The physics of glaciers, third ed. Pergamon Press, New York.
Pelkey, S.M., Mustard, J.F., Murchie, S., Clancy, R.T., Wolff, M., Smith, M., Milliken, R., Bibring, J.-P., Gendrin, A., Poulet, F., Langevin, Y., Gondet, B., 2007. CRISM multispectral summary products: Parameterizing mineral diversity on Mars from reflectance. J. Geophys. Res. 112, E08S14.
Poulet, F., Bibring, J.P., Langevin, Y., Mustard, J.F., Mangold, N., Vincendon, M., Gondet, B., Pinet, P., Bardintzeff, J.M., Platevoet, B., 2009a. Quantitative compositional analysis of martian mafic regions using the MEx/OMEGA reflectance data 1. Methodology, uncertainties and examples of application. Icarus 201, 69–83.
Poulet, F., Mangold, N., Platevoet, B., Bardintzeff, J.-M., Sautter, V., Mustard, J.F., Bibring, J.-P., Pinet, P.C., Langevin, Y., Gondet, B., Aléon-Toppani, A., 2009b. Quantitative compositional analysis of martian mafic regions using the MEx/OMEGA reflectance data 2. Petrological implications. Icarus 201, 84–101.
Quantin, C., Flahaut, J., Clenet, H., Allemand, P., Thomas, P., 2012. Composition and structures of the subsurface in the vicinity of Valles Marineris as revealed by central uplifts of impact craters. Icarus 221, 436–452.
Quantin-Nataf, C., Lozac'h, L., Thollot, P., Loizeau, D., Bultel, B., Fernando, J., Allemand, P., Dubuffet, F., Poulet, F., Ody, A., Clenet, H., Leyrat, C., Harrisson, S., 2018. MarsSI: Martian surface data processing information system. Planet. Space Sci. 150, 157–170.
Robbins, S.J., Hynek, B.M., 2012. A new global database of Mars impact craters ≥1 km: global crater properties and regional variations of the simple-to-complex transition diameter. J. Geophys. Res. 117, E06001.
Rogers, A.D., Warner, N.H., Golombek, M.P., Head, J.W., Cowart, J.C., 2018. Areally extensive surface bedrock exposures on Mars: many are clastic rocks, not lavas. Geophys. Res. Lett. 45, 1767–1777. https://doi.org/10.1002/2018GL077030.
Salvatore, M.R., Mustard, J.F., Wyatt, M.B., Murchie, S.L., 2010. Definitive evidence of Hesperian basalt in Acidalia and Chryse planitiae. J. Geophys. Res. 115, E7 https://doi.org/10.1029/2009JE003519.
Scanlon, K.E., Head, J.W., Wilson, L., Marchant, D.R., 2014. Volcano–ice interactions in the Arsia Mons tropical mountain glacier deposits. Icarus 237, 315–339. https://doi.org/10.1016/j.icarus.2014.04.024.
Scanlon, K.E., Head, J.W., Marchant, D.R., 2015. Volcanism-induced, local wet-based glacial conditions recorded in the Late Amazonian Arsia Mons tropical mountain glacier deposits. Icarus 250, 18–31. https://doi.org/10.1016/j.icarus.2014.11.016.
Scott, D.H., Tanaka, K.L., 1986. Geologic map of the western equatorial region of Mars. In: U.S. Geol. Surv. Misc. Invest. Ser. Map, I-1802-A.
Shean, D.E., 2010. Candidate ice-rich material within equatorial craters on Mars. Geophys. Res. Lett. 37, L24202 https://doi.org/10.1029/2010GL045181.
Shean, D.E., Head, J.W., Marchant, D.R., 2005. Origin and evolution of a cold-based tropical mountain glacier on Mars: the Pavonis Mons fan-shaped deposit. J. Geophys. Res. 110, E05001.
Siebach, K.L., Grotzinger, J.P., 2014. Volumetric estimates of ancient water on Mount Sharp based on boxwork deposits, Gale Crater, Mars. J. Geophys. Res: Planets 119 (1), 189–198. https://doi.org/10.1002/2013JE004508.
Sinha, R.K., Vijayan, S., 2017. Geomorphic investigation of craters in Alba Mons, Mars: implications for Late Amazonian glacial activity in the region. Planet. Space Sci. 144, 32–48. https://doi.org/10.1016/j.pss.2017.05.014.
Skok, J.R., Mustard, J.F., Murchie, S.L., Wyatt, M.B., Ehlmann, B.L., 2010. Spectrally distinct ejecta in Syrtis Major, Mars: Evidence for environmental change at the Hesperian-Amazonian boundary. J. Geophys. Res. 115, E00D14. https://doi.org/10.1029/2009JE003338.
Skok, J.R., Mustard, J.F., Tornabene, L.L., Pan, C., Rogers, D., Murchie, S.L., 2012. A spectroscopic analysis of Martian crater central peaks: Formation of the ancient crust. J. Geophys. Res. 117, E00J18. https://doi.org/10.1029/2012JE004148.
Smith, D.E., et al., 2001. Mars orbiter laser altimeter: experiment summary after the first year of global mapping of Mars. J. Geophys. Res. 106 (E10), 23689–23722. https://doi.org/10.1029/2000JE001364.
Soare, R.J., Conwat, S.J., Dohm, J.M., 2014. Possible ice-wedge polygons and recent landscape modification by "wet" periglacial processes in and around the Argyre impact basin, Mars. Icarus 233, 214–228. https://doi.org/10.1016/j.icarus.2014.01.034.
Sun, V.Z., Milliken, R.E., 2015. The geology and mineralogy of Ritchey crater, Mars: evidence for post-Noachian clay formation. J. Geophys. Res. Planets 119, 810–836. https://doi.org/10.1002/2013JE004602.
Sunshine, J.M., Pieters, C.M., 1998. Determining the composition of olivine from reflectance spectroscopy. J. Geophys. Res. 103, 13,675–13,688. https://doi.org/10.1029/98JE01217.
Sunshine, J.M., Pieters, C.M., Pratt, S.F., 1990. Deconvolution of mineral absorption bands: an improved approach. J. Geophys. Res. 95, 6955–6966. https://doi.org/10.1029/JB095iB05p06955.
Tanaka, K.L., Skinner, J.A., Dohm, J.M., Irwin, R.P., Kolb, E.J., Fortezzo, C.M., Platz, T., Michael, G.G., Hare, T.M., 2014. Geologic map of Mars: U.S. Geological Survey

Scientific Investigations Map 3292, scale 1:20,000,000, pamphlet, p. 43. https://doi.org/10.3133/sim3292.

Tornabene, L.L., Moersch, J.E., McSween, H.Y., Hamilton, V.E., Piatek, J.L., Christensen, P.R., 2008. Surface and crater-exposed lithologic units of the Isidis Basin as mapped by coanalysis of THEMIS and TES derived data products. J. Geophys. Res. 113, E10001 https://doi.org/10.1029/2007JE002988.

Vijayan, S., Sinha, R.K., Harish, Anilkumar, R., 2020. Evidence for multiple superposed fluvial deposits within Reuyl crater, Mars. J. Geophys. Res. Planets 125. https://doi.org/10.1029/2019JE006136 e2019JE006136.

Viviano-Beck, C.E., et al., 2014. Revised CRISM spectral parameters and summary products based on the currently detected mineral diversity on Mars. J. Geophys. Res. Planets 119, 1403–1431. https://doi.org/10.1002/2014JE004627.

Viviano-Beck, C.E., et al., 2015. MRO CRISM Type Spectra Library, NASA Planetary Data System. http://crismtypespectra.rsl.wustl.edu.

Viviano-Beck, C.E., Mucrchie, S.L., Daubar, I.J., Morgan, M.F., Seelos, F.P., Plescia, J.B., 2019. Composition of Amazonian volcanic material in Tharsis and Elysium, Mars, from MRO/CRISM reflectance spectra. Icarus 328, 274–286. https://doi.org/10.1016/j.icarus.2019.03.001.

Washburn, A.L., 1980. A Survey of Periglacial Processes and Environments. Geocryology, The Blackburn Press, New Jersey.

Weiss, D.K., Head, J.W., 2016. Impact ejecta induced melting of surface ice deposits on Mars. Icarus 280, 205–233. https://doi.org/10.1016/j.icarus.2016.07.007.

Williams, K., Toon, O., Heldmann, J., Mellon, M., 2009. Ancient melting of mid-latitude snowpacks on mars as a water source for gullies. Icarus 200, 418–425.

Wilson, S.A., Zimbelman, J.R., 2004. Latitude-dependent nature and physical characteristics of transverse aeolian ridges on Mars. J. Geophys. Res. E: Planets 109, E10003. https://doi.org/10.1029/2004JE002247.

Wilson, S.A., Morgan, A.M., Howard, A.D., Grant, J.A., 2021. The global distribution of craters with alluvial fans and deltas on Mars. Geophys. Res. Lett. https://doi.org/10.1029/2020GL091653.

Wordsworth, R., Forget, F., Millour, E., Head, J.W., Madeleine, J.B., Charnay, B., 2013. Global modeling of the early Martian climate under a denser CO2 atmosphere: water cycle and ice evolution. Icarus 222 (1), 1–19. https://doi.org/10.1016/j.icarus.2012.09.036.

Xiao, L., Huang, J., Christensen, P.R., Greeley, R., Williams, D.A., Zhao, J., He, Q., 2012. Ancient volcanism and its implication for thermal evolution of Mars. Earth Planet. Sci. Lett. 323–324, 9–18.

Yoshikawa, K., 2003. Origin of the polygons and the thickness of Vastitas borealis formation in Western Utopia Planitia on Mars. Geophys. Res. Lett. 30 (12), 1603. https://doi.org/10.1029/2003GL017165.

Icarus 343 (2020) 113704

Contents lists available at ScienceDirect

Icarus

journal homepage: www.elsevier.com/locate/icarus

Craters in the vicinity of Valles Marineris region, Mars: Chronological implications to the graben and pits activities

Harish [a,b], S. Vijayan [a,*]

[a] Planetary Science Division, Physical Research Laboratory, Ahmedabad 380009, India
[b] Indian Institute of Technology, Gandhinagar 382355, India

ARTICLE INFO

Keywords:
Impact process
Mars
Geologic processes

ABSTRACT

Graben and pits are features closely associated with the Valles Marineris (VM) region on Mars. Earlier studies indicated that they are likely precursors for the VM trough formation, and thus they may assist in our understanding of how long the trough formation prevailed in the vicinity of VM. This study aims to understand how the graben and pit formation varied chronologically and spatially within a ~100 km vicinity of the VM region. We examined 1516 craters and found 48 craters that are superposed/cross-cut by graben, pits, and troughs or vice-versa with adequate ejecta or floor area for dating. Tithonium region graben and troughs cross-cut the craters around ~3.7 Ga. In the Ophir region, pits are formed on or post ~3.92 Ga at different elevations and have variable depths. Pital crater in the Ophir region interestingly hosts: 1) a broad *catena* ~14 km wide crosscutting its NE rim likely formed on or post to ~2.61 Ga, which inferred to be one-tenth to the adjoining Candor Chasma width of VM, 2) lobe like deposits associated with the *catena* emplaced over the Pital ejecta formed around ~1.14 Ga and 3) ~2 km wide pit superposed the lobe that reveals pit activity plausibly prolonged during Mid-Amazonian. Overall, our results likely point towards the contribution of graben and pits in the modification/development of peripheral areas of VM up to at least Mid-Amazonian. Thus, this study substantiated that the period and extent of graben and pit activities varied around the VM region.

1. Introduction

Valles Marineris (VM) is one of the longest and widest spatial features on the surface of Mars, whose formation possibly occurred over a large period ranges from ~200 million to billions of years (Schultz, 1998; Andrews-Hanna, 2012a, 2012b, 2012c). Spatially, VM covers an area up to ~4000 km in length, ~100 to 500 km in width, and has an average depth of 10 km (McCauley et al., 1972; Andrews-Hanna, 2012a; Brustel et al., 2017). The periphery of the VM region is dominated by graben and pits, which are considered as primordial features for the trough formation (McCauley et al., 1972; Sharp, 1973; Tanaka and Golombek, 1989; Okubo and Schultz, 2005). Their presence on the exterior/interior of VM are one of the indicators to understand the activities regarding its formation and their likely extension/development (McCauley et al., 1972; Sharp, 1973; Frey, 1979; Tanaka and Golombek, 1989; Lucchitta et al., 1994; Schultz, 1998; Okubo and Schultz, 2005; Carr and Head, 2010; Andrews-Hanna, 2012a; Brustel et al., 2017; Harish and Vijayan, 2019). Carr and Head (2010) stated that the age of the VM troughs and the canyon is difficult to determine, as they are spatially large. However, the formation of VM was predicted to be of late Noachian age due to its very large extent and is most likely related to the Tharsis tectonic and volcanic activities (Schultz, 1998; Dohm and Tanaka, 1999; Carr and Head, 2010; Carr, 2012). Additionally, faults in the VM region most likely occurred in the Late Noachian period (Dohm and Tanaka, 1999), whereas uplift and rifting considered to have occurred in Early to Late Hesperian (Schultz, 1998). Anderson et al. (2001) reported that the graben that formed along the length of VM probably formed during the Late Noachian to Early Hesperian. However, Greeley and Guest (1987) proposed that early Hesperian ridge plains formed before the rim of VM; this suggests that most of the opening occurred after the early Hesperian (Webb and Head, 2002; Montgomery et al., 2009). Also, graben which terminate against the VM were suggested to pre-date the VM opening (Hager et al., 2018). Additionally, many studies suggest that the broadening of the VM varied with location and took place at different rates and time (Baker et al., 1992; Lucchitta et al., 1994; Quantin et al., 2004; Fueten et al., 2011). These previous studies pose a question for the period of VM opening and development of its surrounding region.

* Corresponding author.
E-mail address: vijayan@prl.res.in (S. Vijayan).

https://doi.org/10.1016/j.icarus.2020.113704
Received 9 October 2019; Received in revised form 9 February 2020; Accepted 14 February 2020
Available online 19 February 2020
0019-1035/

In this regard, the duration of VM's formation remains an outstanding question. Also, which regions around the VM have been modified, and how is this observed over the surface, and how does this modification vary spatially as well as chronologically? Analyzing the graben and pits formed in the exterior vicinity of VM will possibly allow us to decipher the history of their development and modification. Chronologically, there is no detailed study on these graben and pits, which are closely associated with the exterior part of the VM region. Also, spatially there is no detailed study on how they differ associated with the coordinated chronological reference. We used the association of graben and pits with the craters (evaluating superposition and/or cross-cut relationships) to decipher the possible period up to which the extension/modification occurred in the VM region (Sharp, 1973; Tanaka and Golombek, 1989). As part of this evaluation, we carried out: 1) a detailed analysis of craters having superposition relationship with graben/pits/troughs, 2) estimated the chronological epoch for these craters which are located within 100 km vicinity of VM region, and 3) geometric analysis of pits over different regions of VM.

2. Regional context of VM

The most notable features of the Valles Marineris province are deep troughs, chasmata, graben, pits, collapsed pits, pit chains, valleys, interior layered deposits and landslides (Andrews-Hanna, 2012a, 2012b, 2012c; McCauley et al., 1972; Sharp, 1973; Tanaka and Golombek, 1989; Okubo and Schultz, 2005; Anderson et al., 2001; Wyrick et al., 2004; Quantin et al., 2004). Among these, graben are tectonic features with a very high length to depth ratio on the order of 10^5 (Golombek, 1979; Schultz, 1998; Mège et al., 2003). Martian graben are classified based on their morphology and relief (Anderson et al., 2001). Graben having lengths of tens to hundreds of kilometers and widths of less than five kilometers were considered simple graben (Tanaka and Davis, 1988; Tanaka et al., 1991; Davis et al., 1995), while complex graben were having more widths ranging between 10 and 100 km and depths up to a few kilometers (Plescia and Saunders, 1982; Banerdt et al., 1992; Anderson et al., 2001). On Mars, simple graben are more dominant features and their rate of formation decreases with time to other extensional tectonic features, such as complex graben, rifts, tension cracks and troughs (Anderson et al., 2001). The regional distribution of graben in and around the VM region is mapped by many studies (Golombek, 1979; Tanaka and Davis, 1988; Tanaka, 1990; Anderson et al., 2001; Kumar et al., 2018). In addition, troughs of VM were considered as large graben by many other studies (Hartmann, 1973; Sharp, 1973; Frey, 1979; Tanaka and Golombek, 1989). For instance, Schultz (1998) documented that different sequential processes superposed over graben formed the final Valles Marineris. Overall, the distribution suggests the vast presence of graben along VM and their role in VM trough formation (Tanaka and Golombek, 1989).

Pits or pit craters are generally circular to elliptical depressions, possibly shaped by tectonics and/or volcanism and frequently observed associated with the graben and parallel to border faults (Mège et al., 2003; Wyrick et al., 2004 and references therein; Vamshi et al., 2014). Pits on Mars typically have a conical shape with high slope walls and their floor is mainly concave-upwards at their centers (Wyrick et al., 2004). They are mainly found in alignments or chains and found collinear with normal faults (Sharp, 1973; Tanaka and Golombek, 1989; Wyrick et al., 2004; Wyrick and Smart, 2009). Pits are depressions similar to impact craters. Impact craters are distinguished from pits based on the following (Wyrick et al., 2004): 1) Craters are generally circular, whereas pits are generally elliptical (Fig. S1), 2) Craters are surrounded by ejecta, whereas pits don't, 3) Craters have clear elevated rim in most cases, whereas pits don't (Fig. S1), 4) Craters are much shallower than to the similar size pit (Fig. S1). In another way, pits are much deeper than the similar size craters. Wyrick et al. (2004) reported elliptical-shaped pits with the long axis parallel to the chain; such pits are enlarged by collapse and later coalesce to form a linear feature called

Table 1
Crater chronology for craters/lobe in the vicinity of Valles Marineris

Crater ID[a]	Name	Coordinates [°]		Diameter [km]	Area [km²]	Total no. craters	D[km] in fit range		No. craters in fit range	Age (Ga)[b]			N_{cum} (1 km)/10^6 km^2 of fitted isochron	Epoch		Geological unit on which crater superposed[d]
	This study	Latitude	Longitude				D_{min}	D_{max}		Best fit	Error +	Error −		This study[c]	Tanaka[d]	
18-000195	C6	−83.99	−5.41	17.78	1706.7	98	1.0	12.0	8	3.60	0.09	0.17	3980	lH	AHi	eHh
18-000070	C7	−81.89	−6.27	32.19	7515.1	502	1.6	7.8	9	3.63	0.08	0.12	4480	eH	AHi	eHh
18-000022	C10	−84.54	−4.19	56.29	16,205.5	830	1.8	7.8	19	3.71	0.04	0.05	8650	eH	AHi	eHh
18-000008	Perrotin	−77.95	−2.81	78.79	36,010.2	587	2.7	5.5	2	3.70	0.17	0.83	6620	eH	AHi	eHh
18-000103	C21	−69.68	−4.60	27.02	4809.1	582	4.0	20.0	5	3.92	0.07	0.08	22,400	mN	-	eHv
18-000043	Pital	−62.30	−9.22	38.50	10,968.2	597	1.0	11.0	14	2.61	0.45	0.54	1270	eA	AHi	eHv
18-000036	Saravan	−54.01	−16.93	45.99	582.9	337	1.1	3.6	4	3.76	0.09	0.16	8340	lN	-	mNh
	Pital_lobe	−61.24	−8.58		1100.0	170	0.39	2.70	17	1.14	0.29	0.25	556	mA	-	eHv

[a] Robbins and Hynek, 2012.
[b] Absolute model ages are derived using the poisson timing analysis of Michael et al. (2016) in the chronology system of Neukum–Ivanov, 2001 [production function of Ivanov (2001) and the chronology function of Hartmann and Neukum (2001).
[c] Epoch boundaries in the Neukum chronology system as recalculated in table 2 of Michael (2013).
[d] Tanaka et al., 2014.

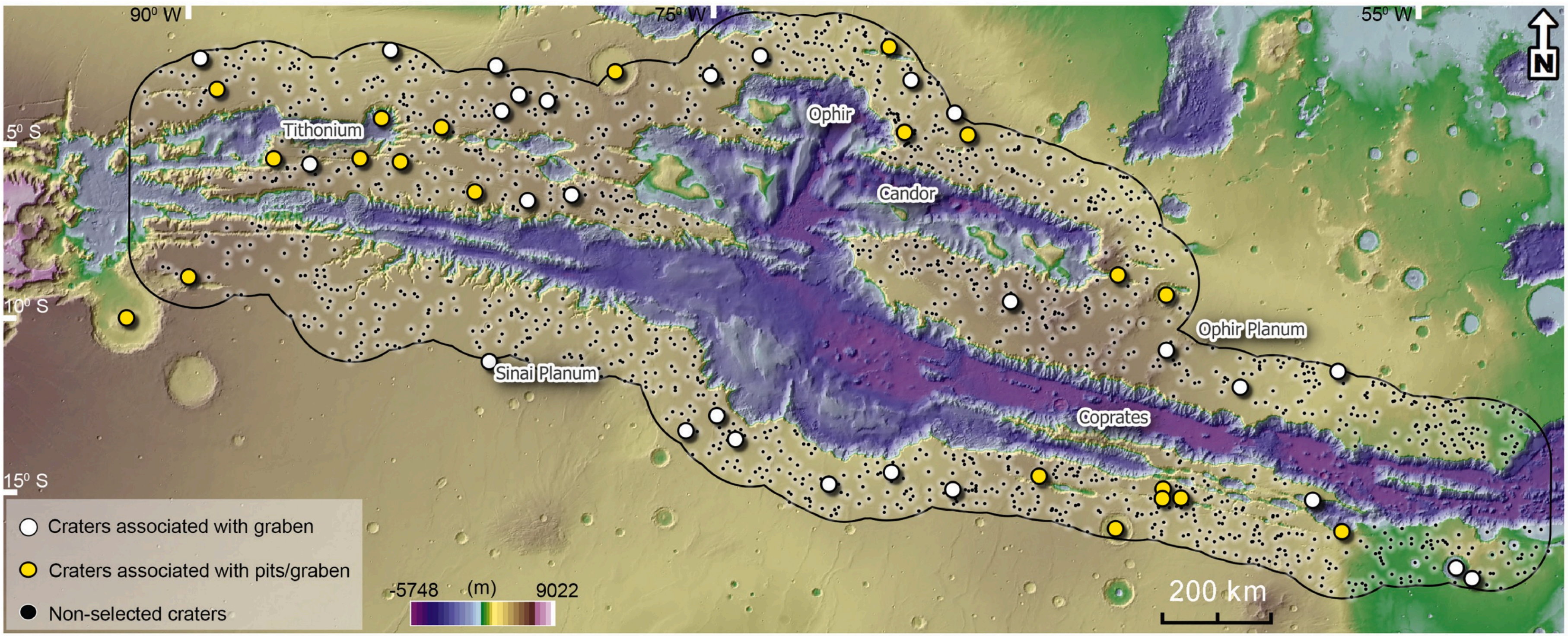

Fig. 1. Color shaded-relief map derived from MOLA topography (20°S to 0°N) of the Valles Marineris region, and distribution of craters within ~100 km vicinity. The location of 1516 craters within ~100 km vicinity used for analysis around the Valles Marineris region. (For interpretation of the references to color in this figure legend, the reader is referred to the online version of this chapter.)

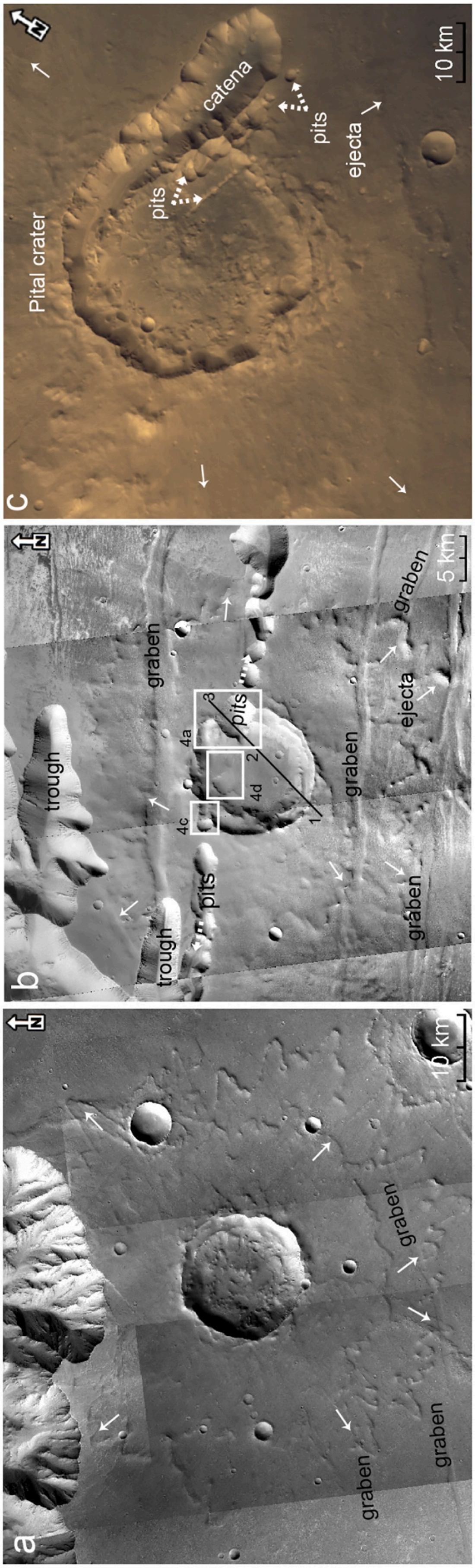

Fig. 2. Example craters having association with graben and pits in the 100 km vicinity from the VM wall. a) Craters associated with graben and emplacement of ejecta over the graben or vice-versa) (CTX id: D21_035450_1674_XI_12S070W, G23_027169_1673_XN_12S069W, D04_028712_1663_XI_13S070W), b) Craters associated with graben and pits, and rim of the crater crosscut by pit. (CTX id: J01_045077_1737_XI_06S084W, F17_042400_1748_XI_05S083W, P07_003949_1738_XN_06S083W). c) Pital crater with superposed pits, pit chains and *catena*. The northeastern rim of the crater is crosscut by catena. (Mars Orbiter Mission-MCC image id: MCC_MRR_20150423T072306117_G_D32). (White arrows – ejecta, dashed arrow – pit chains).

as trough (Sharp, 1973; Tanaka and Golombek, 1989). Two morphologies were suggested for pits: one for smaller pits (<2 km) and another for larger (4–10 km) (Scott and Wilson, 2002). Smaller pits have a regular shape and are in some cases contained within a graben, while larger pits have an irregular shape and are coalesced within each other (Scott and Wilson, 2002). Some of the pits have stratification on their walls, and there walls are differentially eroded (Wyrick et al., 2004). In the VM region, the pits are superposed on or crosscutting the graben, which suggests that the pits formed after the graben formation (Mège et al., 2003). Pits on Mars can also occur as continuous features known as pit crater chains, which are strongly associated with graben or faults (Wyrick et al., 2004). There are many pit crater chains and coalesced pits located almost parallel to VM, including Tithoniae Catenae, Ganges Catena, Ophir Catenae and Coprates Catena (Witbeck et al., 1991).

The boundary of VM also hosts several amphitheater-headed valleys (Lamb et al., 2007; Schmidt et al., 2018). Box-shaped planform geometry was proposed for these valleys/troughs having steep, stubby headwalls, and flat floors (Lamb et al., 2007). These valleys seem to follow the path of previously formed graben running parallel-subparallel to the VM and believed to have been produced by headward erosion due to preferential weathering through groundwater sapping, springs, or overland flows (Sharp and Malin, 1975, Pieri, 1980, Howard, 1988; Mangold et al., 2004; Lamb et al., 2007; Schmidt et al., 2018). However, Andrews-Hanna (2012c) defined them as collapse structures that trend parallel to the blunt end of the trough, which may be the planes of weakness generated due to minor tectonic activity and collapse. A recent study by Schmidt et al. (2018) identified long U-shaped valleys with amphitheater-shaped heads that extend from the chasma as graben. We, therefore, refer to such a feature as a trough in our study.

3. Data and methods

For the morphological analysis, we used Mars Reconnaissance Orbiter (MRO) and Context Camera (CTX) images at 6 m/pixel resolution (Malin et al., 2007), CTX mosaic images (Dickson et al., 2018) and Mars Orbiter Mission (MOM) Mars Color Camera (MCC) image at ~20 m/pixel resolution (Arya et al., 2015). We used ortho-projected daytime infrared (IR) data from the Mars Odyssey THermal EMission Imaging System (THEMIS) at 100 m/pixel resolution for the analysis of regional morphology (Christensen et al., 2004; Fergason et al., 2013). For the topographic analysis, we used individual altimetry readings of Precision Experiment Data Record (PEDR) products and a digital elevation model (DEM) mosaic of the Mars Global Surveyor (MGS) Mars Orbiter Laser Altimeter (MOLA) data at ~463 m/pixel resolution (Smith et al., 2001).

We used the CraterTools extension in ESRI's ArcMap 10.2.1 software to derive the absolute model ages. In our study, we utilized the Neukum–Ivanov (2001) system, which used the production function of Ivanov (2001) and the chronology function of Hartmann and Neukum (2001) for deriving the absolute model ages and epochs boundaries by Michael (2013). As we encountered less count in many areas, therefore we also used Poisson timing analysis (Michael et al., 2016) to estimate the ages more precisely and supporting the ages derived using the cumulative fit of Neukum–Ivanov (2001) system. We have taken care to not include highly clustered and ordered secondary craters in our counting area to minimize the error (Salese et al., 2016). For the chronological study, we demarcated the crater ejecta and counted the superposed craters (Figs. S2–S5). The dust cover over the study region, lead to difficulty in demarcating the ejecta boundary. For craters with no discernible ejecta, we counted the craters over their floor region. Using cumulative crater size-frequency distribution, we have obtained absolute ages for each of the forty-eight craters in Neukum–Ivanov (2001) system and details including their crater IDs from Robbins and Hynek (2012) are provided in Table 1 and Supplementary Table S1.

For the geometrical characterization of pits, we measured the semimajor and semiminor axis along with the vertical extent of the pit. The approximate length (along VM) and width (perpendicular to VM) of

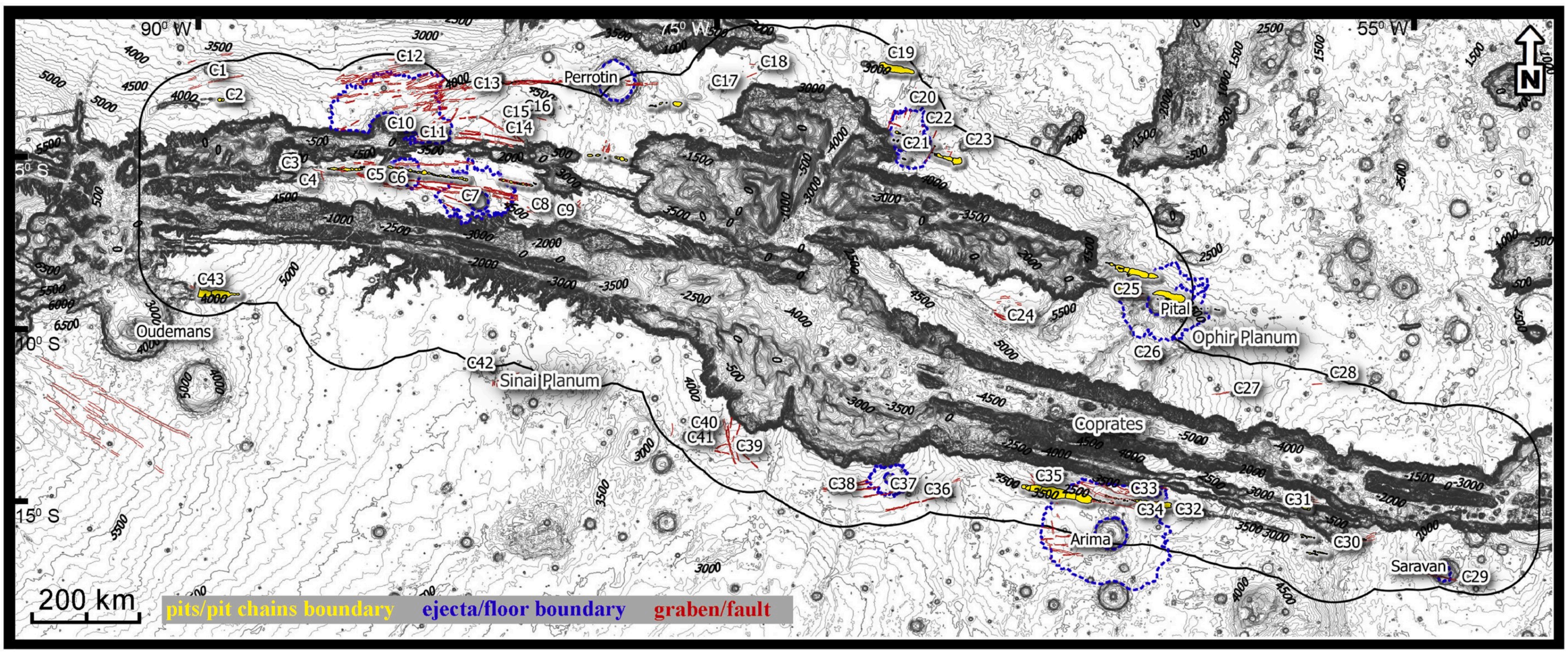

Fig. 3. MOLA DEM derived contour map of the VM region with a contour interval at of 100 m. The contour map also shows the distribution of graben/faults, pit/pit chains, and crater ejecta/floor boundary. The location of marked 48 craters represent the craters selected for this study.

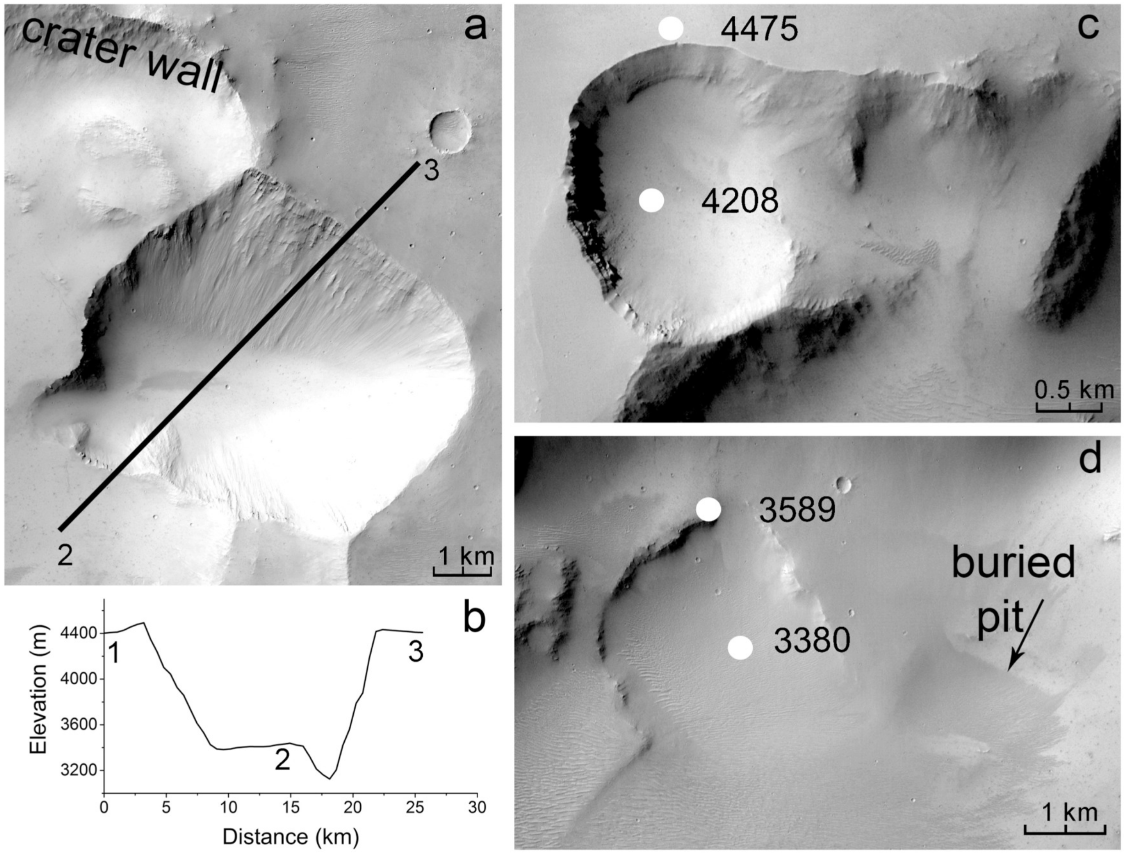

Fig. 4. Pits associated with crater C6 in Tithonium region, a) typical example of superposed pit over the crater eastern rim (CTX id: P18_007931_1737_XN_06S083W), b) elevation profile cross-section of pit, note that the pit depth is more in comparison to the crater floor depth (full profile is shown in Fig. 2b), c) pit formed over the western rim, which is smaller in size and depth when compared to pit on eastern side (4a) (CTX id: J10_048703_1754_XI_04S084W 2016-12-16), d) pit present over the crater floor mantled by dust cover, Adjacent to this pit, a buried pit is present (black arrow) (CTX id: P08_004160_1736_XN_06S084W 2007-6-16). (White dot: MOLA elevation values in meter; for location refer to Fig. 2b).

each pit are measured and given in Supplementary Table S2. The depth of the pits is measured using the MOLA PEDR point data and MOLA DEM. The maximum elevation of the pit is obtained by averaging the elevation points on the rim along its width, and the minimum elevation is taken from the deepest point of the floor. The difference obtained is taken as the pit depth. However, due to the inclined topography, it is difficult to measure the exact value, hence here we provided an approximate depth for the pits. Similarly, for *catena*, the elongated coalesced pit, the maximum elevation is obtained by averaging the elevation points on its rim along the line that passed through its deepest point (point of minimum elevation). The minimum elevation is obtained by generating contours of interval ranging between 10 and 50 m and the innermost contour was taken as the minimum elevation. The difference between the maximum and minimum elevation is assumed as the possible depth of catena.

4. Selection of craters, their associations, and distribution

We scouted craters located within ~100 km boundary of VM (Andrews-Hanna, 2012a) and found 1516 craters. Only those craters which exhibit a clear association with graben and pits (superimposing and/or crosscutting relationship) and have discernible ejecta or adequate floor for age estimation were selected for our study (Fig. 1). Craters with diameter <3 km do not have discernible ejecta, and the area of the ejecta/floor unit is not adequate for interpretation of the age (Warner et al., 2015). Therefore these craters were not selected for our study. Of the 1516 scouted craters, 1228 of them have a diameter <3 km. Out of the remaining 288 craters, 48 craters have a clear association with graben and/or pits.

Fig. 1 shows the distribution of craters around the VM region, and we have analyzed those 48 craters in detail. These include: (1) craters that exhibit an association with only graben and 2) craters that are associated with both graben and pits. Very few craters are associated with catenae/troughs, which have either crosscut the rim or have formed near to the crater rim. Fig. 2 shows examples of such crater types. Fig. 2a shows one of the selected craters with an association to graben and have distinguishable ejecta blanket. Among our selected craters, graben were generally observed in association with the crater ejecta, except for a few craters where they were observed on the crater floor (Fig. 1). In a few cases, graben are observed to pass very near to the rim of the crater (Fig. 2), while in other cases they passes near to the crater ejecta. In these cases, either ejecta emplacement has taken place over the graben or vice versa; we analyze these craters carefully to determine their superposition relationship. Fig. 2b shows another selected crater from our study, which has an association with both graben and pits. Fig. 2c shows the Pital crater, associated with pits chains and one big catena, which crosscuts the northeast rim.

Craters chosen for this study are analyzed based on their regional locations. The selected 48 craters are distributed primarily over the regions of Tithonium (22 craters), Ophir (11 craters), and Coprates (15 craters) Chasmata (Fig. 1). Among these craters, ~60% situated to the north of VM, whereas ~40% towards the south of VM. Fig. 3 shows the distribution of selected craters, their association with graben/pits, and variation in topography observed over the VM vicinity, especially over the three named regions. Many craters in the VM region are surrounded by parallel running graben and pit chains (Fig. 3). Pits/graben were not

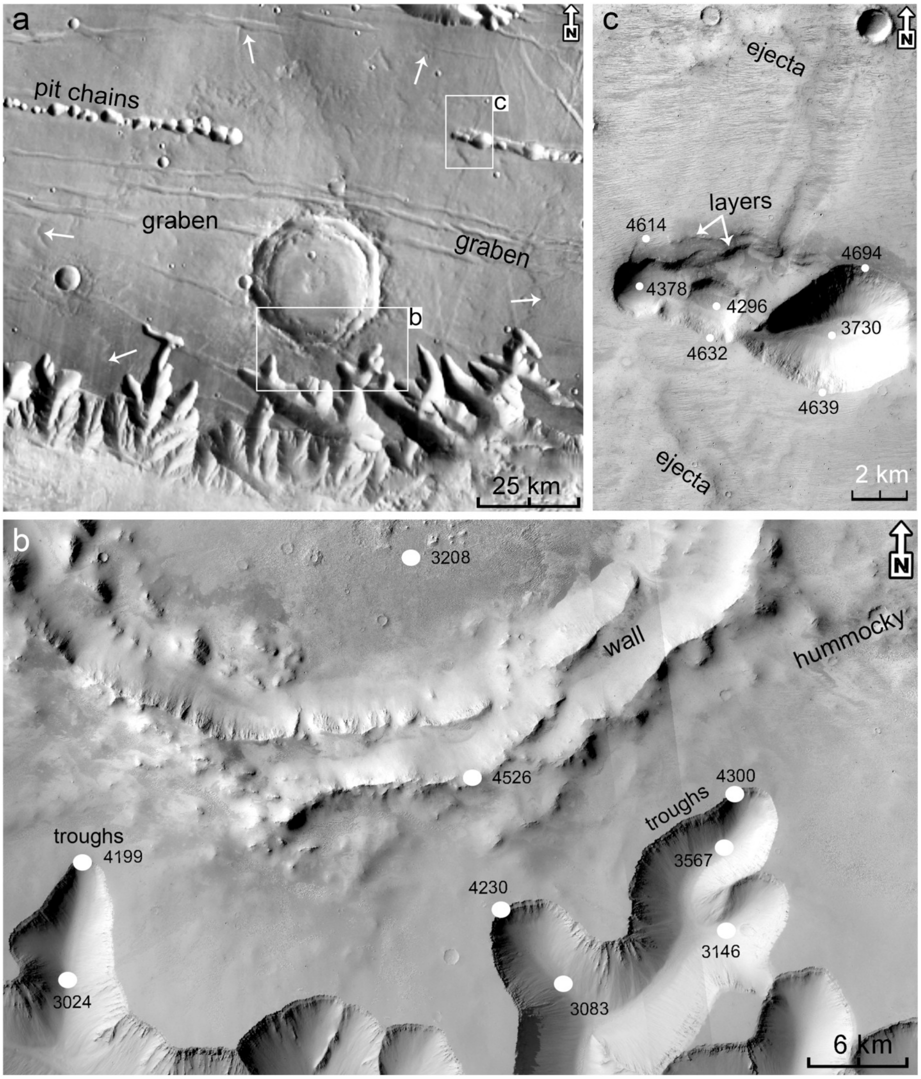

Fig. 5. a) THEMIS daytime infrared controlled mosaic image of the crater C7 with the distribution of graben, pits, pit chains (NW and NE) and troughs (South) in Tithonium region, b) The southern part of the crater dominated by troughs, whose width and depth are varying widely. The closest head trough from the southern wall is ~5 km. Outside the crater rim, hummocky and elevated terrain due to the impact is observed over the SE part, whereas such hummocky uplift is absent over the southern side where troughs are emplaced (CTX id: J03_045789_1724_XN_07S081W 2016-5-3, J05_046923_1731_XI_06S081W 2016-7-30), c) Pits in the NE side of crater ejecta, likely formed with underlying graben. These pits also exposes layers or multiple collapses (CTX id: P16_007364_1733_XN_06S081W 2008-2-21). (White dot: MOLA elevation values in meter; White arrow: C7 ejecta boundary).

mapped regionally and only those pits/graben that are associated with the selected craters are mapped in Fig. 3. In the Tithonium region (TR), crater C10 and surrounding craters formed at relatively low elevated terrain than the adjoining Perrotin crater which situated over relatively elevated terrain (Figs. 1, 3). In the Ophir region (OR) near to the Pital crater, the topography shows (Figs. 1, 3) gently sloping terrain from south to north and also towards the northeast. In the Coprates region (CR), craters near Arima crater have formed over a relatively elevated topography, while craters surrounding Saravan crater have formed over a relatively low relief topography (Figs. 1, 3). This is carried out to understand the topography effects, if any, on graben and pits activity as the associated craters and regions are located over different elevated terrain. This analysis suggests that the chosen craters formed spatially apart and over differently elevated terrains.

5. Observations

We present our observations with respect to the selected 48 craters and how they are associated (superposed/crosscut) with the graben, pits, and troughs. In this study, the superposition relationship interpreted based on: 1) graben/pits superpose/crosscuts the crater rim, 2) graben/pits dissects or superposed the crater ejecta, 3) graben/pits forming within the crater, and 4) craters and/or their ejecta superposing the graben/pits.

5.1. *Craters in Tithonium region*

In the TR, four craters (C6, C7, C10, and Perrotin) have relationship with graben, pits, coalesced pits, and troughs. The first crater in this region is C6 (Fig. 3), which is ~17 km in diameter centered at −5.41°, −83.99°, with a depth of ~1 km. The crater ejecta spread over more than two crater radii from the rim. Within crater C6 we have observed pits that are emplaced over the crater at three locations (Fig. 2b). The easternmost pit has carved into a section of the crater rim (Fig. 4a), with an extent of ~6.8 km and depth of ~1.17 km. It is observed that this pit depth is relatively more than the crater depth (Fig. 4b). The other superposed pit is observed over the western part of the rim (Fig. 4c), whose depth is >200 m. These two pits jointly occupy ~10% area of the crater rim. The third superposed pit is observed over the crater floor (Fig. 4d); its size is almost half of the easternmost pit which carved into the crater rim. From Fig. 4d, the floor appears to be dust-covered and the floor pit is likely aligned along the line of wall origin pits. Also, there appears to be a buried pit over the floor currently mantled by the dust (Fig. 4d). These are clear evidence for the superposed emplacement of pits over crater C6. We have observed that pits of different lengths and depth have formed (Table S2) within the crater. Outside the crater, pits were observed in chains oriented in W-E side (Fig. 2b). Towards the east of the crater, we observed coalesced pits within the plausible graben (Fig. 2b). The maximum length and depth of pits are ~7 km and ~1.2 km respectively located within the ejecta boundary. In Fig. 2b, the

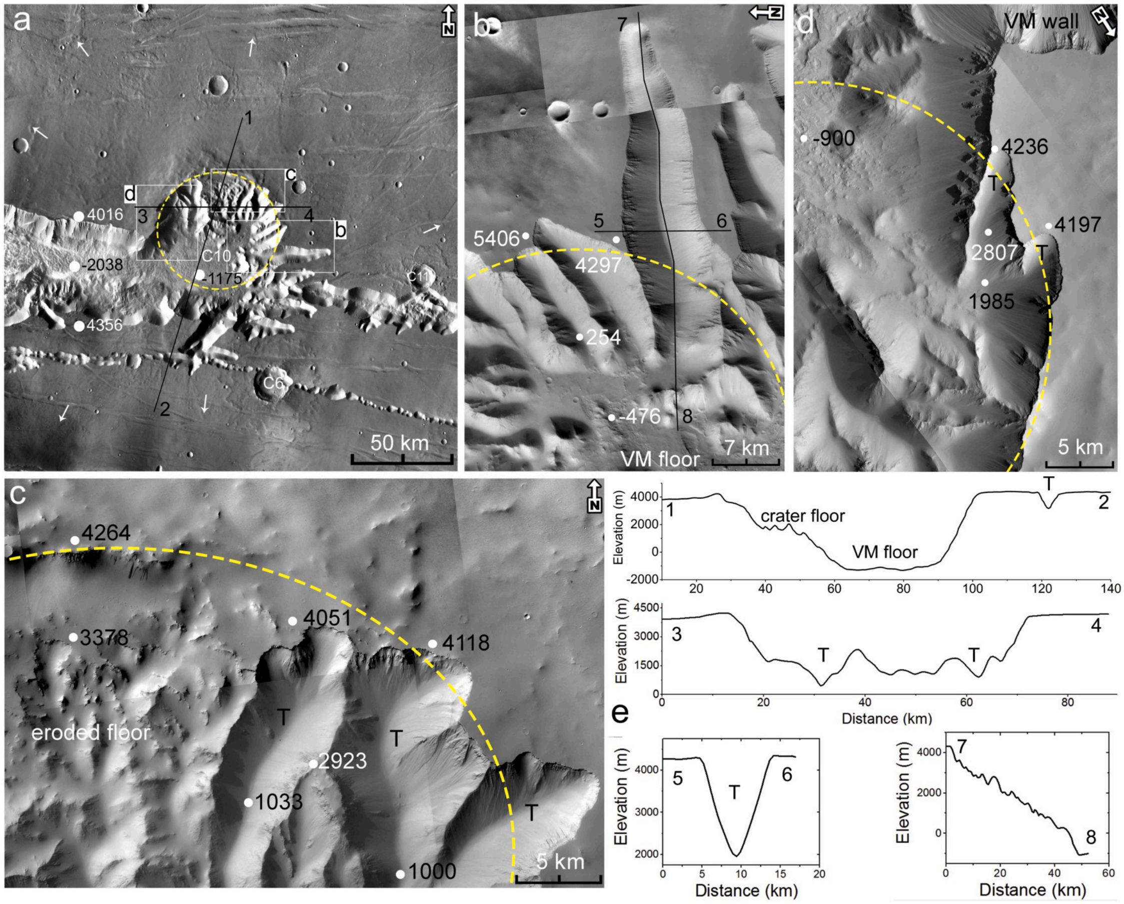

Fig. 6. a) THEMIS daytime infrared image of degraded crater C10 with presence of graben (to its north), pits, pit chains (to its south) and troughs (over east, west and south side), b) troughs dissected the eastern rim of crater, whose spatial extent and depth are varying diversely (CTX id: P08_004160_1736_XN_06S084W, P18_007931_1737_XN_06S083W, P07_003949_1738_XN_06S083W, G06_020695_1777_XN_02S084W), c) preserved crater rim and terraced wall over the northern side, however, towards the floor side, the surface is eroded and hummocky. The NE side is dissected by a trough, which extends towards the floor (CTX id: F03_036835_1757_XN_04S084W, F19_043178_1748_XI_05S083W), d) troughs dissected the crater rim and the orientation is different from other troughs present within the crater. Over the western side a part of the crater wall shares the boundary with the Valles Marineris wall region (CTX id: F18_042888_1751_XI_04S084W), e) elevation profiles taken along the N-S direction where the crater floor and VM floor show ~3 km elevation difference. The elevation profile along the W-E direction shows a hummocky crater floor with multiple troughs. Elevation cross profile along a trough on the eastern side (profile location in Fig. 6b) shows trough depth is ~2 km, whereas the elevation along the trough varies up to ~4 km representing slope variation. (White dot- MOLA elevation values in meter; White arrow- C10 ejecta boundary; dashed yellow line- the tentative boundary of crater C10; T- trough). (For interpretation of the references to color in this figure legend, the reader is referred to the web version of this article.)

northwest side hosts an elongated depression marked as trough. It is observed within the crater ejecta blanket, and it is situated parallel to the western pit chain. Both the trough and pit chains are observed to align along the graben (Fig. 2b). Due to the dust cover, there is no clear evidence of whether trough superposes the crater ejecta or vice versa (Fig. 2b). On observing the graben present over this crater region, we found emplacement of ejecta over the graben and inferred that they are likely superposed by the crater ejecta (Figs. 2b, S6). The features associated with this crater, like pits, pit chains, troughs and graben, are found to vary in their spatial extent and pits provide clear evidence for their superposed presence.

The next crater in the TR is C7 centered at −6.27°, −81.89° (Fig. 3), whose diameter and depth are ~32 km and ~1.2 km, respectively. The ejecta spreads radially outward up to ~60 km, except in the south, where the troughs are present (Fig. 5a). Crater C7 has an association with parallel and sub-parallel graben trending W-E and NW-SE direction (Fig. 5a). From Fig. 5a, notable evidence are observed for the emplacement of the crater over the parallel graben based on their discontinuity. This suggests that the graben were superposed by the crater. Another associated feature with this crater is the elongated troughs which are present on the southern part (Fig. 5b). It is observed that the head part of the troughs is ~5 km away from the southern rim of crater C7 and the tail part of the troughs is associated with the walls of VM (Fig. 5a). The troughs observed have multiple branches with varying extent and depth (Fig. 5b). The trough heads close to the rim are rounded and visually appear smooth. We observed only three troughs whose heads are close to the southern crater wall within ~10 km (Fig. 5b). However, as no distinguishable ejecta was observed within the trough heads, it is difficult to determine their superposition relationship with the crater based on the ejecta emplacement. As an alternative method to decipher their relationship, we observed that around the crater rim there are raised hummocky surface due to rim formation (Fig. 5b) within ~0.5 crater radii in all directions except towards the southern side. The closest trough head is ~5 km from the crater rim (Fig. 5b). In addition, though these troughs are very close (~5 km) to the crater rim, they are still intact and not affected by the crater formation. If the troughs were pre-existing before C7 crater formation, then they should be affected due to the formation of a ~32 km diameter crater C7. These observations may hint that troughs could likely be superposed over the ejecta of crater C7. Within the very close vicinity of the crater C7 rim, the size of the trough varies from a few kilometers to tens of kilometers (2 to ~11 km) and depth varies up to ~1 km. We have found

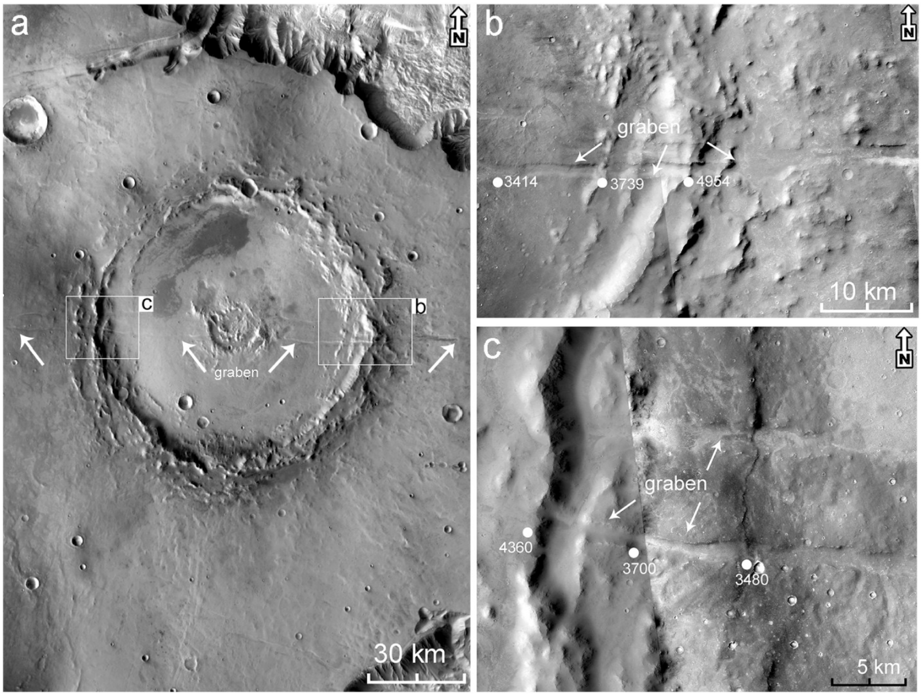

Fig. 7. a) THEMIS daytime infrared image of Perrotin crater in the Tithonium region. The presence of graben over its floor and rim is indicated by white arrows, b) graben crosscutting the eastern rim part and extended over the crater floor (CTX id: D22_035793_1751_XN_04S076W, P15_007087_1779_XN_02S077W), c) graben crosscutting the western rim at two places and extended over the crater floor (CTX id: B03_010726_1785_XI_01S078W, G05_020141_1769_XN_03S078W). (White dot-MOLA elevation values in meter).

that the depth of troughs increases away from their heads and it is relatively deeper than the depth of crater C7 (Fig. 5b). It is also observed in Fig. 5a that most of the troughs aligned and formed along the graben. On observing the pits, the NW side of the crater ejecta holds pit chains that are possibly aligned to the pit chain associated to the crater C6 (Fig. 3). Nearly a 30 km long pit chain located within the ejecta blanket of C7 (Fig. 5a). The other chain is observed on the NE side of crater C7 with a spatial extent of ~60 km, but only ~35% observed within the ejecta. This pit chain is emplaced within the graben and they are surrounded by other cross-cutting graben (Figs. 3, 5a). Parallel to this pit chain, we have observed scarps and layers within the troughs (Fig. 5c). Hauber et al. (2009) also observed scarps parallel to a long, linear vent (fissure) and interpreted that such scarps indicate a multi-stage collapse. On deciphering the superposition relationship of pits with the crater C7, only two possibilities exist: 1) the ejecta might have been deposited and covered underlying structures over course of time or 2) pits were emplaced over the ejecta. However, the dust cover hinders the stratigraphic evaluation of the pits to the north of crater C7, but the troughs around the southern side provide evidence for their post crater formation.

The next crater analyzed from the TR is C10 (Fig. 3), which is ~40 km diameter centered at −4.19°, −84.54°, whose southern part is completely obliterated as shown in Fig. 6a. We interpret this feature as an impact crater based on 1) the distinguishable and radially spread ejecta on the northern part, 2) elevated and raised rim in the northern side and 3) based on the geologic map of Mars by Tanaka et al. (2014). This crater and its surrounding region are occupied by graben, pits and troughs (Fig. 6a). Troughs were observed to cut through the entire eastern crater wall (Fig. 6b,c), which completely obliterated it. These troughs have variable size and depth. The longest one is ~35 km in length, with a maximum width of ~5 km and has an average depth of ~3 km (Fig. 6b). Fig. 6b also shows elevation point over the trough floor and adjacent VM floor, which has a difference of ~700 m. Troughs have also dissected the western part of the crater rim (Fig. 6d) but the extent is relative less when compared to the eastern rim. Though most of the troughs have been observed to be oriented towards the east, still a few were observed to be oriented towards the southwest (Fig. 6b,d). Over the northern side, there are few troughs observed within the crater wall and floor (Fig. 6c). These troughs were observed to degrade the rim of the crater partially and suggest their post emplacement after the formation of C10 crater. On observing the graben around this C10 crater, we found that the northern side hosts several of them (Fig. 6a). It is observed from Fig. 6a that the crater ejecta has been emplaced over it. The graben over this region has been mapped by earlier works (Anderson et al., 2001; Kumar et al., 2018) which indicates discontinuous graben over this region due to crater formation.

Topographic profiles extracted through the crater and the VM wall (N-S profile) (Fig. 6e) suggest that the hummocky crater floor and the adjoining VM floor have a ~3 km elevation difference. Fig. 6e shows another elevation profile taken along the W-E direction where the floor of the crater and troughs display a significant elevation difference between them. The crater depth measured from the MOLA DEM is varied within ~2 to 3 km due to the hummocky floor. Whereas the empirically derived depth for a similar diameter crater is ~2.4 km (Robbins and Hynek, 2012). To decipher the terrain over which this C10 crater formed, we determined the depth to the immediate west of the crater within the Tithonium chasma (Fig. 6a), which is ~6 km and almost equal to the depth of chasma in the southern side of the crater C10 (Fig. 6e). The significant correlation between the chasma situated in the southern side of the C10 crater and the adjoining chasma in the west suggests that it could be a continuous feature. This infers that the chasma likely existed before the formation of crater C10. Topographic profiles were also extracted along and across a trough (Fig. 6b,e), which suggest that the trough is >2 km deep and the depth is increasing away from the head of the trough.

From crater C10, it is inferred that the entire eastern part of the rim is dissected by the trough, which is one of the strong evidence for their cross-cut superposed activity. Some of the graben that observed north of C10 crater (Fig. 3) have shown extension towards the western side of Perrotin crater. Perrotin is ~80 km in diameter with a depth of ~1 km and has a central pit over its floor (centered at −2.81°, −77.95°). The adjoining C10 crater and Perrotin crater have an elevation difference of ~600 m. Perrotin crater is mainly surrounded by graben, some of the graben are observed over the floor and the rest are observed outside the

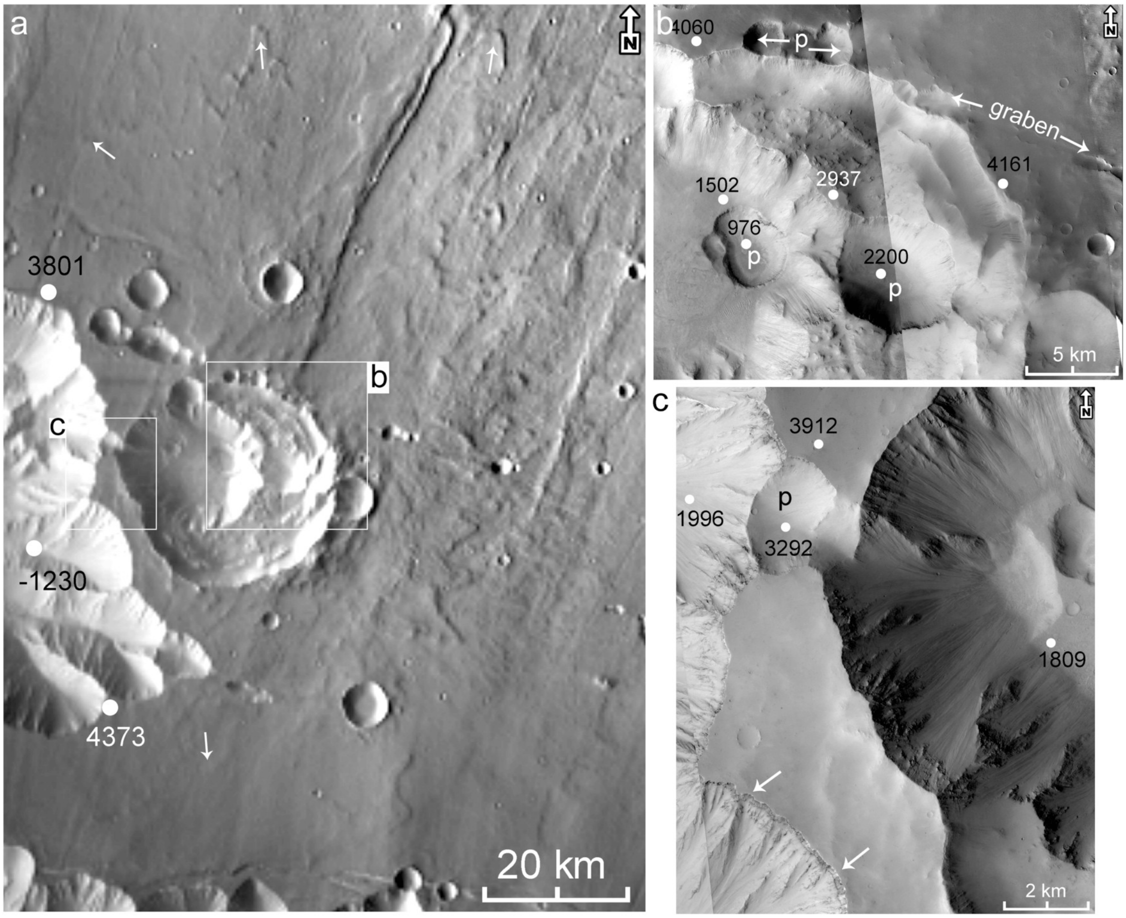

Fig. 8. Crater C21 in the Ophir region a) THEMIS day time infrared image of pits and graben, which formed adjacent to VM wall, b) northern part of crater superposed by multiple pits, formed at a different elevations and with different depth and size. Over the northern rim, few pits emplaced over the region. This is evidence for their superposed presence after C21 formation (CTX id: P09_004410_1733_XI_06S069W), c) Pit likely formed in between the VM wall and crater wall. The C21 crater rim uplifted hummocky surface adjacent over the SW side is likely obliterated by the VM wall (CTX id: F10_039736_1740_XI_06S069W). (White dot- MOLA elevation values in meter; White arrow- C21 ejecta boundary; black arrow- graben/pit or VM wall).

crater towards the western and eastern sides (Fig. 7a). These graben have dissected the crater floor, the eastern and western rim (Fig. 7b,c), which is a direct evidence for their superposed emplacement. However, it is difficult to interpret whether the full length of the graben formed over the same time or if they are all interlinked to each other. We limit our observation within the crater floor and wall, which is superposed by graben (Fig. 7b, c). Graben within the floor is ~82 km long (partially covered the entire crater along W-E), ~1 to 2.5 km wide and ~50 m deep. In the east, graben formation spanned over 1.5 km of elevation (Fig. 7b), whereas in the west, the elevation difference tends to be ~1 km (Fig. 7c). Perrotin crater ejecta is indistinguishable and the dust cover is significant over this part. Thus, the superposed graben over the crater floor and wall are used in our analysis (Fig. 7b,c). As parallel and sub-parallel graben extends for several hundreds of km in the TR (Anderson et al., 2001), therefore, those observed around the Perrotin crater are significantly useful in deciphering a graben emplacement scenario.

5.2. Craters in Ophir region

The Ophir region of VM is known for its interior layered deposits, landslides, and faults (Lucchitta et al., 1994; Chojnacki et al., 2006; Fueten et al., 2010). Over this region, two craters (C21 and Pital) were analyzed in detail. Crater C21 (centered at −4.60°, −69.68°) (Fig. 3), is ~27 km in diameter and a depth of ~1.5 km. The ejecta blanket extends ~40 km outward radially from the crater rim, except in the western part (Fig. 8a). The crater is associated with graben, pits and pit chains (Fig. 8a). Pits are present within and outside the crater (Fig. 8b). Over the C21 western wall and floor, a circular depression with a diameter of ~15 km is observed (Fig. 8a) having a raised rim, which is inferred as a superposed crater. The other depressions within the crater floor and over the eastern rim are observed to be pits (Fig. 8b) due to lack of a raised rim. The pits are observed at different floor elevations ~1 km and ~2.2 km respectively (Fig. 8b). Along with that, pits are observed to crosscut the rim over the northern and western part (Fig. 8b,c). We have observed that pits over the floor have covered more than ~15% of the floor area and the pits on the rim carved into ~10% of the crater rim (Fig. 8a). Few discontinuous pits were also observed in the north, north-west and north-east side of the rim (Fig. 8a). In addition to this, we observed that the southwest crater wall is located just within ~3 km from the steep VM wall (Fig. 8c). This observation raises the question of whether any extension of VM wall occurred towards the crater. To decipher this observation, the pits over the western wall which is located intermediate to the crater wall and the VM wall, are used (Fig. 8c). The presence of these pits provides consolidated evidence for their superposition over the crater rim and their association with VM and indicates that this area has undergone modification after C21 formed. This crater exhibits an east-west trending set of pits that are superposed on the floor and rim, forming a nearly mature pit chain. On observing the pits outside the crater rim, they are most likely associated with the graben (Fig. 8b), whereas the pits within the crater floor are observed without any graben association. To the southern side of crater C21, we observed elongated

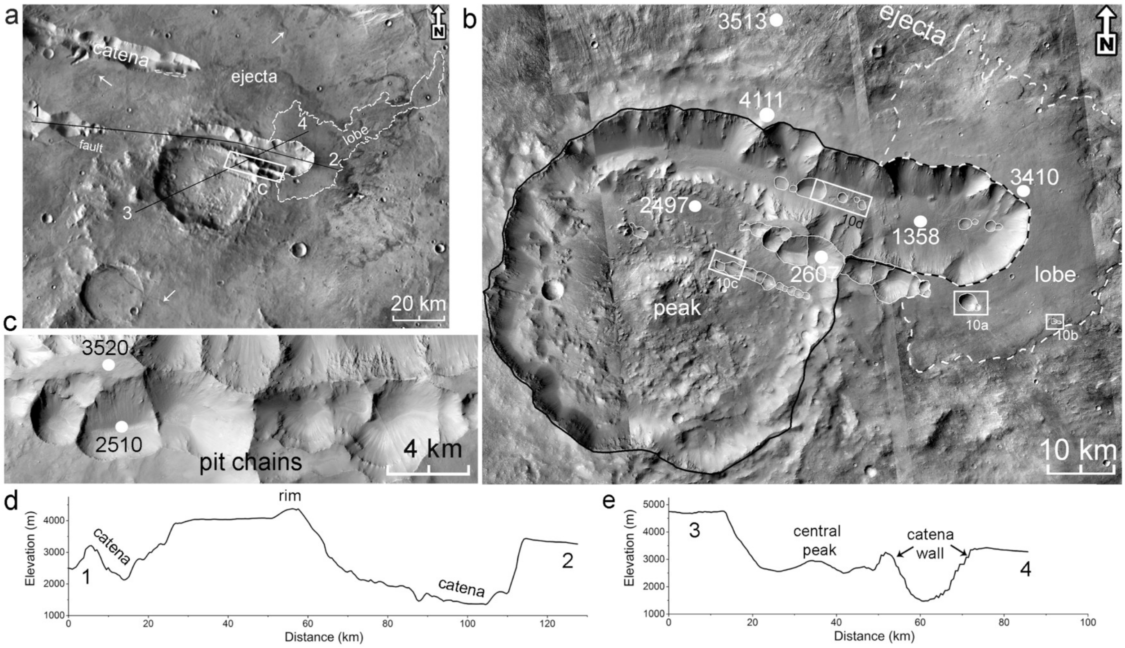

Fig. 9. Pital crater in the Ophir region, a) THEMIS day time infrared image of Pital crater with presence of pits, catena, lobe deposits on NE side and graben. b) CTX mosaic of Pital crater, with distinguishable lobe deposits associated with the catena, which dissected the NE crater rim. The catena to its eastern side is broadened and deeper when compared to the western side. Multiple pits were observed within the catena. The lobe associated to the catena is only present towards the NE side where the topography is also inclined in this direction (Fig. 3) (CTX id: J18_051867_1724_XI_07S062W, J04_046408_1711_XN_08S062W, J18_051946_1715_XN_08S061W, B19_016923_1696_XN_10S061W, G02_018980_1713_XN_08S061W), c) A portion pit chain interpreted to superpose over the floor and rim of the crater (CTX id: F22_044298_1719_XN_08S062W). The size and depth of the pit chains varies throughout its length, d) elevation profile along the W-E direction, note that the catena on western sided is relatively less deep than the catena crosscut the Pital NE rim, e) elevation profile along the rim-central peak and catena suggest that the catena is relatively deeper than the Pital crater.

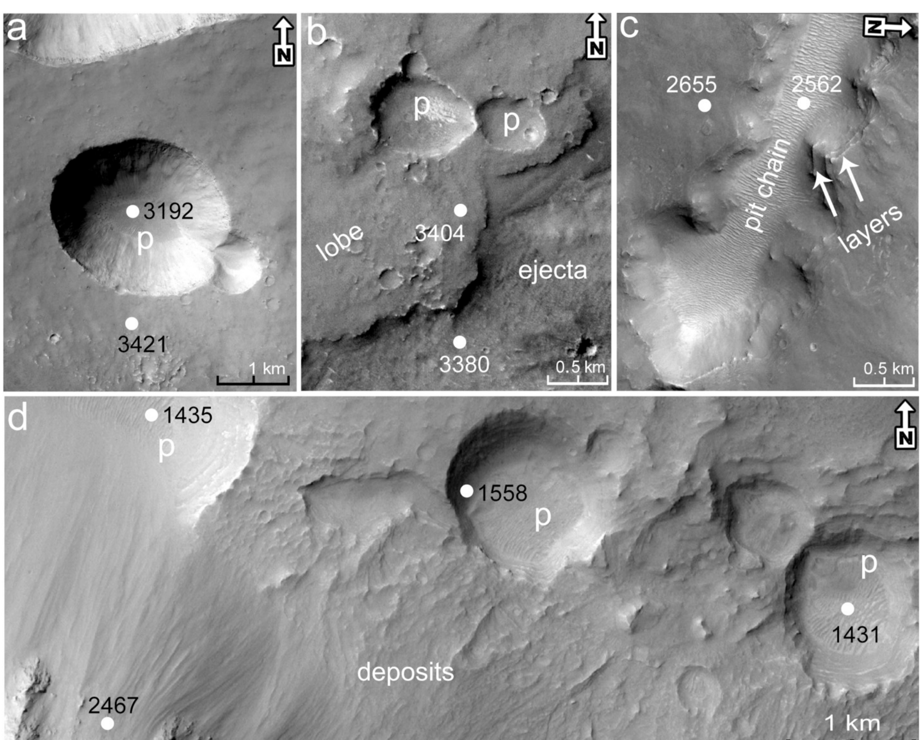

Fig. 10. Pits associated with Pital crater, a) A ~2 km wide pit emplaced over the lobe deposits associated with the catena. This pit and lobe are emplaced above the Pital crater ejecta. This suggests that stratigraphically the pit is the youngest feature in this region (CTX id: J18_051946_1715_XN_08S061W), b) continuous pit observed at the termini of the lobe deposit, note that the Pital ejecta is underlying below the pit (CTX id: B19_016923_1696_XN_10S061W), c) pit chains with collapsed nature formed within the crater floor and with possible exposure of layers over their walls. This pit chain emplaced over the wall continued till the flank of the crater rim (Fig. 9b) is evidence for their superposed activity after crater formation (CTX id: J07_047542_1708_XN_09S062W), d) pits formed within the catena and they are further mantled by wall origin deposits. The pits within catena are found to be of different depth and size. These pits have formed ~2 km below than those formed over the lobe/ejecta deposits (10a). The fan-shaped deposits from the southern wall of catena likely have an abrupt end at the pit. Note the visible distinguishable layers within the pit over this region (CTX id: J18_051946_1715_XN_08S061W).

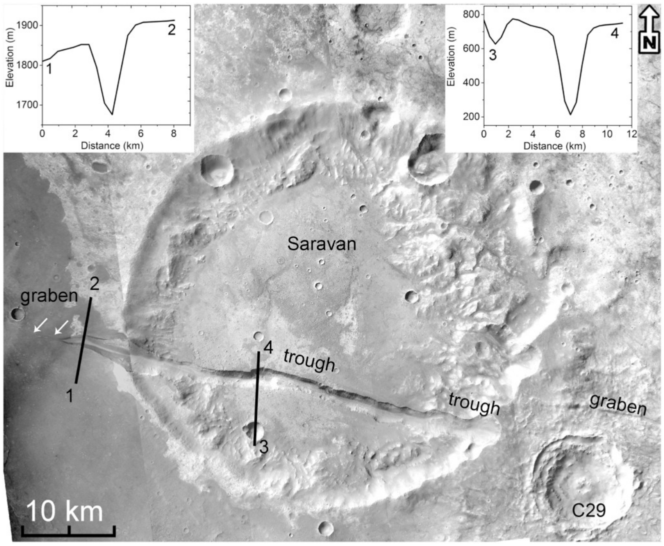

Fig. 11. CTX mosaic of Saravan crater located in the Coprates region with a graben associated trough in the floor. The crater floor hosts a long trough, which dissects the rim and suggests superposed activity after crater formation. Inset images show the elevation profiles across the trough and indicates their variation in width and depth. The trough is relatively deeper than a small crater located on the southern side of Saravan crater. (CTX id: D04_028751_1641_XN_15S054W, P11_005438_1649_XN_15S053W, B16_016026_1643_XN_15S054W, B19_016870_1633_XN_16S054W).

catena in discontinuity with the Ophir Chasma (Fig. 8a). However, correlating their relationship with the crater is hindered due to dust cover. Apart from pits, we observed long, narrow and shallow graben directed parallel and perpendicular to the VM (Fig. 3). Overall, it is observed that both pits and graben are superposed over the crater C21 at multiple places (Fig. 8).

The other crater over the OR region is Pital crater (Figs. 2c, 3), whose diameter is ~39 km and has a depth of ~1.8 km centered at −9.22°, −62.30°. The ejecta of this crater spreads up to more than one crater radii (Fig. 9a). We observed pit chains, catenae, a lobe-shaped deposit (Marra et al., 2015), and graben within the crater and ejecta blanket (Figs. 9a–c, 10a–d). The striking observation of this crater is the presence of W-E oriented elongated coalesced pit or catena like depression (Marra et al., 2015) formed cutting through the NE rim (Fig. 9b). This coalesced pit-like structure observed to be narrower and shallower over the western floor side but has a broad and deep opening towards the east side (Fig. 9b). This broad opening is referred to as *catena* (Marra et al., 2015), which clearly substantiates its superposed nature over the crater. The catena is observed to be ~50 km long (W-E side), and ~14 km wide (N-S side) and ~2 km deep (Fig. 9b). This catena is much deeper than the probable catena in the west of the Pital crater (Fig. 9d) and also to the depth of the Pital crater (Fig. 9e). When compared with the regional topography, the catena is declining towards the eastern side (Fig. 1). We observed that the catena is in alignment with the adjacent Candor Chasma (Marra et al., 2015).

Apart from this catena, several pits and pit chains of variable sizes are observed within the Pital crater (Table S2). To the immediate southern wall of catena, pit chains are observed, which shows extension within and outside the crater rim (Fig. 9c). The pits over this part (Fig. 9c) are continuous, and their maximum extent and depth are ~5 km and ~500 m respectively. This continuous pit shares the wall with the W-E aligned catena. To further south of this pit chain, one more pits chain is observed within the floor and over the wall flank region (Fig. 10c), but relatively smaller in size and width (Table S2) with an overall extent of ~15 km (Fig. 9b). Spatially these two pit chains are ~2 km apart but both host pits of different sizes and depth. This suggests that within such close vicinity, the pit formation varied (Figs. 9c, 10c).

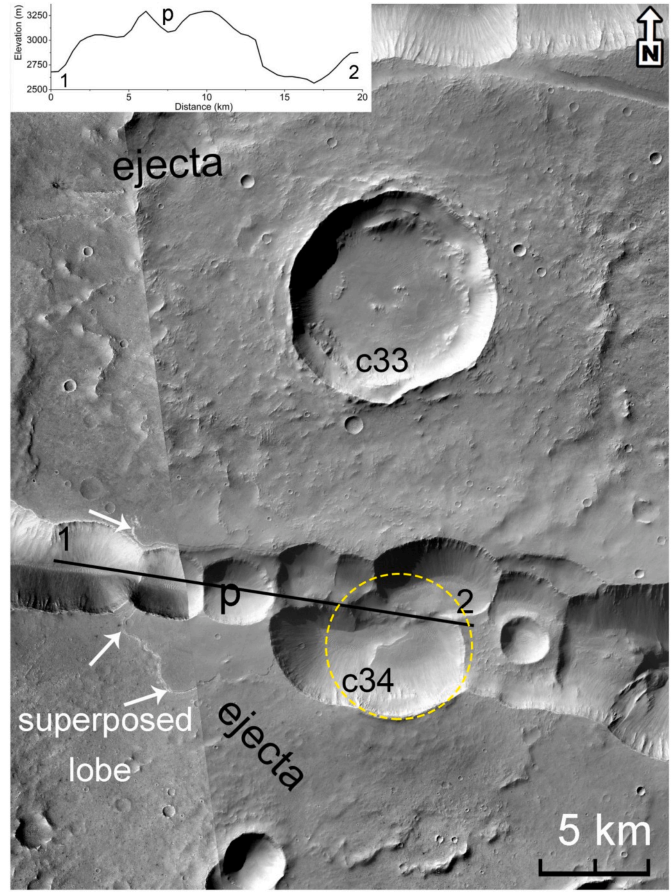

Fig. 12. CTX mosaic of two craters over the Coprates region, in which one of the craters is degraded (C34). The pit chains over this region are having a wide variation in depth and width, as inferred from the elevation profile along the pit chain. The yellow dashed line indicates the possible crater C34 rim. Towards the western side of C34, the lobe-like deposit emplaced over its ejecta and has closely associated with one of the pits. The lobe deposits superposed the C34 ejecta blanket and suggests their post activity. However, note that this lobe-shaped deposit is only observed adjacent to only one pit. (P-pits; White arrow- superposed location of lobe deposits over the ejecta; CTX id: B20_017556_1659_XN_14S062W, J05_046619_1666_XN_13S062W). (For interpretation of the references to color in this figure legend, the reader is referred to the web version of this article.)

Fig. 10d shows the several pits, however, these are formed within the floor of catena. These pits formed ~2 km below the adjoining surface (Figs. 9b, 10d). The catena and the pits present over the crater floor and rim are aligned in the same direction as VM, which is tending towards the W-E side.

In close association and to NE of this catena, we have observed a probable lobe-shaped deposit (Fig. 9a), which is emplaced over the Pital crater ejecta and mantled >10% of the crater ejecta (Marra et al., 2015). This lobe-shaped deposit extended up to ~70 km from the catena NE boundary, and the average thickness estimated to be ~50 m (Marra et al., 2015). Marra et al. (2015) suggested that this lobe must have formed either during the formation of catena or before the formation of the catena. In another study, pits likely interpreted to associate with the lava flows on the volcanic plains of the Tharsis region (Hauber et al., 2009). Cushing et al. (2015) mentioned that if the radial pattern of lava flows is present in association to a pit then that could indicate effusive volcanic conduits. This lobe is in agreement with the regional topography, which is tending towards SW-NE (Figs. 1, 3). In this study, we utilized this lobe deposit to interpret the pit activity. Remarkably, we observed few pits visible over this lobe deposit (Figs. 9b, 10a,b) which is overlying the ejecta blanket. This stratigraphic emplacement is used to

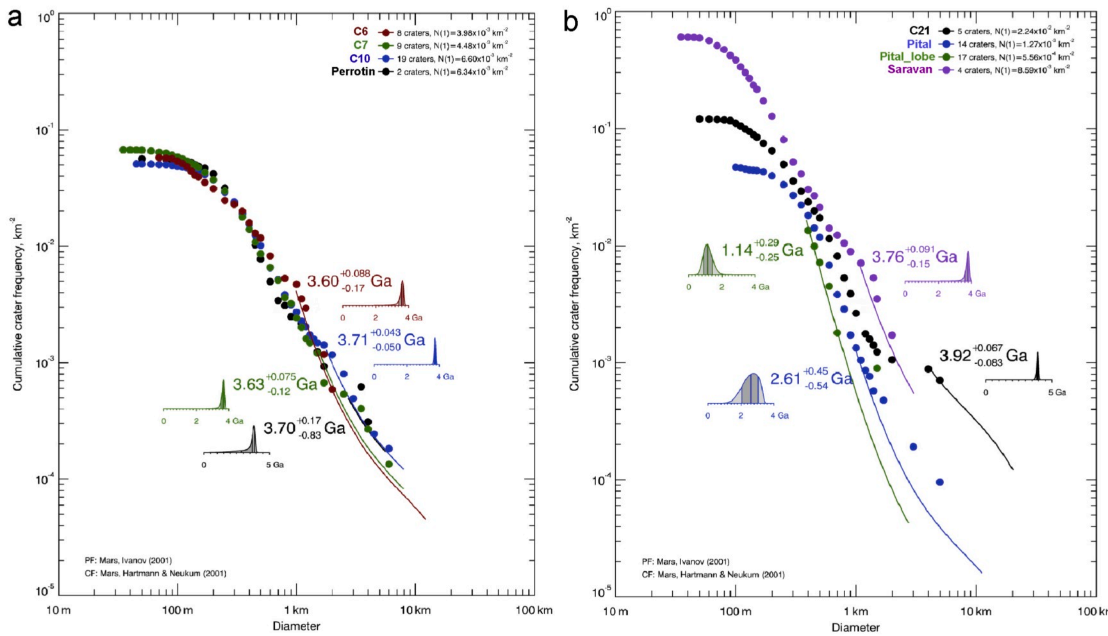

Fig. 13. Crater size-frequency distribution for craters superposed by pits, graben, catena. The model ages obtained for seven craters and one lobe deposits are given for craters from a) Tithonium region and b) Ophir and Coprates region.

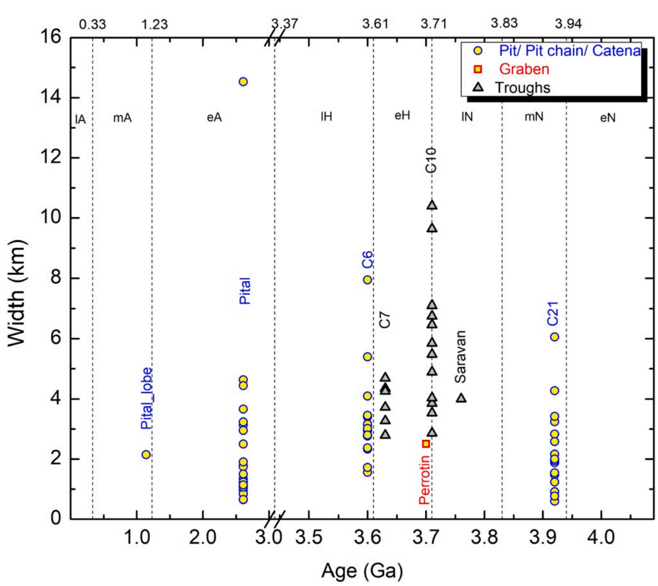

Fig. 14. Model absolute ages for seven craters and Pital lobe versus the pits, graben, trough, and catena width. Perrotin crater provides an evidence for graben formation on or post late Noachian epoch. Pit formation over the VM widely varied spatially and chronologically, with the pit formed over crater C21 on or post to middle Noachian, whereas the youngest pit is ~2 km in size and formed during middle Amazonian. Pital crater catena possibly formed during the early Amazonian and is nearly one-tenth of Candor Chasma width. Troughs are observed within the Saravan crater and close to craters C10 and C7, which widely observed on or post to the late Noachian epoch.

decipher the series of events occurred over this region. Fig. 10a shows a pit over the lobe which is ~3 km long, ~2 km wide and ~200 m deep, suggesting its youngest formation when compared to Pital ejecta and *catena* associated lobe deposits. We observed two smaller continuous pits over this lobe (Fig. 10b), where the stratigraphy of the Pital ejecta, lobe and pits is evident. Thus, the evidence provided is a clear indicator of the superposition of pits over the lobe deposits.

Towards the west and NW side of the Pital crater, two broad elongated pits or catenae exist (Marra et al., 2015), whereas they are partially bound within the Pital ejecta (Fig. 9a). The upper elongated catena on the NW side shows small lobe-like deposits emplaced over the Pital ejecta (Marra et al., 2015) suggesting their plausible superposed emplacement over the ejecta. The lower elongated catena on the western side have pits of various size (Table S2) and emplaced within a graben or fault (Fig. 9a). Overall, it is observed that the Pital crater and its ejecta host superposed features like catenae and pits and altered predominantly over the eastern part.

5.3. *Craters in Coprates region*

The craters chosen in the CR are located towards the southern side of the VM region (Fig. 1). In this region, we discuss two craters, which are associated with pits, troughs, and graben. Saravan crater (−16.93°, −54.01°) is ~46 km in diameter, ~2 km deep and exhibits no distinguishable ejecta blanket (Figs. 3, 11). We observed an elongated trough ~50 km in length over the southern floor which dissected the crater from the western rim to the eastern rim (Fig. 11). The trough has formed over the crater floor and carved its rim (Fig. 11). The maximum width and depth of the trough are ~2.4 km and ~0.5 km respectively. We have observed that the trough near to the eastern rim is more circular and deep, whereas to its west it is more linear and shallow (Fig. 11). The trough over the eastern side of the Saravan crater was mantled by C29 ejecta (Fig. 11). The superposed trough within Saravan crater indicate evidence for trough activity on the southern side of VM.

The next crater in this CR region is crater C34, which is ~6 km in diameter and has a depth of ~1.3 km centered at −14.99°, −62.32° (Figs. 3, 12). While the northern part of the crater is completely degraded, we base our interpretation of this feature as an impact crater on the observations of ejecta over the south side and the raised southern rim, which we interpret as the original rim of the impact crater (Fig. 12). However, it is not clear that the crater formed over the pit or vice-versa. To infer the possible emplacement scenario, we observed a pit with lobe-shaped deposits present on the western side of the C34 crater, which spread up to ~4.5 km from the pit rim (Fig. 12). The lobe is further examined for its association with the crater C34; it appears that the lobe was possibly emplaced over some portion of C34 ejecta (Fig. 11). Marra et al. (2015) reported similar deposits adjoining catenae in the Ophir region, which were emplaced over Pital crater ejecta (Fig. 9a). Therefore, if the lobe is associated with the pits, then these pits likely represent a superposition relationship with the crater. Topographic profile extracted along the pit chain in W-E direction shows variation in pits depth (Fig. 12). Overall, the superposed pits/graben over the chosen craters are used to decipher their chronological variations over the VM region.

6. Spatial and chronological modification in the vicinity of VM

We interpreted the chronological relationship for only those craters that formed before graben, pits/pit chains, catena, and trough with considerable count area to get an absolute model crater age. Based on this, the estimated ages for seven craters are shown in Fig. 13. The TR and its surrounding plateaus have been mapped as early Hesperian highland units by Tanaka et al. (2014). In this region, although pits superposed the crater (evident over crater C6) (Fig. 4) and troughs cut through the rim of the crater (evident over crater C10) (Fig. 6), the period of activity in TR is not well constrained by stratigraphy alone. We obtained the absolute model ages for four example craters, which are superposed and cross-cut by graben, pits, and troughs. The estimated ages (Fig. 13a, Table 1) for the C6 (Fig. 4), C7 (Fig. 5), C10 (Fig. 6), and Perrotin crater (Fig. 7) likely represents an upper age limit for the formation of features associated to it (Fig. 14). For crater C6, where pit chains superposed over the crater rim (Fig. 4), we obtained the absolute model age as ~3.6 Ga or Early Hesperian epoch (Fig. 13a, Table 1). This model age suggests that the pit chains have developed after crater C6 formation post to Early Hesperian epoch (Fig. 14). For crater C10, where several parts of the rim crosscut by the troughs (Fig. 6b), we obtained an age of ~3.71 Ga (Fig. 13), which indicates that the troughs are preferably formed after the Early Hesperian epoch (Fig. 14, Table 1). The other crater in the TR is Perrotin, whose ejecta is indistinguishable from CTX or THEMIS datasets (Fig. 7), which led to an estimation of the absolute model age from the crater floor. This crater is known for its graben superimposing the wall and floor region (Fig. 7b,c), which stratigraphically indicates their post activity. Thus, the estimated model age for the Perrotin floor is ~3.70 Ga (Early Hesperian) (Fig. 13a). In addition to this, we followed the buffered crater counting method of Fassett and Head (2008) and counted craters superposed within one crater diameter from the Perrotin rim. Buffered crater counting technique was used to validate craters age where the ejecta is not visible. In this study, we used this technique to validate the ages of two craters only (out of 48 craters). The ages were determined by considering one diameter circle form the rim of the crater and counting all craters within the circle and these estimated ages were validated with the ages determined using superposed craters on the floor of the crater. The estimated model of Perrotin crater age is almost equal to the floor age, which is tending to the Early Hesperian epoch. The notable point from the Perrotin and crater C10 is that they are likely associated with the same graben. In a combined analysis of C10 and Perrotin crater, we inferred that the C10 crater ejecta emplaced over the graben located to its north side (Fig. 6a) and suggests that graben are older than ~3.71 Ga. These graben extend up to Perrotin crater with a discontinuity, but the obtained Perrotin floor age is ~3.70 Ga (Fig. 13a, Table 1). Thus, we interpret that the graben activity along the TR likely developed over time, which is evident from this chronological analysis. However, we are not constraining the formation period of graben as ~0.01 Ga, rather as an alternative we interpret they are regionally varying over time, which is consistent with morphological and other earlier interpretations (Anderson et al., 2001). In TR, the superposition, cross-cutting and chronological relationships between the features and craters suggest that within this region, the formation of pits, troughs and graben varied widely and likely formed on or post Early Hesperian epoch (Fig. 14).

The OR has been mapped as the Early Hesperian highland unit by Tanaka et al. (2014). From this region, we obtained the model ages for two craters (C21 and Pital), which hosts superposed pits (Figs. 8b, 9c), *catena* cutting through the Pital rim (Fig. 9b) and coalesced pits in association with VM walls (Figs. 8c, 9a). For crater C21, where pits superposed the crater floor and wall (Fig. 8b), the crater count statistics provide an absolute model age ~3.92 Ga, which indicates Mid to Late Noachian epoch (Table 1, Fig. 13b). We interpret that these pits have developed on or post of the Mid-Noachian epoch (Fig. 14). The western pits (Fig. 8b), which are directly associated with the VM wall, indicate that they also developed after the crater formation (Fig. 14).

Pital crater is the other crater from the OR, whose crater count statistics give an absolute model age ~2.61 Ga, which represents the Early Amazonian epoch (Fig. 13b, Table 1). Chronologically, the Pital crater is the best example for Early to Mid Amazonian activities over the VM region, which is in support of Carr and Head (2010). We obtained the absolute model age for the lobe-shaped deposit formed over the Pital ejecta (Fig. 13b). The crater count statistics were determined over this lobe and determined the model absolute age ~1.14 Ga (Middle Amazonian) (Fig. 13b). Marra et al. (2015) mapped this lobe and estimated the age that is similar to our estimated age. The origin of these lobes was previously studied and likely identified as fluvial lobes. However, the study didn't deny the role of lava in lobe formation (Marra et al., 2015) and argued that the elliptical features (pits) could be related to volcanic activity. Marra et al. (2015) inferred that the lobes cannot be younger than pits (Fig. 9b) and may have formed during the formation of pits. Thus, pits superposed over this lobe (Fig. 10a,b) lead to the interpretation that they might have formed after ~1.14 Ga and be one of the youngest pit related activities over the VM region (Fig. 14). Thus, the OR region of VM host the youngest pits, which is of Mid to Late Amazonian epoch.

The Coprates region mapped as Early Hesperian highland unit by Tanaka et al. (2014). From this region, we obtained model ages for Saravan crater and crater C34 (Figs. 11, 12) crater. The ejecta of Saravan crater is not visible; therefore we carried out crater count statistics over the crater floor, which indicates an age of ~3.76 Ga or Late Noachian epoch (Fig. 13b, Table 1). Therefore, the elongated trough, which cut through the floor and rim of the crater (Fig. 11), indicates that it probably formed on or later than the Late Noachian epoch. Similarly, for crater C34 (Fig. 3) which is adjacent to C33, the crater count approach samples a small area (only southern ejecta is available for crater counting) which leads to an age ~414 Ma (Late Amazonian) (Table 1). If the lobe formation, which likely superposed over the C34 ejecta, is associated with the pits (Fig. 12), then pit activity has occurred during the Late Amazonian epoch in this region. Fig. S7 provides the regional context of seven craters and their chronological variation around the VM region. This reveals that the pits and trough activities are varying chronologically over the large spatial extent of VM. Fig. S8 provides the complete chronological analysis carried out for 48 craters; however, this is given for completeness. Three more craters (Oudemans, Arima, C30) also show association with pits but the superposition between the craters and pits is unclear (Figs. S9–S11) and thus no conclusion has made from these crater. We want to clarify here that for interpretation, in most cases, we took those pits and troughs that are superposed over the crater rim (C6 (Fig. 4), Pital (Fig. 9), and C10 (Fig. 6)). If the pits/troughs are superposed over the crater, then they are post-event relative to crater formation. Also, we are not contesting for their reactivation, such superposed pits/troughs can be modified over time and it is very difficult to address these ambiguities fully, therefore, in this study we have considered the current state of pits/troughs.

7. Summary and conclusion

A comprehensive survey of craters associated with graben, pits, and troughs around the VM vicinity was carried out to understand the chronological and spatial modification of these features. Chronologically, pits and pit chains are superposed over several craters, among them the oldest pit to be formed on or post to ~3.92 Ga (Middle Noachian) and the youngest pit to be formed on or post to ~1.14 Ga

(Middle Amazonian) (Fig. 14). Spatially, the formation of pits occurred over a wide extent spanning different regions of the VM and pits of variable sizes (length, width, and depth) (Table S2) are witnessed within the craters and among the regions.

From the Tithonium region, the Perrotin crater provides evidence for post-Noachian graben formation that is evident on the crater floor and through the rim and agrees with Sharp (1973). The unnamed crater C10 provides evidence for Hesperian aged multiple dissecting troughs across the crater rim and also suggest a clear association with the VM wall. Moreover, crater C6 dated as ~3.6 Ga and the pits on the crater floor provide evidence for post Hesperian aged pit activities in this region of the VM.

From the Ophir region, Pital crater has preserved stratigraphic events like *catena* formation (~14 km wide on or after ~2.61 Ga), followed by lobe deposition (~1.14 Ga) and pit formation above it (~2 km wide) that possibly occurred during Mid to Late Amazonian. The Pital crater that preserved stratigraphic record is one typical location on Mars to infer the diverse pit activities around a crater, and interestingly formed at different epochs. Pital crater also revealed that on or after the Early Amazonian epoch, this region of Mars was capable of providing comprehensive evidence for one of the longest reported catena formation activity. The mean width of this catena seems to be one-tenth to the Candor Chasma width of the VM, which is located to the western side of Pital crater. In concurrence to this, the catena orientation does match with that of the Candor Chasma, suggesting that the Pital catena could have a possible association with Candor Chasma, but formed during the younger epoch. Our results provide evidence in support of Carr and Head (2010), which stated that the transition of individual pits to chains of coalescing pits and later to continuous canyons by surface material collapse over graben took place over a wide range of scale and time.

On comparing the Tithonium and Ophir regions, which are ~700 km apart, we observed superposed graben, pits, and troughs. It is evident from this regional comparison that these features not only varied chronologically among the regions; however, they also varied in size and extent. Based on this regional chronological and geometric variation, we likely interpret that they may indicate geological variations undergone in the subsurface that is recorded on the surface. The presence of graben, pits, and troughs on the surface and their spatial and chronological variations may likely be a record of the internal activity of Mars. The acquisition of more HiRISE and CRISM datasets can be used to study small notable features and their mineralogical variations. Overall, the superposition and/or crosscutting relationship of these graben and pits with craters concerning chronological interpretation revealed that the VM region likely witnessed the modification till the Middle Amazonian epoch, which is much later than what is generally presumed.

Supplementary data to this article can be found online at https://doi.org/10.1016/j.icarus.2020.113704.

Acknowledgment

We thank the two anonymous reviewers and the Editor for the significant reviews, which improved the manuscript. We thank Physical Research Laboratory, Department of Space, India for supporting our work. We thank Varun Sheel, Anil Shukla, Dwijesh Ray, Rishitosh K Sinha, Bhalamurugan Sivaraman and Nandita Kumari for their suggestions and discussions in this work.

References

Anderson, R.C., Dohm, J.M., Golombek, M.P., Haldemann, A.F.C., Franklin, B.J., Tanaka, K.L., Lias, J., Peer, B., 2001. Primary centers and secondary concentrations of tectonic activity through time in the western hemisphere of Mars. J. Geophys. Res. 106 (E9), 20,563. https://doi.org/10.1029/2000JE001278.

Andrews-Hanna, J.C., 2012a. The formation of Valles Marineris: 1. Tectonic architecture and the relative roles of extension and subsidence. J. Geophys. Res. 117, E03006 https://doi.org/10.1029/2011JE003953.

Andrews-Hanna, J.C., 2012b. The formation of Valles Marineris: 2. Stress focusing along the buried dichotomy boundary. J. Geophys. Res. 117, E04009 https://doi.org/10.1029/2011JE003954.

Andrews-Hanna, J.C., 2012c. The formation of Valles Marineris: 3. Trough formation through super-isostasy, stress, sedimentation, and subsidence. J. Geophys. Res. 117, E06002 https://doi.org/10.1029/2012JE004059.

Arya, A.S., Sarkar, S.S., Srinivas, A.R., et al., 2015. Mars Colour Camera: the payload characterization/calibration and data analysis from Earth imaging phase. Curr. Sci. 109 (6).

Baker, V., Carr, M. H., Gulick, V. C., Williams, C. R., and Marley, M. S., 1992. Channels and valley networks. In H. H. Kieffer (Ed.), Mars (pp. 493–522). University of Arizona Press, Space Science Series.

Banerdt, W. B., Golombek, M. P., and Tanaka, K. L., 1992. Stress and tectonics on Mars. Edited by Kieffer, H. H. et al., 249–297, Univ. of Ariz. Press, Tucson.

Brustel, C., Flahaut, J., Hauber, E., Fueten, F., Quantin, C., Stesky, R., Davies, G.R., 2017. Valles Marineris tectonic and volcanic history inferred from dikes in eastern Coprates Chasma. J. Geophys. Res. Planets 122, 1353–1371. https://doi.org/10.1002/2016JE005231.

Carr, M.H., 2012. The fluvial history of Mars. Phil. Trans. R. Soc. A 370 (1966), 2193–2215.

Carr, M.H., Head, J.W., 2010. Geologic history of Mars. Earth Planet. Sci. Lett. 294 (3), 185–203.

Chojnacki, M., Jakosky, B.M., Hynek, B.M., 2006. Surficial properties of landslides and surrounding units in Ophir Chasma, Mars. J. Geophys. Res. 111, E04005 https://doi.org/10.1029/2005JE002601.

Christensen, P.R., et al., 2004. The Thermal Emission Imaging System (Themis) for the Mars 2001 Odyssey Mission. In: Russell, C.T. (Ed.), 2001 Mars Odyssey. Springer, Dordrecht.

Cushing, G.E., et al., 2015. Atypical pit craters on Mars: new insights from THEMIS, CTX, and HiRISE observations. J. Geophys. Res. Planets 120, 1023–1043. https://doi.org/10.1002/2014JE004735.

Davis, P.A., Tanaka, K.L., Golombek, M.P., 1995. Topography of closed depressions, scarps, and graben in the north Tharsis region of Mars: implications for shallow crustal discontinuities and graben formation. Icarus 114 (403–422), 1995.

Dickson, J.L., Kerber, L.A., Fassett, C.I., and Ehlmann, B.L., 2018. A global, blended CTX mosaic of Mars with vectorized seam mapping: A new mosaicking pipeline using principles of non-destructive image editing. Proc. Lunar Planet. Sci. Conf. 49th, abstract#2480.

Dohm, J.M., Tanaka, K.L., 1999. Geology of the Thaumasia region, Mars: plateau development, valley origins, and magmatic evolution. Planet. Space Sci. 47 (411–431), 1999.

Fassett, C.I., Head, J.W., 2008. The timing of martian valley network activity: constraints from buffered crater counting. Icarus 195, 61–89. https://doi.org/10.1016/j.icarus.2007.12.009.

Fergason, R.L., Lee, E.M., Weller, L., 2013. THEMIS Geodetically Controlled Mosaics of Mars. 44th Lunar and Planetary Science Conference, the Woodlands, TX. In: abstract #1642.

Frey, H., 1979. Thaumasia: a fossilized early forming Tharsis uplift. J. Geophys. Res. 84 (1009–1023), 1979.

Fueten, F., et al., 2010. Dip of Chasm walls fault in Ophir Chasma, Valles Marineris, Mars. Lunar Planet. Sci. Conf. 41. In: abstract #1449.

Fueten, F., Flahaut, J., Deit, L.L., Stesky, R., Hauber, E., Gwinner, K., 2011. Interior layered deposits within a perched basin, southern Coprates Chasma, Mars: evidence for their formation, alteration, and erosion. J. Geophys. Res. 116, E02003 https://doi.org/10.1029/2010JE003695.

Golombek, M.P., 1979. Structural analysis of lunar graben and the shallow crustal structure of the Moon. J. Geophys. Res. 84, 4657–4666.

Greeley, R. and Guest, J.E., 1987. Geologic Map of the Eastern Equatorial Region of Mars. United States Geological Survey Miscellaneous Investigations Series, Scale 1: 15,000,000.

Hager, A., et al., 2018. Ages of fault structures adjacent and running subparallel to parallel to Valles Marineris. Lunar Planet. Sci. Conf. 49. In: abstract #2062.

Harish, Vijayan, S., 2019. Understanding chronological evolution of Valles Marineris vicinity region on Mars, through graben, pits and craters. Lunar and Planet. Sci. Conf. 50th. In: abstract #2132.

Hartmann, W.K., 1973. Martian surface and crust: review and synthesis. Icarus 19, 550–575.

Hartmann, W.K., Neukum, G., 2001. Cratering chronology and the evolution of Mars. Space Sci. Rev. 96, 165–194. https://doi.org/10.1023/A:1011945222010.

Hauber, E., Bleacher, J., Gwinner, K., Williams, D., Greeley, R., 2009. The topography and morphology of low shields and associated landforms of plains volcanism in the Tharsis region of Mars. J. Volcanol. Geotherm. Res. 185, 69–95. https://doi.org/10.1016/j.jvolgeores.2009.04.015.

Howard, A.D., 1988. Introduction: groundwater sapping on Mars and Earth. Sapping Features of the Colorado Plateau. NASA Spec. Publ. 491, 1–5.

Ivanov, B.A., 2001. Mars/Moon cratering rate ratio estimates. Space Sci. Rev. 96, 87–104. https://doi.org/10.1023/A:1011941121102.

Kumar, P.S., Nagula, K., Lakshmi, J.P.K., Stg, R., Dhabi, A.& Platz, T., 2018. Recent seismicity in Valles Marineris, Mars: insights from young faults, landslides, boulder falls and possible mud volcanoes. Earth and Planetary Science Letters. 505. 51–64. https://doi.org/10.1016/j.epsl.2018.10.008.

Lamb, M.P., Howard, A.D., Dietrich, W.E., Perron, J.T., 2007. Formation of amphitheater-headed valleys by waterfall erosion after large-scale slumping on Hawai'i. Geol. Soc. Am. Bull. 119 (7–8), 805–822. https://doi.org/10.1130/B25986.1.

Lucchitta, B.K., Isbell, N.K., Howington-Kraus, A., 1994. Topography of Valles Marineris: implications for erosional and structural history. J. Geophys. Res. 99 (E2), 3783–3798. https://doi.org/10.1029/93JE03095.

Malin, M. C. et al., 2007. Context Camera investigation on board the Mars Reconnaissance Orbiter, J. Geophys. Res., 112, E05S04, DOI:https://doi.org/10.1029/2006JE002808.

Mangold, N., Quantin, C., Ansan, V., Delacourt, C., Allemand, P., 2004. Evidence for precipitation on Mars from dendritic valleys in the Valles Marineris area. Science 305 (5680), 78–81.

Marra, W.A., Hauber, E., Jong, S.M., and Kleinhans, M.G., 2015. Pressurized groundwater systems in Lunae and Ophir Plana (Mars): insights from small-scale morphology and experiments. Geo. Res. J., Volume 8, 2015, Pages 1–13, ISSN 2214–2428, https://doi.org/10.1016/j.grj.2015.08.001.

McCauley, J.F., Carr, M.H., Cutts, J.A., Hartmann, W.K., Masursky, H., Milton, D.J., Sharp, R.P., Wilhelms, D.E., 1972. Preliminary report on the geology of Mars. Icarus 17, 289–327.

Mège, D., Cook, A.C., Garel, E., Lagabrielle, Y., Cormier, M.H., 2003. Volcanic rifting at Martian graben. J. Geophys. Res. 108 (E5), 5044. https://doi.org/10.1029/2002JE001852.

Michael, G.G., 2013. Planetary surface dating from crater size-frequency distribution measurements: multiple resurfacing episodes and differential isochron fitting. Icarus 226, 885–890.

Michael, G.G., Kneissl, T., Neesemann, A., 2016. Planetary Surface Dating from Crater Size-Frequency Distribution Measurements: Poisson Timing Analysis, 227, 279–285.

Montgomery, D.R., Som, S.M., Jackson, M.P.A., Schreiber, B.C., Gillespie, A.R., Adams, J. B., 2009. Continental-scale salt tectonics on Mars and the origin of Valles Marineris and associated outflow channels. Geol. Soc. Am. Bull. 121, 117–133. https://doi.org/10.1130/B26307.1.

Neukum, G. and Ivanov, B.A., 2001. Crater Production function on Mars. Proc. Lunar Planet. Sci. Conf. 32th, abstract#1757.

Okubo, C. H., and Schultz, R. A., 2005. Evidence of normal faulting and dike intrusion at Valles Marineris from pit crater topography. Proc. Lunar Planet. Sci. Conf. 36th, abstract #1008.

Pieri, D.C., 1980. Martian valleys: morphology, distribution, age, and origin. Science 210 (4472), 895–897.

Platz, T., Michael, G., Tanaka, K.L., Skinner, J.A., and Fortezza, C.M., 2013. Crater-based dating of geological units on Mars: Methods and application for the new global geological map. Icarus, Volume 225, Issue 1, 2013, Pages 806–827, ISSN 0019–1035, https://doi.org/10.1016/j.icarus.2013.04.021.

Plescia, J.B., Saunders, R.S., 1982. Tectonic history of the Tharsis region. Mars. J. Geophys. Res. 87 (9775–9791), 1982.

Quantin, C., Allemand, P., Mangold, N., Delcourt, C., 2004. Ages of Valles Marineris (Mars) landslides and implications for canyon history. Icarus 172 (2), 555–572. https://doi.org/10.1016/j.icarus.2004.06.013.

Robbins, S.J., Hynek, B.M., 2012. Utility of laser altimeter and stereoscopic terrain models: application to Martian craters. Planet. Space Sci. 86, 57–65. https://doi.org/10.1016/j.pss.2013.06.019.

Salese, F., Ansan, V., Mangold, N., Carter, J., Ody, A., Poulet, F., Ori, G.G., 2016. A sedimentary origin for intercrater plains north of the Hellas basin: implications for climate conditions and erosion rates on early Mars. Planets, Journal of Geophysical Research, p. 121. https://doi.org/10.1002/2016JE005039.

Schmidt, G., Fueten, F., Stesky, R., Flahaut, J., Hauber, E., 2018. Geology of Hebes Chasma. In: Mars, 1. structure, stratigraphy, and mineralogy of the interior layered deposits. Journal of Geophysical Research, Planets, p. 123. https://doi.org/10.1029/2018JE005658.

Schultz, R.A., 1998. Multiple-process origin of Valles Marineris basins and troughs. Mars. Planet. Space Sci. 46, 827–834.

Scott, E.D., Wilson, L., 2002. Plinian eruptions and passive collapse events as mechanisms of formation for Martian pit chain craters. Journal of Geophysical Research (Planets) 107 (E04). https://doi.org/10.1029/2000JE001432.

Sharp, R.P., Malin, M.C, 1975. Channels on mars. Geol. Soc. Am. Bull. 86 (5), 593–609.

Sharp, R.P., 1973. Mars: troughed terrain. J. Geophys. Res. 78 (20), 4063. https://doi.org/10.1029/JB078i020p04063.

Smith, D. E. et al., 2001. Mars Orbiter Laser Altimeter: Experiment summary after the first year of global mapping of Mars. J. Geophys. Res., 106(E10), 23689–23722, DOI: https://doi.org/10.1029/2000JE001364.

Tanaka, K.L., 1990. Tectonic history of the Alba Patera-Ceraunius Fossae region of Mars. Proc. Lunar Planet. Sci. Conf., 20th 1990, 515–523.

Tanaka, K.L., Davis, P.A., 1988. Tectonic history of the Syria Planum province of Mars. J. Geophys. Res. 93 (B12), 14893–14917. https://doi.org/10.1029/JB093iB12p14893.

Tanaka, K.L., Golombek, M.P., 1989. Martian tension fractures and the formation of graben and collapse features at Valles Marineris. Proc. Lunar Planet. Sci. Conf. 19 (383–396), 1989.

Tanaka, K.L., Golombek, M.P., Banerdt, W.B., 1991. Reconciliation of stress and structural histories of the Tharsis region of Mars. J. Geophys. Res. 96 (15617–15633), 1991.

Tanaka, K.L., Skinner, J.A., Jr., Dohm, J.M., Irwin, R.P., III, Kolb, E.J., Fortezzo, C.M., Platz, T., Michael, G.G., and Hare, T.M., 2014. Geologic map of Mars: U.S. Geological Survey Scientific Investigations Map 3292, scale 1:20,000,000, pamphlet 43 p., https://doi.org/10.3133/sim3292.

Vamshi, G.T., Martha, T.R., and Kumar, K.V., 2014. Origin of collapsed pits and branched valleys surrounding the Ius chasma on Mars. The International Archives of the Photogrammetry, Remote Sensing and Spatial Information Sciences, Volume XL-8, 2014 ISPRS Technical Commission VIII Symposium. DOI:https://doi.org/10.5194/isprsarchives-XL-8-485-2014.

Warner, N.H., Gupta, S., Calef, F., Grindrod, P., Boll, N., Goddard, K., 2015. Minimum effective area for high resolution crater counting of Martian terrains. Icarus 245, 198–240.

Webb, B.M., and Head, J.W., 2002. Terrestrial analogs for Noachian tectonics of the Tharsis rise and Thaumasia plateau, Mars. Lunar Planet. Sci. Conf. 33 abstract #1825.

Witbeck, N. E., Tanaka, K. L., and Scott, D. H., 1991. Geologic map of the Valles Marineris region, Mars (east half and west half), scale 1:2,000,000. U.S. Geol. Surv. Misc. Invest. Ser. Map, I-2010, 1991.

Wyrick, D., Ferrill, D.A., Morris, A.P., Colton, S.L., Sims, D.W., 2004. Distribution, morphology, and origins of Martian pit crater chains. J. Geophys. Res. 109, E06005 https://doi.org/10.1029/2004JE002240.

Wyrick, D.Y., Smart, K.J., 2009. Dike-induced deformation and Martian graben systems. J. Volcanol. Geotherm. Res. 185 (1–2), 1–11. https://doi.org/10.1016/j.jvolgeores.2008.11.022.